Investigations of Carbonic Acid, Dimethyl Carbonate and the Adsorption of CO_2 in Framework Solids

A Thesis
Submitted For the Degree of
DOCTOR OF PHILOSOPHY
in the Faculty of Science

by

Sandeep Kumar Reddy

CHEMISTRY AND PHYSICS OF MATERIALS UNIT
JAWAHARLAL NEHRU CENTRE FOR ADVANCED SCIENTIFIC RESEARCH
Bangalore – 560 064, India

MAY 2013

To My Mother

DECLARATION

I hereby declare that the matter embodied in the thesis entitled “**Investigations of Carbonic Acid, Dimethyl Carbonate and the Adsorption of CO_2 in Framework Solids**” is the result of investigations carried out by me at the Chemistry and Physics of Materials Unit, Jawaharlal Nehru Centre for Advanced Scientific Research, Bangalore, India under the supervision of Prof. S. Balasubramanian and that it has not been submitted elsewhere for the award of any degree or diploma.

In keeping with the general practice in reporting scientific observations, due acknowledgement has been made whenever the work described is based on the findings of other investigators. Any omission that might have occurred by oversight or error of judgement is regretted.

Sandeep Kumar Reddy

CERTIFICATE

I hereby certify that the matter embodied in this thesis entitled “**Investigations of Carbonic Acid, Dimethyl Carbonate and the Adsorption of CO_2 in Framework Solids**” has been carried out by Mr. Sandeep Kumar Reddy at the Chemistry and Physics of Materials Unit, Jawaharlal Nehru Centre for Advanced Scientific Research, Bangalore, India under my supervision and that it has not been submitted elsewhere for the award of any degree or diploma.

Prof. S. Balasubramanian
(Research Supervisor)

Acknowledgements

I wish to thank, first and foremost, my research supervisor, Prof. S. Balasubramanian for giving me the opportunity to explore the field of computational science. I am extremely thankful to him for teaching me molecular dynamics simulations and FORTRAN language. I sincerely acknowledge the suggestions and advice he provided on many occasions during my work. I also liked the academic freedom that I received in his group. I am greatly thankful to him for the excellent computing resources he has provided for the group and for his help during research and writing of this thesis.

I thank the Jawaharlal Nehru Centre for providing excellent research facilities, stimulating research ambience, and for financial support. I acknowledge JNCASR, Thematic Unit of Excellence on Computational Materials Science (TUE-CMS), Centre for Development of Advanced Computing (C-DAC) - Bangalore, CSIR Centre for Mathematical Modelling and Computer Simulation (CSIR C-MMACS) - Bangalore for providing computational resources and their support. I thank CSIR for Junior and Senior Fellowships. I thank all the staff members of JNCASR for their constant help.

I thank my collaborators Prof. Tapas Kumar Maji, Prof. Chandrabhas Narayana, Jayaramulu, Dr. Prakash, Ritesh, Gayatri, Arpan and Suresh for helpful discussions.

I am thankful to open source community for their service in providing the useful softwares and operating systems. I particularly acknowledge the developers of

CPMD, CP2K, LAMMPS, JMOL and VMD softwares.

I express my sincere thanks to Prof. Swapan Pati, Prof. Shobhana Narasimhan, Prof. N. S. Vidyadhiraja and Mrs. K. V. Shobha for the various courses they offered. I thank all members of the faculty of CPMU and TSU for fruitful discussions that I had with them.

I owe my sincere gratitude to my lab mate, Dr. Srinivas Raju for his help and guidance during my first three years of Ph.D. I thank all past and present lab mates; Dr. Saswati, Kanchan, Chidambar, Bharat, Rajdeep, Dr. Ganga, Satyanarayana, Sharma, Anirban, Karteek, Tarak and Pallabi for their joyous company and help.

I thank all my friends for all the moments I shared with them.

I thank my family members, especially my mother and brother for their constant support and encouragement throughout the years.

I thank all those who have helped me directly or indirectly.

Preface

The work outlined in this thesis is mainly devoted to (a) an understanding of the structural aspects of two CO_2 derived compounds – crystalline carbonic acid and liquid dimethyl carbonate and (b) an understanding of adsorption characteristics of CO_2 and other gases in metal-organic frameworks (MOF). This thesis is divided into two parts.

Part-I consists of four chapters. Chapter 1 provides a general introduction to carbonic acid and dimethyl carbonate. The fundamental characteristics of these molecules are discussed and their roles in environmental chemistry are presented. The current status of experimental and theoretical research in this area is also reviewed.

In Chapter 2, candidate crystal structures of β-carbonic acid are examined through a multi-tiered approach involving computational techniques including gas phase quantum chemistry, solid state total energy methods based on force fields, density functional theory (DFT) and molecular dynamics based on DFT. Crystal structures with one-dimensional chainlike motifs are found to be more stable than ones with sheetlike motifs. The predicted crystal structure is validated by comparing its infra-red (IR) spectrum, powder X-ray diffraction pattern and crystal stability against experimental data. Under dry conditions, the model crystal is found to be stable up to 359 K at 1 atm. It is also shown that the far-IR spectrum can be used to distinguish between crystal structures with chainlike or sheetlike hydrogen bonding topologies.

Chapter 3 presents gas phase quantum chemical calculations on one-dimensional oligomers of carbonic acid. The results obtained reinforce the conclusions obtained from solid state calculations of Chapter 2. The calculated IR and Raman spectra compare well with those determined experimentally for the centrosymmetric β-carbonic acid, rather than those for the α-polymorph. These calculations support the hypothesis that one-dimensionally hydrogen bonded anti-anti conformers of carbonic acid constitute crystalline β-carbonic acid.

In Chapter 4, a Car-Parrinello molecular dynamics simulation of liquid dimethyl carbonate is carried out to study its microscopic structure and dynamics. Conformational excitations of the molecule are probed in both its gas and liquid phases. The cis-trans conformer possesses a dipole moment of around 4.5 D in the liquid state, a value that is nearly five times as large as that for the cis-cis conformer. Using empirical potential based molecular dynamics simulations, weakly hydrogen bonded clusters of cis-trans conformers are observed in the liquid. The vibrational spectrum of liquid dimethyl carbonate is obtained from the trajectory and is shown to agree quite well with available experimental data.

Part-II consists of four chapters. Chapter 5 introduces metal-organic frameworks with an emphasis on their gas adsorption characteristics. It provides a brief survey of role of computer simulations in this rapidly growing field.

In Chapter 6, the locations of gas molecules and their nature of interaction with MOF are obtained using Kohn-Sham density functional theory. The chief interaction between CO_2 and MOF is of Lewis acid-base nature. The calculated interaction energies of CO_2 and H_2 with MOF are in agreement with experimentally determined enthalpies of adsorption. Electron density difference maps aid in the understanding of the interaction between the gas and the MOF.

Chapter 7 studies an unusual room-temperature CO_2 adsorption in a cubic MOF containing SiF_6 groups and pyrazine rings, using density functional theory and molecular dynamics simulations. The pyrazine rings are observed to be oriented at an angle of 17.2°with respect to the (200) Zn(II)-Si plane at low temperatures. These constrict the channel windows and reduce the uptake amount of CO_2. Ab initio molecular dynamics and Monte Carlo simulations support these observations.

In Chapter 8, the phenomenon variously described as gate-opening or breathing effect is studied in a MOF containing two interpenetrated nets. A model for the desolvated MOF is obtained from DFT calculations. The specificity of CO_2 in the opening of the gate is rationalized based on its large interaction strength with the MOF. Specifically, the role of the linker is found to be important and a direct correlation to experimentally observed gate-opening pressure is established.

A brief discussion on the theoretical methods employed in the thesis is provided in the Appendix.

Contents

Acknowledgements **v**

Preface **vii**

List of Figures **xvii**

List of Tables **xxvii**

Introduction **1**

Bibliography 5

I Carbonic Acid and Dimethyl Carbonate

1 Introduction **9**

1.1 Carbonic acid 9

1.2 Existence in solid phase 10

1.3 Gas phase detection and kinetic stability 13

1.4 Aqueous solution 17

1.4.1 MD simulations 17

1.4.2 Reaction equilibrium 18

1.4.3 pK_a 20

1.4.4 High temperature 20

1.5 Surface species 21
1.6 Dimethyl carbonate 22
1.7 Properties of DMC 23
Bibliography 24

2 Theoretical Investigations of Candidate Crystal Structures for β-Carbonic Acid 31

2.1 Introduction 31
2.2 Computational details 33
2.3 Results and discussion 43
  2.3.1 Crystal structure search 44
  2.3.2 Stabilization energies 50
  2.3.3 Infrared and Raman spectra 50
  2.3.4 Effect of van der Waals corrections 59
  2.3.5 Phase diagram and crystal stability 60
2.4 Discussion and conclusions 62
Bibliography 66

3 Vibrational Spectra of Linear Oligomers of Carbonic Acid: A Quantum Chemical Study 71

3.1 Computational details 72
3.2 Results and discussion 74
  3.2.1 Geometry optimization 74
  3.2.2 Vibrational frequencies 79
  3.2.3 Comparison with experimental data for the crystals 89
  3.2.4 A note on low-frequency vibrations 99
3.3 Discussion and conclusions 101
Bibliography 102

4 **Liquid Dimethyl Carbonate: A Quantum Chemical and Molecular Dynamics Study** **105**
4.1 Introduction 105
4.2 Computational details 107
4.3 Results and discussion 110
  4.3.1 Gas-phase calculations 110
  4.3.2 Liquid structure: molecular dynamics 118
  4.3.3 Spatial distribution functions 124
  4.3.4 Dipole analysis 129
  4.3.5 Conformational dependence of O-HC g(r) 130
  4.3.6 Vibrational spectrum 131
4.4 Discussion and conclusions 135
Bibliography 136

II Metal-Organic Frameworks

5 **Metal-Organic Frameworks for Gas Adsorption** **143**
5.1 Ligands 148
5.2 Properties and applications 150
5.3 Gas storage 151
  5.3.1 Hydrogen storage 152
  5.3.2 CO_2 storage 154
5.4 Role of computational studies 157
  5.4.1 Classical force fields 157
  5.4.2 Quantum mechanical calculations 160
Bibliography 162

6 **Ab initio Studies of H_2 and CO_2 Adsorption in a Three-Dimensional**

Metal-Organic Framework with Highly Polar Pore Surface 169

6.1 Introduction 169

6.2 Computational details 173

6.3 Results and discussion 175

  6.3.1 H_2 adsorption 177

  6.3.2 CO_2 adsorption 178

6.4 Conclusions 180

Bibliography 181

7 Unusual Room Temperature CO_2 Uptake in a Fluoro-Functionalized MOF: Insights from Theoretical Studies 185

7.1 Introduction 185

7.2 Computational details 186

7.3 Results and discussion 189

7.4 Conclusions 193

Bibliography 194

8 Breathing Effect and Gate-Opening in an Interpenetrated Metal-Organic Framework: A Computational Study 197

8.1 Introduction 197

8.2 Computational details 201

8.3 Results and discussions 203

  8.3.1 Desolvated structure 203

  8.3.2 Structural changes 206

  8.3.3 Effect of gas adsorption 206

  8.3.4 Role of linker in gate-opening 208

8.4 Conclusions 209

Bibliography 210

A Theoretical Methods **213**

A.1 Molecular dynamics 213

A.2 Classical molecular dynamics simulations 214

A.2.1 Force calculation and integrators 216

A.3 Ab initio molecular dynamics simulations 217

A.3.1 Born-Oppenheimer molecular dynamics 218

A.3.2 Car-Parrinello molecular dynamics 219

A.3.3 Hohenberg-Kohn theorem and Kohn-Sham functional 221

A.3.4 Forces in BOMD and CPMD 222

A.4 Pseudopotentials 222

Bibliography 224

List of Publications **227**

List of Figures

1.1 Three conformers of carbonic acid, namely a) anti-anti b) anti-syn and c) syn-syn. 10

1.2 Carbonic acid in the presence of zero, one, two and three water molecules. Energies (in kcal/mol) are with respect to the complex formed from carbonic acid and water molecules. For three water molecules case, experimental value is used for energy. [21] 15

1.3 Free energy difference (black colour) and concentration (grey colour) of CO_2, H_2CO_3, $HCO_3{}^-$ and $CO_3{}^{2-}$ species in aqueous solution at 298 K. Energies are given with respect to CO_2. Hydration of CO_2 is assumed to be first order reaction. 16

1.4 Dimethyl carbonate. 22

2.1 AA dimer. 33

2.2 Lattice energies of carbonic acid polymorphs as a function of their densities. Blue coloured rectangles show the most probable regions for finding exact crystal structure. 43

2.3 Molecular configuration in the crystal, Candidate I in the $P2_1$/c space group. Hydrogen bonds are in red colour. Top Panel: View along a-axis of the unit cell. Bottom Panel: Parallel chains of hydrogen bonded carbonic acid molecules form one layer. Chains present in the layer above or below run perpendicular to a chains in a central layer. 46

2.4 Molecular configuration in the structure, Candidate II in the $P2_1$/c space group. Hydrogen bonds are shown in red colour, and the network topology is sheetlike. Layers are separated by half the c-parameter. 47

2.5 Calculated XRD pattern of all crystal structures studied in the region 12 to 21° (lower) and 21 to 35° (upper) obtained using Cu-Kα radiation. Legends in lower panel are common for both. The values on y-axis are in arbitrary units. 49

2.6 Molecular configuration in the Candidate III crystal structure in the $P2_1$/c space group. Hydrogen bonds are shown in red colour. 51

2.7 Structure of Candidate IV in the $C222_1$ space group. Hydrogen bonds are shown in red colour. 51

2.8 Molecular configuration in the crystal structure $C2$/c (Candidate V). Hydrogen bonds are shown in red colour. 52

2.9 Infrared spectrum of the C2/c crystal structure (Candidate V) compared against experimental data. [3, 4] The far infrared region of the calculated spectrum is shown in inset. 52

2.10 Comparison of the calculated vibrational density of states (VDOS), Raman and Infrared spectra of D_2CO_3 belonging to the $C2$/c space group (Candidate V) in the region 900 to 1150 cm^{-1}. Assignment of the peaks can be found in text. 53

2.11 Calculated XRD pattern of all crystal structures studied with vdW corrections in the region 12 to 21° (lower) and 21 to 35° (upper) obtained using Cu-Kα radiation. Legends in lower panel are common for both. The values on y-axis are in arbitrary units. 55

2.12 Vibrational density of states (VDOS) calculated from Born-Oppenheimer MD simulations and from a Hessian calculation in the harmonic approximation for Candidate V. 57

2.13 Infrared (IR) spectrum of four crystals studied compared against experimental infrared spectrum. Roman numbers correspond to Candidate no. of crystal studied. 58

2.14 Far infrared spectrum of the four crystal structures studied in the region below 500 cm^{-1}. 58

2.15 Free energy of gas composed of anti-anti monomers and crystal as a function of temperature at constant pressure of 10^{-5}atm. 61

2.16 Phase diagram showing regions of stability of β-carbonic acid (violet) with respect to gas composed of anti-anti monomers (blue) based on Born-Oppenheimer MD simulations. 61

2.17 Raman spectra of Candidates I and V are shown. The zero axis is shifted up for clarity. 63

3.1 Three conformers of carbonic acid located on potential energy surface drawn as a function of two dihedrals as shown. Energies are calculated at CBS-QB3 level of theory. [11, 12] 75

3.2 Optimized geometries of dimer a (top) and dimer b (bottom). 76

3.3 Optimized geometry of tetramer. 77

3.4 Optimized geometry of octamer. 77

3.5 Tetramer consisting of two dimer a species. 77

3.6 Binding energy of oligomers as a function of oligomer size. Binding energy is calculated in two ways; E_n - n*E_1 divided by (n-1) (continuous lines) and E_n - E_{n-1} (dashed lines) where ‘n’ is the size of oligomer, E_1 is the energy of monomer and E_n is the energy of n^{th} oligomer. 78

3.7 Atomic displacement vectors of various vibrational modes of dimer b (a-a dimer) are shown. Hydrogen bonds are shown as red dashed lines and the vectors are black in colour. Colour code: C, gray; O, orange; H, white. 87

3.8 Comparison of the infrared spectra of the linear octamer (calculated), against experimental spectra of α and β forms of carbonic acid. [18, 20] Peaks due to terminal atoms are not shown. Calculated frequencies of the octamer are also shown as sticks (blue colour). 94

3.9 Comparison of the Raman spectra of the linear octamer (calculated), against experimental spectra of α, β forms of carbonic acid. [5, 17] Peaks due to terminal atoms are not shown. 98

3.10 Calculated far infrared spectrum of the linear octamer of carbonic acid. Atomic displacements observed for the mode at 239.3 cm^{-1} for a dimer is shown as inset. Colour code: C, gray; O, orange; H, white. Peaks denoted by asterisks are from terminal molecules in the oligomer. 100

3.11 Comparison of the low frequency Raman spectrum of the linear octamer (calculated) with the experimental spectra of α- and β-carbonic acid. [5, 17] Features of the octamer spectrum are also shown as blue sticks. 100

4.1 Intermolecular pair correlation functions (g(r)) between carbonyl oxygen and methyl hydrogen calculated in different windows of the CPMD trajectory, i.e., between 0-1, 1-2, 2-3 and 9-10 ps. These functions are compared against that obtained from the force field based simulation (FFMD). The g(r) calculated from CPMD evolves from that for the FFMD simulation, to a time-independent behaviour within a couple of picoseconds. 109

4.2 Cis-cis conformer of dimethyl carbonate. 111

4.3 Conformers of dimethyl carbonate. Dipole moment vector is shown in blue colour. Colour code: C, Black; O, Yellow; H, white. 111

4.4 Energy profile of dimethyl carbonate (bottom) as a function of two dihedral angles, ϕ_1 and ϕ_2 calculated at MP2/aug-cc-pVDZ level of theory. The vertical dotted lines show the positions of the three minima. Corresponding structures are also shown (top). 113

4.5 Potential energy of dimethyl carbonate as a function of two dihedrals, ϕ_1 and ϕ_2. The position of the (near-trans)-(near-trans) minimum is indicated by an arrow. 114

4.6 Dipole moment (in Debye) surface of dimethyl carbonate as a function of two dihedrals, ϕ_1 and ϕ_2. Colour scale is also shown. 116

4.7 (a) (cis-cis)-(cis-cis), (b) (cis-cis)-(cis-trans) and (c) (cis-trans)-(cis-trans) dimers. Blue dotted lines are hydrogen bonds formed between atom types O and HC. 117

4.8 Energy as a function of distance between two molecules both in the cis-cis conformation, calculated at OPLS force field, MP2/aug-cc-pVDZ and PBE+vdW/PW levels of theory. 119

4.9 Intermolecular pair correlation functions between different pairs of atoms in liquid DMC. 120

4.10 Intramolecular pair correlation function between atom types CT and OS. A bin width of 0.01 Åis used. 122

4.11 Probability distribution of dihedral angles, C2-O2-C1-O1 or C3-O3-C1-O1. 122

4.12 Probability distribution of the size of cluster consisting of cis-trans conformers in liquid DMC. 123

4.13 Snapshot of liquid dimethyl carbonate showing clustered cis-trans molecules along with cis-cis molecules. Cis-trans and cis-cis molecules are coloured in violet and grey, respectively. 125

4.14 Spatial distribution functions of carbonyl carbon (a-d) and carbonyl oxygen atoms (e-h) around the center of mass of dimethyl carbonate are shown at an isosurface value of 0.0165 Å^{-3}. (a), (b), (e) and (f) are obtained from the CPMD run while (c), (d), (g) and (h) are calculated from the force field based simulation. In each simulation, two views, one in which the carbonyl group is pointing towards the reader and in another, it is in the plane of the paper and pointing upwards are shown. Colour code: C-black; O-yellow; H-grey. 127

4.15 Probability distribution of angle between intermolecular (a) & (b): C-O vectors, (c) & (d) CT-CT vectors and (e) & (f): normal vectors to the plane of dimethyl carbonate molecules, obtained with both Kohn-Sham density functional theory (left) and force field (right) based molecular dynamics simulations. Marked values in legends are distances between center of mass of neighbouring molecules. 128

4.16 Probability distribution of molecular dipole moment in liquid dimethyl carbonate. The experimental value (0.91 D) is shown as dotted line. [6] 130

4.17 Intermolecular pair correlation functions between atom types O and HC obtained from both force field based molecular dynamics (FF) and Car-Parrinello molecular dynamics (CPMD) simulations. The legend also displays the conformational state of the central molecule. 131

4.18 Power spectrum of deuterated liquid dimethyl carbonate in the range 0 to 2500 cm^{-1}. The spectrum multiplied by a prefactor, $\omega\beta\hbar\omega$, is also shown (orange colour). Spectrum for the cis-cis conformer in gas-phase obtained from a Hessian calculation is shown in as sticks (green colour). 132

4.19 Power spectrum of deuterated liquid dimethyl carbonate in the range 400-1100 cm^{-1} (top) and 1100-2500 cm^{-1} (bottom) compared with its atomically decomposed vibrational density of states. Y-axis in bottom figure is scaled for clarity. Label scheme is same in both the panels. 133

5.1 Crystal structures of a) MOF-5 b) HKUST-1 or Cu-BTC. Both are shown along the a-axis. [6, 9] 145

5.2 Crystal structure of MIL-53. [11] View along c-axis. 147

5.3 Examples of common ligands used. Colour code: C, grey; O, red; N, blue; H, white. 149

6.1 View of the 3D framework along the c-axis showing oval shaped channels decorated with pendent carboxylate oxygen atoms and pyridyl moieties. Colour Code: C, gray; H, yellow; N, blue; O, red; Cd, wheat.172

6.2 Experimentally determined H_2 and CO_2 sorption profiles for **1’**. Left panel shows H_2 isotherms at 77 and 87 K and the right panel shows CO_2 isotherms at 195 and 298 K. 173

6.3 Locations of the (a) two H_2 molecules (shown as yellow dumbbells) (top panel) and (b) one CO_2 molecule (bottom panel) as determined using DFT calculations. The molecules are present in the oval shaped channels of the crystal viewed along the c-axis. 176

6.4 (a) Environment around the two adsorbed H_2 molecules at two different sites I and II as obtained from DFT calculations (distances are in Å). (b, c) Isosurface of the difference in the electron density of the system due to the adsorption of the H_2 molecules at I and II sites, respectively. Negative and positive values of electron density difference are shown in orange and black, respectively. Isosurface value is 0.0003 a.u. Colour code: C, gray; H, magenta; N, blue; O, red. Other atoms of MOF are not shown for clarity. 177

6.5 (a) View of the environment around the adsorbed CO_2 molecule obtained from DFT calculations (measured distances are in Å). Other atoms of the MOF are not shown for the sake of clarity. (b) Isosurface of the difference in the electron density of the system due to the adsorption of CO_2 molecule. Negative and positive electron density differences are shown in orange and black, respectively. The isosurface value is 0.0006 a.u. Colour code: C, gray; H, magenta; N, blue; O, red. Other atoms of MOF are not shown for clarity. 179

7.1 (a) View of the 1D pore showing that electronegative pendant fluorine atoms are aligned on the pore surface; (b) CPK diagram showing pores along the c-direction; (c) CO_2 adsorption-desorption isotherm measured at 298 K; (d) CO_2 adsorption-desorption isotherm measured at 195 K. 187

7.2 Trajectory of center of mass of CO_2 within MOF, shown in two crystallographic directions, obtained from Born-Oppenheimer molecular dynamics simulation at 195 K (shown in red). Panel (a) shows view along crystallographic c-axis. Adjacent pyrazine rings along the c-axis are not coplanar, (b) shows view along b-axis. Coordinates of the MOF shown here are those obtained from geometry optimization at zero Kelvin. 190

7.3 Electron density difference maps of **1'** plotted using an iso value of 0.00009 a.u. obtained from Kohn-Sham density functional theory. (a) View along c-axis and (b) view along a-axis. Regions in red and violet colour show electron loss and those in white and green show electron gain upon adsorption of CO_2. Loss of electrons from the π-cloud of pyrazines forms dumbbell-shaped iso surfaces (violet colour). 191

7.4 Time averaged structure of **1'** obtained from Born-Oppenheimer molecular dynamics simulations at temperatures (a) 195 and (b) 300 K. The blue surface denotes the position of any MOF atom with an isosurface value of 0.3 Å^3. The CO_2 molecule is shown inserted to easily identify the reduction in pore size at 195 K. 191

7.5 Calculated accessible surface area for CO_2 molecule as a function of the angle between planes of adjacent pyrazine rings and that formed by Si-Zn-Si atoms. [13] 192

8.1 a) Building unit of MOF **1** b) Its supercell of size 3x1x1 shown along b-direction. Solvent molecules are not shown. 199

8.2 Experimentally determined CO_2, N_2, H_2, Ar adsorption isotherms of **1'** at 195 K. 199

8.3 a) In situ powder X-ray diffraction (PXRD) patterns collected during CO_2 adsorption on **1'** at 195 K. b) Adsorption isotherm of CO_2 gas at 195 K. 201

8.4 Relative energies (in kJ/mol) of **1** as a function of angle β obtained when MOF is fully loaded with either solvent molecules or CO_2 gas. Values are given with respect to the corresponding minima. 202

8.5 Relative energy (in kJ/mol) of **1'** as a function of β-value obtained from density functional theory calculations. Experimental β-value is shown as green dashed line. Error in cell volume between simulations and experiment is 4.7%. 204

8.6 Powder XRD pattern of the calculated **1'** structure compared against experiment. The refinement was performed using GSAS software. [13] 205

8.7 Comparison of experimental structure of **1** against the calculated one of **1"**. The main difference, that causes the sliding of the nets, is the movement of the linker towards carboxylate group(s) for additional stability (enclosed in red boxes). View along b-axis. More details are given in text. 207

8.8 Comparison of experimentally determined CO_2 adsorption profiles at 195 K: (a) **1'** (b) **2'**. 209

List of Tables

1.1 Physical properties of dimethyl carbonate. [45, 54] 24

2.1 Atom types, charges and 6-9 Lennard-Jones parameters of the force field used in this work. 34

2.2 Comparison of geometries calculated at B3LYP/CBSB7, MP2/CBSB7, force field (FF) and PBE/85Ry level of theory. The geometry obtained from CBS-QB3 is the same as that from B3LYP/CBSB7. . . . 35

2.3 Fractional coordinates of atoms in the five crystal structures optimized using DFT at PBE/85Ry level of theory. 37

2.4 Cell parameters of the five candidate crystal structures obtained at PBE/85Ry level of theory. 38

2.5 Cell parameters of four crystal structures obtained using B3LYP/6-21g(d) calculations. 41

2.6 Fractional coordinates of four crystal structures studied using B3LYP/6-21g(d). 42

2.7 Comparison of energies calculated at B3LYP/CBSB7, MP2/CBSB7, CBS-QB3, force field (FF) and PBE/85Ry level of theory. The energies do not include the zero point energy and are in kJ/mol. 45

2.8 Comparison of energies, densities and nature of hydrogen bonding network of the crystal structures optimized at PBE/85Ry level of theory. 45

2.9 Comparison of the infrared vibrational features of β-D_2CO_3 obtained from our simulations (Candidate V) and experiments. [4] 56

2.10 Cell parameters and fractional coordinates of Candidate V, obtained upon the addition of empirical vdW corrections to the PBE functional. 60

3.1 Energies (in kcal/mol) of oligomers calculated at B3LYP/6-311G(2d,d,p) and MP2/6-311G(2d,d,p) levels of theory. Values are calculated as E_n - n*E_1 where E_n is the total energy of the oligomer of size n and E_1 is that for the monomer. Energies are in kcal/mol. Values in parentheses include zero point energy (ZPE) contribution. 78

3.2 Harmonic and anharmonic frequencies (in cm^{-1}) of the anti-anti (a-a) and anti-syn (a-s) monomers, calculated at B3LYP/6-311G(2d,d,p) and MP2/6-311G(2d,d,dp) levels of theory. Mode assignments are also shown. 80

3.4 Calculated harmonic and anharmonic frequencies (in cm^{-1}) of the two dimers along with mode assignments. IR and Raman intensities of corresponding modes are given in columns 3 and 6. Letter T stands for modes due to terminal atoms. The data is from B3LYP/6-311G(2d,d,p) level of theory. 81

3.3 Calculated harmonic and anharmonic frequencies of the anti-anti (a-a), anti-syn (a-s) monomer along with mode assignments. R and I stand for Raman active and IR active, respectively. Values in parentheses refer to intensities of the corresponding modes. The data is from B3LYP/6-311G(2d,d,p) level of theory. 84

3.5 Comparison of IR spectra of anti-anti monomer, anti-syn monomer and dimer b with experimental matrix isolated gas-phase spectrum. [13] Mode assignments are given. The data is obtained using B3LYP/6-311G(2d,d,p) level of theory. Values are in cm^{-1}. 85

3.6 Comparison of unscaled harmonic and anharmonic frequencies of the anti-anti dimer (dimer b) obtained at B3LYP/6-311G(2d,d,p) and MP2/6-311G(2d,d,p) levels of theory. Letter T stands for modes due to terminal atoms. 88

3.7 Comparison of unscaled harmonic frequencies of tetramer obtained at B3LYP/6-311G(2d,d,p) and MP2/6-311G(2d,d,p) levels of theory. Letter T stands for modes due to terminal atoms. 90

3.8 Spectral features in the infrared spectrum of the octamer (calculated), and in the α and β forms of carbonic acid (experimental). [18, 20] The calculations are performed at B3LYP/6-311G(2d,d,p) level of theory. Each mode of the octamer is scaled by a factor given in column 2 to take into account the anharmonicity of the mode. See text for discussions. Values in parentheses denote the IR intensities in arbitrary units. [a]from Ref. [21] 91

3.9 Spectral features in the Raman spectrum of the octamer (calculated), and in α and β forms of carbonic acid (experimental). [5, 17] The calculations are performed at B3LYP/6-311G(2d,d,p) level of theory. Each mode of the octamer is scaled by a factor given in column 2 to take into account the anharmonicity of the mode. See text for details. Values in parentheses denote the Raman intensities in arbitrary units. 96

4.1 Energy (kcal/mol) of cis-trans conformer compared to cis-cis conformer calculated at different levels of theory. 112

4.2 Binding energy and relative energy (kcal/mol) of (cis-cis)-(cis-cis) (CC-CC), (cis-cis)-(cis-trans) (CC-CT) and (cis-trans)-(cis-trans) (CT-CT) dimers calculated at OPLS force field, MP2/aug-cc-pVDZ and PBE+vdW/PW levels of theory. [a]Values are with respect to CC-CC dimer. 118

4.3 Hydrogen bond lengths (in Å) and angles (in °) formed between (cis-cis)-(cis-cis) (CC-CC), (cis-cis)-(cis-trans) (CC-CT) and (cis-trans)-(cis-trans) (CT-CT) dimers calculated at OPLS force field, MP2/aug-cc-pVDZ and PBE+vdW/PW levels of theory. 119
4.4 Vibrational density of states of liquid and gas-phase monomer along with mode assignments. Frequencies are not scaled. 135

6.1 Binding energies of H_2 and CO_2 molecules in the MOF calculated using BLYP/85 Ry level of theory with [28] and without empirical van der Waals corrections compared against experimental values of the heat of adsorption^a. 175

8.1 Calculated cell parameters and volume of **1** and **1’** along with their experimental values. 203
8.2 Binding energies (kJ/mol) of four gas molecules (CO_2, H_2, N_2 and Ar) calculated for MOF **1’** using density functional theory. Here, site-I and site-II refer to adsorption near aromatic ring and carboxylate group or metal center, respectively. 207

Introduction

Carbon dioxide is present in the Earth's atmosphere and is naturally a part of the carbon cycle. Its increasing concentration in the atmosphere is a matter of serious concern. Apart from attempts to reduce its release into the atmosphere at source, an alternate solution is to use it as a renewable source similar to sunlight, water, wind, etc. It is easily available and has advantages like it is non-toxic, abundant and economical. As a carbon source, it can be converted into useful compounds for diverse applications. The constraint in the chemical modification of carbon dioxide is its stability. Being the most oxidised form of carbon, it is chemically quite inert and stable both thermodynamically and kinetically. Thus, a metal catalyst or high energy source is required to activate it, which makes the production of chemicals from CO_2 expensive relative to traditional synthetic methods. Research on the activation of carbon dioxide could make the former processes economically viable.

Carbonic acid: From a molecular perspective, its linear geometry in the electronic ground state does not lend it a dipole moment; however, the polarity of the C=O bond imparts it a significant quadrupole moment. This enables CO_2 to be partially soluble in water. A small fraction of the dissolved species is converted into carbonic acid, H_2CO_3. H_2CO_3 has a short lifetime in the presence of water at ambient conditions, and it further decomposes into bicarbonate and carbonate. The amount of carbonic acid can be altered by varying the pressure and/or proton concentration in aqueous solution. Under ambient conditions, carbonic acid is estimated to have a lifetime of about 300 ns in water and several million years in a dry environment. [1] Based on this, Tossell has proposed that CO_2 can be stored in the form of H_2CO_3 under dry conditions. [2] Despite its compositional and structural simplicity, it is still not considered a "mainstream molecule" and thus has not received attention from researchers, commensurate to its role in the acid-base chemistry of carbonated aqueous solutions. Recently, ultrafast infrared spectroscopic measurements have shown that carbonic acid is not a weak acid and its acidity is comparable to that of formic acid. [3] Even though its presence in aqueous solution is known for a long time, its appearance in other states has been studied only over the last two decades.

In the gas phase, the anti-anti conformer of H_2CO_3 molecule is the predominant species, as determined using matrix isolation techniques, while the anti-syn monomer and a dimer of carbonic acid are the other two species identified. [4–6] These recent studies mark the first detection of carbonic acid molecule in gas phase. Interesting possibilities for the formation and adsorption of carbonic acid on the surface of calcium carbonate particles, under cold laboratory conditions have emerged recently. [7, 8] Dust aerosols in the troposphere constituted with mineral particles can react with acidic gases to generate carbonic acid molecules as surface species. Crystalline carbonic acid, in contrast, has been studied more extensively. The synthesis of thin films of two polymorphs of carbonic acid under equilibrium conditions has been pioneered by the group at Innsbruck. [9] However, due to high desorption rates and the poor crystallinity of the sample prohibited them from determining the the crystal structure of either polymorphs.

Dimethyl carbonate: The carbon atom in CO_2 is electron deficient, and thus shows an affinity for electron-donating agents and nucleophiles. This property can be used to convert it into useful chemicals. It can be converted into carbonic and carbamic acids, organic carbonates and carbamates, five- or six- membered ring carbonates. [10] One of the CO_2 derivatives, organic carbonates are recognized as alternative to volatile organic solvents due to their low volatality, non-flammability, non-toxicity, low cost and biodegradability. [11, 12] In addition to their use in electrochemical and extractive applications, they are extremely useful in replacing toxic compounds such as methyl halide, dimethylsulfate and phosgene, etc. in methylation and carbonylation reactions. They are used in place of phosgene in the synthesis of polycarbonates and polyurethanes. The former is used in electronic applications, construction materials, production of CD, DVD and Blu-Ray discs, medical applications and many more. Unlike carbonic acid, organic carbonates are stable under ambient conditions. The linear carbonates have densities similar to water. Among them, dimethyl carbonate (DMC) is extensively used as a solvent in many chemical reactions. It plays a dynamic role in some reactions and influences the nature of the product type with change in temperature. [10] It can be prepared from the reaction of CO_2 with methanol in the presence of an inorganic dehydrating agent or a heterogeneous catalyst. [13, 14] To understand the role of solvent in chemical reaction mechanisms, its microscopic structure needs to be understood. Computer simulations such as either classical or Kohn-Sham density functional theory (DFT) based molecular dynamics (MD) can be used which also allows to compute the physical properties. More details of such analyses devoted to the liquid state can be found in the literature. [15–20]

Metal organic frameworks: For using CO_2 in industries, one needs a capture mechanism at point sources and release it easily whenever it is required. Adsorbents should possess unique properties such as high adsorption amounts, selective gas uptake, high thermal stability, etc. at ambient conditions. Several materials are available which possesses the above characteristics. For example, alkanolamine, zeolites, amine-grafted silica, activated carbons, covalent organic frameworks and metal-organic frameworks (MOF) come under this category. [21] MOFs are promising materials because they offer high surface areas and porosity which can be utilized to store large amounts of gas. Among the three generations documented in the literature, the second generation MOFs, which are rigid after solvent removal, are useful in gas storage and separation. Third generation MOFs, which show flexibility upon guest removal while retaining the crystallinity, are found extremely useful in recent times due to their inherent diverse properties which are responsive to external stimuli such as light, gas molecules, temperature, electric field, etc. [22] While most of the properties, for example adsorption characteristics, can be easily studied from experimental methods, the microscopic understanding of underlying structural transformations, gas molecule location and their impact on MOF rigidity are not easily amenable to many experimental methods. One needs to employ neutron or synchrotron X-ray scattering techniques, which are less accessible, to obtain such information. In an alternate and simpler approach, computational techniques can be used to obtain an atomic picture of adsorption characteristics and structural transformations (if any). Density functional theory (DFT) allows us to study condensed phase systems within a reasonable computational time.

This thesis is mainly devoted to (a) understanding the structural aspects of two CO_2 derived compounds – crystalline carbonic acid and liquid dimethyl carbonate and (b) understanding adsorption characteristics of CO_2 and other gases in metal-organic frameworks. The thesis examines these problems using modern simulation methodologies. The problems pose considerable challenges requiring the use of multiple computational techniques ranging from classical, quantum chemical and periodic density functional theory methods.

The thesis is divided into two parts. The first part describes studies on identifying possible crystal structures of β-carbonic acid, and a section devoted to the study of liquid dimethyl carbonate using both classical and density functional theory based molecular dynamics simulations. The second part is devoted to the study of metal-organic framework solids. It describes the use of computational techniques to locate gas binding sites in these porous materials. This part also discusses mechanistic aspects involved in gas uptake as a function of temperature as well as interesting structural transformations in a MOF upon, specifically, CO_2 uptake. A brief description of the theoretical methods employed in the thesis is presented in the Appendix.

Bibliography

[1] Loerting, T.; Tautermann, C.; Kroemer, R. T.; Kohl, I.; Hallbrucker, A.; Mayer, E.; Liedl, K. R. *Angew. Chem. Int. Ed.* **2000**, *39*, 891–894.

[2] Tossell, J. A. *Environ. Sci. Technol.* **2009**, *43*, 2575–2580.

[3] Adamczyk, K.; Premont-Schwarz, M.; Pines, D.; Pines, E.; Nibbering, E. T. J. *Science* **2009**, *326*, 1690–1694.

[4] Bernard, J.; Seidl, M.; Kohl, I.; Liedl, K. R.; Mayer, E.; Galvez, O.; Grothe, H.; Loerting, T. *Angew. Chem. Int. Ed.* **2011**, *50*, 1939–1943.

[5] Mori, T.; Suma, K.; Sumiyoshi, Y.; Endo, Y. *J. Chem. Phys.* **2009**, *130*, 204308.

[6] Mori, T.; Suma, K.; Sumiyoshi, Y.; Endo, Y. *J. Chem. Phys.* **2011**, *134*, 044319.

[7] Al-Hosney, H. A.; Grassian, V. H. *J. Am. Chem. Soc.* **2004**, *126*, 8068–8069.

[8] Bernard, J.; Seidl, M.; Mayer, E.; Loerting, T. *ChemPhysChem* **2012**, *13*, 3087–3091.

[9] Loerting, T.; Bernard, J. *ChemPhysChem* **2010**, *11*, 2305–2309.

[10] Sakakura, T.; Choi, J.-C.; Yasuda, H. *Chem. Rev.* **2007**, *107*, 2365–2387.

[11] Righi, G.; Bovicelli, P.; Barontini, M.; Tirotta, I. *Green Chem.* **2012**, *14*, 495–502.

[12] Tundo, P.; Selva, M. *Acc. Chem. Res.* **2002**, *35*, 706–716.

[13] Bian, J.; Xiao, M.; Wang, S.; Wang, X.; Lu, Y.; Meng, Y. *Chem. Eng. J.* **2009**, *147*, 287–296.

[14] Honda, M.; Suzuki, A.; Noorjahan, B.; Fujimoto, K.-i.; Suzuki, K.; Tomishige, K. *Chem. Commun.* **2009**, *0*, 4596–4598.

[15] Tuckerman, M. E.; Marx, D.; Parrinello, M. *Nature* **2002**, *417*, 925–929.

[16] Kuo, I.-F. W.; Mundy, C. J.; McGrath, M. J.; Siepmann, J. I.; VandeVondele, J.; Sprik, M.; Hutter, J.; Chen, B.; Klein, M. L.; Mohamed, F.; Krack, M.; Parrinello, M. *J. Phys. Chem. B* **2004**, *108*, 12990–12998.

[17] Kuo, I.-F. W.; Mundy, C. J. *Science* **2004**, *303*, 658–660.

[18] Todorova, T.; Seitsonen, A. P.; Hutter, J.; Kuo, I.-F. W.; Mundy, C. J. *J. Phys. Chem. B* **2006**, *110*, 3685–3691.

[19] Tuckerman, M. E.; Chandra, A.; Marx, D. *Acc. Chem. Res.* **2006**, *39*, 151–158.

[20] Senapati, S.; Chandra, A. *J. Chem. Phys.* **1999**, *111*, 1223–1230.

[21] Sumida, K.; Rogow, D. L.; Mason, J. A.; McDonald, T. M.; Bloch, E. D.; Herm, Z. R.; Bae, T.-H.; Long, J. R. *Chem. Rev.* **2012**, *112*, 724–781.

[22] Horike, S.; Shimomura, S.; Kitagawa, S. *Nat. Chem.* **2009**, *1*, 695–704.

Part I

Carbonic Acid and Dimethyl Carbonate

Chapter 1

Introduction

1.1 Carbonic acid

CO_2-rich water contains low amounts of carbonic acid (H_2CO_3) which can dissociate into its structural analogs: bicarbonate (${HCO_3}^-$) and carbonate (${CO_3}^{2-}$). Carbonic acid has often been unjustly termed as a weak acid due to its short lifetime in water and the presence of undissociated carbon dioxide in aqueous solution. [1–3] Carbonic acid (CA) is a diprotic acid with its ability to donate two protons in aqueous solution. Three stable conformers of CA are known, namely anti-anti, anti-syn and syn-syn. High level quantum chemistry calculations at the CBS-QB3 level show the anti-anti conformer to be the most stable in gas phase, while the other two are higher in energy by 1.53 and 9.85 kcal/mol, respectively. These energies are corrected for zero-point energy. Figure 1.1 shows these conformers along with dihedral angle values of ϕ_1 and ϕ_2. CA is considered to be elusive in nature because of its ready dissociation in the presence of moisture. It possesses both hydrogen bond donating (hydroxyl) and acceptor (carbonyl) groups. Strong intermolecular hydrogen bonds leading to stable homodimers can thus be formed.

Carbonic acid has often been termed as a weak acid due to (i) its short lifetime in water and (ii) the presence of undissociated carbon dioxide in aqueous solution. [1, 2]

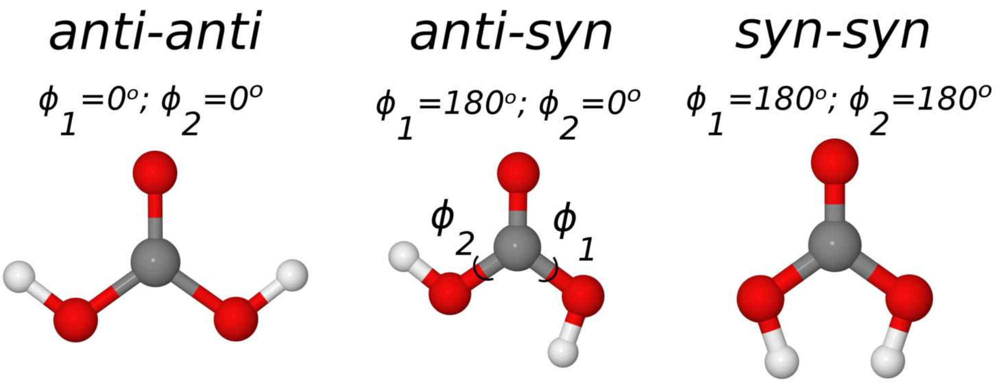

Figure 1.1: Three conformers of carbonic acid, namely a) anti-anti b) anti-syn and c) syn-syn.

The importance of carbonic acid in fields ranging from atmospheric, surface and geochemistry cannot be overstressed. Despite its structural simplicity, it is still not considered a "mainstream molecule" and thus has not received attention from researchers commensurate to its role in the acid-base chemistry of carbonated aqueous solutions. Being a diprotic acid, its equilibrium constants for its two deprotonation processes have been determined experimentally. Under ambient conditions, carbonic acid is estimated to have a lifetime of about 300 ns in water and several million years in a dry environment. The barrier for deprotonation decreases drastically upon the addition of few water molecules to CA. The stability of CA under dry conditions is kinetic; the equilibrium of course, favours CO_2+H_2O over a CA molecule.

1.2 Existence in solid phase

Although CA is a small molecule formed from the combination of even smaller and simple molecules (CO_2 and H_2O), it is only recently that it has started gaining attention. The notion that CA cannot be isolated in pure form either in gas or condensed phase was held for a long time; it was considered elusive. However, Schwarz and coworkers, detected CA upon the thermal decomposition of NH_4HCO_3. [4] Moore and Khanna condensed mixtures of gaseous CO_2 and H_2O to form thin films which were irradiated with high energy protons to expedite protonation. [5] CA was identified using both infrared (IR) and mass spectroscopy. This experiment mimics conditions present in outer space and thus shows the plausibility of CA to exist under such conditions.

Mayer and co-workers demonstrated the possibility of synthesizing carbonic acid in crystalline form without employing any radiation sources. [6] By successive injections of potassium bicarbonate and hydrogen chloride on to a cold substrate within a cold finger setup, they were able to prepare thin films of crystalline CA. The initially cold layers were warmed gradually from liquid nitrogen temperature and the infrared spectrum was recorded in situ. They observed evidence for the presence of individual layers of the salt and the acid up to a temperature of 180 K, however upon increasing the temperature further, protons from the acid layers interacted with the bicarbonate leading to the formation of crystalline CA. The use of a methanolic bicarbonate solution yielded the α-polymorph of CA, while an aqueous one yielded β-carbonic acid. [7–10] They were differentiated based on infrared vibrational spectroscopy and their distinct thermal stabilities. While the IR spectrum of α-carbonic acid exhibits a peak at 1304 cm^{-1} which is assigned to the symmetric stretching of the $C(OH)_2$ group, it is absent in β-carbonic acid. Further, in-plane bending of the CO_3 group shows a peak at 583 cm^{-1} in α-carbonic acid whereas in β-carbonic acid, it is split into two peaks located at 655 and 682 cm^{-1}. Also, several other mode frequencies exhibit differences. In particular, a large difference of 124 cm^{-1} was observed for the in-plane bending of C-OH group between the two polymorphs. [8, 9]

Although crystalline thin films of CA can be synthesized, they have been characterized only through vibrational spectroscopy so far. The crystal structure of polymorphs of CA have not been determined yet, as single crystals could not be grown and the powder X-ray diffraction patterns from the thin films are not good enough for the purpose of refinement. [11, 12] The mass density of the crystals have not been reported as well. Vibrational spectroscopy have been used to identify the building blocks or structural synthons present in these crystals. Mayer's (and currently, Loerting's) group have studied the phase transition from amorphous to crystalline carbonic acid by monitoring the spectral changes within a narrow temperature range – from 200 to 230 K. For instance, the protonation of an aqueous solution of $KHCO_3$ with HCl leads to amorphous CA film at 200 K which transforms to β-form upon heating. However, protonation with HBr (instead of HCl) leads to the direct generation of the crystalline phase. The changes in the IR spectrum due to amorphization in the former scenario include shifts in peak positions, broadening and splitting of bands. Interestingly, they observed that the amorphous samples which crystallize to either the α or β polymorph upon heating, exhibit IR spectra which are more or less characteristic of their crystalline counterparts. Thus, the amorphous films themselves can be distinguished. One can also conclude that the structural synthon present in the crystalline phase of the two polymorphs was already developed in the corresponding distinct amorphous states. [11] The X-ray diffraction pattern of amorphous compounds synthesized from each of these polymorphs too were different, indicating that the building blocks in these two crystal structures are different. [11]

Interestingly, on heating the samples above 200 K, both polymorphs sublime without decomposition, indicating the stability of carbonic acid in gas phase. The stability is likely due to the high energy barrier for its decomposition into CO_2 and H_2O, as calculations have shown. [13, 14] This observation is instrumental in providing an insight into the possible presence of CA in outer space. The existence of CA in many extraterrestrial systems has been proposed. [15] The two polymorphs of CA can be differentiated by their IR spectra.

1.3 Gas phase detection and kinetic stability

Gas phase: Although carbonic acid was detected in its solid phase in mid-90's, it was not until recently that the molecule was identified in its gas phase. Employing microwave spectroscopy, Mori et al. have observed the anti-anti and anti-syn conformer of CA, generated by passing CO_2 gas (along with a carrier gas, Ar) through a water reservoir. [16, 17] The resulting gas mixture was subjected to a high, pulsed electrical potential. Recently Bernard et al. were able to isolate several species of CA from gas phase onto an inert argon matrix. [18, 19] As mentioned earlier, this group had pioneered the synthesis and spectroscopic characterization of crystalline polymorphs of CA. The molecule in gas phase was generated by the sublimation of α-carbonic acid at 210 K, and was later trapped in a cold argon matrix and characterized using high-resolution infrared spectroscopy.

They showed that α-carbonic acid can be sublimed at 210 K and trapped as monomers and dimers in argon matrix at 6 K and can be recrystallized back to the same polymorph by evaporating the matrix at 180 K. This observation demonstrated that the CA molecule is intact in gas phase and does not dissociate into water and carbon dioxide, demonstrating its kinetic stability. Interestingly, Bernard et al. found a gas phase composition of 1:10:1 for the mixture of anti-syn conformer, anti-anti conformer and anti-anti hydrogen bonded dimer, respectively. [19] Boltzmann inversion of these population ratio indicates the free energy difference between anti-syn and anti-anti monomers in gas phase to be about 0.9 kcal/mol at 210 K. This estimate is not inconsistent with the internal energy difference of 1.53 kcal/mol between these species estimated from high level quantum chemical calculations.

Stability: Early theoretical studies focused on relative stabilities for the reaction of CO_2 and H_2O to form H_2CO_3. In 1995, employing quantum chemical calculations, Wright and Boldyrev suggested a pathway for the conversion of H_2CO_3 to CO_2 and H_2O by internal dihedral rotation followed by an intramolecular proton transfer in gas phase. [20] Later, to investigate how water molecules affect the stability of carbonic acid, Liedl et al. performed ab initio calculations of H_2CO_3 interacting with either one, two or three water molecules. [13, 14] The reaction pathway leading to the formation of carbon dioxide was explored. Under dry conditions, the equilibrium favours the dissociated (product) state, i.e., CO_2+H_2O over the carbonic acid molecule (reactant). However, the reaction path involves a transition state whose energy is 43.55 and 52.60 kcal/mol with respect to CA and CO_2-H_2O states, respectively. [13, 14] Thus, the CA molecule, once formed, can be kinetically stable for millions of years, a possibility in outer space with such favourable conditions. However, the scenario changes in the presence of water.

Liedl and coworkers found the barrier for the dissociation of CA molecule to decrease systematically with increase in the number of water molecules interacting with it. This observation is consistent with the rapid dissociation of CA in aqueous solution. Another interesting observation by the same group is that the energy of the anti-anti CA dimer is nearly the same as or even lower than its dissociated molecular components, viz. two molecules each of carbon dioxide and water. [22] These data suggest a mixture of monomers and dimers could be expected to found in outer space.

Nguyen et al. carried out a complete gas phase and implicit solvation study of neutral hydration of CO_2 with different number of water molecules. They examined the role of water on the transition state for the dissociation of carbonic acid. [21] Energy change, geometries of transition, reactant and product states with increasing number of water molecules from zero to three are shown in Figure 1.2. Water plays catalytic role and it directly involves in the transition state by forming cyclic structures with CA. It shows that three water molecules are enough to achieve experimental rate constants.

At ambient conditions, the concentration of CO_2 in aqueous solution is obtained

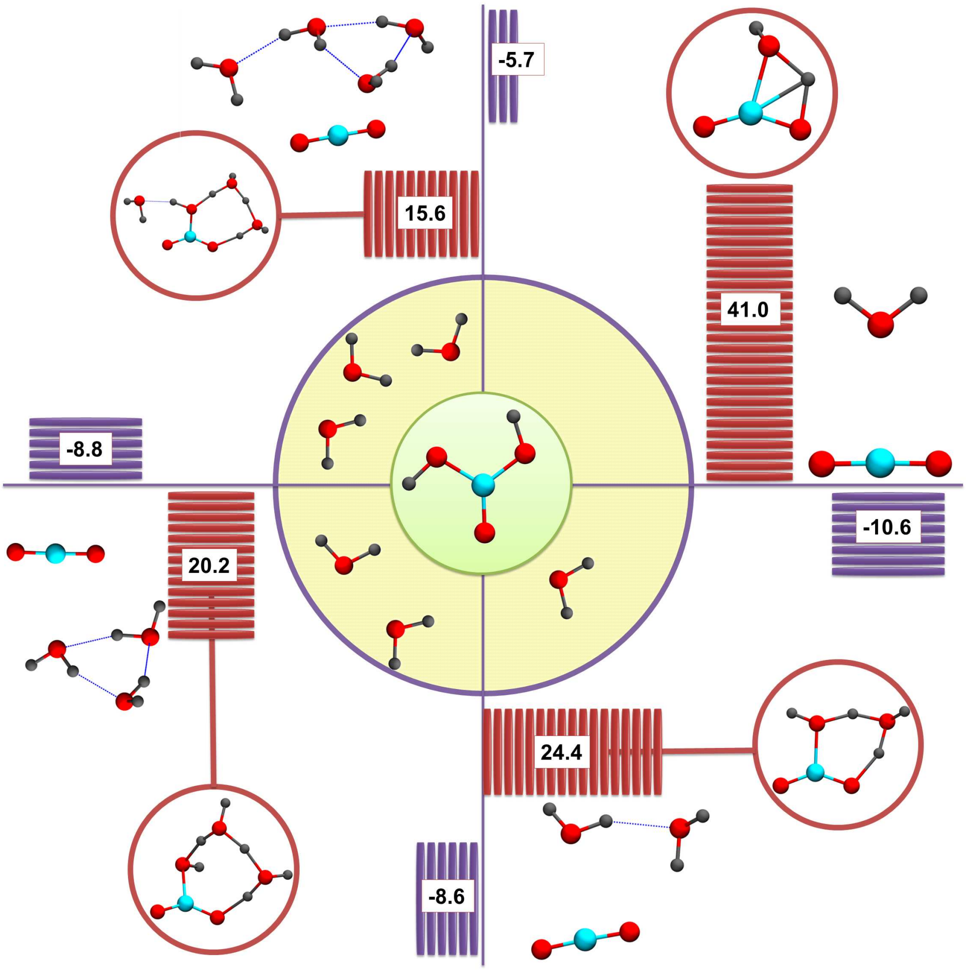

Figure 1.2: Carbonic acid in the presence of zero, one, two and three water molecules. Energies (in kcal/mol) are with respect to the complex formed from carbonic acid and water molecules. For three water molecules case, experimental value is used for energy. [21]

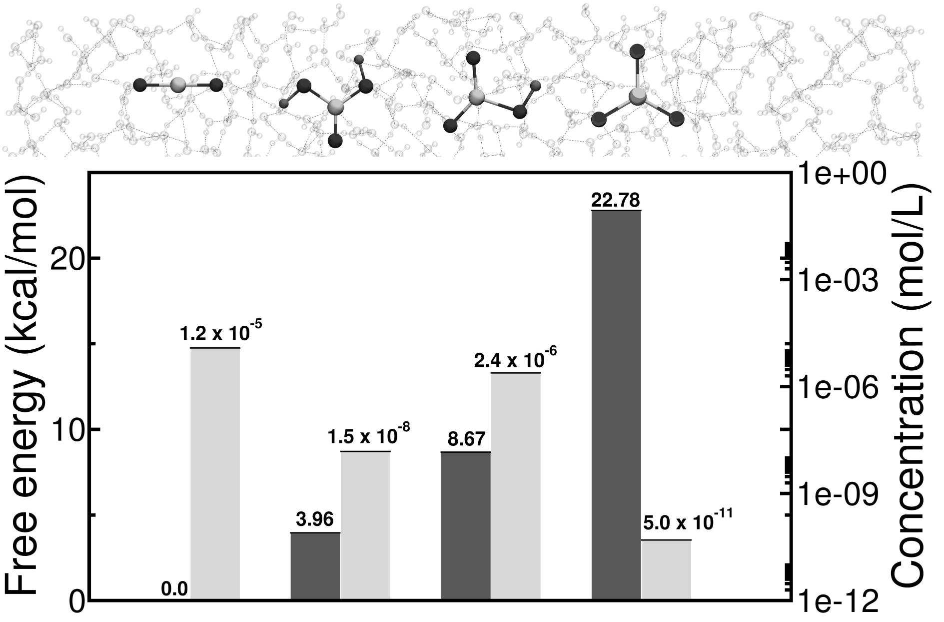

Figure 1.3: Free energy difference (black colour) and concentration (grey colour) of CO_2, H_2CO_3, $HCO_3{}^-$ and $CO_3{}^{2-}$ species in aqueous solution at 298 K. Energies are given with respect to CO_2. Hydration of CO_2 is assumed to be first order reaction.

from Henry's law that uses the partial pressure of CO_2 in the atmosphere and the equilibrium constant (3.38 x 10^{-2}) for the reaction between CO_2 gas and its aqueous phase. Using this value and the equilibrium constants reported among CO_2 and carbonate species in aqueous solution, the concentrations of H_2CO_3, $HCO_3{}^-$, $CO_3{}^{2-}$ and H^+ can be calculated. [23, 24] Figure 1.3 shows the concentrations and free energies of these species in aqueous solution. At ambient conditions, the hydrated CO_2 concentration is higher than those of other species. Carbonic acid concentration is about three orders of magnitude lesser compared to that of CO_2 and also, it is slightly lesser than bicarbonate. The concentration of $CO_3{}^{2-}$ species is negligible.

1.4 Aqueous solution

1.4.1 MD simulations

Very few molecular dynamics simulations have been attempted owing to the rapid dissociation of CA molecule in water. Our group have carried out Born-Oppenheimer molecular dynamics simulations of one molecule of CA in either anti-anti or anti-syn conformation in a bath of water by employing van der Waals corrections. Simulations were run for 40 ps out of which 30 ps was used for analysis. Recently, Kumar et al. have carried out Car-Parrinello molecular dynamics simulations of one molecule of CA in either anti-anti or anti-syn conformation in a bath of water. [25] Its hydration structure and dynamics were compared against those of other carbonate species and of CO_2 in aqueous solution. Water was found to interact strongly with the hydroxyl group of CA rather than to the carbonyl group. In water, the syn-syn conformer dissociates into a bicarbonate and a proton within a few picoseconds. [26] By employing free energy sampling methods in combination with Kohn-Sham density functional theory based MD simulations, Liu et al. have calculated the pK_a for each non-equivalent hydrogen to be 3.11 for the anti-anti conformer and 2.60 and 3.75 for the anti-syn conformer, in agreement with the value obtained for deuterated carbonic acid using femtosecond infrared spectroscopy. [24, 26]

In a pioneering work, Stirling and P*á*pai have demonstrated that in aqueous solution, unlike in gas-phase, the conversion of CO_2 to H_2CO_3 proceeds via two steps: (i) formation of HCO_3^-, followed by (ii) its combination with the proton to form H_2CO_3. [27] The rate-determining step of this reaction is the formation of HCO_3^-. Using metadynamics technique, they calculated the energy barrier for CO_2 hydration to HCO_3^- or H_2CO_3 to be 18.8 kcal/mol, close to the experimental value of 21.8 kcal/mol.

Similar calculations have been carried out by Galib and Hanna, [28] whose focus was on determining the dissociation mechanism of H_2CO_3 to $HCO_3{}^-$ and CO_2. In gas phase, the anti-anti and syn-syn conformers of CA transform to the anti-syn conformer through a dihedral angle change, prior to decomposition. However, in liquid water, it is facilitated by proton transfer from CA to a water molecule and an abstraction of a proton from water (possibly another water molecule) to CA, through water chains. In fact, conformational change in the solution would require dislodging of water molecules and hence will involve a larger barrier than in gas phase. Further, the dissociation in aqueous phase is shown to proceed via the formation of a bicarbonate species.

1.4.2 Reaction equilibrium

In water, carbonic acid is in equilibrium with aqueous CO_2 and bicarbonate and this reaction is represented by, [29, 30]

$$CO_2 + H_2O \rightleftharpoons CO_2(aq) \tag{1.1}$$

$$CO_2(aq) \rightleftharpoons HCO_3^- + H^+ \tag{1.2}$$

where $[CO_2(aq)] = [H_2CO_3 + CO_2]$. Since the concentration of H_2CO_3 is much less compared to that of dissolved CO_2, the overall reaction is assumed to be a single step i.e., by skipping the intermediate step of the formation of carbonic acid. Thus, the dissociation constant, called as an apparent dissociation constant (K_1), for this reaction is defined as

$$K_1 = \frac{[H^+][HCO_3^-]}{[CO_2 + H_2CO_3]} \tag{1.3}$$

Here the reactants consist of CO_2 along with trace amounts of H_2CO_3. But, the true dissociation constant (K_a) of H_2CO_3 is independent of the CO_2 hydration reaction

(1) and is defined as,

$$K_a = \frac{[H^+][HCO_3^-]}{[H_2CO_3]} \tag{1.4}$$

Dividing equation 1.4 by 1.3 gives,

$$\frac{K_a}{K_1} = \frac{[CO_2 + H_2CO_3]}{[H_2CO_3]} \tag{1.5}$$

$$K_a = K_1 \left[1 + \frac{[CO_2]}{[H_2CO_3]}\right] \tag{1.6}$$

Eq. 1.6 gives the relation between the true and apparent dissociation constants. The direct measurement of concentration ratio of CO_2 to H_2CO_3 is difficult due to the very low concentration of the latter. The value of K_a can be obtained indirectly from the ratio of rate constants of deprotonation and protonation of H_2CO_3 using carbamino quenching method, rapid flow and manometric methods, thermometric method, isotopic exchange method, high field conductance method and stopped flow method, all of which incidentally are techniques which could not determine the rate constants accurately due to shorter life time of CA in aqueous solution. [23, 29–35] Further, since the concentration ratio of CO_2 to H_2CO_3 is equal to the ratio of rate constants of H_2CO_3 to CO_2 in aqueous solution, rate measurements of these reactions too can provide an estimate of K_a. However, K_a values obtained with the above methods do not agree well with each other and a range of values between 3.35-3.80 have been reported. [23] Until recently, carbonic acid was not detected directly by any means in aqueous solution and its chemical reactivity used to be poorly understood due to inaccurate estimates of K_a. Taking into account the concentration of dissolved CO_2 and CA (the precise determination of which posed difficulties), Eq. 1.6 leads to an estimate of pK_a to be around 4 or so. What is the pK_a of CA?

1.4.3 pK_a

The acid dissociation constant of carbonic acid was determined recently using ultrafast spectroscopy by Nibbering and co-workers through the real-time protonation of HCO_3^- to form carbonic acid. [24] Note that this was the method employed by Mayer's group as well for the synthesis of thin films of crystalline CA. They used a photo acid to protonate DCO_3^- in deuterated aqueous solution. [24] Carbonic acid formation was detected by monitoring the infrared active C=O stretching mode using time-resolved infrared spectroscopy. The advantage of focussing on this mode alone is that it can be used to identify the three different species: carbonic acid, bicarbonate and carbonate. They report the rate for the deuteron transfer from the photo acid to bicarbonate to be 1.7×10^{11} s^{-1} and calculate the pK_a of H_2CO_3 to be 3.45 ± 0.15. It is thus conclusively established that carbonic acid is a strong acid whose acidity is comparable to that of formic acid. [36] Further, CA was estimated to have a lifetime of 300 ns in water before it deprotonates. This short, but finite lifetime had effectively prohibited its detection in aqueous phase for a long time, and led to it being misappropriately tagged as "elusive". Theoretical calculations have shown that the difference in pK_a between anti-anti and anti-syn conformers is small and is within the range of experimental error. [37, 38] Its determination should dispel notions of carbonic acid being weak; CA is as strong as formic acid.

1.4.4 High temperature

High-temperature water (HTW), defined as water in the temperature range 423 - 623 K, is regarded as a good solvent for carrying out acid-catalyzed organic chemical reactions that can proceed without the addition of a catalyst. Its characteristics, such as low dielectric constant, increased acidity and high isothermal compressibility are conducive for the dissolution of many small organic molecules. Since the ionic product of water increases thousand-fold in the temperature range 300 K to 573

K, [39] such reactions can be carried out in HTW relatively easily than at ambient conditions. Pressurized CO_2 pumped into HTW has been shown to further increase the reaction rates. [40] The reduction in the pH of CO_2-enriched HTW increases reaction rates and product yield. This methodology bears an advantage over the addition of an acid catalyst in that it does not require a neutralization step; after the completion of the reaction, the CO_2 can be pumped off easily by depressuring. Many organic reactions have been carried out in such solutions in an effective manner. [40, 41] The equilibrium concentrations of carbonate, bicarbonate, carbonic acid, proton and hydroxyl ions in carbonated HTW has not been determined by either experiment or simulations so far and thus constitutes one of our aims in this area.

1.5 Surface species

Heterogeneous reactions between dust aerosols formed with minerals such as calcium carbonate and atmospheric gases are important in troposphere as they can alter the species equilibrium. Calcium carbonate surface, in general, is terminated with one or two layers of water at environmentally relevant conditions. Water, in turn modifies the surface so as to terminate it as $Ca(OH)(CO_3H)$ and OH functional groups. Grassian and coworkers have shown that carbonic acid is an important intermediate formed when acidic gases such as nitric acid, sulphur dioxide, formic acid and acetic acid react with calcium carbonate surface. [42] The adsorbed carbonic acid was stable up to 350 K without decomposition. [43] On heating it above this temperature, CA dissociated to release CO_2.

Loerting et al. have recently used FTIR spectroscopy to study bulk carbonic acid formation under conditions existing in the troposphere. [44] First, $CaCO_3$ dust particles were protonated using HCl at a temperature above 200 K under humid environment. The formation of carbonic acid was detected by comparing the infrared bands with that of β-carbonic acid. On heating it further to 250 K and at 60-100%

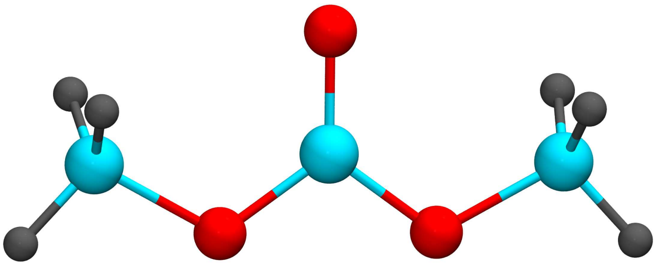

Figure 1.4: Dimethyl carbonate.

relative humidity, carbonic acid was found to be surprisingly stable for long periods without decomposition. At 260 K, it started decomposing and disappeared in about an hour. This provides a tantalising possibility for the existence of carbonic acid in troposphere. Further, one should take into account the possible presence of carbonic acid in understanding the acidity of atmosphere.

1.6 Dimethyl carbonate

In addition to carbonic acid, we have also examined one more environmentally benign compound related to CO_2, i.e., dimethyl carbonate (DMC). Its gas phase structure is similar to that of carbonic acid with the latter's two protons replaced by methyl groups. DMC contains both polar and non-polar groups (shown in Figure 1.4). It belongs to the family of carbonate esters and has been used as a solvent for several chemical reactions over many decades. It is almost immiscible in water but soluble in many organic solvents such as diethyl ether, methanol, etc. It has been used as a solvent for electrochemical and extractive applications. In recent years, researchers have promoted the use of dimethyl carbonate as a viable, green solvent due to its low volatality, non-flammability, non-toxicity and biodegradability. [45, 46] It is used in methylation and carbonylation reactions to substitute for harmful, toxic and corrosive solvents such as dimethyl sulfate, methyl halides and phosgene and to conduct chemical reactions in environmentally safety media. [46, 47] It has found applications in the fuel industry due to its high oxygen weighting (53 %), higher than the normally used additive solvent, tert-butyl methyl ether. [48] It is regarded as a good additive to gasoline to reduce carbon monoxide in auto exhaust. [47, 49–51] DMC is used in lithium batteries to dissolve lithium ions due to its low volatility, long shelf life, increased battery power density and an overall reduction in manufacturing costs. Very recently, it was shown that DMC can be used in completely controlled stereo- and regioselective ring-opening chemical reactions in an eco friendly, green condition by replacing toxic solvents, dichloromethane, diethyl ether, acetonitrile and acetone. [46] Although the Suzuki-Miyaura coupling reaction was reported to have been carried out in DMC without any metal, a recent report has found trace amounts of metal which could have catalyzed the reaction. [52] It has been used as a replacement for dimethylsulfate and methyl halides in methylation reactions. [53] Due to its environmentally benign characteristics, DMC is the only organic liquid which is exempted by the US Environmental Protection Agency (EPA) from being classified as a volatile organic compound (VOC).

1.7 Properties of DMC

- It is a non-toxic compound. Prior to mid-1980s, it was thought to be toxic as the synthetic methods involved toxic reagents such as phosgene. Later, it was prepared by carbonylation of methanol with oxygen or carbon dioxide [55], without adding harmful compounds.

- It is a flammable liquid with a boiling point at 363.3 K.

- Depending on the experimental conditions, DMC can act as either methylating or methoxycarbonylating agent in the presence of a nucleophile.

Table 1.1: Physical properties of dimethyl carbonate. [45, 54]

Property	Value
Melting point (K)	277.6
Boiling point (K)	363.3
Density (gm/c)	1.07
Viscosity (cps)	0.625
Dielectric constant	3.087
Dipole moment (D) in liquid phase	0.91
ΔH_{vap} (kcal/kg)	88.2
Solubility in H_2O (g/100g)	13.9

Other properties of DMC are listed in Table 1.1. DMC reacts selectively with many organic compounds such as amines, alcohols, thiols, sugars, amino acid, etc. on addition of a small amount of base for catalysis and it produces no waste, that greatly reduces the cost. [56–67] Many industries have started using DMC as a solvent in methylation and/or methoxycarbonylation reactions.

Bibliography

[1] Lide, D. R.; Bruno, T. J. In *CRC Handbook of Chemistry and Physics*, 93rd ed.; Haynes, W. M., Ed.; CRC Press: Florida, 2012.

[2] Hornback, J. M. *Organic Chemistry*, 2nd ed.; Thomson Brooks/cole, 2005.

[3] Campbell, M. K.; Farrel, S. O. *Biochemistry*, 0007th ed.; Thomson Brooks/Cole, 2011.

[4] Terlouw, J. K.; Lebrilla, C. B.; Schwarz, H. *Angew. Chem. Int. Ed. Engl.* **1987**, *26*, 354–555.

[5] Moore, M. H.; Khanna, R. K. *Spectrochim. Acta, Part A: Mol. Biomol. Spectrosc.* **1991**, *47*, 255–262.

[6] Hage, W.; Hallbrucker, A.; Mayer, E. *J. Chem. Soc., Faraday Trans.* **1995**, *91*, 2823–2826.

[7] Hage, W.; Hallbrucker, A.; Mayer, E. *J. Am. Chem. Soc.* **1993**, *115*, 8427–8431.

[8] Hage, W.; Hallbrucker, A.; Mayer, E. *J. Chem. Soc., Faraday Trans.* **1996**, *92*, 3183–3195.

[9] Hage, W.; Hallbrucker, A.; Mayer, E. *J. Chem. Soc., Faraday Trans.* **1996**, *92*, 3197–3209.

[10] Hage, W.; Hallbrucker, A.; Mayer, E. *J. Mol. Struct.* **1997**, *408*, 527–531.

[11] Winkel, K.; Hage, W.; Loerting, T.; Price, S. L.; Mayer, E. *J. Am. Chem. Soc.* **2007**, *129*, 13863–13871.

[12] Loerting, T.; Bernard, J. *ChemPhysChem* **2010**, *11*, 2305–2309.

[13] Loerting, T.; Tautermann, C.; Kroemer, R. T.; Kohl, I.; Hallbrucker, A.; Mayer, E.; Liedl, K. R. *Angew. Chem. Int. Ed.* **2000**, *39*, 891–894.

[14] Ludwig, R.; Kornath, A. *Angew. Chem. Int. Ed.* **2000**, *39*, 1421–1423.

[15] Hage, W.; Liedl, K. R.; Hallbrucker, A.; Mayer, E. *Science* **1998**, *279*, 1332–1335.

[16] Mori, T.; Suma, K.; Sumiyoshi, Y.; Endo, Y. *J. Chem. Phys.* **2009**, *130*, 204308.

[17] Mori, T.; Suma, K.; Sumiyoshi, Y.; Endo, Y. *J. Chem. Phys.* **2011**, *134*, 044319.

[18] Jacoby, M. Gaseous Carbonic Acid Trapped And Analyzed. Chem. Eng. News, https://pubs.acs.org/isubscribe/journals/cen/89/i03/html/8903scic7.html, Jan 17, 2011, pp 33.

[19] Bernard, J.; Seidl, M.; Kohl, I.; Liedl, K. R.; Mayer, E.; Galvez, O.; Grothe, H.; Loerting, T. *Angew. Chem. Int. Ed.* **2011**, *50*, 1939–1943.

[20] Wight, C. A.; Boldyrev, A. I. *J. Phys. Chem.* **1995**, *99*, 12125–12130.

[21] Nguyen, M. T.; Matus, M. H.; Jackson, V. E.; Ngan, V. T.; Rustad, J. R.; Dixon, D. A. *J. Phys. Chem. A* **2008**, *112*, 10386–10398.

[22] Liedl, K. R.; Sekusak, S.; Mayer, E. *J. Am. Chem. Soc.* **1997**, *119*, 3782–3784.

[23] Kern, D. M. *J. Chem. Educ.* **1960**, *37*, 14.

[24] Adamczyk, K.; Premont-Schwarz, M.; Pines, D.; Pines, E.; Nibbering, E. T. J. *Science* **2009**, *326*, 1690–1694.

[25] Kumar, P. P.; Kalinichev, A. G.; Kirkpatrick, R. J. *J. Phys. Chem. B* **2009**, *113*, 794–802.

[26] Liu, X. D.; Lu, X. C.; Wang, R. C.; Zhou, H. Q. *J. Phys. Chem. A* **2010**, *114*, 12914–12917.

[27] Stirling, A.; Papai, I. *J. Phys. Chem. B* **2010**, *114*, 16854–16859.

[28] Galib, M.; Hanna, G. *J. Phys. Chem. B* **2011**, *115*, 15024–15035.

[29] Edsall, J. T. *NASA Special Publication* **1969**, *188*, 15.

[30] Eigen, M.; de Maeyer, L. *Proc. R. Soc. London, A* **1958**, *247*, 505–533.

[31] Roughton, F. J. W. *Proc. R. Soc. London, A* **1930**, *126*, 470–486.

[32] Harned, H. S.; Davis, R. *J. Am. Chem. Soc.* **1943**, *65*, 2030–2037.

[33] Roughton, F. J. W. *J. Am. Chem. Soc.* **1941**, *63*, 2930–2934.

[34] Berg, D.; Patterson, A. *J. Am. Chem. Soc.* **1953**, *75*, 5197–5200.

[35] Wissbrun, K. F.; French, D. M.; Patterson, A. *J. Phys. Chem.* **1954**, *58*, 693–695.

[36] Hadlington, S. Carbonic Acid Captured [Online]. Chem. World, http://www.rsc.org/chemistryworld/News/2009/November/12110902.asp, Nov 12, 2009.

[37] Ritter, S. Carbonic Acid Could be a Fix for Carbon. Chem. Eng. News, http://pubs.acs.org/isubscribe/journals/cen/87/i13/html/8713scic5.html, Mar 30, 2009, pp 29.

[38] Tossell, J. A. *Environ. Sci. Technol.* **2009**, *43*, 2575–2580.

[39] Akiya, N.; Savage, P. E. *Chem. Rev.* **2002**, *102*, 2725–2750.

[40] Hunter, S. E.; Savage, P. E. *Ind. Eng. Chem. Res.* **2003**, *42*, 290–294.

[41] Yamaguchi, A.; Hiyoshi, N.; Sato, O.; Shirai, M. *Green Chem.* **2011**, *13*, 873–881.

[42] Al-Hosney, H. A.; Grassian, V. H. *J. Am. Chem. Soc.* **2004**, *126*, 8068–8069.

[43] Al-Hosney, H. A.; Grassian, V. H. *Phys. Chem. Chem. Phys.* **2005**, *7*, 1266–1276.

[44] Bernard, J.; Seidl, M.; Mayer, E.; Loerting, T. *ChemPhysChem* **2012**, *13*, 3087–3091.

[45] Tundo, P.; Selva, M. *Acc. Chem. Res.* **2002**, *35*, 706–716.

[46] Righi, G.; Bovicelli, P.; Barontini, M.; Tirotta, I. *Green Chem.* **2012**, *14*, 495–502.

[47] Ono, Y. *Pure Appl. Chem.* **1996**, *68*, 367–375.

[48] Rounce, P.; Tsolakis, A.; Leung, P.; York, A. P. E. *Energy Fuels* **2010**, *24*, 4812–4819.

[49] Chia, L. H. L.; Kwan, K. J.; Huang, H. H. *Aust. J. Chem.* **197**, *34*, 349–355.

[50] Bernini, R.; Mincione, E.; Barontini, M.; Crisante, F.; Fabrizi, G.; Gambacorta, A. *Tetrahedron* **2007**, *63*, 6895–6900.

[51] Gaylor, P. J. Modified fuel. U. S. Patent 2,331,386, Standard Oil Development Co., 1943.

[52] Inamoto, K.; Campbell, L. D.; Doi, T.; Koide, K. *Tetrahedron Lett.* **2012**, *53*, 3147–3148.

[53] Memoli, S.; Selva, M.; Tundo, P. *Chemosphere* **2001**, *43*, 115–121.

[54] Mikolajczyk, M.; Grzejszczak, S.; Zatorski, A.; Montanari, F.; Cinquini, M. *Tetrahedron Lett.* **1975**, 3757–3760.

[55] Aricó, F.; Tundo, P. *Russ. Chem. Rev.* **2010**, *79*, 479–489.

[56] Rosamilia, A. E.; Aric, F.; Tundo, P. *J. Org. Chem.* **2008**, *73*, 1559–1562.

[57] Rosamilia, A. E.; Arico, F.; Tundo, P. *J. Phys. Chem. B* **2008**, *112*, 14525–14529.

[58] Selva, M.; Marques, C. A.; Tundo, P. *Gazz. Chim. Ital.* **1993**, *123*, 515–518.

[59] Trotta, F.; Tundo, P.; Moraglio, G. *J. Org. Chem.* **1987**, *52*, 1300–1304.

[60] Tundo, P.; Anastas, P.; Black, D. S.; Breen, J.; Collins, T.; Memoli, S.; Miyamoto, J.; Polyakoff, M.; Tumas, W. *Pure Appl. Chem.* **2000**, *72*, 1207–1228.

[61] Shieh, W. C.; Dell, S.; Bach, A.; Repic, J.; Blacklock, T. J. *J. Org. Chem.* **2003**, *68*, 1954–1957.

[62] Tundo, P.; Bressanello, S.; Loris, A.; Sathicq, G. *Pure Appl. Chem.* **2005**, *77*, 1719–1725.

[63] Tundo, P.; Rossi, L.; Loris, A. *J. Org. Chem.* **2005**, *70*, 2219–2224.

[64] Tundo, P.; Selva, M. *Chem. Tech.* **1995**, *25*, 31–35.

[65] Tundo, P.; Selva, M.; Bomben, A. *Organic Syntheses* **1999**, *76*, 169–177.

[66] Tundo, P.; Trotta, F.; Moraglio, G.; Ligorati, F. *Ind. Eng. Chem. Res.* **1988**, *27*, 1565–1571.

[67] Tundo, P.; Selva, M.; Perosa, A.; Memoli, S. *J. Org. Chem.* **2002**, *67*, 1071–1077.

Chapter 2

Theoretical Investigations of Candidate Crystal Structures for β-Carbonic Acid

2.1 Introduction

Computational prediction of the crystal structure of a compound, especially an organic one, is a challenging task. Hydrogen bonds are the primary interactions present in crystals of carboxylic acids as they have both donor and acceptor functionalities. Conformational isomerism adds another dimension to intermolecular interaction, as a particular conformer can form a stronger hydrogen bond than others. Conformational isomerism and weak interactions such as hydrogen bonding, and those involving the π orbitals make the problem of crystal structure prediction, a complex one. Many competing and distinct crystal structures can have cohesive energies within

---

Reprinted with permission from "Theoretical investigations of candidate crystal structures for β-carbonic acid" *J. Chem. Phys.* **2011**, *134*, 124511. Copyright 2011, American Institute of Physics. `http://jcp.aip.org/resource/1/jcpsa6/v134/i12/p124511_s1`

a few kcal/mol, thus making it difficult for computations to discriminate between them. One can of course, employ physical intuition and available empirical evidence to come up with model structures and evaluate their stabilization energies, based either on classical interatomic potentials (force field) or using Kohn-Sham density functional theory. The lack of even experimental density data for the crystals of carbonic acid has considerably hindered theoretical studies.

The cyclic hydrogen-bonded dimer and catemer are the main building blocks found in many carboxylic acids. Such motifs could also constitute carbonic acid (CA) polymorphs. A crucial clue on the identification of the symmetry of the building unit in crystalline CA came from Raman spectra of these compounds. The Raman- and IR- active modes of β-carbonic acid were mutually exclusive, suggesting it to have a centro-symmetric building block, whereas no such symmetry was observed in α-carbonic acid. [1] Quantum chemical calculations have shown the high stability of cyclic dimers, made either of two anti-anti conformer molecules or of two anti-syn conformer molecules. Both possess an inversion center and hence are ideal candidates for consideration as building blocks for β-carbonic acid. In case of α-carbonic acid, the stretching of the OH bond shows two sharp peaks at 2585 and 2694 cm^{-1} implying a stronger hydrogen bonding compared to that in the β-form which shows a very broad peak extended in the region 2600-3200 cm^{-1}. [2–4] It indicates that the α-form is more stable than the β-form, however sublimation data shows opposite behaviour. At a base pressure of 10^{-7} mbar, α- and β-forms are stable up to 210 and 230 K, respectively, beyond which they sublime.

In the following, we aim to elucidate crucial principles of organization of molecules in the β-phase of carbonic acid. Toward this purpose, we have refined an empirical force field for carbonic acid employing gas phase quantum chemical calculations of oligomers as a benchmark. The force field is then used to obtain several crystalline

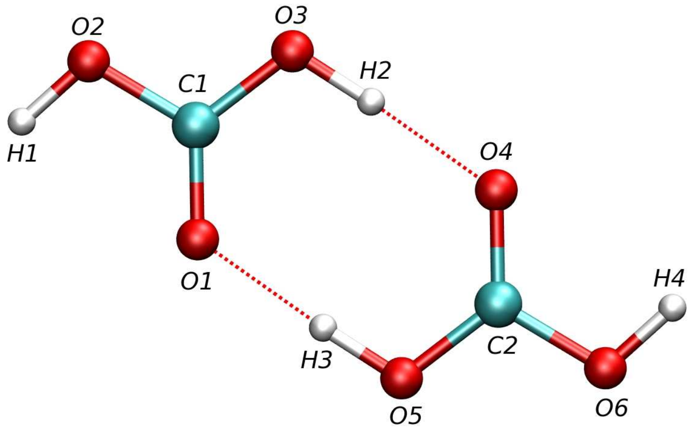

Figure 2.1: AA dimer.

structures, some of which are examined critically using DFT based zero Kelvin calculations and finite temperature Born-Oppenheimer molecular dynamics methods. Anticipating our results, we observe that structures with one-dimensional (chainlike) hydrogen bonding networks are more stable than those in which the network is two dimensional. This chapter is divided as follows. Details of the computation are presented in the next section followed by the results. Conclusions drawn from this work are presented subsequently.

2.2 Computational details

Four different software programs were used in these calculations, namely GAUSSIAN03, [5] UPACK, [6] CPMD, [7] and CRYSTAL09. [8, 9] To start with, the optimization of the geometry of the monomer and dimer (presented as Figure 2.1) in the AA and AS conformations was carried out at B3LYP/CBSB7 level of theory within GAUSSIAN03. The energies from the Gaussian calculations were corrected for the basis set superposition error (BSSE) using the counterpoise method. The geometry (bond lengths, angles) and the energy differences between isolated molecules

Table 2.1: Atom types, charges and 6-9 Lennard-Jones parameters of the force field used in this work.

Atom	Type	Charge(e)	ϵ(kJ/mol)	σ(Å)
Carbon	C'	+0.35	0.27	4.01
Carbonyl oxygen	O'	-0.55	1.12	2.90
Ester oxygen	O	-0.29	1.00	3.20
Hydrogen	H*	+0.39	0.21	1.30

or oligomers obtained from these B3LYP/CBSB7 calculations were used to refine an empirical force field, CFF93. [10] The CFF93 force field contains terms for bond stretches, bends, and torsional interactions. In addition, 6-9 nonbonded interactions are applied for atom pairs which are separated by at least two covalent bonds within the same molecule and for all pairs of atoms belonging to different molecules. The atom types we employed are the same as in CFF93. The form of the intramolecular potential terms as well as the parameters used in the current work are exactly the same as in CFF93 and hence are not provided here. However, we have modified the charges on the atoms as well as their 6-9 Lennard-Jones parameters in order to obtain near agreement with the quantum chemical estimates of the dimerization energy of the AA conformer, as well as the geometry of the dimer. An exact match with the B3LYP results was not attempted as we noticed marginal differences between the dimerization energies obtained using B3LYP and second order (MP2) methods. The dimerization energy for the $(AA)_2$ dimer obtained from the force field is also in good agreement with very recent CCSD(T)/aug-ccpVDZ//MP2/6-311++G** calculations of Restrepo et al. [11] The modified force field parameters are provided in Table 2.1.

Using the force field discussed above, optimization (at zero Kelvin) of the geometry of the AA monomer and the dimer was carried out using the LAMMPS code. [12] Results of these calculations are presented in Table 2.2. The coordinates of the geometry optimized monomer were provided as an input to the crystal packing

Table 2.2: Comparison of geometries calculated at B3LYP/CBSB7, MP2/CBSB7, force field (FF) and PBE/85Ry level of theory. The geometry obtained from CBS-QB3 is the same as that from B3LYP/CBSB7.

	B3LYP/ CBSB7	MP2/ CBSB7	Force field (FF)	PBE/ 85 Ry	PBE+vdW/ 85 Ry
AA monomer					
Bond length(Å)					
C1-O1	1.203	1.206	1.186	1.215	1.216
C1-O2	1.340	1.340	1.319	1.354	1.354
C1-O3	1.340	1.340	1.319	1.353	1.354
O2-H1	0.966	0.964	0.948	0.978	0.978
O3-H2	0.966	0.964	0.948	0.978	0.978
Angle(°)					
O1-C1-O3	125.7	125.9	123.1	125.9	126.1
C1-O3-H2	106.2	104.8	106.6	105.5	105.6
O1-C1-O2	125.7	125.9	123.1	125.9	126.1
C1-O2-H1	106.2	104.8	106.6	105.5	105.4
O2-C1-O3	108.6	108.2	113.8	108.2	108.2
AS monomer					
Bond length(Å)					
C1-O1	1.19	1.197	1.186	1.206	1.206
C1-O2	1.359	1.359	1.325	1.373	1.373
C1-O3	1.339	1.339	1.318	1.351	1.351
O2-H1	0.965	0.964	0.950	0.978	0.978
O3-H2	0.965	0.963	0.946	0.978	0.978
Angle(°)					
O1-C1-O3	125.2	124.6	125.4	125.4	125.6
C1-O3-H2	109.1	107.6	109.9	108.8	108.7
O1-C1-O2	125.2	125.4	121.8	125.4	124.1
C1-O2-H1	106.9	105.5	105.7	106.0	106.1
O2-C1-O3	110.3	110.1	112.7	110.4	110.3
Dimer					
Bond length(Å)					
C1-O1, C2-O4	1.226	1.225	1.186	1.242	1.244
C1-O2, C2-O5	1.334	1.335	1.322	1.348	1.348
C1-O3, C2-O6	1.305	1.309	1.319	1.311	1.309
O2-H1, O5-H3	0.966	0.964	0.947	0.978	0.978
O3-H2, O6-H4	0.999	0.989	0.955	1.028	1.031
H2—O4	1.643	1.667	1.623	1.573	1.548
H3—O1					
Angle(°)					
O1-C1-O3, O4-C2-O6	126.8	127.0	123.9	127.2	127.3
C1-O3-H2, C2-O6-H4	109.3	107.6	108.8	109.5	109.5
O1-C1-O2, O4-C2-O5	122.1	122.6	122.7	121.6	121.6
C1-O2-H1, C2-O5-H3	106.6	105.1	107.0	106.1	106.2
O2-C1-O3, O5-C2-O6	111.1	110.5	113.3	111.3	111.2
O3-H2-O4, O1-H3-O5	177.5	178.4	171.5	178.9	179.2

software, UPACK. Within this code, packing of rigid carbonic acid molecules (AA conformer) in various crystalline space groups were attempted. These calculations consisted of steps which involved (i) generating candidate structures within the specified space group, (ii) performing energy minimization using the force field described above, and (iii) sorting the structures based on the total energy of the crystal. In all these calculations, the molecule was assumed to be rigid. Hence the detailed intramolecular potential terms described above (CFF93) were not transported to UPACK. The difference in the total energies of any two crystal structures is independent of intramolecular potential energy terms, as the molecules were treated to be rigid. Periodic Kohn-Sham density functional theory calculations (at zero temperature) were performed with the CPMD code [7] which uses a plane wave basis set. The starting configurations of the atoms were a few selected structures obtained through UPACK as described above. These structures were chosen on the basis of their energies as well as the topology of the hydrogen bond network that they exhibited.

In the CPMD calculations, all valence electrons were considered explicitly while the effect of the core electrons and the nuclei on the valence electrons was treated using norm conserving Troullier-Martins pseudopotentials. [13] The cutoff radii of (s, p) orbitals used in pseudopotentials are (1.23, 1.23), (1.12, 1.12), (0.5, 0.38) (in a.u.) respectively for C, O and H elements. The Perdew, Burke, and Ernzerhof (PBE) exchange-correlation functional was employed. [14] The valence electrons were represented in a plane wave basis with an energy cutoff of 85 Ry. The initial configurations for the zero Kelvin DFT calculations were supercells of the selected crystals obtained from UPACK. Their sizes in terms of the cell vectors were: 2x2x1, 2x3x1, 2x2x3, 1x1x1, 1x3x1 for the I through V crystal structures, respectively. In addition, k-point sampling was performed using a 2x2x2 Monkhorst-Pack scheme. [15] Single point DFT calculations were carried out by varying the cell parameters as well as

Table 2.3: Fractional coordinates of atoms in the five crystal structures optimized using DFT at PBE/85Ry level of theory.

Candidate no.	Atom	x	y	z
I	C1	0.756216	0.21653	0.089717
	O1	0.752022	1.25439	-0.017362
	O2	0.591237	1.02714	0.150878
	O3	0.926812	1.36154	0.150724
	H1	0.459016	0.923932	0.100787
	H2	1.04616	1.50986	0.100575
II	C1	0.781913	0.129733	0.166536
	O1	0.739154	0.118700	0.272084
	O2	0.98132	0.279500	0.106692
	O3	0.630371	-0.007109	0.105044
	H1	1.08484	0.401586	0.156947
	H2	0.488572	-0.139137	0.154294
III	C1	0.233817	0.484356	0.186012
	O1	0.199479	0.374325	0.021767
	O2	0.253514	0.65298	0.122429
	O3	0.257877	0.458646	0.443456
	H1	0.233303	0.675827	-0.068853
	H2	0.238011	0.332127	0.494893
IV	C1	0.159237	0.138064	0.500158
	O1	-0.038160	0.130763	0.500176
	O2	0.271529	0.142007	0.330481
	O3	0.271548	0.142013	0.669826
	H1	0.176704	0.137589	0.203484
	H2	0.176733	0.137595	0.796823
V	C1	0.413877	0.334969	0.192738
	O1	0.517103	0.443957	0.113592
	O2	0.358228	0.302042	0.147522
	O3	0.353196	0.241172	0.329020
	H1	0.408102	0.400654	0.044635
	H2	0.399157	0.308762	0.357636

Table 2.4: Cell parameters of the five candidate crystal structures obtained at PBE/85Ry level of theory.

Candidate No.	a(Å)	b(Å)	c(Å)	α(°)	β(°)	γ(°)	Density (gm/cc)
I	4.636	4.586	11.690	90.00	82.90	90.00	1.670
II	5.446	3.649	12.187	90.00	79.20	90.00	1.731
III	6.308	7.790	4.850	90.00	72.78	90.00	1.809
IV	6.390	15.850	6.440	90.00	90.00	90.00	1.263
V	15.458	3.900	12.311	90.00	48.18	90.00	1.489

the fractional coordinates of atoms in order to identify values of these quantities at which the total energy is a minimum. Needless to state, the initial set of internal coordinates obtained from UPACK and used in the CPMD calculations obeyed the symmetry operations for the respective space groups. Although no restrictions were placed on the symmetry of these coordinates during the optimization runs, the final set of coordinates too were found to obey the symmetry operations of the respective space groups. These fractional coordinates are displayed in Table 2.3 for the various structures investigated. Table 2.4 reports the corresponding unit cell parameters.

Finite temperature simulations were performed using the Born-Oppenheimer molecular dynamics (BOMD) algorithm. As mentioned earlier, five structures were examined. The initial configuration for each of these was the optimized structure obtained from zero Kelvin DFT calculations. The simulations were carried out in the canonical (constant NVT) ensemble. The temperature of ions was maintained at 200 K using Nos*é*-Hoover chain thermostats [16] with a coupling constant of 1500 cm^{-1}. This is the temperature at which the experimental infrared spectrum was recorded. [3, 4] Hydrogen atoms were replaced by the deuterium isotope to enable the use of a larger time step within classical nuclear dynamics. A time step of 25 a.u. was used. The guess wave function for the self-consistent field (SCF) cycle in a given time step was obtained by extrapolation from its values in the preceding four time steps. The degree of conservation of the total energy (rather, the conserved quantity for NVT dynamics) was around 5 parts in 10^7. The BOMD trajectory was generated for 28 ps for Candidate V and for 12 ps for the other candidate structures. Dipole moments (with contributions from the ions and from the electronic wave functions) were calculated classically during the BOMD trajectory every fifth step. These dipole moment values were used to calculate the infrared spectra from the Fourier transform of the dipole time autocorrelation function using the following formula, [17]

$$\alpha(\omega) = \frac{4\pi\omega \tanh(\beta\hbar\omega/2)}{3\hbar n(\omega)cV} \int_{-\infty}^{\infty} dt e^{-i\omega t} \langle \mathbf{M}(t).\mathbf{M}(0) \rangle \tag{2.1}$$

where M(t) is the total dipole moment of the system at time t. The dipole time correlation is also approximated to be classical. The prefactor in the above equation approximately accounts for quantum effects as described in Ref. [18]. The infrared spectra shown here have a resolution of around 3 cm^{-1}. The Raman spectrum has been obtained by calculating polarizabilities using the linear response theory as implemented in the CPMD code. First, the vibrational normal modes of the optimized geometry were obtained using a Hessian calculation. Later, the atoms were displaced (up to 0.05 Å) along the direction (positive and negative) of a particular normal mode and the polarizability tensor was calculated at each of these points. The first derivative of the polarizability tensor at the equilibrium geometry was then calculated using finite difference. The Raman activity of a mode is proportional to the square of this derivative. [19] To obtain the Gibbs free energies of the monomer (or of any species) and of the crystal, AIMD simulations were run under the same simulation conditions (same simulation boxes, functionals, cutoffs, etc.). The total Helmholtz free energy of a system is obtained as the internal energy (U) minus temperature times the entropy (S). The internal energy at any temperature is the sum of its value at zero Kelvin with contributions from excitations such as vibrations, rotations, and translations. These terms also contribute to entropy. Since electronic excitations are least probable at the temperatures of interest, it does not contribute to the free energy.

The phonon heat capacity of harmonic oscillators is given by

$$C_v = \frac{1}{k_B} \int_0^{\nu_{max}} \left(\frac{h\nu}{exp(h\nu/k_BT) - 1} \right)^2 \frac{exp(h\nu/k_BT)}{T^2} \rho(\nu) d\nu \tag{2.2}$$

where $\rho(\nu)$ is the vibrational density of states obtained from the CPMD simulation at 200 K. The Gibbs free energy G is given by G(P,T)=H(P,T)-TS(P,T) where H(P,T)=U(P,T)+PV and S(P,T)=S_t+S_r+S_v+S_e (i.e., the sum of translational, rotational, vibrational and electronic contributions). These are given by,

$$S_t = R \left[\frac{3}{2} \ln \left(\frac{2\pi m k_B}{h^2} \right) + \ln \left(\frac{k_B}{P} \right) + \frac{5}{2} \ln T + \frac{5}{2} \right] \tag{2.3}$$

$$S_r = R \left[\frac{1}{2} \ln \pi - \ln \sigma_r - \frac{1}{2} \ln(\Theta_{r,x}\Theta_{r,y}\Theta_{r,z}) + \frac{3}{2} \ln T + \frac{3}{2} \right] \tag{2.4}$$

$$S_v = k_B \int_0^{\nu_{max}} \left(\frac{h\nu/k_BT}{exp(h\nu/k_BT) - 1} - \ln(1 - exp(-h\nu/k_BT)) \right) \rho(\nu) d\nu \tag{2.5}$$

$$S_e = 0 \tag{2.6}$$

$$U(T) = U(0) + \int_0^{\nu_{max}} \left(\frac{h\nu}{2} + \frac{h\nu}{exp(h\nu/k_BT) - 1} \right) \rho(\nu) d\nu \tag{2.7}$$

where U(0) is the total energy at zero Kelvin. The PV term is equated to nRT for gas phase species. The specific heat of the monomer at constant pressure is obtained from the value at constant volume upon addition of the gas constant, R, assuming ideality. For the crystalline solid, the two specific heats were assumed to be identical. The translational and rotational contributions are added to the heat capacity and to the internal energy of the gas phase species. The contribution to the internal energy due to translation is 3RT/2 and to the constant volume heat capacity is 3R/2. The

Table 2.5: Cell parameters of four crystal structures obtained using B3LYP/6-21g(d) calculations.

Candidate no.	a(Å)	b(Å)	c(Å)	$\alpha(^\circ)$	$\beta(^\circ)$	$\gamma(^\circ)$	Density (gm/cc)
I	4.544	4.504	11.896	90.00	80.07	90.00	2.018
II	5.582	3.203	11.896	90.00	79.90	90.00	1.967
III	5.749	7.563	4.695	90.00	72.96	90.00	2.110
IV	5.784	11.679	6.618	90	90	90	1.846
V	13.716	3.229	12.459	90.00	47.04	90.00	2.039

same values are applicable for molecular rotations as well.

Although Kohn-Sham density functional theory lacks a proper treatment of van der Waals (vdW) interactions, [20–23] this lacuna is believed to be redressed to some extent for calculations using the hybrid B3LYP exchange-correlation functional. In order to verify our results, zero Kelvin DFT calculations using this functional were carried out for the candidate structures within B3LYP/6-21g(d) level of theory as implemented in CRYSTAL09 software. [8, 9] The cell parameters and atom coordinates were iteratively optimized. The structural information, cell parameters of all crystal structures calculated from this level of theory are provided in Tables 2.5 and 2.6.

In addition to these set of calculations, these five crystal structures were also optimized using the DFT-D approach, [22] where the dispersive forces are added using empirical vdW corrections. The vdW corrections were treated using parameters specifically prescribed for the PBE functional by Williams and Malhotra recently. [24]

All structures were visualized in Mercury [25] and the vibrational modes in JMOL. [26, 27] Unless otherwise specified, all the results on the crystals discussed below are from the PBE/85 Ry level of theory.

Table 2.6: Fractional coordinates of four crystal structures studied using B3LYP/6-21g(d).

Candidate no.	Atom	x	y	z
I	C1	-0.232559	0.193338	0.101482
	O1	-0.251614	0.260141	-0.019254
	O2	-0.390030	-0.016621	0.170272
	O3	-0.051998	0.323853	0.171610
	H1	0.467342	-0.102440	0.113827
	H2	0.056282	0.490041	0.116709
II	C1	-0.230645	0.085537	0.160002
	O1	-0.266712	0.024559	0.265925
	O2	-0.386982	-0.022335	0.095265
	O3	-0.036458	0.261948	0.102541
	H1	0.072167	0.355996	0.156491
	H2	0.473677	-0.162093	0.144436
III	C1	0.232485	0.484481	0.191613
	O1	0.175410	0.368004	-0.085806
	O2	0.269220	-0.330184	-0.085806
	O3	0.269220	-0.347605	0.101657
	H1	0.269440	0.467023	0.453057
	H2	0.240794	0.340376	-0.480176
IV	C1	0.165223	-0.136969	-0.499996
	O1	-0.050138	-0.122939	-0.499995
	O2	0.291758	-0.143592	0.337048
	O3	0.291751	-0.143631	-0.337042
	H1	0.196319	-0.134704	-0.210852
	H2	0.196329	-0.134666	0.210858
V	C1	-0.408740	0.305505	0.308412
	O1	-0.017936	-0.005224	0.383274
	O2	-0.403811	0.325348	0.456992
	O3	-0.354653	0.194693	0.358110
	H1	-0.340234	0.194514	0.172369
	H2	0.114028	-0.185665	0.141883

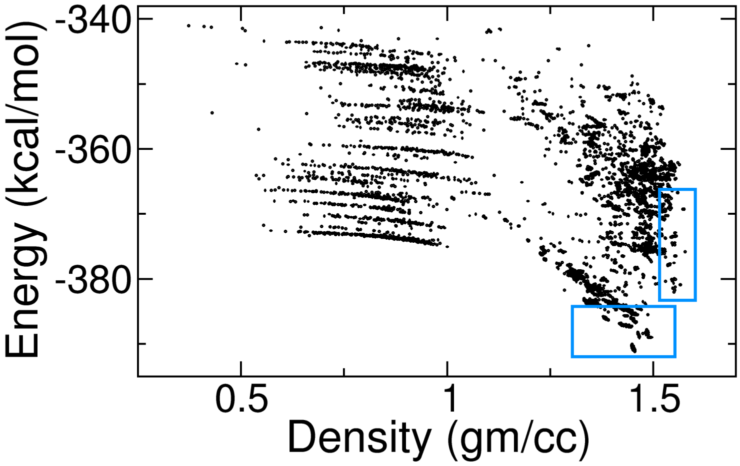

Figure 2.2: Lattice energies of carbonic acid polymorphs as a function of their densities. Blue coloured rectangles show the most probable regions for finding exact crystal structure.

2.3 Results and discussion

In the first place, we have carried out Kohn-Sham density functional theory calculations of oligomers of CA at the B3LYP/CBSB7 level, using GAUSSIAN03 software. [5] The geometry and energies of the monomer and the dimer was also compared against MP2 calculations. The geometries and relative stabilization energies of these molecules/complexes obtained from Gaussian were used to refine the potential parameters of an existing force field (CFF93) specifically for carbonic acid. The binding energies of the two dimers and the energy of AS monomer are given in Table 2.7. The values calculated with the force field and those from the PBE functional (using the CPMD code) match well with those values calculated with B3LYP, CBS-QB3 or MP2 methods.

Other geometrical information of the monomer and dimer calculated with these methods are provided in Table 2.2. These data serve as a benchmark for further simulations of the crystal structures carried out using either the force field or DFT.

2.3.1 Crystal structure search

The interaction potential was used in the molecular packing code, UPACK to predict many crystal forms of carbonic acid in various space groups. The energies of these structures modelled with the empirical force field lie within a few kJ/mole. Figure 2.2 shows the energies of these crystals along with their densities. Each data point in this Figure corresponds to single crystal. Crystals with high densities and/or low energies are most probable candidates for either α- or β-carbonic acid. From figure, it can be noticed that many data points exist in these regions (shown by rectangles). Hence, we have opted to study, using periodic quantum methods, only a few (five) of those structures which exhibit different hydrogen bonding topologies in the hope that one can at least deduce generic aspects of the hydrogen bond network in β-carbonic acid. These structures represent different topologies in the oligomerization of CA. Three of them are based on one-dimensional chainlike structures, while in the other two, the hydrogen bond network spans two dimensions and thus the structures are sheetlike. These structures are referred to as Candidate I through V in this chapter. Due to the mutual exclusion of infrared and Raman active modes of β-carbonic acid, the molecular motif present in the crystal structure is expected to have a center of symmetry. [1] All the crystals selected obey the mutual exclusion rule and possess a center of inversion symmetry. The five structures were further examined using DFT based AIMD methods using the CPMD code. Details of these DFT optimized crystal structures are provided in Table 2.8.

In the following, we describe the structural features of the five crystals as obtained using PBE/85Ry level of theory. The DFT optimized structure of Candidate I in the $P2_1$/c space group is shown in Figure 2.3. Within a unit cell, the hydrogen bonded H_2CO_3 dimer is present as a unit. The length of each hydrogen bond is 0.162 nm and the D-H$\cdots$A angle is 177°. They form a one-dimensional chain in the crystal. Such chains lie parallel to each other with a separation of 0.33 nm. Layers

Table 2.7: Comparison of energies calculated at B3LYP/CBSB7, MP2/CBSB7, CBS-QB3, force field (FF) and PBE/85Ry level of theory. The energies do not include the zero point energy and are in kJ/mol.

	AA dimerization	AS dimerization	AS monomer
B3LYP/CBSB7	-69.41	-76.40	8.03
MP2/CBSB7	-56.09 (-76.57)[b]	-62.73	9.12 (7.28)[c]
CBS-QB3	-78.29	-84.85	7.39
Force field (FF)	-81.13	-98.87	8.03
PBE/85 Ry	-82.80	-87.91	6.15
PBE/85Ry + vdW	-93.87	-100.16	-

[a] energy with respect to AA conformer

[b] value in parentheses is an estimate from MP2/aug-cc-pVxZ calculation, without BSSE correction from Ref. [28]

[c] value in parentheses is CCSD(T)/cc-pVQZ result from Ref. [29]

Table 2.8: Comparison of energies, densities and nature of hydrogen bonding network of the crystal structures optimized at PBE/85Ry level of theory.

Candidate No.	Space group	Energy (kJ/mol)[a]	Energy with vdW (kJ/mol)	Density (gm/cc)	Remarks
I	$P2_1$/c	-69.585 (-83.334)	-85.056 (-99.780)	1.670	1D parallel chains with 1D h-boding network
II	$P2_1$/c	-54.223 (-64.496)	-81.109	1.731	Sheets with 2D h-bonding network
III	$P2_1$/c	-53.963 (-67.046)	-72.416	1.809	Sheet with 2D h-bonding network
IV	$C222_1$	-73.086 (-86.305)	-76.350	1.263	1D parallel chains
V	$C2$/c	-73.477 (-88.400)	-82.120 (-100.100)	1.489	Parallel chains with 1D twisted hydrogen bonding network

[a] Energy is calculated as $(E(crystal) - n \times E(mono))$ divided by n where n is the number of molecules in the crystal considered. E(mono) is the energy of an isolated monomer (gas phase) calculated in the corresponding crystalline simulation cell. Energies in parentheses include zero point contribution.

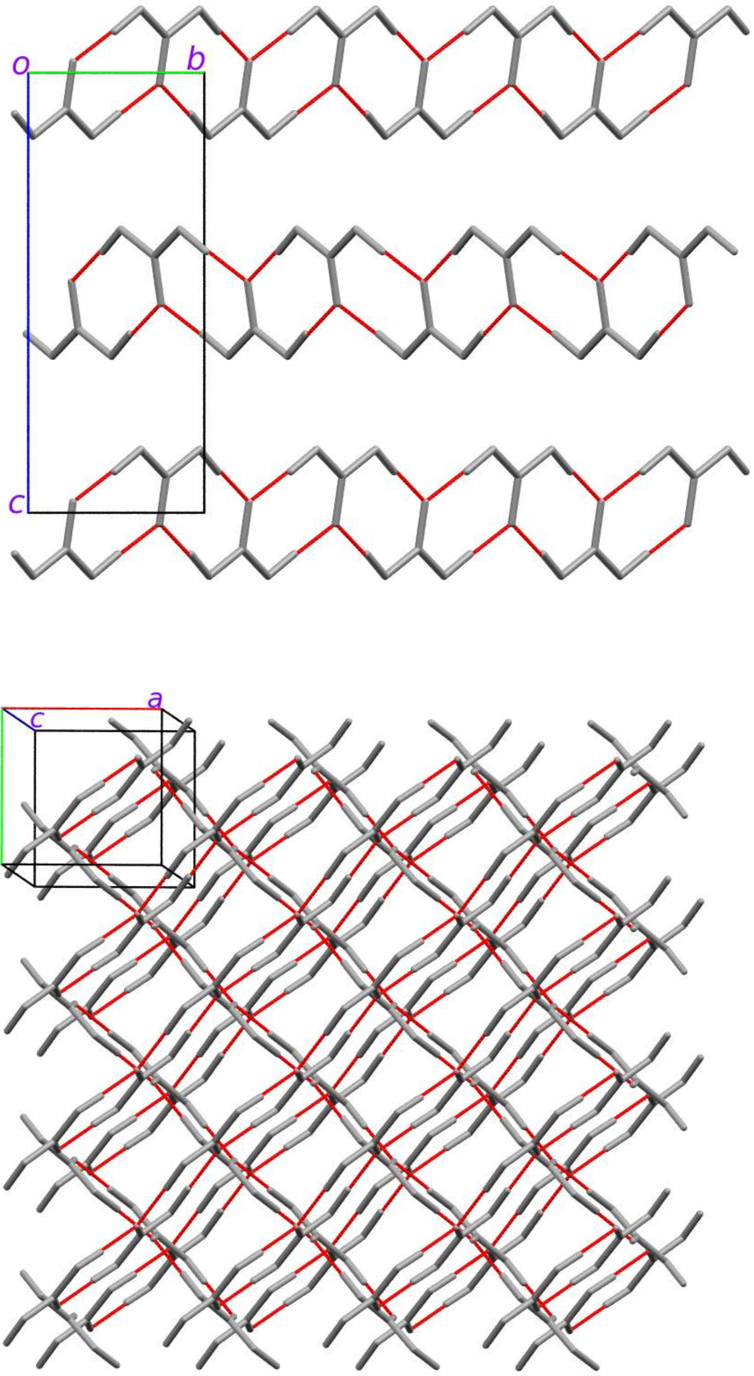

Figure 2.3: Molecular configuration in the crystal, Candidate I in the $P2_1/c$ space group. Hydrogen bonds are in red colour. Top Panel: View along a-axis of the unit cell. Bottom Panel: Parallel chains of hydrogen bonded carbonic acid molecules form one layer. Chains present in the layer above or below run perpendicular to a chains in a central layer.

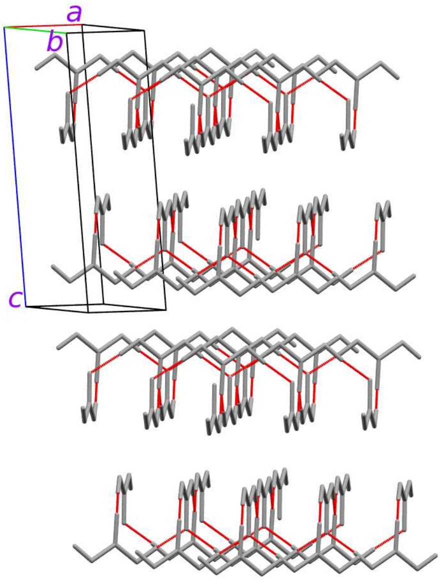

Figure 2.4: Molecular configuration in the structure, Candidate II in the $P2_1$/c space group. Hydrogen bonds are shown in red colour, and the network topology is sheetlike. Layers are separated by half the c-parameter.

formed by these chains are spaced from each other by half of the c-parameter of the unit cell around 0.58 nm. The one-dimensional chains in adjacent layers are oriented perpendicular to each other, as can be seen from Figure 2.3. Each molecule participates in four hydrogen bonds formed with its two neighbour molecules.

The structure of Candidate II, again in the $P2_1$/c space group is shown in Figure 2.4. The length of each hydrogen bond is 0.164 nm and the hydrogen bond angle is 175°. Hydrogen bonded molecules lie in parallel planes. Within a plane, each molecule forms four hydrogen bonds with different neighbour molecules. Although this structure is in the same space group as Candidate I, the topology of hydrogen bond network is sheetlike.

The structure of the third candidate crystal is shown in Figure 2.6. It too belongs to the $P2_1$/c space group. Each molecule participates in four hydrogen bonds with four of its neighbours. The length of each hydrogen bond is 0.162 nm and the $D \cdots H \cdots A$ angle is 170°. Molecules in the anti-anti conformation are arranged in two-dimensional sheets which are separated by 0.32 nm. The crystal structure of Candidate IV belongs to the $C222_1$ space group. There are eight molecules per unit cell and it contains two dimeric units within the unit cell. The length of each hydrogen bond is 0.158 nm and angle is 177.5°. CA molecules form one-dimensional chains and these are arranged parallel to each other (as opposed to the perpendicular arrangement seen in Candidate I). The energy of this crystal is more negative compared to Candidate I. Although these two structures (I and IV) contain a similar hydrogen bonding motif of one-dimensional chains, Candidate IV is more stable. This is also reflected in the reduced hydrogen bond distance in Structure IV, compared to Structure I. The arrangement of chains in Candidate IV can be seen in Figure 2.7.

The last crystal structure studied (Candidate V) belongs to the $C2/c$ space group. It has eight molecules in the unit cell. It has two different types of hydrogen bonds, one which is strong ($H\cdots A$ distance being 0.158 nm and $D\text{-}H\cdots A$ being 177.7°) and another which is weak ($H\cdots A$ distance being 0.162 nm and $D\text{-}H\cdots A$ being 173°). The topology of hydrogen bond network is one dimensional. Unlike the hydrogen bonded chains seen in the earlier structures, the chains present in this space group are twisted with a pitch corresponding to four monomer units, as can be seen in Figure 2.8.

The PXRD of all the DFT optimized crystal structures were calculated within MERCURY software [25] using Cu-K_α as the incident radiation. These are shown in Figure 2.5. Loerting and co-workers have observed three peaks between 10° and 20° and five between 20° and 35° (all in terms of 2θ) in the powder pattern of β-carbonic acid. [30] Out of all the structures we have examined (around a 100 using force field calculations), the crystal belonging to the $C2/c$ space group (Candidate V) is the only one which shows three peaks in the range 10°-20°. The number and nature of these peaks remained nearly unaltered in the DFT treatment. Within the

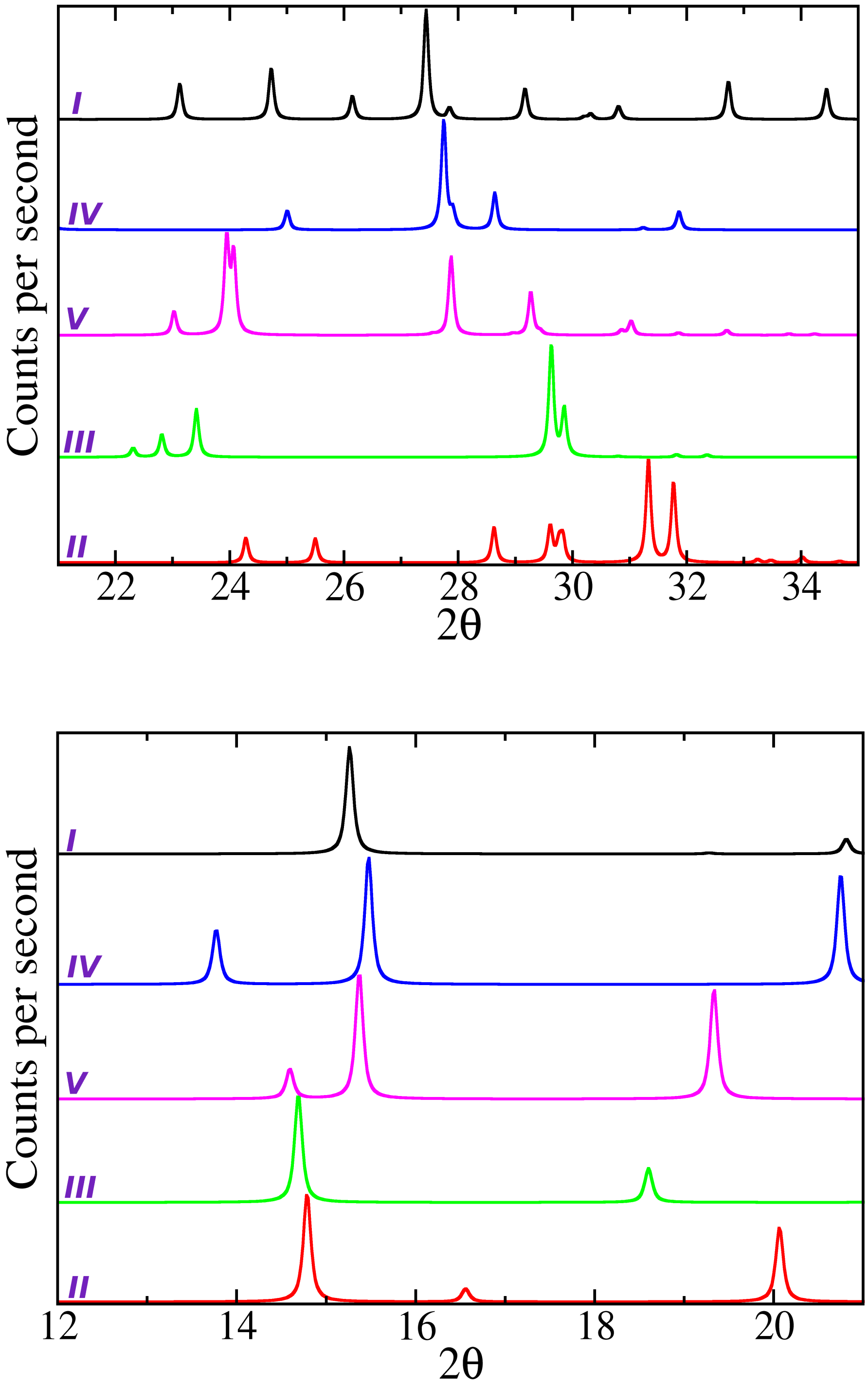

Figure 2.5: Calculated XRD pattern of all crystal structures studied in the region 12 to 21° (lower) and 21 to 35° (upper) obtained using Cu-Kα radiation. Legends in lower panel are common for both. The values on y-axis are in arbitrary units.

current set of calculations, this is the most promising candidate structure, based on a qualitative comparison with the experimental powder X-ray pattern.

2.3.2 Stabilization energies

The internal energy per molecule of Candidate V including zero point energy, obtained from DFT relative to the gas phase AA monomer is found to be -88.40 kJ/mol. This value is significant and is higher than the estimate of -71.96 kJ/mol obtained by Tossell based on quantum chemical calculations of isolated oligomers. [31] As can be seen in Table 2.8, the ranking of energies of various crystal structures considered here suggests Candidate V to be a likely structure for β-D_2CO_3. This is found to be valid even in calculations which include the empirical vdW corrections. However, since the energy difference between Candidates I and V is very small, one cannot unequivocally claim Candidate V as the crystal structure for the compound. Zero point energy for Candidates II, III, and IV were not calculated as the unit cell sizes are very large and the Hessian calculation is quite time consuming. However, we expect the energy ranking provided in Table 2.8 to remain unaltered.

2.3.3 Infrared and Raman spectra

The AIMD simulations, using the Born-Oppenheimer MD algorithm, were carried out on a simulation cell of size mentioned in earlier for four crystals, at a temperature of 200 K. The simulations for Candidate IV were not carried out as the nature of hydrogen bonding network in IV is similar to that in I and hence is expected to have a similar vibrational density of states (at least within the resolution of our simulations). The infrared spectra for these crystals were calculated as the Fourier transform of the dipole-dipole (dipole here refers to the total dipole moment of the system with contributions from both nuclear and electronic degrees of freedom) time correlation function and is compared against the experimental data. Figure 2.9

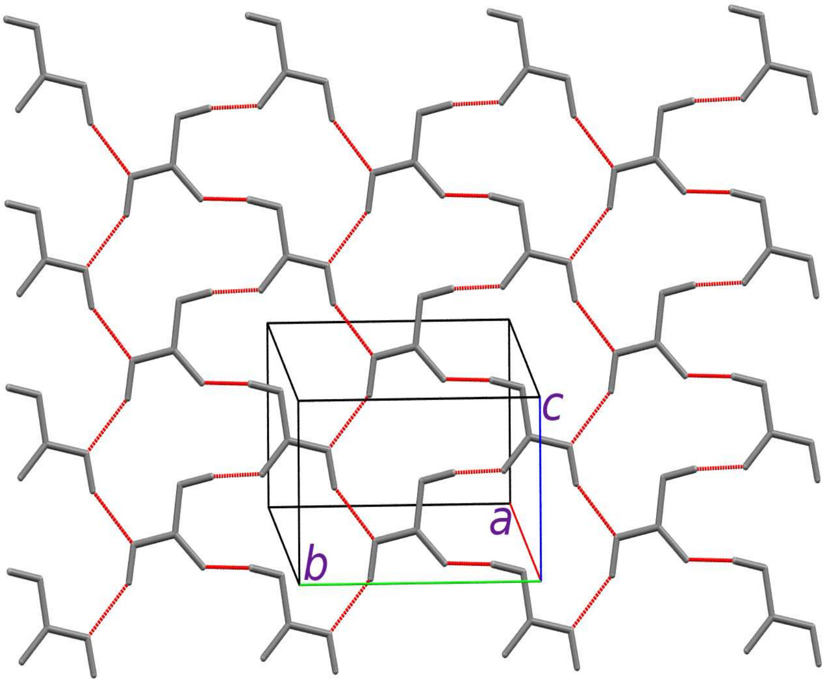

Figure 2.6: Molecular configuration in the Candidate III crystal structure in the $P2_1/\mathrm{c}$ space group. Hydrogen bonds are shown in red colour.

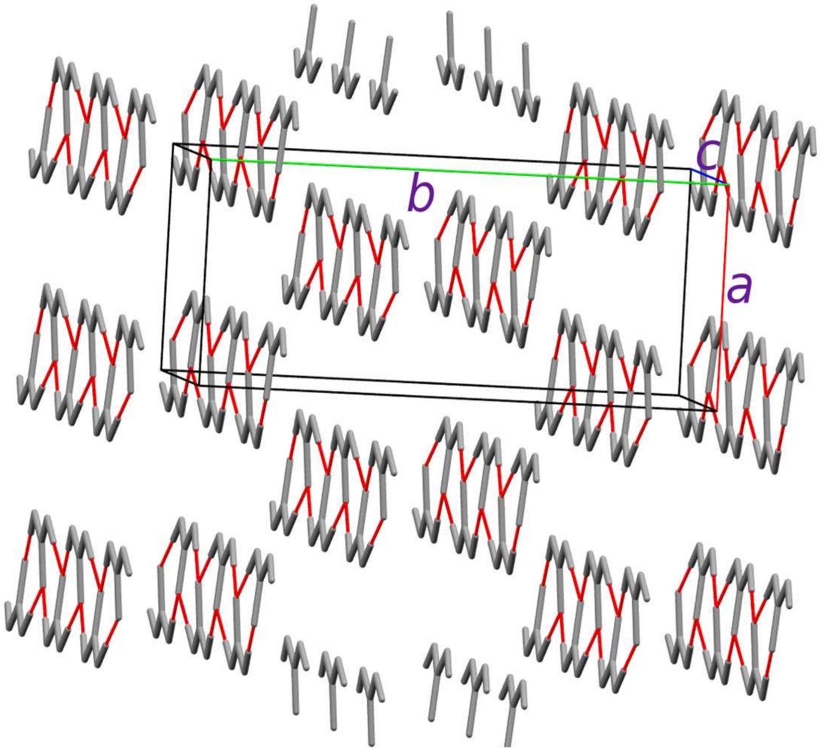

Figure 2.7: Structure of Candidate IV in the $C222_1$ space group. Hydrogen bonds are shown in red colour.

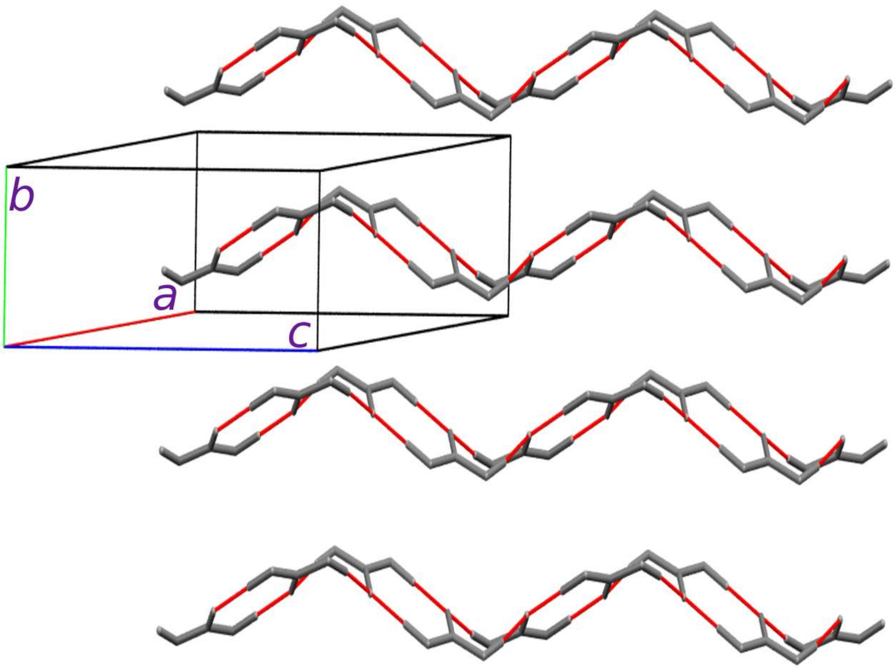

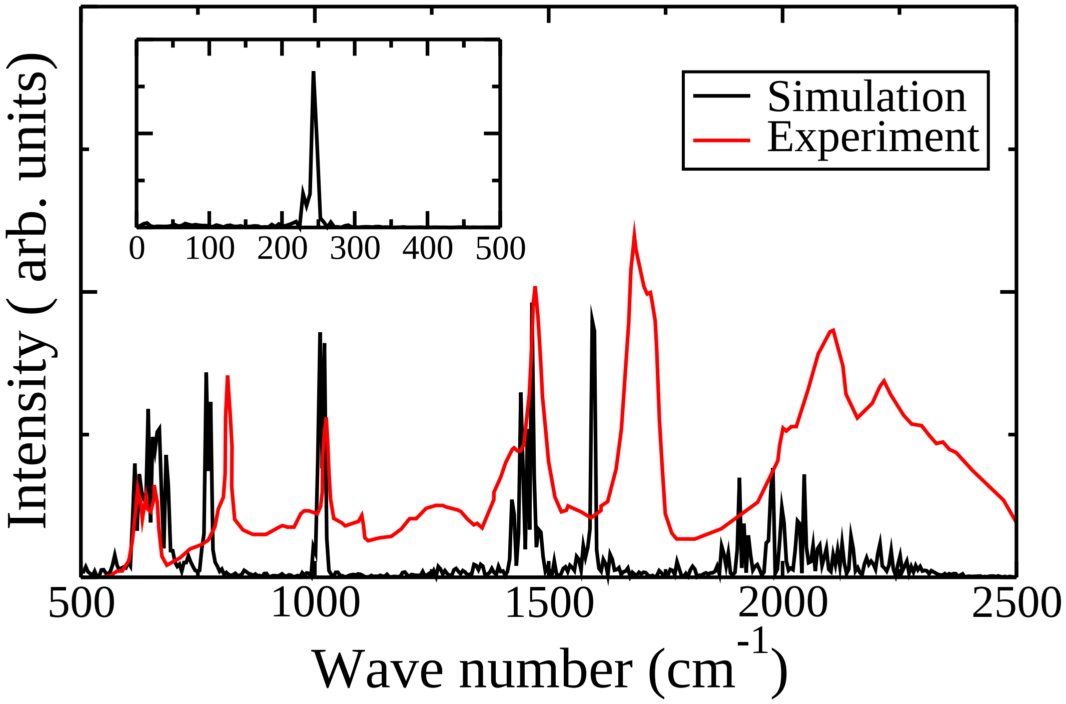

Figure 2.9: Infrared spectrum of the C2/c crystal structure (Candidate V) compared against experimental data. [3, 4] The far infrared region of the calculated spectrum is shown in inset.

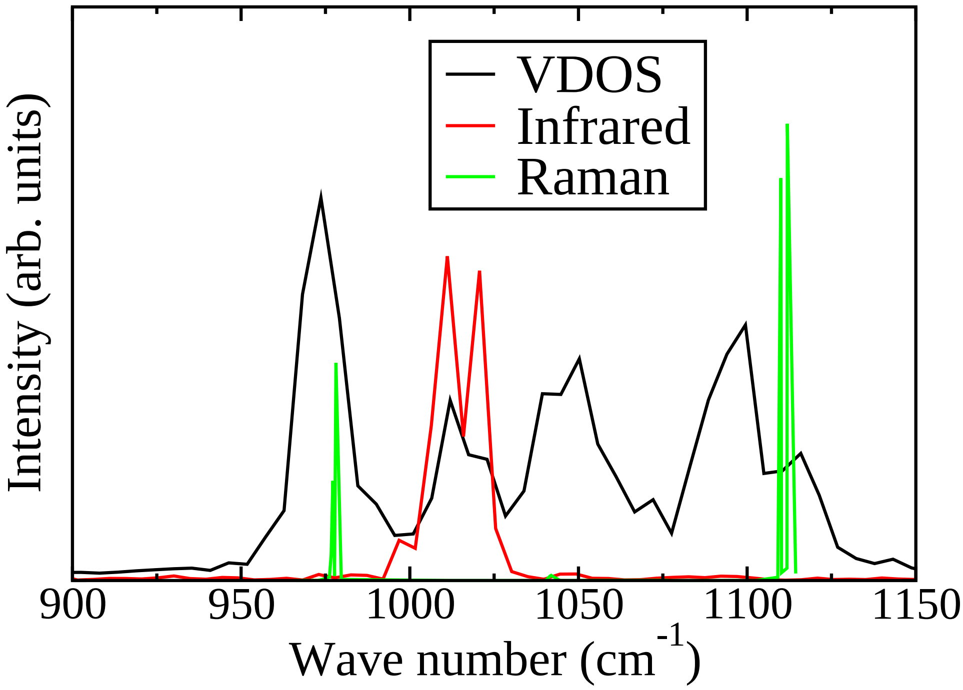

Figure 2.10: Comparison of the calculated vibrational density of states (VDOS), Raman and Infrared spectra of D_2CO_3 belonging to the $C2/c$ space group (Candidate V) in the region 900 to 1150 cm^{-1}. Assignment of the peaks can be found in text.

shows the comparison of the infrared spectrum of Candidate V against experimental data. All the features observed in experiment are reproduced in the AIMD result. Aside from the features present at 623 and 661 cm^{-1}, all other peaks present in the simulation are slightly red shifted relative to experiment. Such a shift is a generic lacunae of current Kohn-Sham density functional theory calculations and has been documented by earlier workers. [32]

In order to quantify the shift and to demonstrate that it is indeed due to the approximations involved in the simulations, we have carried out BOMD simulations of one D_2O monomer under isolated conditions in a supercell (gas phase), with exactly the same XC functional and energy cutoff as were used for the simulations of the crystal. The O-D stretch mode in these calculations was observed at 2690 cm^{-1}, while the corresponding experimental value for an isolated molecule is 2727 cm^{-1}. [33] Thus, with the protocols employed here, one can expect a red shift of about 40 cm^{-1} in other modes in the near-IR and mid-IR regions as well. This is precisely the magnitude of shifts that was observed in the calculated spectrum for crystalline β-D_2CO_3 relative to experiment. However, while the C=O stretch mode is present in the experimental spectrum at 1678 cm^{-1}, the same is observed in simulations at 1592 cm^{-1}, a value considerably lesser than what can be accounted for by arguments given above. Since the carbonyl oxygen is involved in two hydrogen bonds in the crystal, such a difference with experimental data could likely point to inadequate treatment of hydrogen bonding by the exchange and correlation functionals used here. This argument gains credence if one compares the bond length of the carbonyl group displayed in Table 2.2 obtained from the hybrid B3LYP functional and the PBE functional used in the AIMD simulations. The latter predicts a marginally longer C=O bond which could impact the stretch frequency, making it red shifted with respect to the experimental or the B3LYP result. Further confirmation of this argument is provided by results of zero Kelvin, periodic calculations of the $C2/c$ crystal carried out using the B3LYP functional as implemented in the CRYSTAL09 code. These calculations show that the scaled frequency of stretching of C=O bond is 1645 cm^{-1} [scaled by a factor of 0.97 (Ref. [34])] which is closer to the experimental value compared to that obtained with the PBE functional.

A Hessian calculation of the optimized $C2/c$ crystal was carried out in the harmonic approximation using the CPMD code. The vibrational frequencies thus obtained matched with the features present in the vibrational density of states obtained from finite temperature BOMD (shown in Figure 2.11). The latter was calculated as the power spectrum of the velocity time autocorrelation function of all the atoms. The atomic displacements corresponding to these modes were visualized using JMOL. [26] The vibrational mode assignments thus obtained are compared to experimental data in Table 2.9. [3, 4]

The inset of Figure 2.9 displays the IR spectrum at low wave numbers, where

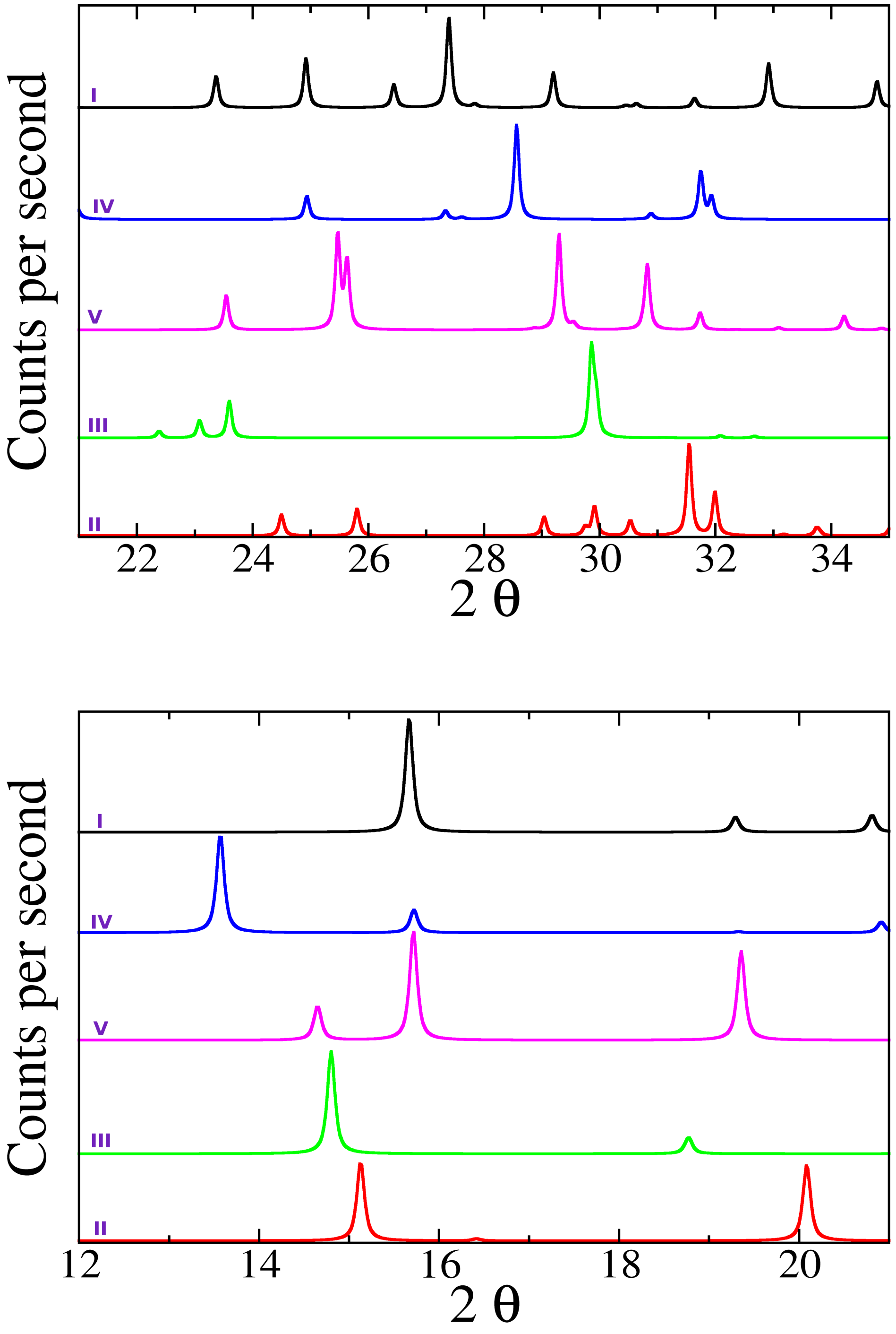

Figure 2.11: Calculated XRD pattern of all crystal structures studied with vdW corrections in the region 12 to 21° (lower) and 21 to 35° (upper) obtained using Cu-Kα radiation. Legends in lower panel are common for both. The values on y-axis are in arbitrary units.

Table 2.9: Comparison of the infrared vibrational features of β-D_2CO_3 obtained from our simulations (Candidate V) and experiments. [4]

Mode frequency (Simulation) (cm^{-1})	Mode frequency (Experiment) (cm^{-1})	Assignment
1800-2400	1900-2600	ν(O-D)
1594	1678	ν(C=O)
1464	1468	$\nu_{as}(C(OD)_2)$
1064	1099	$\nu_{ns}(C(OD)_2)$
1011, 1020	1022	δ_{ip}(COD)
777, 767	813	$\delta_{oop}(CO_3)$
615, 624, 644	622, 638	$\delta_{ip}(CO_3)$
668, 682	658	δ_{oop}(COD)
242	Not reported yet	Molecular rocking

experimental data are not available. A strong peak at around 242 cm^{-1} is observed. Based on visualization of the mode, we identify it to be due to the rocking motion of the CA molecule, which was also observed in B3LYP/CBSB7 calculations of oligomers in gas phase using the Gaussian software.

The calculated infrared spectrum in the region between 900 and 1150 cm^{-1} is shown along with the vibrational density of states (VDOS) in Figure 2.10. The VDOS contains eight features (some of them present as shoulders) in this region. The peak centered at 973 cm^{-1} is due to the symmetric stretching of $C(OD)_2$ and the stretching of C=O bond. The peaks at 1011, 1023, 1039, and 1050 cm^{-1} are assigned to in-plane bending of $C(OD)_2$ group. The peaks present at 1011, 1023 cm^{-1} are assumed to be infrared active based on the overlapping of these peaks with the infrared spectrum calculated using dipole dynamics. The peaks at 1072 and 1116 cm^{-1} are assigned to the in-plane bending of $C(OD)_2$ group and stretching of C=O bond. The peak centered at 1099 cm^{-1} is due to the in-plane bending of C(OD) and stretching of C=O bond.

The Raman activity of the modes in the region 900-1200 cm^{-1} were calculated using the procedure described earlier. The two peaks present at 978 and 1110 cm^{-1}

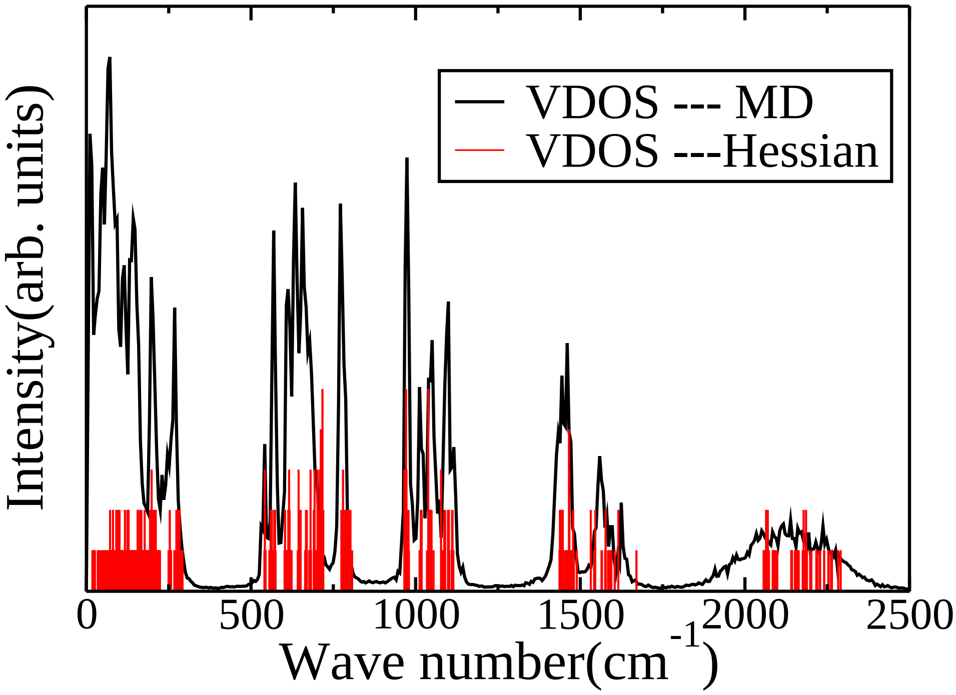

Figure 2.12: Vibrational density of states (VDOS) calculated from Born-Oppenheimer MD simulations and from a Hessian calculation in the harmonic approximation for Candidate V.

are found to be Raman active. The former is assigned to the stretching of C-O and C=O bond and its position is consistent with the experimentally observed Raman peak at 985 cm^{-1}. [30] The same peak was observed at 1054 cm^{-1} for β-H_2CO_3 crystal. [1] A similar calculation carried out for Candidate I showed no difference in the positions of Raman active peaks compared to those for Candidate V in the range 900-1200 cm^{-1} (Figure 2.12).

The infrared spectra of other crystals in the range 500-2500 cm^{-1} are shown in Figure 2.13. The spectra of Candidates I and II match well with experiment except that the peak positions are red shifted compared to the experimental data. For Candidate III, an additional peak is observed in the calculated spectrum at around 868 cm^{-1}. The experimental data exhibits a hump at 934 cm^{-1}; however, it has not been assigned to any vibrational mode. [3, 4]

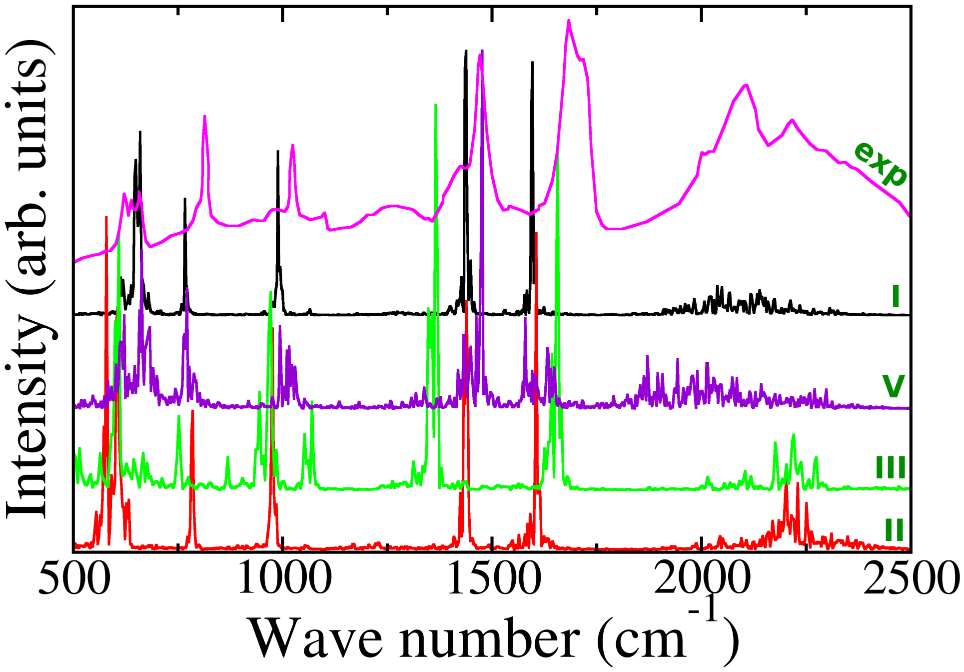

Figure 2.13: Infrared (IR) spectrum of four crystals studied compared against experimental infrared spectrum. Roman numbers correspond to Candidate no. of crystal studied.

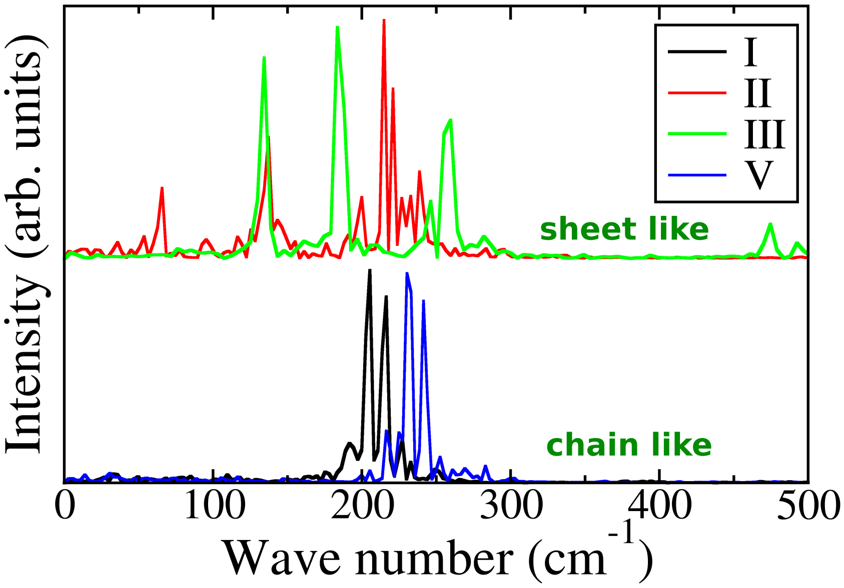

Figure 2.14: Far infrared spectrum of the four crystal structures studied in the region below 500 cm^{-1}.

An examination of the low frequency (< 200 cm^{-1}) region of the infrared spectrum (far IR) of these structures is very revealing (Figure 2.14). While sheetlike structures exhibit at least one prominent IR active band at around 135 cm^{-1}, chain-like structures do not. The far infrared region of the spectrum is likely to probe intermolecular vibrations. While the exact nature of these modes need to be characterized in future, it is a noteworthy pointer that our computational studies have shown a clear distinction in this region of the IR spectrum between crystal structures possessing two different hydrogen bond network topologies.

2.3.4 Effect of van der Waals corrections

The effect of including empirical vdW corrections to the DFT potential energy surface on the crystal structure of all the candidates has also been examined. Toward this purpose, vdW corrections to the PBE functional as prescribed by Williams and Malhotra were employed. [24] Similar empirical corrections to DFT have been employed by Vashishta and co-workers recently to examine molecular crystals. [35] The cell parameters and the internal coordinates of the structures were iteratively optimized with vdW corrections included. Specifically, for Candidate V, as expected, the c-parameter (along which the chains are oriented) did not change due to this addition, while the other two cell parameters, a and b decreased by 0.3 and 0.7 Å, respectively. These led to an increase in the value of density of the crystal by about 9%, implying the significance of these additional vdW interactions in describing the crystal structures. These cell parameters and fractional coordinates are also provided in Table 2.10. Note that the energy ranking of the structures remains unaltered upon addition of the vdW contribution to the lattice energy III. The qualitative nature of the calculated X-ray powder patterns too were found to be unaffected by the minor changes in the cell parameters brought about by the inclusion of these empirical vdW corrections to DFT. Many computational studies have been carried

Table 2.10: Cell parameters and fractional coordinates of Candidate V, obtained upon the addition of empirical vdW corrections to the PBE functional.

a=15.14Å, b=3.65Å, c=12.311Å, α=90°, β=48.1°, γ=90°

Atom	x	y	z
C1	0.414722	0.0366212	0.190254
O1	0.513595	0.0516746	0.116148
O2	0.359593	0.0295587	0.143479
O3	0.352156	0.0250956	0.327350
H1	0.409317	0.0413745	0.041807
H2	0.396928	0.0344790	0.356630

out to study the stability of carbonic acid monomer and higher oligomers with respect to the dissociation products CO_2 and H_2O, in gas phase [28, 36] and also in aqueous solution. [37–42] These suggest that although the equilibrium disfavored the formation of carbonic acid, the energy of the carbonic acid dimer and the sum of energies of isolated CO_2 and H_2O were comparable. [28]

2.3.5 Phase diagram and crystal stability

In 1998, Mayer's group observed β-carbonic acid to be stable up to a temperature of 220 K beyond which it sublimes. [43] Based on high level quantum chemical calculations, they expected the presence of a monomer-dimer mixture in the gas phase. But the recent spectroscopic studies showed that about 90% of species in gas phase are in anti-anti conformer. [44] To check the stability of the crystal structures studied here, we have calculated the free energies of the monomer and the crystal within DFT, as a function of temperature and pressure. Anti-syn conformer and the dimer were not considered due to their low concentration in gas phase. At a constant pressure of 10^{-5} atm, the free energies of these systems as a function of temperature are shown in Figure 2.15. Many such curves have been calculated at different pressure values. For a given pressure, the temperatures at which the

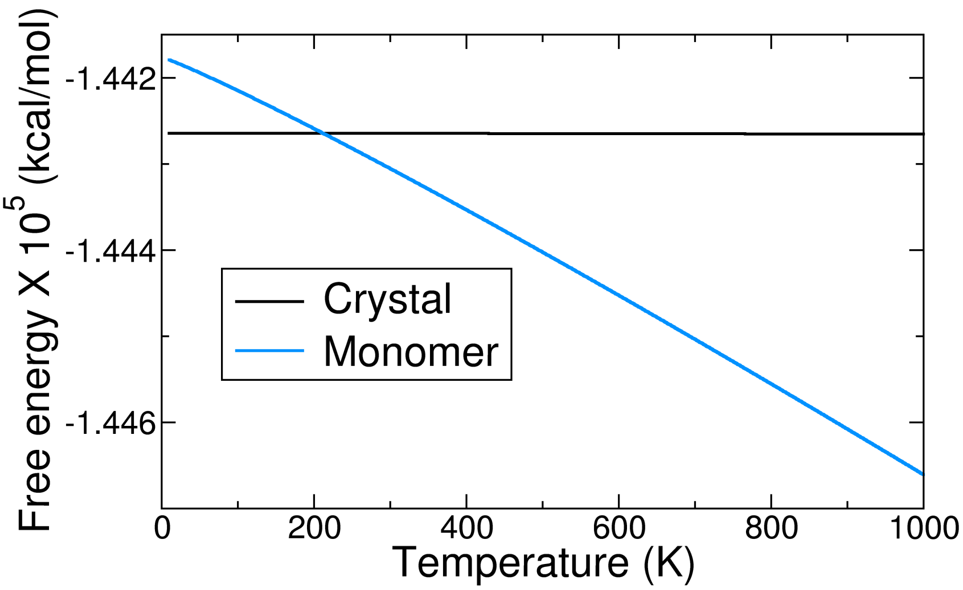

Figure 2.15: Free energy of gas composed of anti-anti monomers and crystal as a function of temperature at constant pressure of 10^{-5}atm.

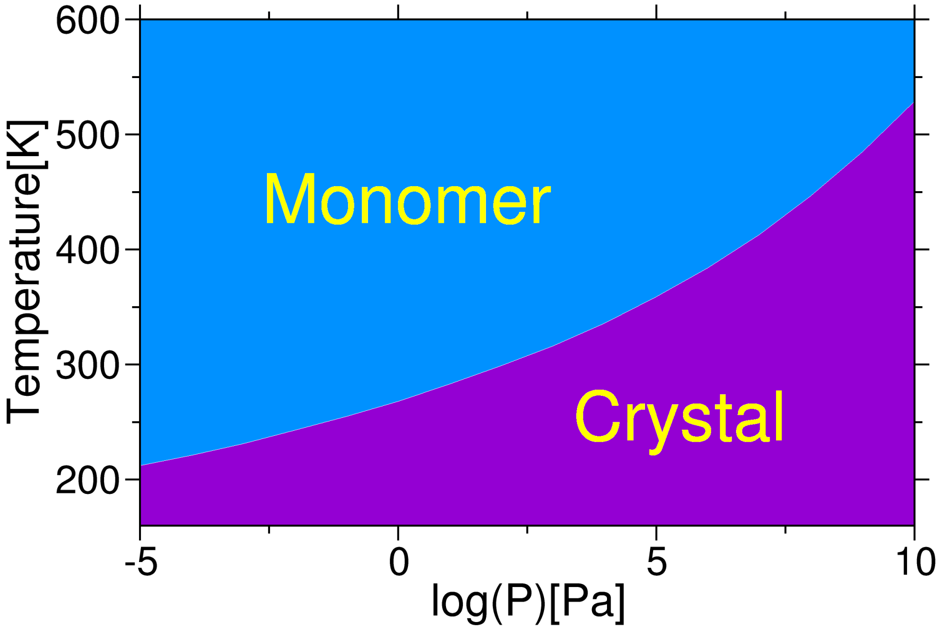

Figure 2.16: Phase diagram showing regions of stability of β-carbonic acid (violet) with respect to gas composed of anti-anti monomers (blue) based on Born-Oppenheimer MD simulations.

free energy of the crystal crosses that of the monomer were noted down. Such a procedure was carried out for a range of pressure values. Using these data, we have developed a nominal phase diagram which is presented in Figure 2.16. At a pressure of 10^{-10} atm, we find that Candidate V is stable up to 212 K compared to the gas phase containing monomers in gas phase. These values are close to the experimental observation on the stability of β-carbonic acid. [43] At 1 atm pressure, we observe that the $C2$/c crystal (Candidate V) is stable up to 359 K in comparison to gas phase monomer. So, we estimate candidate V to be stable up to a temperature of 359 K at 1 atm pressure. Note that the liquid state of carbonic acid has not been studied for the phase diagram. A possibly more serious lacunae is the assumption that the gas phase is composed of AA conformers alone. These issues need to be addressed in future. It is also important to note that among the five crystals studied here, chainlike structures are more stable than sheetlike structures at both 0 K and at finite temperatures. The free energies of all the crystals have been calculated. Their thermal stability have been compared against the gas phase monomer as a function of pressure. The data are presented in Figure 2.17 which confirms again the thermodynamic stability of Candidate V.

2.4 Discussion and conclusions

Prediction of structures of molecular crystals is a challenging task. The problem is exacerbated for a compound such as carbonic acid on which not much experimental data exist, against which quantum chemical or empirical potential data can be benchmarked. Although coupled cluster calculations with very good basis sets have been carried out for the different conformers of the molecule, geometry optimizations of oligomers of carbonic acid have still not been explored using this method. The gas phase quantum calculations reported here were albeit performed for a different purpose, i.e., employ them as benchmarks in the refinement as an empirical force

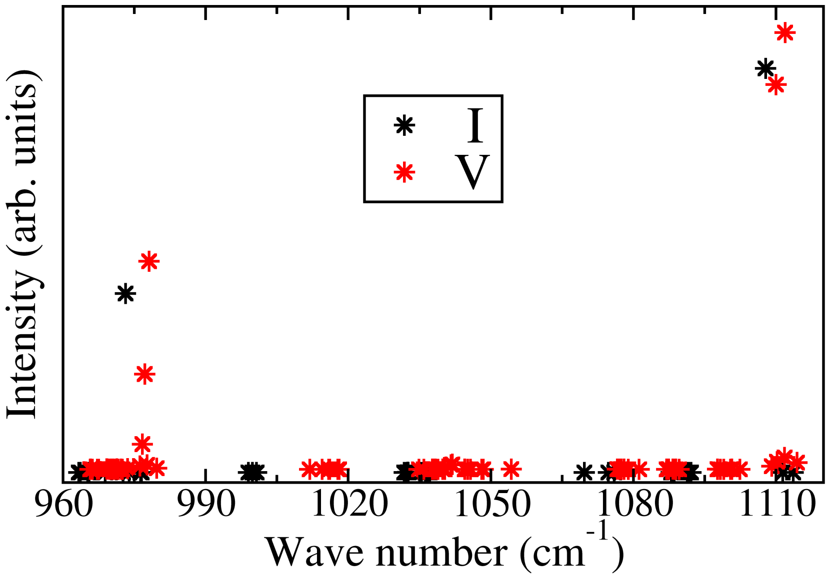

Figure 2.17: Raman spectra of Candidates I and V are shown. The zero axis is shifted up for clarity.

field in order to describe the intermolecular interactions and geometry.

The empirical force field has been used to generate hundreds of crystal structures obtained through packing of rigid molecules in various space groups. These were manually screened for their (i) energetic stability, (ii) the variety they exhibit in their hydrogen bond network topologies, and (iii) based on their powder X-ray patterns. Five crystal structures which were selected through this process were further studied using periodic Kohn-Sham density functional theory calculations carried out at zero temperature as well as using DFT based Born-Oppenheimer MD simulations performed at 200 K. Three of the structures consisted of carbonic acid molecules hydrogen bonded as one-dimensional chains, while in two other structures, the network topology was sheetlike. Our calculations indicate a crystal with twisted one-dimensional chains to be the most stable in energy. The infrared and Raman spectra calculated for this crystal structure compare well with the experimental data. This crystal (named Candidate V in this chapter) is present in the $C2/c$ space group with a density of 1.49 g/cc. Relative to the gas phase monomer, this crystal is also stable up to 212 and 359 K at pressures of 10^{-10} and 1 atm, respectively. Another candidate, Candidate I, which too is composed of one-dimensional hydrogen bonded carbonic acid molecules in the $P2_1$/c space group is marginally higher in energy compared to Candidate V. Despite the considerable efforts expended here, we are unable to unequivocally choose Candidate V as the exact crystal structure for β-carbonic acid. Density functional theory is the best quantum method available currently for carrying out periodic calculations. Apart from its documented limitation of not being able to describe the van der Waals interactions accurately, the results obtained (in terms of stabilization energy, intra- and intermolecular geometry) may depend crucially on the exchange and correlation functionals employed. These disadvantages have been redressed, to some extent, through the use of empirical vdW corrections applied over DFT for all the structures studied, as well as by performing periodic B3LYP calculations for Candidate V. Results of these calculations qualitatively confirm those obtained with the PBE functional for this crystal structure.

The challenge is compounded by the fact that there are many structures lying within a few kJ/mole in the stabilization energy, but exhibiting varied hydrogen bond network topologies. The differences in the calculated infrared spectra of the five crystals are comparable in magnitude with the differences between the calculated IR spectrum of any crystal with experiment. Thus, the infrared spectrum calculated beyond 200 cm^{-1} alone cannot be used to unambiguously identify the crystal structure. However, we observe that the far infrared region of the IR spectrum can be profitably used to distinguish between structures of different hydrogen bonding network topologies. While the spectra for chainlike structures are devoid of any features below 200 cm^{-1}, sheetlike structures exhibit at least one IR band near 135 cm^{-1}. As reported in the text, the twisted one-dimensional chains found in Candidate V give the best stability with respect to the monomer. Such a twisting of the chain was also observed in gas phase calculations of large one-dimensional oligomers carried out at the B3LYP/CBSB7 level of theory. [45]

Our key observations from this work are summarized as under:

I. A hydrogen bonded, one-dimensional chainlike configuration for β-carbonic acid is predicted to be stable according to many methods.

II. Between the chainlike structures considered in the $P2_1$/c (Candidate I) and the $C2$/c (Candidate V) space groups, the latter is found to be marginally more stable, in terms of both internal and free energies. Candidate V is the only structure for which the powder X-ray pattern is consistent with the experimental observations.

III. If β-carbonic acid were to adopt a sheetlike hydrogen bonding network, it should show infrared active vibrational band(s) in the region 50-200 cm^{-1}. One should at least be able to identify the topology of the hydrogen bond network based on the experimental far infrared spectrum of the compound.

Further experiments on the crystal as well as on the gas phase of carbonic acid are required. In parallel, theoretical attempts must be devoted to accurately characterize the gas phase dimer, as well as in deriving an improved interatomic potential. The metadynamics and other efficient methods as applied to the crystal structure prediction and transformations could also be used to identify stable crystal structures and rank them. [46–50]

In the next chapter, we employ wave function based quantum chemical methods to study the geometry and vibrational spectra of oligomers of carbonic acid.

Bibliography

[1] Kohl, I.; Winkel, K.; Bauer, M.; Liedl, K. R.; Loerting, T.; Mayer, E. *Angew. Chem. Int. Ed.* **2009**, *48*, 2690–2694.

[2] Hage, W.; Hallbrucker, A.; Mayer, E. *J. Chem. Soc., Faraday Trans.* **1995**, *91*, 2823–2826.

[3] Hage, W.; Hallbrucker, A.; Mayer, E. *J. Chem. Soc., Faraday Trans.* **1995**, *91*, 2823–2826.

[4] Hage, W.; Hallbrucker, A.; Mayer, E. *J. Chem. Soc., Faraday Trans.* **1996**, *92*, 3183–3195.

[5] Frisch, M. J. et al. Gaussian 09 Revision A.1.

[6] Van Eijck, B. P. *J. Comput. Chem.* **2002**, *23*, 456–462.

[7] Hutter, J.; Ballone, J. P.; Bernasconi, M.; Focher, P.; Fois, E.; Goedecker, S.; Marx, D.; Parrinello, M.; Tuckerman, M. E. CPMD, Version 3.13.2; Max Planck Institut fuer Festkoerperforschung: Stuttgart. 1990.

[8] Dovesi, R.; Orlando, R.; Civalleri, B.; Roetti, C.; Saunders, V. R.; Zicovich-Wilson, C. M. *Z. Kristallogr.* **2005**, *220*, 571–573.

[9] Dovesi, R.; Saunders, V. R.; Roetti, C.; Orlando, R.; Zicovich-Wilson, C. M.; Pascale, F.; Civalleri, B.; Doll, K.; Harrison, N. M.; Bush, I. J.; D'Arco, P.; Llunell, M. CRYSTAL09 User's Manual. University of Torino: Torino. 2009.

[10] Sun, H.; Mumby, S. J.; Maple, J. R.; Hagler, A. T. *J. Am. Chem. Soc.* **1994**, *116*, 2978–2987.

[11] Murillo, J.; David, J.; Restrepo, A. *Phys. Chem. Chem. Phys.* **2010**, *12*, 10963–10970.

[12] Plimpton, S. *J. Comput. Phys.* **1995**, *117*, 1–19.

[13] Troullier, N.; Martins, J. L. *Phys. Rev. B* **1991**, *43*, 1993–2006.

[14] Perdew, J. P.; Burke, K.; Ernzerhof, M. *Phys. Rev. Lett.* **1996**, *77*, 3865–3868.

[15] Monkhorst, H. J.; Pack, J. D. *Phys. Rev. B* **1976**, *13*, 5188–5192.

[16] Martyna, G. J.; Klein, M. L.; Tuckerman, M. *J. Chem. Phys.* **1992**, *97*, 2635–2643.

[17] Silvestrelli, P. L.; Bernasconi, M.; Parrinello, M. *Chem. Phys. Lett.* **1997**, *277*, 478–482.

[18] Guillot, B. *J. Chem. Phys.* **1991**, *95*, 1543–1551.

[19] Giannozzi, P.; Baroni, S. *J. Chem. Phys.* **1994**, *100*, 8537–8539.

[20] Kristyan, S.; Pulay, P. *Chem. Phys. Lett.* **1994**, *229*, 175–180.

[21] Meijer, E. J.; Sprik, M. *J. Chem. Phys.* **1996**, *105*, 8684–8689.

[22] Grimme, S. *J. Comput. Chem.* **2006**, *27*, 1787–1799.

[23] Balasubramanian, S.; Kohlmeyer, A.; Klein, M. L. *J. Chem. Phys.* **2009**, *131*, 144506.

[24] Williams, R. W.; Malhotra, D. *Chem. Phys.* **2006**, *327*, 54–62.

[25] Macrae, C. F.; Bruno, I. J.; Chisholm, J. A.; Edgington, P. R.; McCabe, P.; Pidcock, E.; Rodriguez-Monge, L.; Taylor, R.; van de Streek, J.; Wood, P. A. *J. Appl. Crystallogr.* **2008**, *41*, 466–470.

[26] JMOL: An open-source Java viewer for chemical structures in 3D; available at http://www.jmol.org/.

[27] McMahon, B.; Hanson, R. M. *J. Appl. Crystallogr.* **2008**, *41*, 811–814.

[28] Liedl, K. R.; Sekusak, S.; Mayer, E. *J. Am. Chem. Soc.* **1997**, *119*, 3782–3784.

[29] Mori, T.; Suma, K.; Sumiyoshi, Y.; Endo, Y. *J. Chem. Phys.* **2009**, *130*.

[30] Loerting, T. personal communication (14 May 2010).

[31] Tossell, J. A. *Environ. Sci. Technol.* **2009**, *43*, 2575–2580.

[32] Handgraaf, J. W.; Meijer, E. J.; Gaigeot, M. P. *J. Chem. Phys.* **2004**, *121*, 10111–10119.

[33] Benedict, W. S.; Gailar, N.; Plyler, E. K. *J. Chem. Phys.* **1956**, *24*, 1139–1165.

[34] Merrick, J. P.; Moran, D.; Radom, L. *J. Phys. Chem. A* **2007**, *111*, 11683–11700.

[35] Shimojo, F.; Wu, Z.; Nakano, A.; Kalia, R. K.; Vashishta, P. *J. Chem. Phys.* **2010**, *132*.

[36] Wight, C. A.; Boldyrev, A. I. *J. Phys. Chem.* **1995**, *99*, 12125–12130.

[37] Adamczyk, K.; Premont-Schwarz, M.; Pines, D.; Pines, E.; Nibbering, E. T. J. *Science* **2009**, *326*, 1690–1694.

[38] Nguyen, M. T.; Raspoet, G.; Vanquickenborne, L. G.; VanDuijnen, P. T. *J. Phys. Chem. A* **1997**, *101*, 7379–7388.

[39] Jena, N. R.; Mishra, P. C. *Theor. Chem. Acc.* **2005**, *114*, 189–199.

[40] Loerting, T.; Tautermann, C.; Kroemer, R. T.; Kohl, I.; Hallbrucker, A.; Mayer, E.; Liedl, K. R. *Angew. Chem. Int. Ed.* **2000**, *39*, 891–894.

[41] Tautermann, C. S.; Voegele, A. F.; Loerting, T.; Kohl, I.; Hallbrucker, A.; Mayer, E.; Liedl, K. R. *Chem. Eur. J.* **2002**, *8*, 66–73.

[42] Ludwig, R.; Kornath, A. *Angew. Chem. Int. Ed.* **2000**, *39*, 1421–1423.

[43] Terlouw, J. K.; Lebrilla, C. B.; Schwarz, H. *Angew. Chem. Int. Ed. Engl.* **1987**, *26*, 354–555.

[44] Bernard, J.; Seidl, M.; Kohl, I.; Liedl, K. R.; Mayer, E.; Galvez, O.; Grothe, H.; Loerting, T. *Angew. Chem. Int. Ed.* **2011**, *50*, 1939–1943.

[45] Reddy, S. K.; Kulkarni, C. H.; Balasubramanian, S. *J. Phys. Chem. A* **2012**, *116*, 1638–1647.

[46] Martonak, R.; Laio, A.; Parrinello, M. *Phys. Rev. Lett.* **2003**, *90*, 075503.

[47] Raiteri, P.; Martok, R.; Parrinello, M. *Angew. Chem. Int. Ed.* **2005**, *44*, 3769–3773.

[48] Zykova-Timan, T.; Raiteri, P.; Parrinello, M. *J. Phys. Chem. B* **2008**, *112*, 13231–13237.

[49] Karamertzanis, P. G.; Raiteri, P.; Parrinello, M.; Leslie, M.; Price, S. L. *J. Phys. Chem. B* **2008**, *112*, 4298–4308.

[50] Yu, T.-Q.; Tuckerman, M. E. *Phys. Rev. Lett.* **2011**, *107*, 015701.

Chapter 3

Vibrational Spectra of Linear Oligomers of Carbonic Acid: A Quantum Chemical Study

In the previous chapter, we examined many crystal structures as candidates for β-carbonic acid. A strong evidence for the suitability of hydrogen bonded carbonic acid molecules in chainlike topologies to be present as motifs in this crystal was found. In the current chapter, this possibility is further investigated. Employing wave function based quantum chemical calculations, the vibrational spectra of such oligomers is shown to best reproduce the experimental spectra for β-carbonic acid.

Tossell had undertaken such an exercise. [1] He calculated the vibrational spectrum of the anti-anti dimer at CCSD/6-311+G(2d,p)//B3LYP/CBSB7 level of theory and compared the same against experiments. Calculated features for bands related to the carbonyl and hydroxyl groups were found to closely correspond with experimental spectra. As mentioned earlier, the anti-anti dimer is not only the most

---

Reprinted with permission from "Vibrational spectra of linear oligomers of carbonic acid: a quantum chemical study" *J. Phys. Chem. A* **2012**, *116*, 1638-1647. Copyright 2012, American Chemical Society. `http://pubs.acs.org/doi/abs/10.1021/jp209715x` stable dimeric species of CA, but also possesses an inversion center due to which the activity of its vibrational modes will be mutually exclusive between infrared absorption and Raman scattering. While early investigations looked at hydrogen-bonded oligomers as possible species in the solid state, [2] more recent ones employed crystal structure prediction tools. [3, 4]

In our earlier work, [4] described in previous chapter, the Raman spectrum of one of the candidate structures was calculated for a small frequency range around 900 cm^{-1} and was compared against the then available experimental data. In view of the recent experiments of Loerting and co-workers on the low-frequency Raman spectroscopy of solid carbonic acid, [5] it becomes imperative that the vibrational spectra of linear hydrogen-bonded oligomers are obtained using accurate quantum chemical methods. The current work is aimed in this direction. Herein, we have carried out both MP2 and Kohn-Sham density functional theory based calculations using a hybrid functional to obtain the IR and Raman spectra of gas phase oligomers of carbonic acid and compare them with experimental data.

This chapter is divided into four sections. Following this Introduction, we provide the computational methodologies adopted. The stability of oligomers is discussed later. The third section is devoted to describe vibrational analyses of the oligomers, ranging from the monomer to octamer (the mode assignments are also presented) and comparison of the vibrational spectrum of the octamer with the experimental infrared (IR) and Raman spectra of the two polymorphs of CA. The last section summarizes the results.

3.1 Computational details

The geometries and vibrational spectra of all oligomers in gas phase were obtained at B3LYP/6-311G(2d,d,p) level of theory using the Gaussian09 code. [6] Because this functional lacks a complete description of electron correlation, geometry optimizations of all oligomers were also carried out at MP2/ 6-311G(2d,d,p) level of theory. Harmonic vibrational spectra up to a tetramer are obtained at the MP2 level and compared with spectra obtained at B3LYP/6-311G(2d,d,p) level. Initial geometries of the oligomers were modelled using Gaussview. The keywords “Opt=verytight” and “scf=verytight” were employed during optimizations, which limits the root-meansquare of force on the nuclei and on the wave function to 10^{-6} and 10^{-8} a.u., respectively. Further, an ultrafine grid was used in the DFT calculations. Normal mode calculations at the harmonic level showed no imaginary frequency for any of the oligomers.

Binding energy of an oligomer was calculated in two ways. In the first instance, it was defined as

$$\Delta E = E_n - n * E_1 \tag{3.1}$$

Second, it was also defined as the energy gained due to the addition of a molecule to the oligomer, as

$$\Delta E = E_n - E_{n-1} \tag{3.2}$$

Here ‘n’ is the size of the oligomeric unit and E_n is its ground state energy.

The optimized geometries of these oligomers were used to calculate the vibrational spectra. Anharmonic frequencies were calculated using second-order perturbation theory as implemented in Gaussian09. Anharmonic frequencies for the pentamer and for larger oligomers were found to exhibit a few imaginary frequencies, although the corresponding frequencies at the harmonic level were all positive. Anharmonic frequencies are calculated by adding corrections to harmonic values using perturbation theory. So these imaginary values could have arisen due to the failure of the anharmonic approximation in the low-frequency region. Here, we call these floppy modes. At the B3LYP/6-311G(2d,d,p) level, we report here harmonic frequencies for oligomers up to the octamer and anharmonic frequencies up to the tetramer. At the MP2/6-311G(2d,d,p) level, harmonic frequencies up to the linear tetramer are reported. Scale factors between harmonic and anharmonic frequencies obtained from the spectrum of the tetramer, are used to estimate anharmonic frequencies for the octamer. Unless specified, all frequencies provided in this chapter were not scaled by any factor. The intensity of infrared absorption was calculated by applying a finite difference approximation to calculate the gradient of the dipole moment with respect to the normal mode coordinate. The square of this quantity is proportional to the infrared intensity. Raman intensity was obtained by calculating the polarizability tensor, which is equal to the gradient of the induced dipole moment with respect to the external electric field. The finite difference of this tensor with respect to normal mode coordinates is proportional to the Raman intensity of the mode. It is to be noted that these equations are derived within the harmonic approximation, that is, higher order derivatives of energy, dipole moment, and polarizability with respect to the normal mode coordinate were assumed to be negligible. [7] The structures were visualized using Gaussview [6] and Jmol. [8, 9]

3.2 Results and discussion

3.2.1 Geometry optimization

As mentioned earlier, carbonic acid possesses both hydrogen bond donating (hydroxyl) and acceptor (carbonyl) groups. Geometry optimization of the three conformers of carbonic acid, namely, anti-anti (a-a), anti-syn (a-s), and syn-syn (s-s) were carried out. Among these, the a-a conformer is the most stable. The a-s and s-s conformers are less stable than the a-a conformer by 1.9016 and 12.167 kcal/mol, respectively, as calculated at the B3LYP/6-311G(2d,d,p) level. The performance of this functional is also compared against high level quantum chemistry calculations

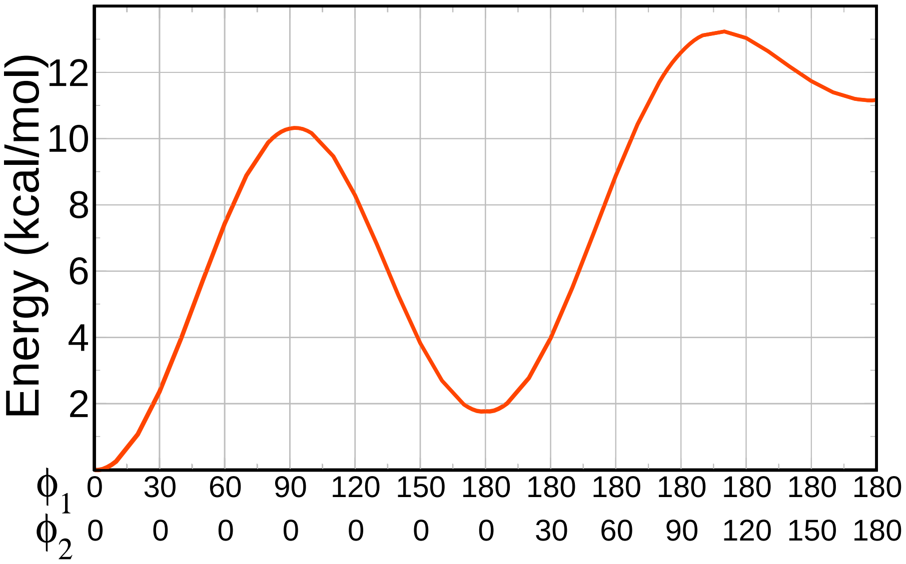

Figure 3.1: Three conformers of carbonic acid located on potential energy surface drawn as a function of two dihedrals as shown. Energies are calculated at CBS-QB3 level of theory. [11, 12]

at CBS-QB3 level. It shows that the anti-anti conformer to be the most stable in gas phase, while the other two are higher in energy by 1.77 and 11.17 kcal/mol, respectively. Values are similar to those reported by Endo et al. [10] Figure 3.1 shows these conformers on a potential energy surface plotted as a function of the dihedrals ϕ_1 and ϕ_2. The values calculated at these two levels (B3LYP and CBS-QB3) are in reasonable agreement. Since the latter method is computationally expensive, simulations on higher oligomers are carried out using the former.

Linear oligomers of the a-a conformer up to the size of an octamer were also studied. A dimer of the a-s conformer was also investigated. The structures of these oligomers are given in Figures 3.2, 3.3, 3.4 and 3.5. Two stable dimers are found, dimer a and dimer b. Dimer a consists of two a-s monomers connected to each other through two hydrogen bonds of equal strength, while dimer b consists of two a-a conformers that form two hydrogen bonds of equal strength (Figure 3.2). The dimerization energy (i.e., E_2 - $2E_1$) of dimer b is more negative than that of dimer a by 1.797 kcal/mol. Loerting et al. reported recently that the gas phase of carbonic

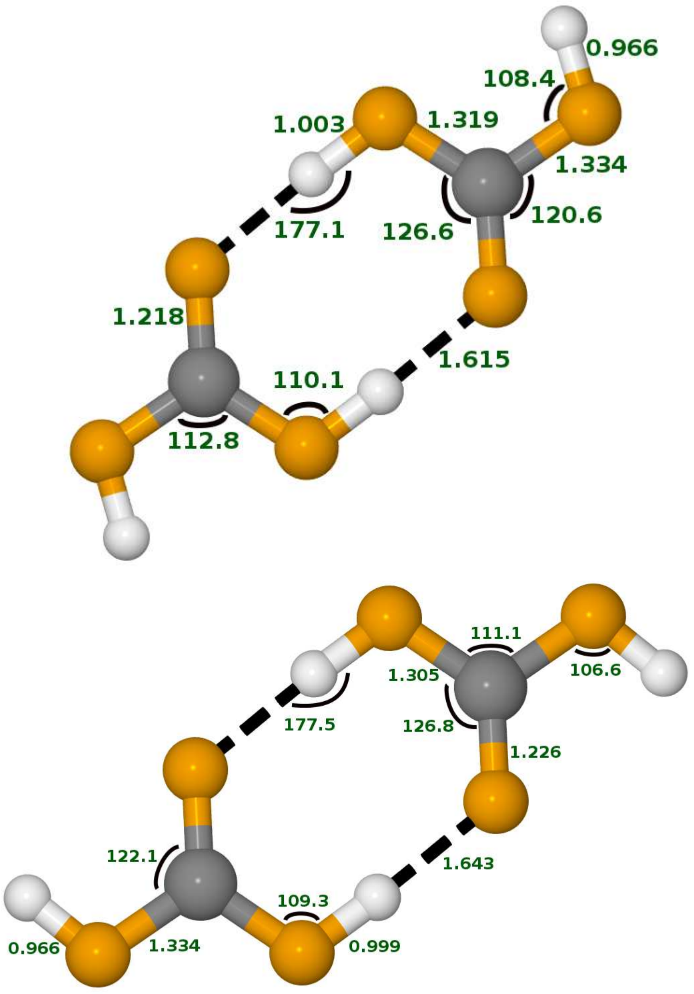

Figure 3.2: Optimized geometries of dimer a (top) and dimer b (bottom).

acid consists of monomers largely (around 90%) in the a-a conformation with the balance being constituted by a-s monomer and dimer b species. [13]

The binding energies of oligomers studied here are provided in Table 3.1. The number of hydrogen bonds in an oligomer is 2n-2 where n is the number of molecules in the oligomer. As n increases, the binding energy, calculated using eq 3.1, decreases and reaches a saturation value as shown in Figure 3.6. The saturation binding energies thus obtained are -15.3 (-18.45) and -12.47 (-17.40) kcal/mol calculated at

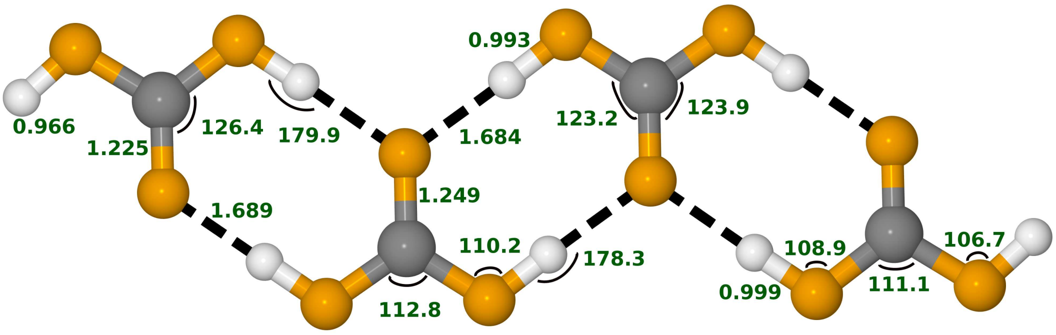

Figure 3.3: Optimized geometry of tetramer.

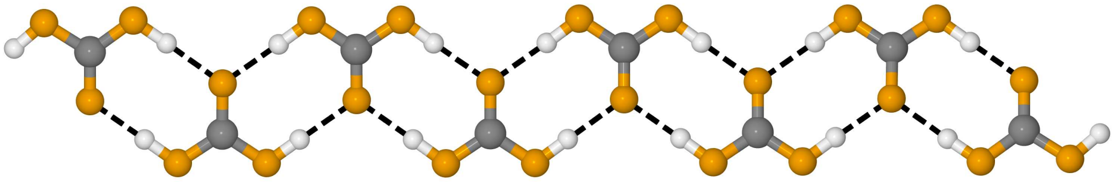

Figure 3.4: Optimized geometry of octamer.

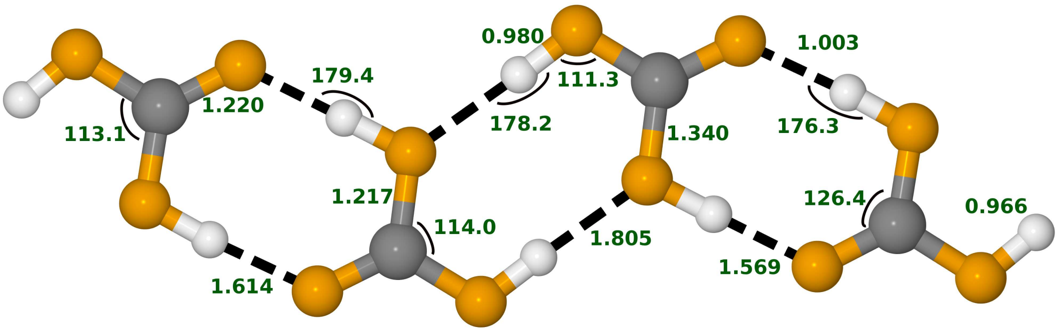

Figure 3.5: Tetramer consisting of two dimer a species.

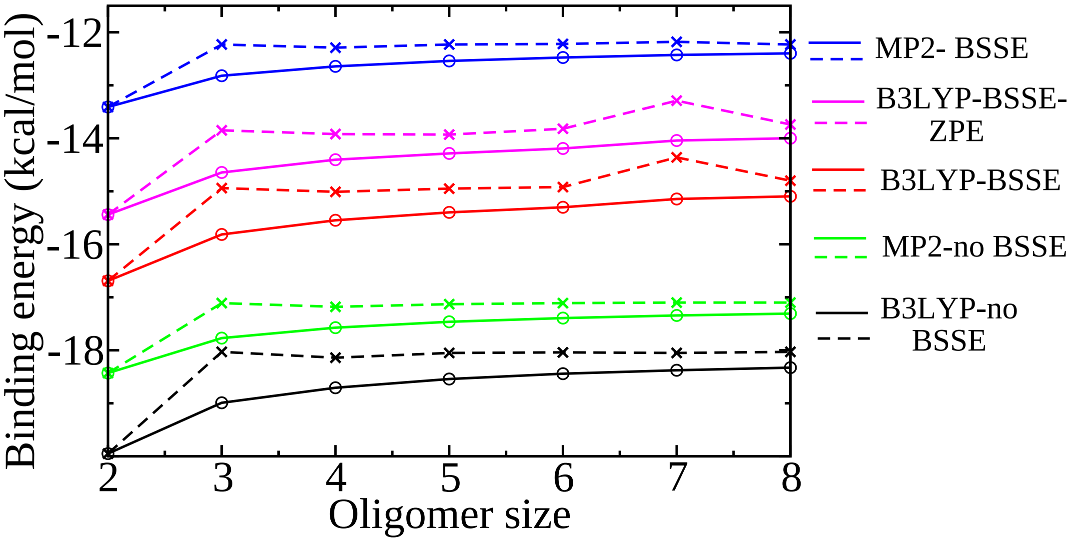

Figure 3.6: Binding energy of oligomers as a function of oligomer size. Binding energy is calculated in two ways; E_n - n*E_1 divided by (n-1) (continuous lines) and E_n - E_{n-1} (dashed lines) where 'n' is the size of oligomer, E_1 is the energy of monomer and E_n is the energy of n^{th} oligomer.

Table 3.1: Energies (in kcal/mol) of oligomers calculated at B3LYP/6-311G(2d,d,p) and MP2/6-311G(2d,d,p) levels of theory. Values are calculated as E_n - n*E_1 where E_n is the total energy of the oligomer of size n and E_1 is that for the monomer. Energies are in kcal/mol. Values in parentheses include zero point energy (ZPE) contribution.

Oligomer	B3LYP/6-311G(2d,d,p)		MP2/6-311G(2d,d,p)	
	without BSSE	with BSSE	without BSSE	with BSSE
a-a monomer	0	0	0	0
Dimer-a	-17.92	-14.43 (-13.53)	-15.95	-10.63
Dimer-b	-19.95	-16.69 (-15.44)	-18.43	-13.41 (-11.89)
Trimer	-37.98	-31.63 (-29.29)	-35.54	-25.64
Tetramer	-56.12	-46.64 (-43.21)	-52.72	-37.93 (-33.82)
Pentamer	-74.17	-61.59 (-57.14)	-69.85	-50.16
Hexamer	-92.21	-76.51 (-70.96)	-86.96	-62.38
Heptamer	-110.26	-90.87 (-84.25)	-104.06	-74.56
Octamer	-128.29	-105.67 (-97.99)	-121.16	-86.79

B3LYP/6-311G(2d,d,p) and MP2/6-311G(2d,d,p) levels of theory, respectively. Values in parentheses are energies without the basis-set superposition error (BSSE) correction. Specifically for CA, it has earlier been shown that counterpoise correction could overestimate the BSSE in the case of MP2 methods. [14] So, the saturation value of -17.4 kcal/mol obtained here without BSSE compares well with the extrapolated value of -18.3 kcal/mol reported by Liedl et al. [14] for the dimerization energy of CA based on MP2/aug-cc-pVDZ and MP2/aug-cc-pVTZ calculations.

3.2.2 Vibrational frequencies

Based on Born-Oppenheimer MD results using the PBE functional, we have recently proposed that linear oligomers of the a-a conformer are likely to be the building blocks for at least one of the crystalline polymorphs of carbonic acid, β. [4] The stability of such oligomeric species as observed in the current accurate gas phase calculations offers further credence to this proposal. Given the fact that the experimental infrared and Raman spectra of the two crystalline polymorphs α and β are available, it becomes important to study the vibrational modes using quantum chemical methods. In the current work, we assume that interchain interactions that could be present in these crystals do not affect the intramolecular vibrational modes, at least the high-frequency ones. In an earlier study of the crystals containing such chain motifs, [4] we had noticed that adjacent chains separated by a distance of 3.1 Å did not affect the vibrational frequencies of a given chain. The vibrational spectra of CA oligomers in the frequency range 500-4000 cm^{-1} are discussed here. Table 3.2 shows the harmonic and anharmonic frequencies of the a-a and a-s monomers along with assignments of the modes (see Table 3.3). The ratio of anharmonic to harmonic frequency of various modes is in the range 0.951-0.994. The largest difference of about 180 cm^{-1} is seen for the O-H stretch. The frequencies obtained from the B3LYP calculations are comparable to those from MP2 calculations. These values

Table 3.2: Harmonic and anharmonic frequencies (in cm^{-1}) of the anti-anti (a-a) and anti-syn (a-s) monomers, calculated at B3LYP/6-311G(2d,d,p) and MP2/6-311G(2d,d,dp) levels of theory. Mode assignments are also shown.

a-a				a-s				
B3LYP		MP2		B3LYP		MP2		Assignment
Harmonic	Anharmonic	Harmonic	Anharmonic	Harmonic	Anharmonic	Harmonic	Anharmonic^{a}	
526.5	534.5	526.1	511.6	485.6	472.1	470.9	465.3 (458)	δ_{oop} COH
603.7	596.8	607.9	580.3	568.5	548.6	567.2	540.9 (533)	
550.6	545.7	558.0	552.0	545.4	538.6	556.6	548.8 (550)	δ_{oop} COO
605.8	602.0	610.7	605.9	609.7	604.5	613.4	608.3 (623)	δ_{iop} CO_3
799.6	787.0	802.9	790.3	785.2	773.8	788.9	777.7 (798)	δ_{oop} CO_3
981.1	957.1	994.9	970.2	967.9	933.7	980.3	948.7 (960)	$\nu_s(C(OH)_2)$
1163.7	1109.3	1195.2	1154.8	1152.8	1127.8	1182.3	1142.2 (1159)	$\nu_{as}(C(OH)_2)$ and $\delta_{ip}C(OH)$
1304.6	1259.1	1325.2	1275.6	1274.1	1220.4	1297.4	1248.6 (1253)	$\delta_{ip}C(OH)$ and $\nu(C{=}O)$
1467.5	1429.1	1494.3	1454.4	1407.0	1369.0	1436.1	1395.8 (1408)	$\nu_{as}(C(OH)_2)$
1851.9	1808.8	1885.7	1851.4	1905.1	1846.5	1930.9	1874.2 (1864)	$\nu(C{=}O)$
3812.9	3627.3	3875.6	3690.5	3804.3	3618.7	3875.1	3690.6 (3660)	ν(O-H)
3816	3629.6	3878.4	3692.3	3806.6	3617.5	3881.4	3696.4 (3664)	

[a] Values in parentheses are estimated anharmonic values reported by Tossell [1] for the a-s monomer, calculated at CCSD/6-311+G(2d,p) level of theory.

are also compared against data reported by Tossell [1] for the a-s monomer. He estimated the anharmonic values at CCSD/6-311+g(2d,p) level of theory by summing the harmonic frequencies at the same level with the difference between harmonic and anharmonic values calculated at B3LYP/6-311g(2d,d,p) level of theory. Our results agree with those of Tossell's. The calculated anharmonic values at the B3LYP/6-311g(2d,d,p) differ by about 20-45 cm^{-1}. This difference is the same as reported by Tossell. [1] Frequencies at the MP2/6- 311g(2d,d,p) level are 530 cm^{-1} larger compared with the CCSD results. [1] At frequencies below 700 cm^{-1}, the difference is small and the largest variation is observed for the O-H stretching motion in both cases. Values reported by Tossell are between those calculated here at B3LYP and MP2 levels of theory.

As stated earlier, harmonic frequencies up to a tetramer have been obtained through MP2 calculations. At the MP2 level, anharmonic frequencies are reported here for the monomer and for the anti-anti dimer. Values of frequencies from B3LYP and MP2 levels of theory are comparable; hence, in the rest of this chapter, we discuss the anharmonic data obtained from B3LYP calculations up to an octamer, unless otherwise stated explicitly.

Table 3.4: Calculated harmonic and anharmonic frequencies (in cm^{-1}) of the two dimers along with mode assignments. IR and Raman intensities of corresponding modes are given in columns 3 and 6. Letter T stands for modes due to terminal atoms. The data is from B3LYP/6-311G(2d,d,p) level of theory.

Dimer-a		Activity	Dimer-b		Activity	Assignment
Harmonic	Anharmonic		Harmonic	Anharmonic^a		
572.2 614.0	564.3 608.0	R(4.6355) I(4.4817)	572.7 604.8	565.5 (566) 598.1 (598)	R(1.3) I(135.6)	δ_{ip}(COO)

Continued on next page

Table 3.4 – continued from previous page

Dimer-a		Activity	Dimer-b		Activity	Assignment
Harmonic	Anharmonic		Harmonic	Anharmonic^a		
545.5	546.6	R(5.0585)	576.0	572.7 (573)	R(6.1)	δ_{oop}(COH)
548.8	549.9	I(262.9165)	577.6	574.2 (574)	I(194.2)	
645.7	642.3	R(4.3975)	642.7	639.6 (639)	R(6.4)	$\delta_{ip}(CO_3)$
658.8	655.3	I(14.9854)	653.9	649.5 (648)	I(44.8)	
796.6	787.1	R(0.2267)	802.4	793.5 (794)	R(0.2)	$\delta_{oop}(CO_3)$
798.8	788.9	I(41.6636)	804.0	794.4 (795)	I(43.9)	
936.2	909.6	R(0.3308)	923.9	899.0 (897)	R(0.2)	δ_{oop}(COH)
983.7	962.4	I(207.9773)	971.9	948.2 (947)	I(264.4)	
1021.7	1004.8	I(63.1800)	1025.2	1006.1 (1006)	I (24.3)	$\nu_s(C(OH)_2)$
1031.0	1014.7	R(18.2964)	1031.9	1012.8 (1013)	R(21.8)	
1239.4	1200.6	R(9.0758)	1237.4	1202.3 (1201)	R(2.5)	$\nu_{as}(C(OH)_2)$ and δ_{ip}C(OH)
1246.7	1202.3	I(161.7219)	1242.5	1205.8 (1204)	I(694.4)	
1362.6	1319.9	R(4.0392)	1390.6	1343.0 (1343)	I (280.0)	δ_{ip}(COH) and ν(C=O)
1365.3	1335.8	I(927.6910)	1392.2	1348.7 (1386)	R(6.6)	
1489.0	1457.5	I(497.0124)	1529.2	1478.4 (1478)	I (405.7)	$\nu_{as}(C\text{-}(OH)_2)$
1525.1	1442.8	R(17.9002)	1561.2	1508.5 (1519)	R(17.7)	
1768.6	1696.0	R(14.1178)	1728.2	1658.3 (1656)	R(8.0)	ν(C=O)

Continued on next page

Table 3.4 – continued from previous page

Dimer-a		Activity	Dimer-b		Activity	Assignment
Harmonic	Anharmonic		Harmonic	Anharmonic[a]		
1838.6	1788.1	I(1039.5765)	1797.0	1751.9 (1752)	I(1149.0)	
3032.2	2516.9	R(227.7607)	3119.5	2684.5 (2752)	R(245.4)	ν(O-H)
3157.1	2741.6	I(3152.0443)	3231.2	2878.9 (2883)	I(2945.8)	
3799.2	3605.2	I(175.9545)	3808.4	3626.7 (3624)	I(189.4)	ν(O-H) (T)
3799.4	3605.3	R(155.2226)	3808.7	3627.0 (3624)	R(123.3)	

[a] Values in parentheses are anharmonic values reported by Tossell using the same method, B3LYP/6-311d(2d,d,p) [1].

Harmonic and anharmonic frequencies along with the mode assignments for dimers a and b are provided in Table 3.2.2. In both dimers, the C=O bond is elongated and its stretching frequency is red-shifted compared with that in the monomer. [15] While the hydrogen bond (H-bond) length and angle in dimer a are 1.615 Å and 177.1°, the corresponding values in dimer b are 1.643 Å and 177.5°. Thus the H-bonds in dimer a are stronger than those present in dimer b. As the strength of the hydrogen bond increases, the C=O stretching frequency is expected to decrease. This can seen from Tables 3.2 and 3.2.2, where the C=O peak is red-shifted by 58.4 and 56.9 cm^{-1} upon dimerization of a-s monomer (dimer a) and a-a monomer (dimer b), respectively, at the anharmonic level. The activities of vibrational modes are shown in columns 3 and 6 of Table 3.2.2, where R and I stand for Raman active and IR active, respectively. Values in parentheses refer to intensities

Table 3.3: Calculated harmonic and anharmonic frequencies of the anti-anti (a-a), anti-syn (a-s) monomer along with mode assignments. R and I stand for Raman active and IR active, respectively. Values in parentheses refer to intensities of the corresponding modes. The data is from B3LYP/6-311G(2d,d,p) level of theory.

a-a		Activity	a-s		Activity	Assignment
Harmonic	Anharmonic		Harmonic	Anharmonic		
526.5	534.5	R(95.0)	485.6	472.1	I(238.7),R(1.6)	δ_{oop} COH
603.7	596.8	I(218)	568.5	548.6	& I(12.0),R(3.5)	
550.6	545.7	I(5.6)	545.4	538.6	I(27.2),R(1.2)	δ_{oop} COO
605.8	602.0	I(50.6),R(3.5)	609.7	604.5	I(8.6),R(2.1)	δ_{iop} CO_3
799.6	787.0	I(64.4)	785.2	773.8	I(35.8),R(0.2)	δ_{oop} CO_3
981.1	957.1	I(16.2),R(9.8)	967.9	933.7	I(38.5),R(8.1)	$\nu_s(C(OH)_2)$
1163.7	1109.3	I(478.9)	1152.8	1127.8	I(228.2),R(1.4)	$\nu_{as}(C(OH)_2)$ and $\delta_{ip}C(OH)$
1304.6	1259.1	I(27.3),R(6.0)	1274.1	1220.4	I(136.3),R(7.2)	$\delta_{ip}C(OH)$ and ν C=O
1467.5	1429.1	I(120.0)	1407.0	1369.0	I(296.2),R(0.4)	$\nu_{as}(C(OH)_2)$
1851.9	1808.8	I(505.5),R(2.0)	1905.1	1846.5	I(462.9),R(5.1)	ν(C=O)
3812.9	3627.3	I(168.5),R(10.2)	3804.3	3618.7	I(89.4),R(55.9)	ν(O-H)
3816	3629.6	I(17.7),R(94.8)	3806.6	3617.5	I(75.4),R(69.6)	

Table 3.5: Comparison of IR spectra of anti-anti monomer, anti-syn monomer and dimer b with experimental matrix isolated gas-phase spectrum. [13] Mode assignments are given. The data is obtained using B3LYP/6-311G(2d,d,p) level of theory. Values are in cm^{-1}.

a-a	a-s	Dimer	Experiment	Assignment
787.0	773.8	794.4	785, 794, 808	$\delta_{oop}CO_3$
1109.3	1127.8	1205.8	1175, 1182	$\nu_{as}C(OH)_2$ and $\delta_{ip}C(OH)$
1259.1	1220.4	1343.0	1270	$\delta_{ip}C(OH)$ and $\nu(C{=}O)$
1429.1	1369.0	1478.4	1452	$\nu_{as}C(OH)_2$
1808.8	1846.5	1751.9	1722, 1779 1799, 1829	$\nu(C{=}O)$
3627.3, 3629.6	3617.5, 3618.7	2878.9, 3626.7	3602, 3604 3608, 3611	ν(O-H)

of the corresponding modes. The anharmonic frequencies of dimer b are also compared with those obtained by Tossell [1] in column 5 of Table 3.2.2. Since the level of calculation of frequencies is the same in both cases, frequencies calculated here are in good agreement with those of Tossell. [1] The marginal difference between the two sets of data is likely due to the “very tight” convergence that was used in our calculations.

Loerting et al. carried out matrix isolated gas phase vibrational spectroscopy of CA recently. [13] They showed that the gas phase of carbonic acid consists of 90% of anti-anti monomer with the remaining matter constituted by the anti- syn monomer and dimer b species. [13] The infrared spectra of anti-anti and anti-syn monomers and of dimer b are compared against this data in Table 3.5. In the experimental spectrum, a peak corresponding to the out-of-plane bending motion of the CO_3 group appears at 785, 794, and 808 cm^{-1}. In the calculated spectrum, the corresponding peaks are present at 787.0, 773.8, 794.4 cm^{-1} for the anti-anti monomer, anti-syn monomer, and dimer b, respectively. Peaks at 1175 and 1182 cm^{-1} are assigned to the antisymmetric stretching of $C(OH)_2$ and the bending of C(OH) groups. The corresponding mode frequencies are 1109.3, 1127.8, and 1205.8 cm^{-1} for the two monomers and dimer b, respectively. Note that the peak present in dimer b is closer to the experimental value. The in-plane bending of the C(OH) group and the stretching mode of C=O show a peak at 1270 cm^{-1} in the experiment. In our calculations, this mode occurs at 1259.1 cm^{-1}. Peaks corresponding to the stretching of C=O and O-H groups match with those of the anti-anti monomer, anti-syn monomer, and dimer b as shown in Table 3.5. It is to be noted that the C=O and O-H mode frequencies calculated using B3LYP/6-311G(2d,d,p) are comparable to values reported by Tossell or MP2/6-311G(2d,d,p) data. [1]

Hydrogen bonding between monomers impacts the vibrational spectrum of the dimer in a significant manner. For instance, the C=O stretch mode present at 1808.8 cm^{-1} in the monomer is red-shifted to values of 1658.3 and 1751.9 cm^{-1} in the dimer (dimer b). The same mode is further red-shifted to 1596.4 and 1643.1 cm^{-1} in the case of the tetramer. The mode frequency is largely unchanged in higher oligomers because the number of hydrogen bonds formed by the carbonyl oxygen saturates to a value of two for the tetramer and higher oligomers. Within the harmonic approximation, the IR active C=O stretching mode exhibits peaks at 1851 (monomer), 1797 (dimer b), 1704 (tetramer), 1674 and 1737 (hexamer), and 1663 and 1700.9 and 1749 cm^{-1} (octamer). Since the C=O stretch frequency is nearly the same for oligomer sizes beyond (and including) the tetramer, one can safely compare the features of the octamer spectra against the experimental data for the α and β forms of CA.

The O-H stretch frequency decreases with increasing H-bond strength. The frequencies for dimer b and dimer a are 2684.5, 2878.9 cm^{-1} and 2516.9, 2741.6 cm^{-1} respectively. Both dimers exhibit the center of inversion symmetry in their

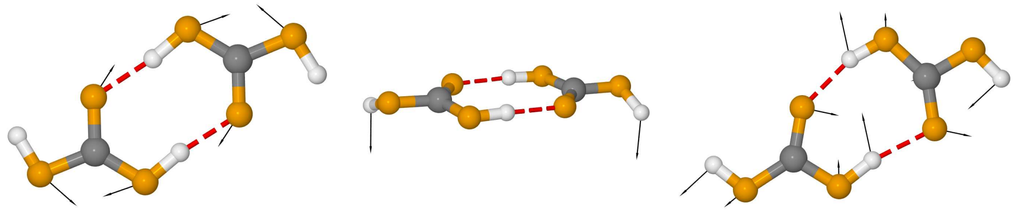

(a) δ_{oop}COO **(b)** δ_{ip}COH **(c)** δ_{ip}CO$_3$

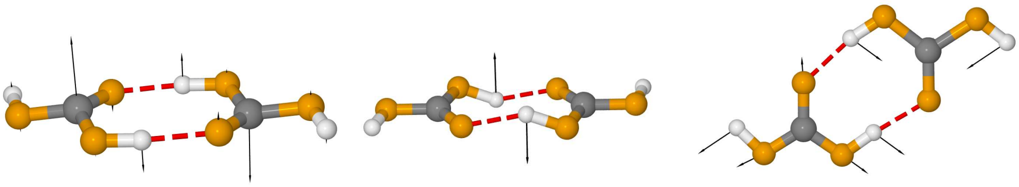

(d) δ_{oop}CO$_3$ **(e)** δ_{oop}COH **(f)** ν_sC(OH)$_2$

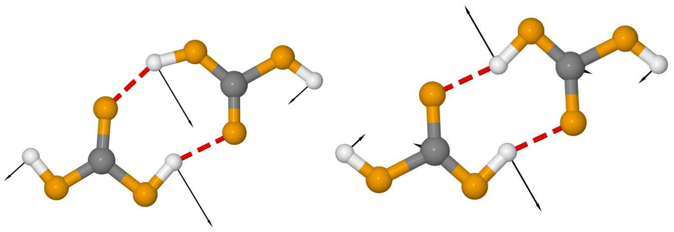

(g) ν_{as}C(OH)$_2$ & δ_{ip}C(OH)$_2$ **(h)** ν_{as}C(OH)$_2$

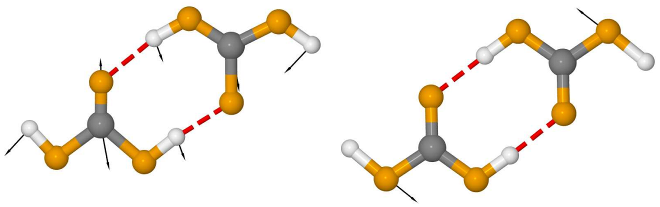

(i) νC=O **(j)** νO-H

Figure 3.7: Atomic displacement vectors of various vibrational modes of dimer b (a-a dimer) are shown. Hydrogen bonds are shown as red dashed lines and the vectors are black in colour. Colour code: C, gray; O, orange; H, white.

Table 3.6: Comparison of unscaled harmonic and anharmonic frequencies of the anti-anti dimer (dimer b) obtained at B3LYP/6-311G(2d,d,p) and MP2/6-311G(2d,d,p) levels of theory. Letter T stands for modes due to terminal atoms.

B3LYP		MP2		Assignment
Harmonic	Anharmonic	Harmonic	Anharmonic	
572.7	565.5	575.7	555.7	δ_{ip}(COO)
576.0, 577.6 604.8	572.7,574.2 598.1	577.2, 578.3 605.8	556.8, 570.8 598.9	δ_{oop}(COH)
642.7, 653.9	639.6, 649.5	644.7, 652.6	639.1, 646.6	$\delta_{ip}(CO_3)$
802.4, 804.0	793.5,794.4	805.6, 808.0	798.5, 799.5	$\delta_{oop}(CO_3)$
923.9, 971.9	899.0,948.2	911.9, 965.1	861.6, 923.4	δ_{oop}(COH)
1025.2, 1031.9	1006.1,1012.8	1033.8, 1041.8	1014.0, 1023.3	$\nu_s(C(OH)_2)$
1237.4, 1242.5	1202.3,1205.8	1261.1, 1264.2	1219.7, 1222.2	$\nu_{as}(C(OH)_2)$ and δ_{ip}C(OH)
1390.6, 1392.2	1343.0,1348.7	1413.3, 1415.5	1374.0, 1380.8	δ_{ip}(COH) and ν(C=O)
1529.2, 1561.2	1478.4,1508.5	1554.6, 1585.2	1506.3, 1534.4	$\nu_{as}(C\text{-}(OH)_2)$
1728.2, 1797.0	1658.3,1751.9	1784.1, 1843.5	1742.0, 1800.7	ν(C=O)
3119.5, 3231.2	2684.5,2878.9	3318.0, 3414.9	3018.7, 3141.0	ν(O-H)
3808.4, 38087	3626.7,3627.0	3871.2, 3871.6	3684.9, 3685.4	ν(O-H) (T)

point group. This property leads to the mutual exclusion of IR and Raman active modes, which can be seen clearly in Table 3.2.2. Atomic displacement for all the vibrational modes of dimer b are shown in Figure 3.7. The vibrational spectrum of the dimer contains some features that correspond to intramolecular modes involving the terminal atoms. Their influence (and the IR or Raman intensities) can be decreased if one studies the spectra of large oligomers. It is for this reason that we examine the vibrational spectrum of the linear octamer constituted by the anti-anti conformers.

MP2 calculations using a large basis set such as the one employed here can yield accurate information on bond frequencies. However, they are computationally demanding. Hence, we have carried out harmonic frequency calculations at the MP2/6-311G(2d,d,p) level for the dimer and the tetramer only. The data are compared against those obtained from B3LYP/6-311G(2d,d,p) level of theory (Tables 3.6 and 3.7). As seen in Tables 3.6 and 3.7, in both cases, the frequencies calculated from the two methods differ only for a few high-frequency modes (mostly bond stretches). Scaling factors (i.e., the ratio of anharmonic to harmonic frequency values at a particular level of theory) can be used to identify systematic errors. Although these are, in general, lower for MP2 than for the B3LYP level of theory, [16] the scale factors for MP2 are not too far off from those for B3LYP. Hence, we continue to discuss the spectral features of the oligomers obtained using B3LYP level of theory against experimental data.

Recently, Loerting and co-workers have measured the infrared and Raman spectra of the two polymorphs of CA and found that while β-carbonic acid has a center of inversion symmetry, the α-polymorph does not. [5, 17] They also postulated that the β form could contain one-dimensional, hydrogen bonded chains. Experimental observations on α-carbonic acid reveal that the O-H stretch bands are more red-shifted compared with those in the β form. [18] This means either that CA molecules in the α form have stronger hydrogen bonds or that the O-H group in the α-form participates in a higher number of hydrogen bonds compared with those in the β form. Since we have noticed that the a-s dimer (dimer a) forms stronger H-bonds than the a-a dimer (dimer b), it is possible that the α-polymorph could consist of carbonic acid molecules in the a-s conformation. They could be in the form of either chains or sheets. However, proton transport in such a crystal could easily transform the conformation from a-s to a-a. Such a phenomenon has earlier been discussed in carboxylic acid crystals. [19] This aspect needs to be investigated in future.

3.2.3 Comparison with experimental data for the crystals

Infrared spectrum. As mentioned before, anharmonic frequencies for oligomers larger

Table 3.7: Comparison of unscaled harmonic frequencies of tetramer obtained at B3LYP/6-311G(2d,d,p) and MP2/6-311G(2d,d,p) levels of theory. Letter T stands for modes due to terminal atoms.

B3LYP	MP2	Assignment
577.4,577.6	576.2, 576.3	δ_{oop}COH (T)
581.2,582.8	585.9, 587.2	δ_{ip}COO (T)
626.5, 658.6	625.9, 656.1	δ_{ip}COO
645.2,645.3	646.3, 646.7	$\delta_{ip}CO_3$ (T)
669.9,684.2	670.0, 682.4	$\delta_{ip}CO_3$
798.4,798.7	802.4, 802.6	$\delta_{oop}CO_3$ (T)
804.4,805.9	806.7, 809.5	$\delta_{oop}CO_3$
831.0,880.4,900.9, 904.3,957.6,977.5	831.9, 879.6, 901.5, 902.4, 956.6, 980.1	δ_{oop}C(OH)
1028.7,1028.7	1038.1, 1038.1	$\nu_s C(OH)_2$ (T)
1058.3,1065.4	1066.9, 1074.1	$\nu_s C(OH)_2$
1235.3,1236.2	1259.6, 1260.7	δ_{ip}C(OH) and $\nu_{as} C(OH)_2$ (T)
1354.0,1359.3	1375.7, 1381.1	δ_{ip}C(OH) and $\nu_{as} C(OH)_2$
1389.1,1395.5,1417.1 1437.2	1414.4, 1419.4, 1444.8 1464.9	δ_{ip}C(OH) and ν(C=O)
1539.4,1543.0	1568.3,1569.4	ν_{as} $C(OH)_2$ (T)
1579.0,1602.4	1606.3, 1626.6	$\nu_{as} C(OH)_2$
1663.1,1704.5	1715.6, 1758.0	ν(C=O)
1773.4,1786.0	1821.8, 1834.2	ν(C=O) (T)
3142.1,3142.8,3225.7, 3243.5, 3310.3,3364.7	3323.8, 3324.9, 3379.2, 3404.3, 3464.2, 3506.9	ν(O-H)
3807.5,3807.6	3869.6, 3869.6	ν(O-H) (T)

Table 3.8: Spectral features in the infrared spectrum of the octamer (calculated), and in the α and β forms of carbonic acid (experimental). [18, 20] The calculations are performed at B3LYP/6-311G(2d,d,p) level of theory. Each mode of the octamer is scaled by a factor given in column 2 to take into account the anharmonicity of the mode. See text for discussions. Values in parentheses denote the IR intensities in arbitrary units. [a]from Ref. [21]

Mode	Scaling factor	Frequency (cm^{-1})		
		Octamer	α	β
δ_{ip}COO	0.9849	607.5(6.3),631.5(37.9) 655.5(114.4)	-	-
δ_{ip}CO$_3$	0.9897	660.0(12.4),674.3(50.5) 680.9(305.7)	583	661,683
δ_{oop}CO$_3$	1.0076	808.1(1.1),809.8(5.7), 811.4(47.1)	801	812
δ_{oop}C(OH)	0.9817	807.0(20.6),851.5(25.9), 857.1(1.6), 875.0(20.2), 902.9(16.4),939.5(44.8), 958.9(1389.3)	920	880-900
ν_sC(OH)$_2$	0.9837	1039.0(17.0),1042.7(0.7), 1048.7(0.4)	1084	1036
δ_{ip}COH and ν_{as}C(OH)$_2$	0.9711	1303.5(3120.0),1312.2(2.0), 1329.8(159.8),1351.4(51.5)	1420	1297
δ_{ip}C(OH) and νC=O	0.9679	1367.8(7.8),1373.2(7.0),	-	-
ν_{as}C(OH)$_2$	0.9605	1501.7(1573.5),1517.4(114.0), 1542.6(8.9)	1304, 1477	1501
νC=O	0.9620	1600.6(10.3),1636.3(58.5), 1682.7(1191.1)	1715	1700
νO-H	0.9109	2854.4(3079.9),2914.2(7859.5), 2929.5(4354.1),2948.2(3523.2), 3007.9(1003.5),3053.9(245.2), 3084.2(2855.3)	2585, 2694	2500-3500 2600-3200[a]

than a tetramer are not reported here, because they exhibit one or more imaginary frequencies at the anharmonic level. Instead, we employed scaling factors to obtain estimates of anharmonic frequencies for the octamer. First, the ratio of anharmonic to harmonic frequencies for each mode of the tetramer was obtained. These ratios (scale factors) were used to obtain the anharmonic frequencies from the calculated harmonic data of the octamer. Where multiple peaks are observed for a particular mode in the tetramer, the mean of the frequencies was used to obtain the scale factor. Features of the "anharmonic" spectrum thus calculated for the octamer are compared against experimental data in Tables 3.8 and 3.9. They show the calculated frequencies along with IR and Raman intensities, the scaling factors employed, and also the experimental frequencies observed for the α- and β-carbonic acid samples. [18, 20] In the following discussion, modes localized on the terminal CA molecule are ignored, and only the "bulk" modes are presented. In Table 3.8 , the mode at 660, 674.3, and 680.9 cm^{-1} corresponds to the inplane bending of the CO_3 group in the octamer. The experimental value for the same mode is present at 583 cm^{-1} for the α-polymorph and at 661 and 683 cm^{-1} for β-carbonic acid. The calculated frequencies are in better agreement with the latter than with the former, giving further credence to the idea that the β form is likely to be made up of hydrogen bonded anti-anti conformers organized to form a one-dimensional chain. The out-of-plane bending mode of the CO_3 group is observed at 808.1, 809.8, and 811.4 cm^{-1} for the octamer. These values are close to the experimental data of both the α and β forms. The out-of-plane bending motion of C(OH) group occurs over a broad range of frequencies, 807-958.9 cm^{-1}. The peak with the highest intensity is present at 958.9 cm^{-1}, which is about 40-60 cm^{-1} shifted relative to the experimental data. The out-of-plane motion may be modulated by interchain interactions, which have not been taken into account in the current calculations. Peaks present at 1039.0, 1042.7, and 1048.7 cm^{-1} correspond to the symmetric stretching of the $C(OH)_2$

group in the octamer. The corresponding mode in the experimental spectrum of β-carbonic acid is close to these values, while the mode in α-carbonic acid is present at a higher frequency of 1084 cm^{-1}.

A mode involving both the in-plane bending of C(OH) and the asymmetric stretching of $C(OH)_2$ exhibits a very strong peak at 1303.5 cm^{-1} in the octamer. This mode frequency also is much closer to that for the β crystal rather than that for the α form. In the former, it is present at 1297 cm^{-1}. [18] However, in α-carbonic acid, it is observed at a frequency around 120 cm^{-1} larger than the calculated value. [18] Peaks corresponding to the asymmetric stretching of $C(OH)_2$ group are present at 1501.7, 1517.4, and 1542.6 cm^{-1} in the octamer. Among these, the peak at 1501.7 cm^{-1} is more intense. The corresponding peak for β-CA is at 1501 cm^{-1}, which matches with that of the octamer. However, this mode is present at 1304 and 1477 cm^{-1} in α-carbonic acid. [20] The calculated IR vibrational spectrum for the octamer has no peaks at 1304 cm^{-1}, indicating that the α-form is unlikely to be composed of hydrogen bonded linear chains of the anti-anti conformer.

As discussed earlier, the symmetric stretching of the C=O bond occurs at 1600.6, 1636.3, and 1682.7 cm^{-1} in the octamer. Among these, the peak at 1682 cm^{-1} is more intense compared with other peaks. This value is very close to the corresponding mode in both the α and β forms (1715 and 1700 cm^{-1}, respectively). The stretching of the O-H bond has a broad range of values between 2854 and 3084 cm^{-1} as given in Table 3.8. For the α polymorph, this mode shows peaks at 2585 and 2694 cm^{-1}, and in β, this mode shows a broad peak between 2500 and 3500 cm^{-1}. The calculated peak positions compare very well with the spectrum for β, while there is no overlap between the peak positions of α-CA and those calculated for the octamer. From the above analyses, it is clear that the linear octamer spectrum matches well with that of β-carbonic acid. The frequencies of the octamer are also shown as blue sticks in Figure 3.8. One can see many groups of sticks with each group representing a

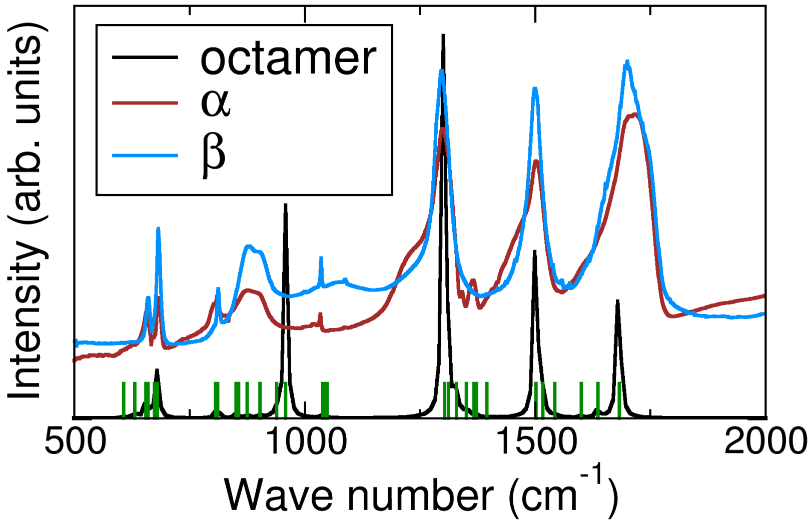

Figure 3.8: Comparison of the infrared spectra of the linear octamer (calculated), against experimental spectra of α and β forms of carbonic acid. [18, 20] Peaks due to terminal atoms are not shown. Calculated frequencies of the octamer are also shown as sticks (blue colour).

vibrational mode that has been described above.

To summarize, the following mode frequencies of the octamer match well with the β form exclusively: $\delta_{ip}CO_3$, $\delta_{oop}CO_3$, $\delta_{oop}C(OH)$, $\nu_s C(OH)_2$, $\delta_{ip}C(OH)$, $\nu_{as}C(OH)_2$, νC=O, and νO-H. Yet there are minor differences between these two spectra. In β-carbonic acid, the out-of-plane bending of the C(OH) group has a broad feature between 790 and 950 cm^{-1}. [18] It exhibits two peaks at 881 and 910 cm^{-1} over this broad feature. In the case of the octamer, there are peaks at 807.0, 851.5, 875.0, and 939.5 cm^{-1}, in addition to the one at 958.9 cm^{-1}. Thus, the difference between the calculated and experimental values for this mode frequency is about 58 cm^{-1}. This large difference is likely due to the following reasons: A part of it could come from methodological deficiencies and another from interchain interactions. Anharmonic frequencies corresponding to this out-of-plane mode based on MP2/6-311(2d,d,p) calculations of the dimer and tetramer yield nearly the same frequencies as the B3LYP calculations for the octamer. Hence, we attribute the difference in the frequency of the δ_{oop}C(OH) mode against experimental data to the lack of interchain interactions in the former. In particular, interchain interactions would shift the calculated frequency for out-of-plane modes to lower values, closer to the experimental data.

In the octamer, a mode ascribed to both the in-plane bending of COH and the stretching of C=O appears at 1367.8, 1373.2, and 1395.2 cm^{-1}, whereas no such peak is seen in the experimental IR spectra of both the α and β forms. However, as can be seen in Table 3.8, the IR intensities of these peaks are very small, and hence this difference is likely to be insignificant. Peaks at 607.5, 631.5, and 655.5 cm^{-1} seen in the octamer spectrum correspond to the in-plane bending of the COO group. Among these, the peak at 655.5 cm^{-1} is the most intense. As seen from the table, no corresponding peak is reported in the experiment for either of the polymorphs. However in β-carbonic acid, peaks at 661 and 683 cm^{-1} are assigned to the in-plane bending mode of CO_3 group. [18] Among these, the peak at 683 cm^{-1} is more than twice as intense compared with the peak at 661 cm^{-1}. Since these two modes are quite close to each other, they may have been assigned to the same mode ($\delta_{ip}CO_3$) in the experiment. In the calculated spectrum, the feature at 680.9 cm^{-1} is again twice as intense as the one at 655.5 cm^{-1}. Based on visualization of the atomic displacements, we assign the 655.5 cm^{-1} mode to δ_{ip}COO and the 680.9 cm^{-1} to $\delta_{ip}CO_3$.

To summarize, the calculated IR modes observed in the octamer match well with those of β-carbonic acid as can be seen in Figure 3.8.

Raman spectrum. The calculated Raman spectrum of the octamer is compared against the experimental Raman spectra of α- and β-carbonic acid [5, 17] in Table 3.9. Octamer frequencies are scaled by factors given in column 2, which are the same as in Table 3.8. For the COO in-plane bending mode, strong peaks are seen at 601.9, 644.4, and 652.0 cm^{-1} for the octamer. For β-CA, this mode is observed at 605 and

Table 3.9: Spectral features in the Raman spectrum of the octamer (calculated), and in α and β forms of carbonic acid (experimental). [5, 17] The calculations are performed at B3LYP/6-311G(2d,d,p) level of theory. Each mode of the octamer is scaled by a factor given in column 2 to take into account the anharmonicity of the mode. See text for details. Values in parentheses denote the Raman intensities in arbitrary units.

Mode	Scaling factor	Raman shift (cm^{-1})		
		Octamer	α	β
δ_{ip}COO	0.9849	601.9(15.5),618.3(1.3), 644.4(5.0),652.0(5.3)	681	605,657
δ_{ip}CO$_3$	0.9897	667.2(0.3),679.4(0.03)	558, 567	-
δ_{oop}CO$_3$	1.0076	808.2(0.07),808.5(0.3), 809.8(0.6)	799	-
δ_{oop}C(OH)	0.9817	793.3(1.2),827.89(0.1), 865.67(0.02),871.2(0.02), 895.3(0.2),920.6(0.08), 954.5(0.2)	928	-
ν_sC(OH)$_2$	0.9837	1040.3(0.9), 1045.7(6.8), 1050.9(92.0)	1093	1051
δ_{ip}COH and ν_{as}C(OH)$_2$	0.9711	1296.0(0.4),1318.2(0.4), 1329.4(0.8),1348.8(2.1)	1203	-
δ_{ip}C(OH) and νC=O	0.9679	1368.6(0.9),1381.4(6.4), 1401.1(57.0)	-	1401
ν_{as}C(OH)$_2$	0.9605	1505.6(1.1),1530.7(7.0), 1550.6(38.3)	1427, 1447 1465, 1489	1530
νC=O	0.9620	1586.8(52.3),1617.0(2.1), 1659.2(0.8)	1630	1607
νO-H	0.9109	2855.3(500.5),2914.9(409.6), 2926.4(272.2),2946.4(541.3), 2986.3(1042.8),3029.8(36.0), 3073.0(10.5)	2976, 3039, 3057	-

657 cm^{-1}, while in the α form it is present at 681 cm^{-1}. [18, 20] In the octamer, the peak at 601.9 cm^{-1} has the maximum intensity compared with other peaks for the mode. The same behavior is observed in the corresponding spectrum of β-carbonic acid. The symmetric stretching mode of C(OH)$_2$ exhibits peaks at 1045.7 and 1050.9 cm^{-1} in the octamer and at 1051 and 1093 cm^{-1} in the β and α forms, respectively. The in-plane bending of the COH group and the stretching of the C=O bond are present at 1381.4 and 1401.1 cm^{-1} in the octamer and at 1401 cm^{-1} in β-carbonic acid. It is pertinent to note that this mode is not observed in the experimental spectrum of the α-form. In the spectrum of the octamer, the peaks corresponding to the asymmetric stretching of C(OH)$_2$ are present at 1530.7 and 1550.6 cm^{-1}, which matches well with that in β-carbonic acid; however, in the α- form, they are shifted to lower wave numbers. In the octamer, the stretching of the C=O bond exhibits peaks at 1586.8 and 1617.0 cm^{-1}, which agrees well with the peak positions of the corresponding mode in β-carbonic acid (at 1607 cm^{-1}). [18] In the α form, this peak is observed at 1630 cm^{-1}. [20] The quantity $\delta\nu$(C=O) is defined as the difference in the peak positions of Raman and IR frequencies of the C=O stretching mode. Its value is 96.0 cm^{-1} for the octamer, which is comparable to the values of 93.0 and 85 cm^{-1} for α- and β-carbonic acid, respectively. [18, 20] Other Raman active modes present in the octamer have very low intensities, and these are not observed in the experimental spectrum of β-carbonic acid. The calculated Raman spectrum of the octamer is compared against the experimental data for α- and β-carbonic acid in Figure 3.9. The main distinction between the Raman spectra of the α and β forms is the peak at 920 cm^{-1}, which is observed in the α form only. This is assigned to out-of-plane bending of the COH group. Not unsurprisingly, this peak is not observed in the calculated spectrum of the octamer. Thus, the Raman data too adds credence to the notion that the β-carbonic acid is likely to be composed of linear hydrogen bonded carbonic acid molecules.

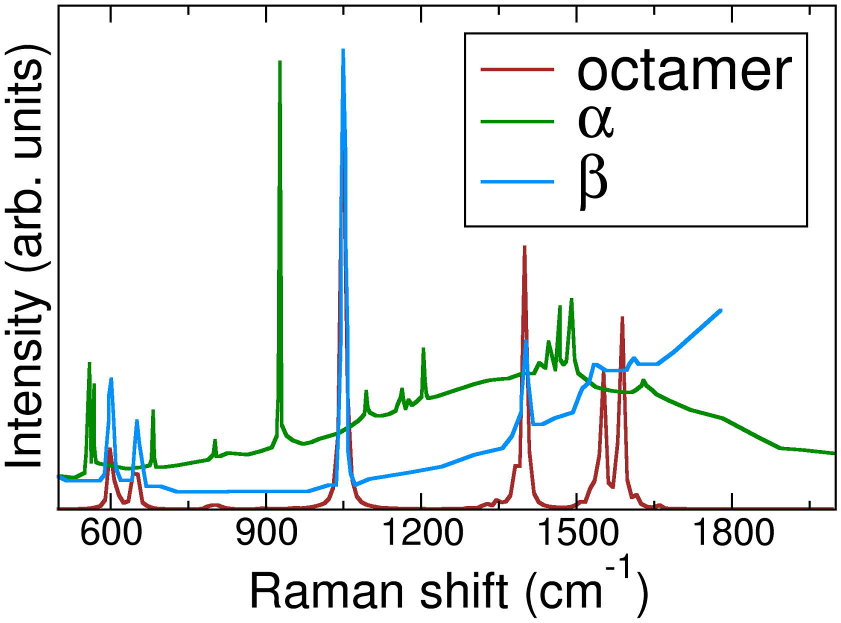

Figure 3.9: Comparison of the Raman spectra of the linear octamer (calculated), against experimental spectra of α, β forms of carbonic acid. [5, 17] Peaks due to terminal atoms are not shown.

Anti-syn oligomers. One dimensional chains formed from a-s conformers were also examined. A linear tetramer, consisting of two dimer a molecules connected to each other with two weak hydrogen bonds (shown as Figure 3.5) is found to be less stable than the linear tetramer made of a-a conformers by 9.2 kcal/mol calculated at B3LYP/6-311G(2d,d,p) level of theory. The linear tetramer formed by s-s conformers can be ruled out based on the large energy difference between the s-s monomer and other conformers. Thus, the one-dimensional chain formed by a-a conformers is the most stable, and the vibrational analysis carried out shows that the anharmonic vibrational spectrum of the octamer matches extremely well with the experimental IR and Raman spectra of β-carbonic acid. In α-carbonic acid, peaks at frequencies 583, 1420, 2585, and 2694 cm^{-1} are either red or blue-shifted by about 100 cm^{-1} compared with values calculated for the linear a-a octamer. Further, the peaks at 920 and 1304 cm^{-1} present in the spectrum of the α form are entirely absent in the calculated Raman and IR spectra of the a-a octamer, respectively.

Based on our earlier work on candidate crystal structures for the β-polymorph, the distance between these parallel chains was calculated to be 3.13 Å. [4] The infrared spectrum of these crystals was observed not to change much from that obtained from a linear oligomer in gas phase, employing the same DFT methods. Double proton transfer between carboxylic acid dimers is a very well-known phenomena and was studied comprehensively using experimental and theoretical methods. [19] Transfer of protons between carboxylic acids is aided by hydrogen bonding. Since carbonic acid molecules exhibit strong hydrogen bonds, double proton transfer between these molecules, which allows them to switch from one conformation to another in the crystalline phase, cannot be ruled out. Such an event in the a-a oligomer would shift the C=O and O-H stretching frequencies to higher and lower wave numbers, respectively.

3.2.4 A note on low-frequency vibrations

Intermolecular modes dominate in the low-frequency region. The environment around the oligomer, interchain interactions, and anharmonicity are expected to play significant roles in this region. Keeping these limitations in our calculations in mind, we compare the estimated anharmonic spectrum obtained for the octamer against experiment.

Figure 3.10 shows the far-IR spectrum. The peak centered at 239.3 cm^{-1} corresponds to the rocking motion of CA molecules, whereas the small feature at 202 cm^{-1} corresponds to the same mode due to terminal molecules present in the octamer. Further, a floppy mode is seen at 169 cm^{-1} due to terminal molecules. The intensity of the peak at 239.3 cm^{-1} is very high and is the only one observed above 200 cm^{-1}, which is consistent with our recent Born-Oppenheimer simulations on chainlike crystal structures. [4] It is to be noted that the experimental low-frequency IR spectra of the α and β forms have not been reported yet.

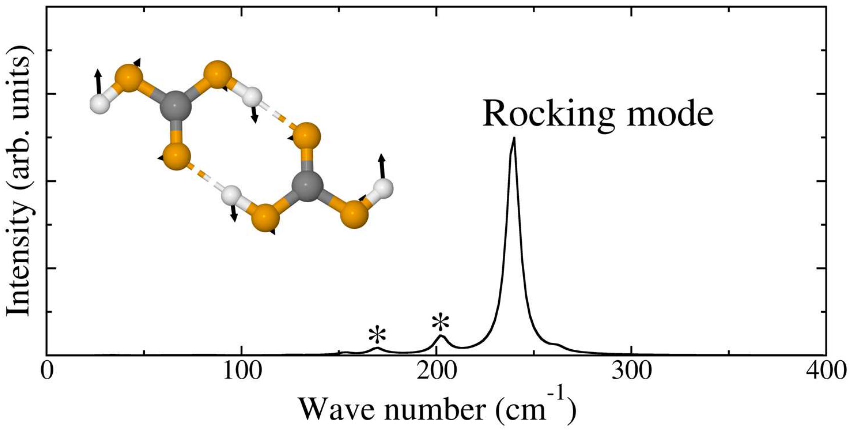

Figure 3.10: Calculated far infrared spectrum of the linear octamer of carbonic acid. Atomic displacements observed for the mode at 239.3 cm^{-1} for a dimer is shown as inset. Colour code: C, gray; O, orange; H, white. Peaks denoted by asterisks are from terminal molecules in the oligomer.

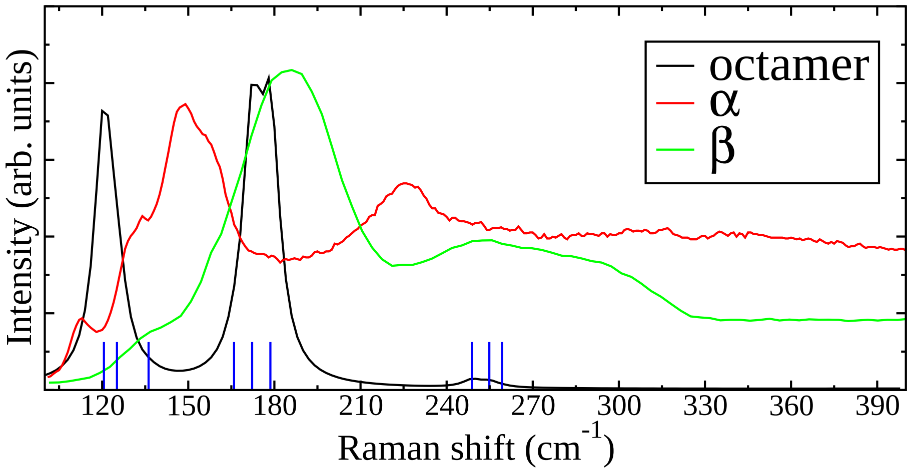

Figure 3.11: Comparison of the low frequency Raman spectrum of the linear octamer (calculated) with the experimental spectra of α- and β-carbonic acid. [5, 17] Features of the octamer spectrum are also shown as blue sticks.

Figure 3.11 shows the calculated low-frequency Raman spectrum of the octamer along with the experimental data for α and β forms. [5] Frequency values are also shown as blue sticks. Peaks at 120.6, 125.2, and 136.2 cm^{-1} in the calculated spectrum correspond to out-of-plane bending of the hydrogen bond. Peaks at 165.9, 172.2, and 178.6 cm^{-1} are assigned to intermonomer stretching of CA molecules, whereas the one at 248.8 cm^{-1} corresponds to the in-plane bending of the hydrogen bond. As mentioned before, the rocking motion of CA molecules exhibits peaks at 254 and 259.3 cm^{-1}. The low frequency Raman spectrum of β-carbonic acid shows peaks at 125, 138, 144, 165, 176, 192, and 258 cm^{-1}. [5] Based on B3LYP and MP2 levels of theory calculations using 6-31+G(d) or aug-cc-pVDZ basis sets of the anti-anti dimer, Loerting et al. assigned peaks at 165, 176, and 192 cm^{-1} to intermonomer stretching mode. [5] These features can be seen in Figure 3.11 where we also show the Raman spectrum calculated by us for the octamer. The octamer spectrum shows features at 165.9, 172.2, and 178.6 cm^{-1}. Based on visualization of atomic displacements, we assign these peaks to intermonomer stretching. As discussed earlier, the peak observed at 258 cm^{-1} in experiments is due to the rocking motion of CA molecules. The peak at 125 cm^{-1} in the β form could be assigned to out-of-plane bending of the hydrogen bond, based on our calculations for the octamer. In general, features below 200 cm^{-1} in the calculated spectrum are red-shifted by about 15-30 cm^{-1} when compared with the experimental data for β-carbonic acid. This shift likely points to the lack of interchain interactions in the present calculations. However, the agreement in the low-frequency region between the calculated and experimental spectra is fair.

3.3 Discussion and conclusions

Quantum chemical calculations of oligomers of carbonic acid in gas phase have been carried out. In particular, linear hydrogen bonded species of the anti-anti conformation, ranging from a monomer to an octamer were studied for their ground state geometry and harmonic and anharmonic vibrational spectra. Our results for small oligomers (monomer and the dimer) match those obtained by Tossell [1] earlier. In the frequency range higher than 500 cm^{-1}, the calculated infrared and Raman spectra of the octamer agree extremely well with the experimental spectra for β-carbonic acid, rather than with that for the α-polymorph. [17, 18, 20] Our earlier work [4] involved periodic DFT calculations using the PBE functional and AIMD simulations. Here, we have reported vibrational spectroscopic data for gas phase oligomers of linearly hydrogen bonded CA molecules calculated using both MP2 and B3LYP levels of theory. The current calculations add further credence to the postulation that the β form is constituted by chainlike species, possessing a center of inversion. The comparison of the calculated spectrum to experimental results for frequencies below 500 cm^{-1} is fair, pointing possibly to the significance of interchain interactions in modulating the frequencies of modes in this region.

Bibliography

[1] Tossell, J. A. *Inorg. Chem.* **2006**, *45*, 5961–5970.

[2] Ballone, P.; Montanari, B.; Jones, R. O. *J. Chem. Phys.* **2000**, *112*, 6571–6575.

[3] Winkel, K.; Hage, W.; Loerting, T.; Price, S. L.; Mayer, E. *J. Am. Chem. Soc.* **2007**, *129*, 13863–13871.

[4] Reddy, S. K.; Kulkarni, C. H.; Balasubramanian, S. *J. Chem. Phys.* **2011**, *134*, 124511.

[5] Mitterdorfer, C.; Bernard, J.; Klauser, F.; Winkel, K.; Kohl, I.; Liedl, K. R.; Grothe, H.; Mayer, E.; Loerting, T. *J. Raman Spectrosc.* **2012**, *43*, 108–115.

[6] Frisch, M. J. et al. Gaussian 09 Revision A.1.

[7] Porezag, D.; Pederson, M. R. *Phys. Rev. B* **1996**, *54*, 7830–7836.

[8] Jmol: An open-source Java viewer for chemical structures in 3D; available at http://www.jmol.org/.

[9] McMahon, B.; Hanson, R. M. *J. Appl. Crystallogr.* **2008**, *41*, 811–814.

[10] Mori, T.; Suma, K.; Sumiyoshi, Y.; Endo, Y. *J. Chem. Phys.* **2011**, *134*, 044319.

[11] J. A. Montgomery, J.; Frisch, M. J.; Ochterski, J. W.; Petersson, G. A. *J. Chem. Phys.* **1999**, *110*, 2822–2827.

[12] J. A. Montgomery, J.; Frisch, M. J.; Ochterski, J. W.; Petersson, G. A. *J. Chem. Phys.* **2000**, *112*, 6532–6542.

[13] Bernard, J.; Seidl, M.; Kohl, I.; Liedl, K. R.; Mayer, E.; Galvez, O.; Grothe, H.; Loerting, T. *Angew. Chem. Int. Ed.* **2011**, *50*, 1939–1943.

[14] Liedl, K. R.; Sekusak, S.; Mayer, E. *J. Am. Chem. Soc.* **1997**, *119*, 3782–3784.

[15] Huber, S. E.; Dalnodar, S.; Kausch, W.; Kimeswenger, S.; Probst, M. *AIP Advances* **2012**, *2*, 032180.

[16] Merrick, J. P.; Moran, D.; Radom, L. *J. Phys. Chem. A* **2007**, *111*, 11683–11700.

[17] Kohl, I.; Winkel, K.; Bauer, M.; Liedl, K. R.; Loerting, T.; Mayer, E. *Angew. Chem. Int. Ed.* **2009**, *48*, 2690–2694.

[18] Hage, W.; Hallbrucker, A.; Mayer, E. *J. Chem. Soc., Faraday Trans.* **1996**, *92*, 3197–3209.

[19] Loerting, T.; Liedl, K. R. *J. Am. Chem. Soc.* **1998**, *120*, 12595–12600.

[20] Hage, W.; Hallbrucker, A.; Mayer, E. *J. Chem. Soc., Faraday Trans.* **1996**, *92*, 3183–3195.

[21] Moore, M. H.; Khanna, R. K. *Spectrochim. Acta, Part A: Mol. Biomol. Spectrosc.* **1991**, *47*, 255–262.

Chapter 4

Liquid Dimethyl Carbonate: A Quantum Chemical and Molecular Dynamics Study

4.1 Introduction

In the last two chapters, we had investigated carbonic acid in its gas and crystalline phases. A compound which is structurally similar to carbonic acid is dimethyl carbonate. It can be seen as being ”derived” from CA with the replacement of the two protons by methyl groups. Unlike CA, dimethyl carbonate is stable both in dry conditions and in the presence of water. Liquid dimethyl carbonate (DMC) is regarded as a green solvent owing to its low volatility, non-flammability, non-toxicity and biodegradability. [1, 2] Despite its wide use as a medium for organic reactions, very few experimental and theoretical studies of DMC have been carried.

Reprinted with permission from “Liquid dimethyl carbonate: a quantum chemical and molecular dynamics study” *J. Phys. Chem. B* **2012**, *116*, 14892-14902. Copyright 2012, American Chemical Society. `http://pubs.acs.org/doi/abs/10.1021/jp309374m`

Spectroscopic studies were carried out to explore the conformational stability of the molecule in gas and liquid phases. They showed that cis-cis conformers are the dominant species among all possible conformers, namely, cis-cis, cis-trans, and (near-trans)-(near-trans). [3–5] Based on IR absorbance data, the enthalpy difference between the cis-cis and cis-trans conformers has been estimated to be 2.60 ± 0.5 kcal/mol. [3, 4] Dielectric studies on liquid DMC at room temperature have discovered the presence of a high dipole moment conformer, the (near-trans)-(near-trans) one. [6] Its gas-phase structure has been determined using electron diffraction.15 The earliest empirical potential based molecular dynamics simulations of the liquid at 80 °C was reported in 1998 and around 68% of molecules were reported to be in the cis-cis conformation at this temperature, which deviates from the value estimated from Boltzmann distribution. [7] Soetens et al. have carried out molecular dynamics simulations using the OPLS and CFF91 derived force field on liquid DMC and their interest was limited to the structure and analyzed using pair correlations functions (PCF). [8] Recently, Gontrani et al. have reported the first X-ray diffraction data of liquid DMC. The structure of the liquid was analyzed by calculating structure factors and pair correlation functions (PCF) and by comparing against OPLS force field based molecular dynamics simulations. [9, 10]

Here, we report a Car-Parrinello molecular dynamics (CPMD) study of liquid DMC. The Kohn-Sham density functional theory protocols are benchmarked against MP2 level quantum chemical calculations for the molecules in gas phase. Liquid state structure is investigated using pair correlation functions and spatial density maps. Conformational equilibrium is compared against both experimental and force field based simulations. This chapter is divided into four sections. The next section details the computational techniques and is followed by results on structure and dynamics analyzed using tools such as pair correlation functions, spatial distribution functions, dipole- dipole correlations, and vibrational power spectrum. The last section summarizes the results.

4.2 Computational details

Three sets of calculations were carried out on dimethyl carbonate. First, gas phase calculations have been performed to obtain the stability and dipole moments of its conformers. Second, classical molecular dynamics simulations were performed to obtain initial configurations for CPMD simulations and also to compare against the CPMD results. Third, using these final geometries, a Car-Parrinello molecular dynamics simulation trajectory of liquid DMC under ambient conditions was generated. In addition, to understand the spatial distribution of molecules with specific conformations, a classical MD simulation of a very large system was also carried out.

The gas phase calculations were performed using the Gaussian09 package for which initial structures were constructed using GaussView. [11] The potential energy of a single molecule was also calculated at MP2/aug-cc-pvdz level of theory as a function of the two dihedrals. Harmonic frequency calculations were also performed at the same level of theory to locate any imaginary modes.

A system consisting of 96 molecules was generated by placing DMC molecules in a cubic box of length 100 Å. Initial coordinates were generated by replicating coordinates of single molecule in three dimensions such that the distance between neighbouring molecules was 9 Å. Three dimensional periodic boundary conditions on a cubic simulation cell were employed. This system was equilibrated in the isothermal-isobaric ensemble (NPT) for 1 ns. The force field was the same as used by Caminiti et al., which belongs to the OPLS framework. [9, 10] Temperature (293 K) and pressure (1 atm) controls were achieved using Nóse-Hoover thermostat and barostat, respectively, with relaxation times of 1 ps each. [12] Nonbonded interactions were calculated using 12-6 Lennard-Jones and Coulombic potentials within a spherical cutoff of 11.5 Å. The long-range part of the electrostatic interaction was calculated using the particle-particle particle mesh (PPPM) solver with a precision of 10^{-5}. All the C-H bonds were constrained to equilibrium values using the SHAKE algorithm. A time step of 1 fs was used. The average density of the simulated system was found to be 1.076 g/cm^3, very close to the experimental value of 1.0687 g/cm^3, resulting in a mean box length of 23.717 Å. The final coordinates of this run were scaled with the mean box length. This set was used as the initial coordinates for a constant NVT MD trajectory for a duration of 10 ns. The final coordinates from this run were used as a starting configuration for the Car-Parrinello molecular dynamics simulation. Classical MD simulations were carried out using LAMMPS. [13]

CPMD simulations were carried out using the CPMD-3.13.2 package. [14] A fictitious electron mass of 400 a.u. and a time step of 4 a.u. were employed. This combination has earlier been employed successfully by others to produce stable trajectories. [15, 16] In our CPMD simulation, the fictitious electron kinetic energy exhibited no drift in time, implying the adiabatic separation between nuclear and electronic degrees of freedom. The ion temperature was maintained at 293 K using the Nóse- Hoover chain thermostat. [17] As mentioned before, the system contained 96 DMC molecules (i.e., 1152 atoms) in a cubic box of edge length 23.7 Å. The wave function of the valence electrons were expanded in a plane wave basis set with an energy cutoff of 85 Ry and a density cutoff of 340 Ry. The effect of all the core electrons and of the nucleus on these valence electrons was considered by using norm conserving Troullier-Martins pseudopotentials. [18] The cutoff radii of (s, p) orbitals used in pseudopotentials are (1.23, 1.23), (1.12, 1.12), (0.5, 0.38) (in a.u.) respectively for C, O and H elements. The total number of valence electrons was 3456. The Perdew, Burke, and Enzerhof (PBE) exchange-correlation functional was employed. [19] The effect of van der Waals interactions (vdW) was considered through empirically determined dispersive interaction terms, the parameters of which were

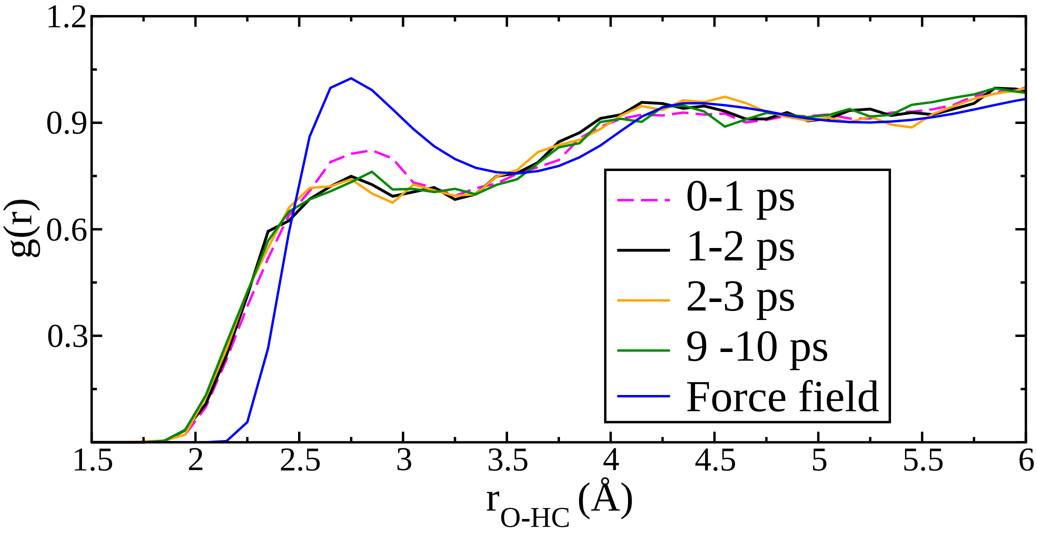

Figure 4.1: Intermolecular pair correlation functions (g(r)) between carbonyl oxygen and methyl hydrogen calculated in different windows of the CPMD trajectory, i.e., between 0-1, 1-2, 2-3 and 9-10 ps. These functions are compared against that obtained from the force field based simulation (FFMD). The g(r) calculated from CPMD evolves from that for the FFMD simulation, to a time-independent behaviour within a couple of picoseconds.

taken from Williams and Malhotra. [20] Such calculations henceforth will be referred to as PBE+vdW in the rest of this chapter. Note that some of these parameters were validated by us in an earlier CPMD simulation study of supercritical carbon dioxide. [21] All hydrogens were replaced by deuterium so as to be able to treat the dynamics classically. The system was equilibrated for 3 ps followed by the generation of an analysis trajectory of 10 ps. Coordinates were dumped at every time step. Unless specified, pair correlation functions were calculated using a bin width of 0.1 Å.

The trajectory in CPMD simulations is likely to explore only local structural rearrangements in the liquid, relative to the initial configuration generated from the initial FFMD simulation. A significant relaxation of the first coordination shell of a given molecule, even within 1 ps of initiating the CPMD run is observed. In Figure 4.1, we compare the pair correlation function between atom types O and HC, obtained over several time windows in the CPMD run and that obtained from the FFMD simulation. The formation of an intermolecular hydrogen bond can be examined through this specific pair correlation function. A significant change in this function calculated within 1 ps of the initiation of the CPMD run, relative to that obtained from FFMD is seen. The functions calculated beyond 2-3 ps of starting the CPMD trajectory are stationary. Thus the CPMD run length, however short, appears sufficient to probe the first neighbour structural relaxations on the PBE+vdW surface.

Dipole moments were calculated using maximally localized Wannier functions (MLWFs). [22] The dipole moments of individual molecules were calculated using the formula,

$$\mu_i = \sum_i e_i * R(i) - 2\sum_j W(j) \tag{4.1}$$

where R(i) and e_i are the position and valency of atom i, respectively, and W(j) is the position of Wannier center. A total of 20 equally spaced configurations from the analysis trajectory were selected for the calculation of the molecular dipole moments. Vibrational density of states in the liquid was calculated by taking the Fourier transform of velocity autocorrelation function.

The systems were visualized using Gaussview, [11] Jmol, [23, 24] and VMD. [25]

4.3 Results and discussion

4.3.1 Gas-phase calculations

Monomers. The molecular geometry of DMC and atom indices are shown in Figure 4.2. Initial geometries of DMC were obtained by fixing the values of the two dihedrals ϕ_1 and ϕ_2, either at 0° or 180°, and varying the other. Geometry optimization was carried out at fixed dihedral angle values at MP2 level of theory

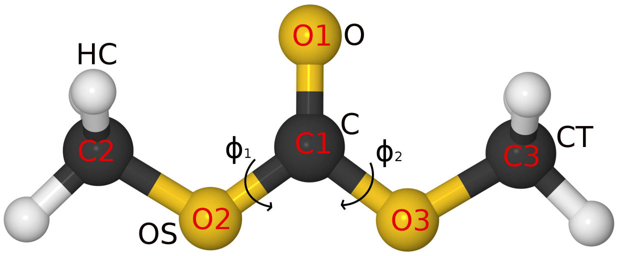

Figure 4.2: Cis-cis conformer of dimethyl carbonate.

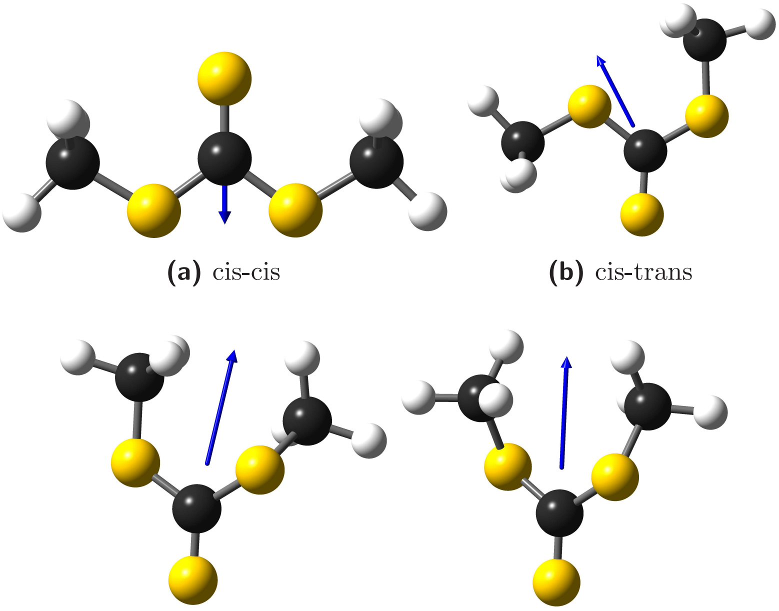

(a) cis-cis **(b)** cis-trans

(c) trans-near-trans **(d)** near-trans-near-trans

Figure 4.3: Conformers of dimethyl carbonate. Dipole moment vector is shown in blue colour. Colour code: C, Black; O, Yellow; H, white.

Table 4.1: Energy (kcal/mol) of cis-trans conformer compared to cis-cis conformer calculated at different levels of theory.

Method	Energy difference [kcal/mol]
HF/6-31(d)	3.75
B3LYP/6-311(2d,d,p)	2.90
MP2/6-311(2d,d,p)	3.50
MP2/aug-cc-pVDZ	3.21
MP2/aug-cc-pVQZ	3.17
OPLS	2.58
PBE/PW	2.72
PBE+vdW/PW	2.46

with different basis sets. Here, ϕ_1 is the torsional angle formed by the two planes, O1-C1-O2 and C1-O2-C2, while ϕ_2 is that formed by O1-C1-O3 and C1-O3-C3 planes. Three stable conformers are located on the potential energy surface. These are cis-cis, cis-trans, and trans-(near-trans). Their geometries and an additional conformer are displayed in Figure 4.3. The energy profile as a function of the torsional angles is shown in Figure 4.4. In the trans-(near-trans) conformer (ϕ_1=180°, ϕ_2=115°), one methyl group is present in the plane of the molecule, while the other methyl group is away from the plane. The cis-cis conformer in which both the dihedral angles are zero is the most stable. Compared to this conformer, the cis-trans and the trans-(near-trans) conformers are higher in energy by 3.17 and 17.29 kcal/mol, respectively. The relative energy of the cis-trans conformer with respect to the most stable conformer, that is, cis-cis, calculated through different methods is shown in Table 4.1. The energy barrier between the cis-cis and cis-trans conformer is 10.10 kcal/mol. The local stabilization of the trans-(near-trans) conformer arises from the electrostatic interaction between the hydrogen atom of the methyl group and the carbonyl oxygen.

The rather large energy difference between the cis-cis and the cis-trans conformers makes the latter quite unfavorable. Occurrence of the trans-(near-trans)

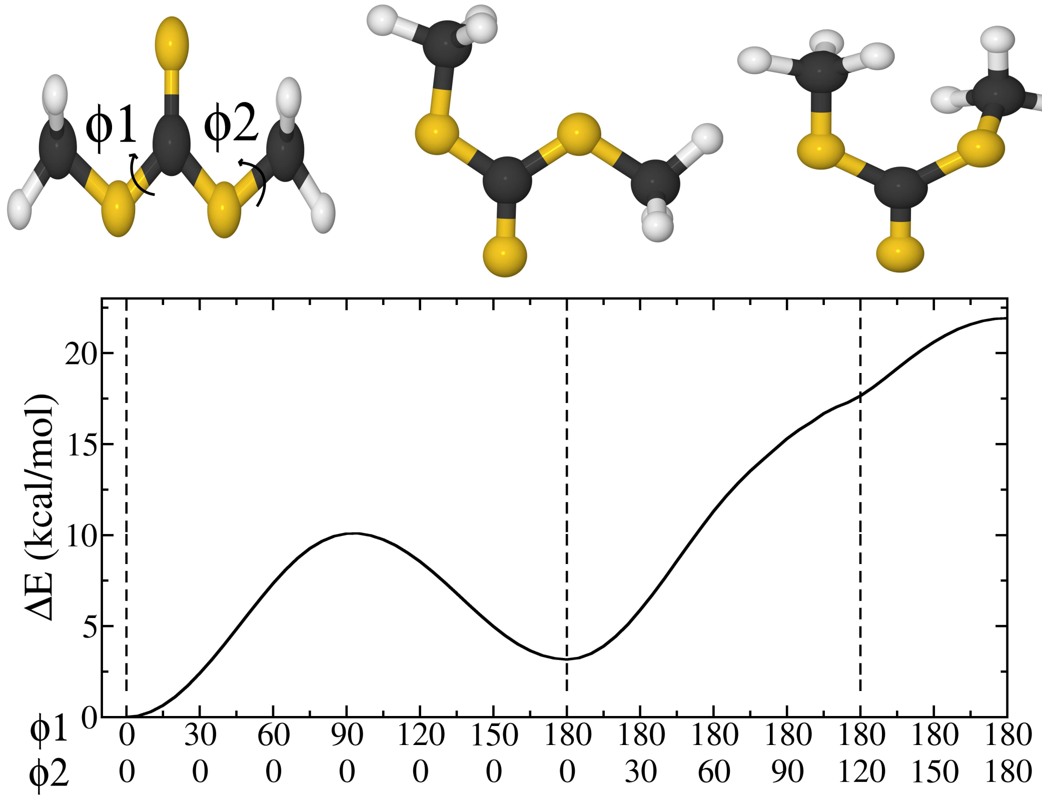

Figure 4.4: Energy profile of dimethyl carbonate (bottom) as a function of two dihedral angles, ϕ_1 and ϕ_2 calculated at MP2/aug-cc-pVDZ level of theory. The vertical dotted lines show the positions of the three minima. Corresponding structures are also shown (top).

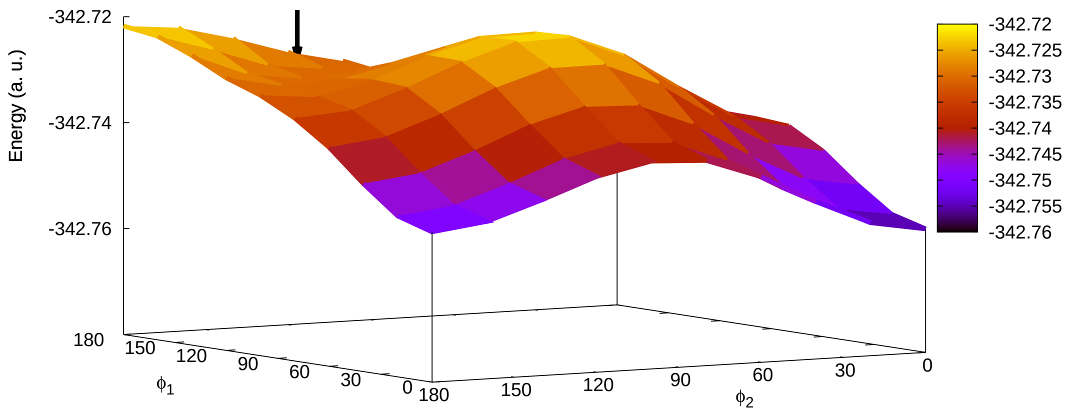

Figure 4.5: Potential energy of dimethyl carbonate as a function of two dihedrals, ϕ_1 and ϕ_2. The position of the (near-trans)-(near-trans) minimum is indicated by an arrow.

conformer is even less likely. To search for any other stable conformer of DMC, a 2D potential energy surface was generated by performing geometry optimization of modelled structures. These structures were obtained by varying the two dihedrals, ϕ_1 and ϕ_2 in steps of 10° each. In this manner, a total of 360 geometries were obtained and all of them were optimized by constraining the values of the two dihedrals. Figure 4.4 shows the 2D potential energy surface. In addition to the above three minima, a new minimum is found corresponding to the dihedrals, ϕ_1=140.8° and ϕ_2=140.8°. The position of this new minimum is shown by an arrow in Figure 4.5 and is named as (near-trans)-(near-trans) conformer. It is higher in energy by 16.06 kcal/mol compared to the cis-cis conformer, but is more stable than the trans-(near-trans) conformer by 1.23 kcal/mol. Hessian-based harmonic frequency calculations of all the above conformers exhibit no imaginary frequency confirming that these are minima on the potential energy surface. Frequency calculation on the trans-trans conformer (ϕ_1=180°, ϕ_2=180°) shows one imaginary frequency indicating that it is unstable.

Knowledge of the dipole moment of different conformers of DMC can help us to better understand the intermolecular structure in the liquid state. Experimental values for the dipole moments of cis-cis and cis-trans conformers in the gas phase have been reported. [5, 6, 26] However, quantitative agreement between values reported by several authors is rather poor. Values reported for the cis-cis conformer are in the range of 0.3-0.8 D and for the cis-trans conformer, they are between 1.7 and 3.1 D. [5, 6, 26, 27] The dipole moment values of all these conformers in gas phase at MP2/aug-ccpVDZ level of theory have been calculated. These are 0.32, 3.98, 5.78, and 5.79 D for the cis-cis, cis-trans, trans-(near-trans), and (near-trans)-(near-trans), respectively. Dipole moments of the cis-cis and cis-trans conformer calculated at MP2/aug-ccpVQZ level of theory were 0.36 and 3.91 D, respectively, which are very close to those obtained with the double-ζ basis set.

Dipole moments were also calculated for the cis-cis and cis-trans monomers using the OPLS force field and values of 0.38 and 4.40 D, respectively, were obtained. Using the PBE functional in a plane wave (DFT/PW) basis set, dipole moments of magnitude 0.35 and 3.6 D are obtained for the cis-cis and cis-trans conformers, respectively. The PBE values are quite comparable to those obtained from MP2 calculations. Figure 4.6 shows dipole moments of dimethyl carbonate molecule as a function of the two dihedrals, ϕ_1 and ϕ_2, obtained at MP2/aug-cc-pVDZ level of theory. If two dihedrals are greater than 150°, they possess larger dipole moments, and if they are less than 30°, they possess relatively smaller values. These regions are shown in dark blue and yellow colours, respectively, in Figure 4.6. The high dipole moment conformers are less likely to exist in the liquid as they are unstable. Figure 4.3 shows the direction of dipole moment for the four stable conformers. In the case of cis-cis and near-trans-near-trans conformers, the dipole moment vector is oriented parallel to the O1-C1 bond, while in the other two conformers, the moment

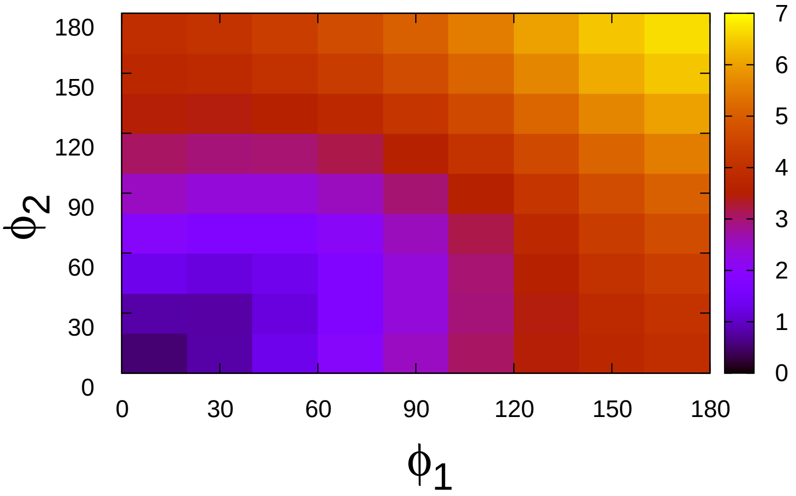

Figure 4.6: Dipole moment (in Debye) surface of dimethyl carbonate as a function of two dihedrals, ϕ_1 and ϕ_2. Colour scale is also shown.

is oriented at a nonzero angle with respect to this vector.

Dimers. An examination of stable dimer configurations in the gas phase can help in a better understanding of the intermolecular structure in the liquid state. Using different combinations of cis-cis and cis-trans conformers, geometry optimization in the gas phase yielded three stable dimers, (cis- cis)-(cis-cis) (denoted as CC-CC), (cis-cis)-(cis-trans) (denoted as CC-CT), and (cis-trans)-(cis-trans) (denoted as CT-CT), as shown in Figure 4.7. Two hydrogen bonds are seen: one between the carbonyl oxygen of one molecule and the hydrogen (O$\cdots$HC) of the other molecule and vice versa. The average H-bond length is 2.44 Å and H-bond angle is 131.7°, implying the formation of a weak hydrogen bond between the DMC molecules. Table 4.2 shows the relative energy and the binding energy of the three dimers calculated at MP2/ aug-cc-pVDZ and PBE+vdW/PW levels of theory. Relative energy is the energy difference between a specific dimer configuration and the CC-CC one. Binding energy is the energy of stabilization of a dimer with respect to its isolated monomers. In the case of the MP2 calculation, which employed a

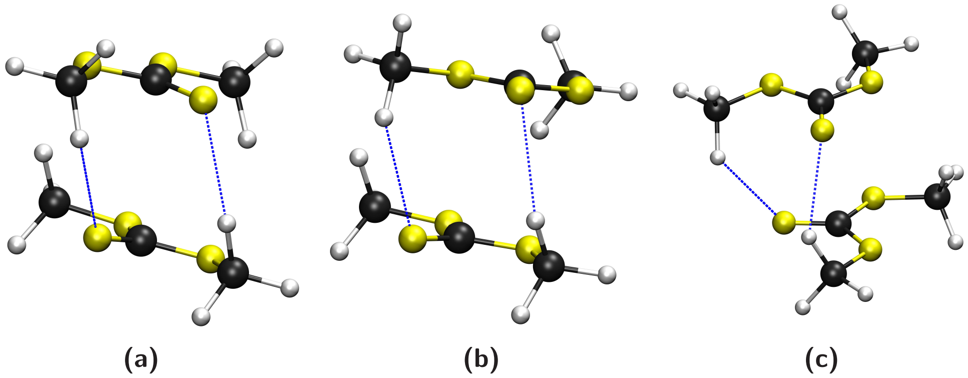
(a) (b) (c)

Figure 4.7: (a) (cis-cis)-(cis-cis), (b) (cis-cis)-(cis-trans) and (c) (cis-trans)-(cis-trans) dimers. Blue dotted lines are hydrogen bonds formed between atom types O and HC.

localized basis set, these energies were corrected for the basis set superposition error (BSSE) using the counterpoise method. Among the three dimers, CC-CC is the most stable, and the CC-CT and CT-CT dimers are less stable than that by 3.83 and 5.92 kcal/mol, respectively.

The binding energy of the CC-CC dimer is calculated to be -6.04 and -4.61 kcal/mol at MP2 and PBE+vdW levels of theory. Both CT-CT and CC-CC dimers have comparable binding energies and this value is greater than that of the CC-CT dimer, that is, dimers of like conformers are more stable than a dimer formed out of unlike conformers. The result is similar for data calculated at PBE+vdW/PW level. Given the fact that the CT monomer is less stable than the CC one by 3.2 kcal/mol, the relative energy difference of 5.92 kcal/mol between the CC-CC and CT-CT dimers is reasonable. Hydrogen bond lengths and angles calculated at OPLS force field, MP2/aug-cc-pVDZ and PBE +vdW/PW levels of theory are tabulated in Table 4.3. However, the CC-CT dimer possesses one H-bond, which is more linear than the ones present in CC-CC or CT-CT dimers. For comparison, values obtained with PBE/PW (i.e., without the empirical vdW correction terms) are also tabulated in Tables 4.2 and 4.3. Hydrogen bond lengths and angles obtained with PBE+vdW/PW are much closer to the MP2 results than those from PBE/PW.

Table 4.2: Binding energy and relative energy (kcal/mol) of (cis-cis)-(cis-cis) (CC-CC), (cis-cis)-(cis-trans) (CC-CT) and (cis-trans)-(cis-trans) (CT-CT) dimers calculated at OPLS force field, MP2/aug-cc-pVDZ and PBE+vdW/PW levels of theory. [a]Values are with respect to CC-CC dimer.

	CC-CC	CC-CT	CT-CT
Binding energy :			
OPLS	-4.30	-4.26	-4.66
MP2/aug-cc-pVDZ	-6.04	-5.04	-6.15
PBE/PW	-2.72	-5.17	-3.59
PBE+vdW/PW	-4.61	-4.02	-5.27
Relative energy[a] :			
OPLS	0	2.25	4.06
MP2/aug-cc-pVDZ	0	3.83	5.92
PBE/PW	0	3.09	4.60
PBE+vdW/PW	0	3.05	4.27

Further, the interaction energy of two molecules both in the (cis-cis) conformation as a function of distance between them was calculated using all these methods. The same is provided in Figure 4.8. It further validates the usage of empirical vdW corrections to the PBE functional in our simulations.

4.3.2 Liquid structure: molecular dynamics

Pair Correlation Functions. Figure 4.9 shows the intermolecular pair correlation function (PCF) between different atoms of DMC. Figure 4.6 shows the PCF between carbonyl carbon atoms belonging to different molecules. While the first peak is present at around 6 Å, a clear shoulder is also visible at around 4.1-4.25 Å in the functions obtained from both CPMD and FFMD. The origin of these two features will be examined later. Compared to the FFMD liquid, molecules in the CPMD liquid are marginally closer to each other, as seen in the shift of the first peak to lower distances. At the position of the first minimum in the PCF, the coordination numbers obtained from CPMD and FFMD simulations are 14.3 (at 7.85 Å) and 12.7 (at 7.5 Å), respectively. The g(r) between atom types CT-CT and OS-OS

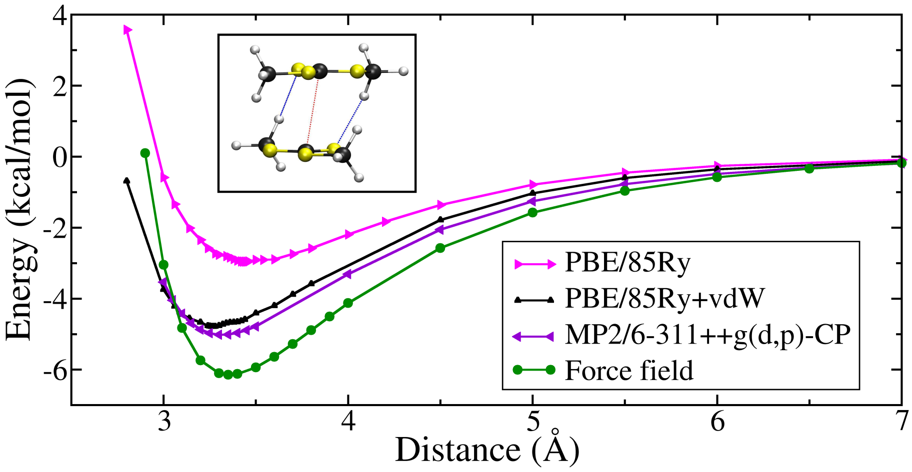

Figure 4.8: Energy as a function of distance between two molecules both in the cis-cis conformation, calculated at OPLS force field, MP2/aug-cc-pVDZ and PBE+vdW/PW levels of theory.

Table 4.3: Hydrogen bond lengths (in Å) and angles (in °) formed between (cis-cis)-(cis-cis) (CC-CC), (cis-cis)-(cis-trans) (CC-CT) and (cis-trans)-(cis-trans) (CT-CT) dimers calculated at OPLS force field, MP2/aug-cc-pVDZ and PBE+vdW/PW levels of theory.

	H-bond-I	H-bond-II
OPLS :		
CC-CC	2.45, 128.6	2.45, 128.6
CC-CT	2.45, 144.8	2.47, 124.5
CT-CT	2.42, 128.6	2.42, 128.6
MP2/aug-cc-pVDZ :		
CC-CC	2.45, 129.6	2.45, 129.7
CC-CT	2.44, 145.9	2.47, 125.6
CT-CT	2.42, 129.6	2.42, 129.6
PBE/PW :		
CC-CC	2.65, 136.6	2.60, 137.1
CC-CT	2.67,135.8	2.61, 149.6
CT-CT	2.77, 127.6	2.57, 137.6
PBE+vdW/PW :		
CC-CC	2.50, 135.0	2.48, 135.7
CC-CT	2.54, 132.4	2.54, 151.6
CT-CT	2.56, 132.5	2.60, 129.6

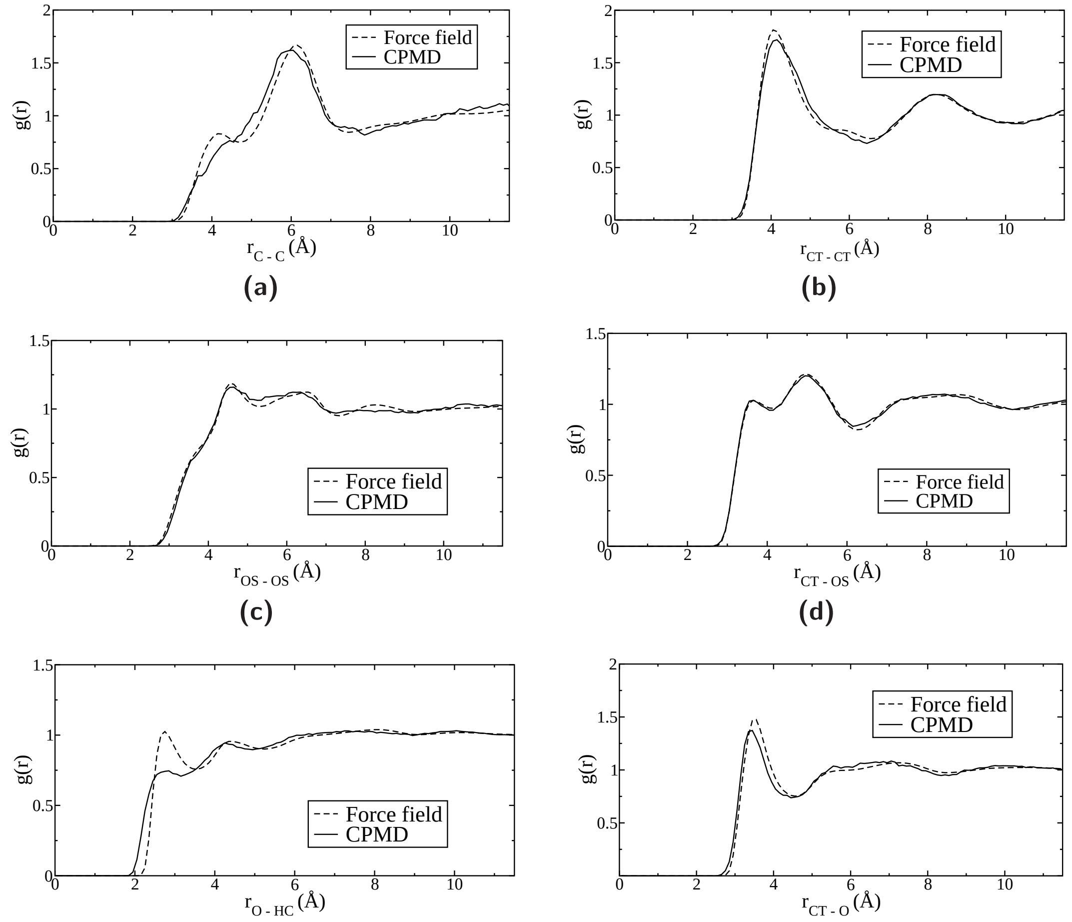

Figure 4.9: Intermolecular pair correlation functions between different pairs of atoms in liquid DMC.

are shown in Figure 4.9b,c. Peak positions and widths are comparable in the two cases, CPMD and FFMD. The first maximum is marginally less intense and more broadened in CPMD compared to that in FFMD. The position of the first minimum is shifted to shorter distances.

Figure 4.9d shows the g(r) between atom types CT and OS. It exhibits two peaks within a distance of 6 Å which are separated by less than 2 Å. These two peaks are due to the two OS type oxygen atoms present within a single molecule. The g(r) between atom types O and HC is shown in Figure 4.9e. Significant differences are observed between the CPMD and FFMD results. In CPMD, the feature begins at 1.77 Å compared to a value of 2.05 Å obtained from the FFMD simulations. The shift in the peak to lower distances within CPMD signifies a stronger binding between hydrogen atoms of the methyl and the carbonyl oxygens (C-H$\cdots$O hydrogen bonding). The first peak (at 2.85 Å) is less intense and broadened in CPMD compared to FFMD simulations. The first minimum of the CPMD PCF is at 3.15 Å and the corresponding coordination number is 2.85. Such large H-bond distances indicate that the hydrogen bond can be characterized as a weak one. Experimentally, these hydrogen bonds can be detected from IR spectroscopy. [28–31]

A discussion on the conformational dependence of the O-HC g(r) is presented later. The pair correlation function between atom types CT and O is shown in Figure 4.9f. The first peak (at 3.40 Å) is less intense and its position is shifted to left compared with that of FFMD, a behavior which is similar to that observed in other g(r)s. The intramolecular g(r) between atom types CT and OS calculated from CPMD and FFMD simulations is shown in Figure 4.10. The intense peak at around 3.5 Å is due to molecules in the cis-cis conformation and that, around 2.6 Å, is due to the cis-trans conformer. The ratio of area under these two features is the ratio of the population of cis-cis to cis-trans conformers. These values are 94.5:5.5 and 97.2:2.8 in FFMD and CPMD simulations, respectively.

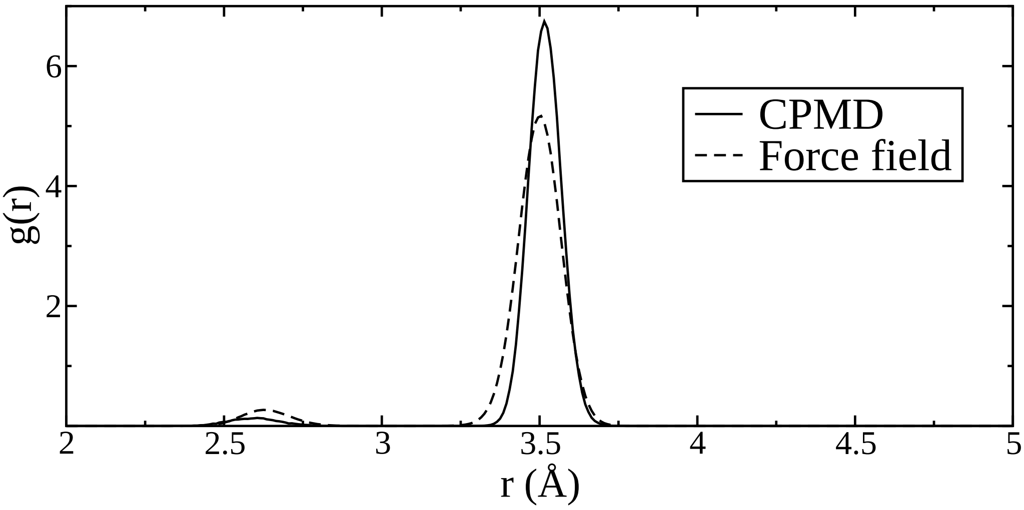

Figure 4.10: Intramolecular pair correlation function between atom types CT and OS. A bin width of 0.01 Åis used.

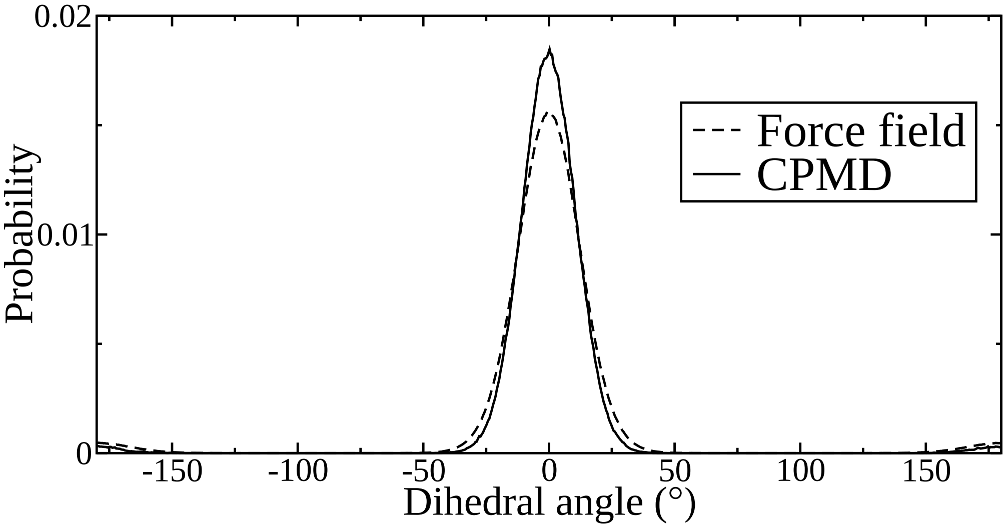

Figure 4.11: Probability distribution of dihedral angles, C2-O2-C1-O1 or C3-O3-C1-O1.

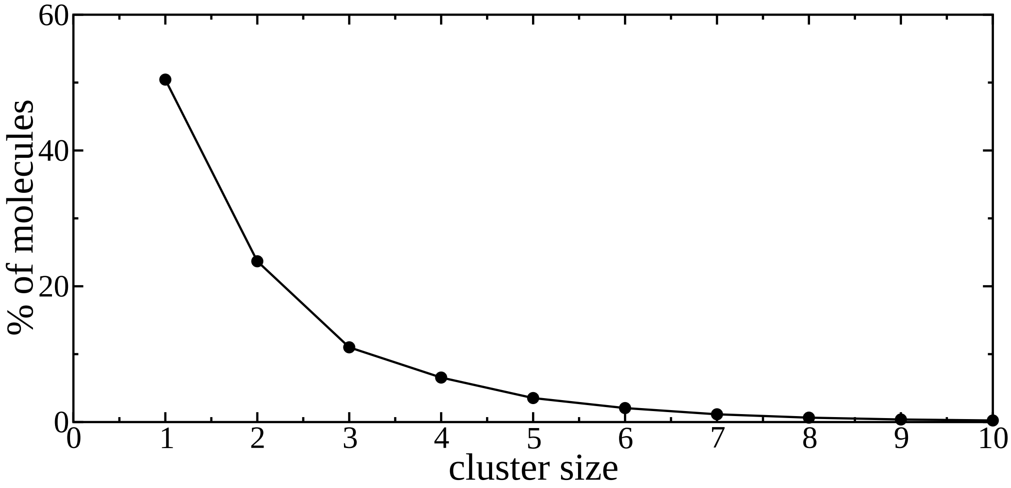

Figure 4.12: Probability distribution of the size of cluster consisting of cis-trans conformers in liquid DMC.

Dihedral Distributions and Clustering. Figure 4.11 shows the probability distribution of dihedral angles for dimethyl carbonate in which both the dihedrals, C2-O2-C1-O1 and C3-O3-C1-O1 contribute. The ratio of cis-cis to cis-trans from CPMD is estimated to be 97.9:2.1, which is close to the experimental value. Two different ratios have been reported in the literature. Katon and Cohen have reported the ratio to be 99:1, whereas Chia et al. reported it to be 98:2. [3, 4, 26] However, the ratio obtained in CPMD is larger than the estimate from FFMD simulations (93.6% in favor of cis-cis). The difference between the results obtained from CPMD and FFMD is unlikely to be of any significance due to the short trajectory length of the former. The duration of the CPMD simulation is much shorter than the time scales required for conformational transitions. The latter can be estimated from barrier heights to be in the order of nanoseconds. It is beyond the scope of this work to investigate the difference (if any) between the conformer populations, due to the prohibitive cost of the CPMD simulations.

The concentration of cis-trans conformers is dilute. However, the dipole moment of the cis-trans conformer is higher than that of the cis-cis conformer. Thus, it is possible that they could cluster together within the sea of cis-cis molecules. To examine this possibility, a large system containing 2532 molecules (27 times the smaller system) was simulated using FFMD. This system was equilibrated for 2 ns, and subsequently, a 8 ns trajectory was generated for analysis.

The clustering analyses was conducted as follows: If the distance between any two atoms of different CT-CT conformers is less than 3 Å, then it is considered as a cluster of size 2, and if one more molecule follows the same criteria with any of the above, then such a cluster is considered to be of size 3 and so on. During the cluster calculation, we verified that each CT-CT conformer belongs to a unique cluster. Figure 4.12 shows the percentage of cis-trans molecules present in clusters of different sizes. Half of the cis-trans molecules are clustered (i.e., they exist in dimers or higher oligomers) and the remaining molecules are isolated, that is, they are surrounded purely by cis-cis conformers. A snapshot of these clusters is shown in Figure 4.13. The observation of clustering of molecules of cis-trans conformation is consistent with the binding energy of gas phase dimers discussed in Table 4.2. It was seen earlier that dimers of like conformation are more stable than the one where the molecules are in different conformations. Naturally, this preference for dimerization of like conformers will lead to the formation of cis-trans clusters in the liquid phase. The clusters cannot grow to large sizes due to entropic effects.

To summarize, relative to FFMD simulations, the CPMD simulation predicts marginally closer intermolecular contacts. In particular, the formation of a weak intermolecular hydrogen bond between the carbonyl oxygen and the methyl hydrogen is observed in CPMD simulations. Clustering of cis-trans molecules is observed in simulations of a large system studied using FFMD.

4.3.3 Spatial distribution functions

Spatial distribution functions (SDF) show the density distribution of atoms in three-dimensional space. Figure 4.14 shows SDF maps around the carbonyl carbon and

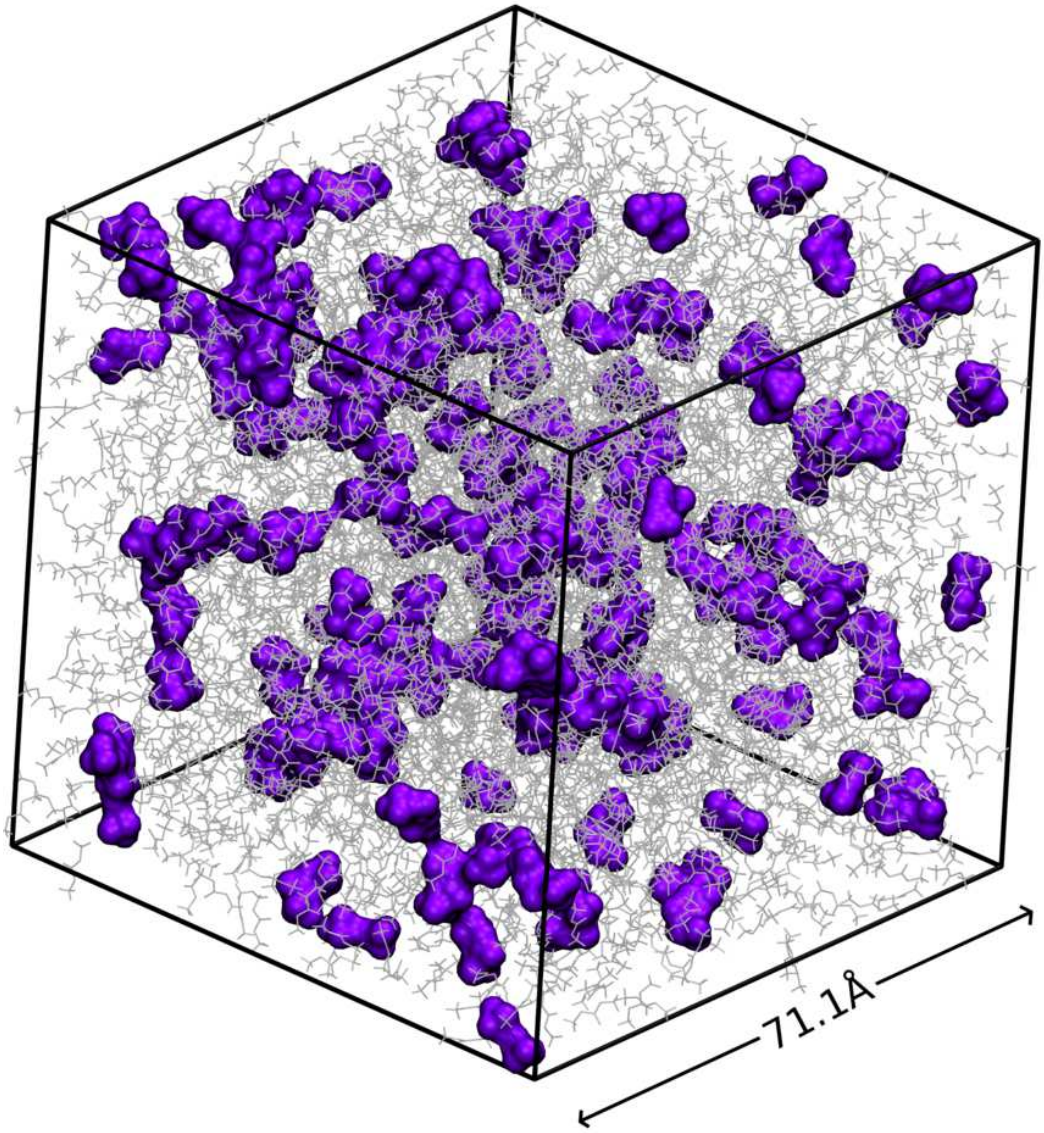

Figure 4.13: Snapshot of liquid dimethyl carbonate showing clustered cis-trans molecules along with cis-cis molecules. Cis-trans and cis-cis molecules are coloured in violet and grey, respectively.

the carbonyl oxygen in two orientations. In one of them, the carbonyl vector is perpendicular to the plane of the paper and is directed toward the reader and in the other, it is parallel to the plane of the paper and is directed upward. It is to be noted that, in this calculation, we assume the central molecule to be in cis-cis conformation. Because the percentage of other conformers is much smaller, the results are unlikely to be much affected by this assumption.

An examination of the isosurfaces of spatial distribution functions reveals the origin of the various features observed in the pair correlation functions. Molecules proximal to the methyl group are responsible for the intense peak at around 6 Å in the C-C g(r) shown in Figure 4.9a. The shoulder at 4 Å in the same g(r) is due to molecules lying in a plane parallel to the equatorial plane of the molecule. In CPMD, the distribution of molecules around the center is less ordered compared to that in FFMD as seen in Figure 4.14a-d. This is reflected in the C-C g(r), which exhibits just a shoulder at around 4 Å distance in CPMD compared to the intense peak at the same distance seen in FFMD simulations (Figure 4.9a).

The SDF between carbonyl oxygen around the dimethyl carbonate molecule is shown in Figure 4.14c-h. Because of electrostatic attraction between the carbonyl oxygen and hydrogen atoms, the former are likely to be surrounded by the methyl groups. Similar to the SDF between carbon and the geometric center of DMC molecule, it too shows more ordered structure in the first coordinations shell in FFMD compared to CPMD.

To find the distance dependence of orientational preferences of dimethyl carbonate molecules around a reference molecule, the angle between two carbonyl vectors of two adjacent DMC molecules is calculated. Figure 4.15a shows the probability distribution of this angle between neighbours which are located within a certain cutoff distance. At the first coordination minimum (7.8 Å), all orientations are possible as shown in Figure 4.15a. At shorter distances, the distribution reveals a

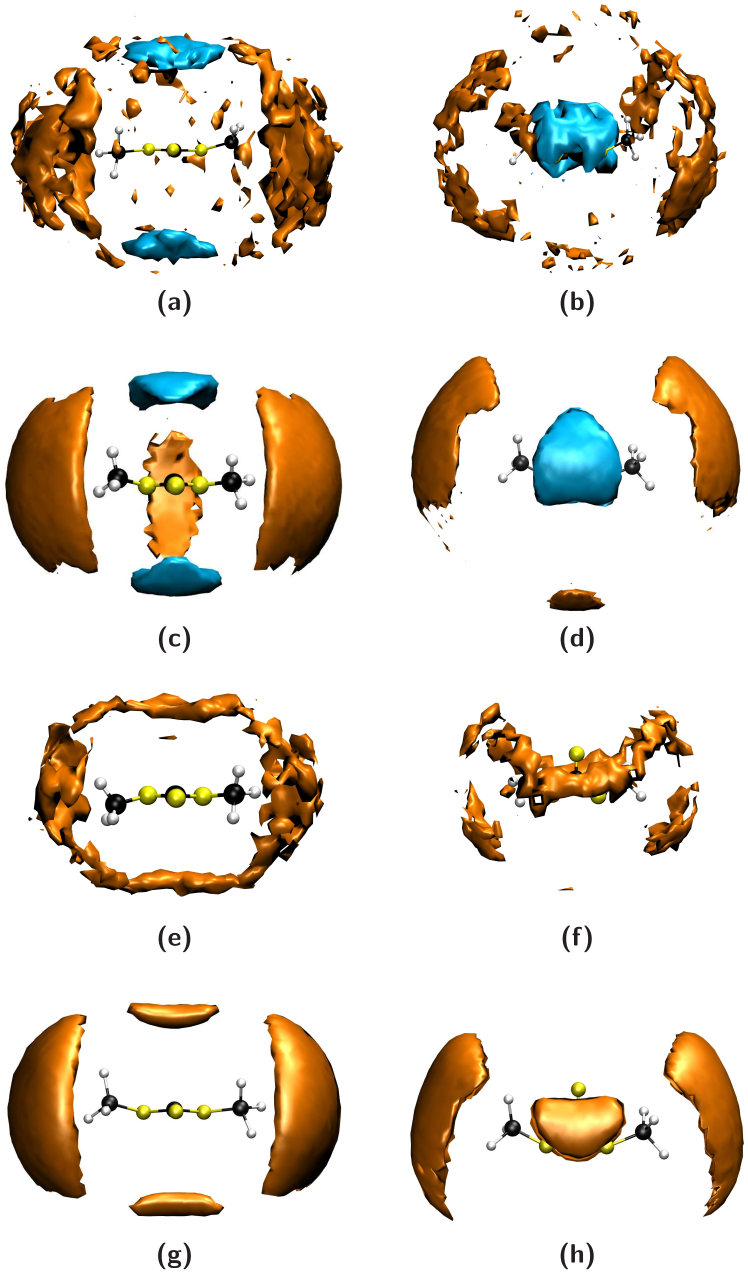

Figure 4.14: Spatial distribution functions of carbonyl carbon (a-d) and carbonyl oxygen atoms (e-h) around the center of mass of dimethyl carbonate are shown at an isosurface value of 0.0165 Å^{-3}. (a), (b), (e) and (f) are obtained from the CPMD run while (c), (d), (g) and (h) are calculated from the force field based simulation. In each simulation, two views, one in which the carbonyl group is pointing towards the reader and in another, it is in the plane of the paper and pointing upwards are shown. Colour code: C-black; O-yellow; H-grey.

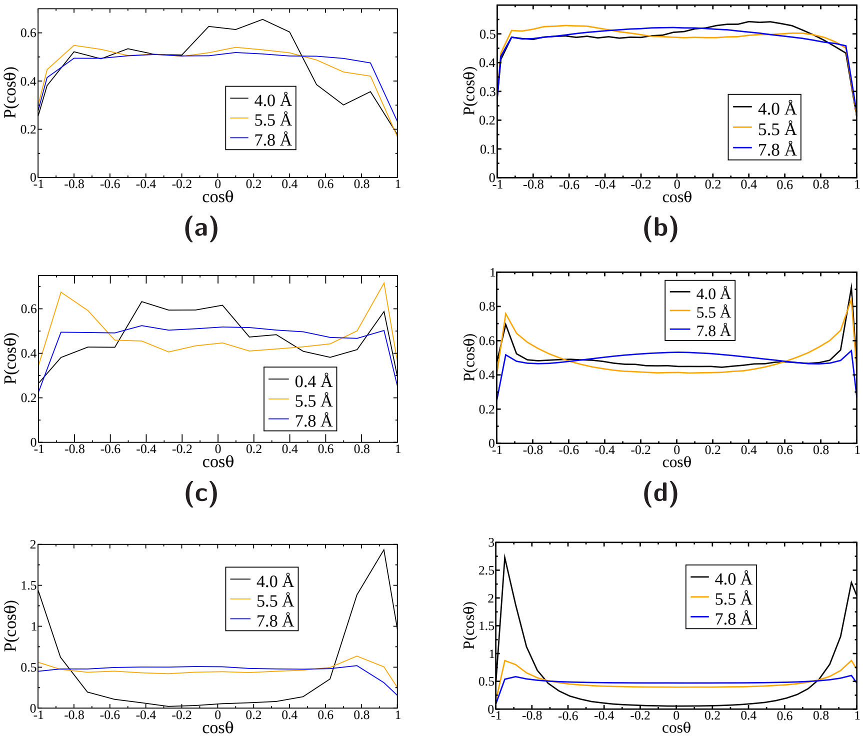

(a) (b) (c) (d) (e) (f)

Figure 4.15: Probability distribution of angle between intermolecular (a) & (b): C-O vectors, (c) & (d) CT-CT vectors and (e) & (f): normal vectors to the plane of dimethyl carbonate molecules, obtained with both Kohn-Sham density functional theory (left) and force field (right) based molecular dynamics simulations. Marked values in legends are distances between center of mass of neighbouring molecules.

marginal orientational preference, which is absent in FFMD simulations. Further, the angle between two CT-CT vectors and also that between normals to the plane of adjacent DMC molecules are calculated. The distribution of these angles are shown in Figure 4.15c-f. The distribution between normal vectors for molecules lying very close to each other show preference toward parallel or antiparallel alignment of planes with almost no preference for perpendicular alignment. One can conclude that close lying DMC molecules are oriented parallel or antiparallel to each other and with increasing distance, all orientations become equally probable. Our analysis confirms the recent X-ray scattering and MD simulation data of Caminiti et al. [10] The CPMD data show a small preference for close lying molecules to lie with their CT-CT vectors (or C-O vectors) perpendicular to each other.

4.3.4 Dipole analysis

Maximally localized Wannier functions have been employed successfully in numerous applications to calculate effective Born charges, the nature of chemical bonding, bond ionicity, electric polarization, and dipole moments. [22, 32–34] The same procedure to obtain the molecular dipole moments is adopted here. When the position of Wannier centers is used for configurations of the liquid, the dipole moment of individual molecules in the liquid state were calculated using eq 4.1.

Figure 4.16 shows the distribution of such molecular dipole moments. Two features, an intense peak centered at around 1.0 D and another, beyond 4.0 D, are observed. The distribution obtained from the force field is shifted to slightly lower values relative to that from CPMD simulations. To find out whether this large dipole moment is due to cis-trans conformers or (near-cis)-(near-trans) conformers, two dihedral angles of each DMC molecule are calculated. If the magnitude of two dihedrals is greater than 100° or less than -100°, they are considered as (near-cis)-(near-trans) or trans-(near-trans) conformers. This value averaged over the entire

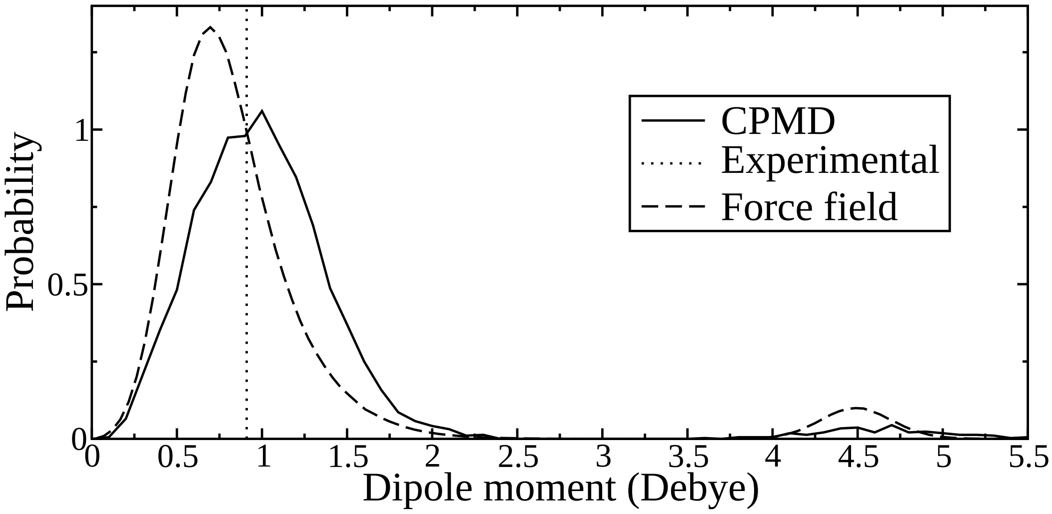

Figure 4.16: Probability distribution of molecular dipole moment in liquid dimethyl carbonate. The experimental value (0.91 D) is shown as dotted line. [6]

trajectory shows that only an insignificant number (0.1%) of molecules are present in that conformational state in the liquid at room temperature. Thus, the peak in the distribution beyond 4.0 D is due to cis-trans conformers alone. The cis-cis (cis-trans) conformer possesses a mean dipole moment of 1.0 D (4.5 D) in the liquid state, which is much higher than its value of 0.35 D (3.6 D) in gas phase. This indicates considerable polarization in the condensed phase. The mean dipole moments of these distributions are 1.01 and 1.05 D obtained using force field and CPMD, respectively. These are comparable to the value determined using dielectric measurements, which is 0.91 D. [6]

4.3.5 Conformational dependence of O-HC g(r)

As discussed earlier, the dipole moment of the cis-trans conformer is nearly five times larger than the cis-cis one. It was also noticed that such cis-trans molecules could be clustered in the solvent. Does the higher dipole moment of this conformer lead to differences in the intermolecular structure in its neighbourhood? To probe this matter further, we calculated the atom-atom pair correlation functions for a

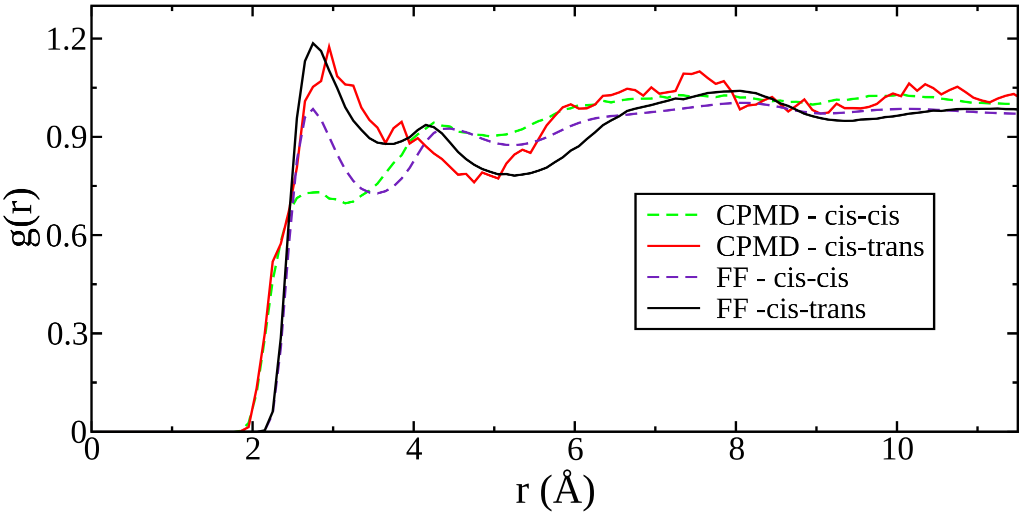

Figure 4.17: Intermolecular pair correlation functions between atom types O and HC obtained from both force field based molecular dynamics (FF) and Car-Parrinello molecular dynamics (CPMD) simulations. The legend also displays the conformational state of the central molecule.

central molecule being either in the cis-cis or in the cis-trans conformation. While all other g(r)s for these two categories matched, that between O and HC showed significant influence of the conformation of the central molecule. Thus, we exhibit them in Figure 4.17. Despite the existence of quantitative differences between the PCFs obtained from force field or CPMD, a common trend is observed; the O-HC PCF for the case of the oxygen atom belonging to a cis-trans molecule shows a much taller first peak than around a cis-cis one. This observation tallies with the H-bond distances shown in Table 4.3. Although the concentration of cis-trans conformers in the liquid is very small, molecular clustering and the stronger hydrogen bonding may likely play a role in the behavior of DMC as a chemical reaction medium.

4.3.6 Vibrational spectrum

To our knowledge, the experimental IR or Raman spectrum of deuterated liquid DMC has not been reported. Thus, we compare our results against estimates obtained on the deuterated liquid from experimental data through mass scaling.

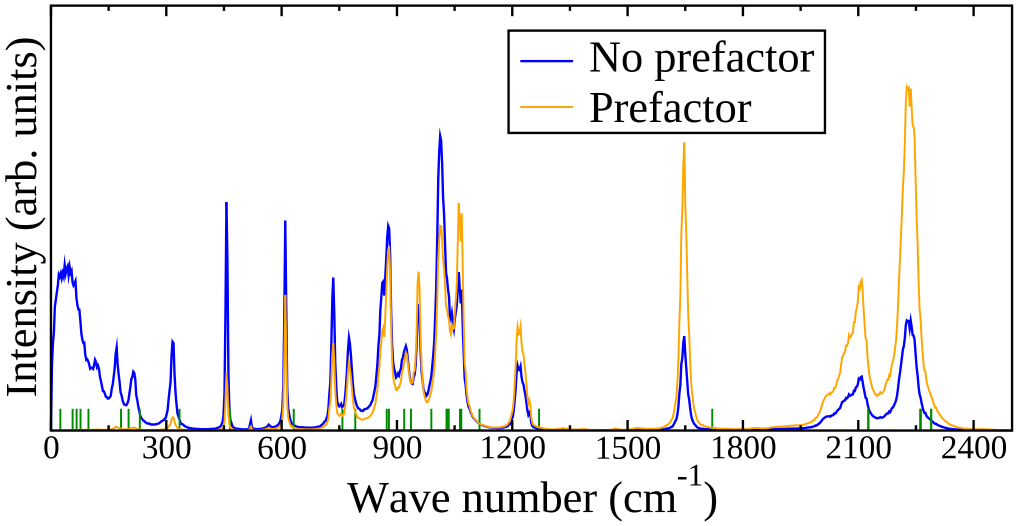

Figure 4.18: Power spectrum of deuterated liquid dimethyl carbonate in the range 0 to 2500 cm^{-1}. The spectrum multiplied by a prefactor, $\omega\beta\hbar\omega$, is also shown (orange colour). Spectrum for the cis-cis conformer in gas-phase obtained from a Hessian calculation is shown in as sticks (green colour).

To assign peaks in the calculated power spectrum or vibrational density of states (VDOS), the contribution of each atom to the total VDOS is calculated. Figure 4.18 shows the VDOS of a cis-cis monomer in gas and liquid phases and contribution from different atoms to it. Quantum effects are included in a semiclassical fashion through a factor, $\omega\beta\hbar\omega$, derived within the harmonic limit. A Hessian analysis was carried out on the gas phase cis-cis monomer to obtain its vibrational modes to aid in the assignment of modes in the liquid state. Further, CPMD trajectories at 300 K were also generated for the cis-cis and cis-trans monomers in the gas phase in order to identify if any spectral features can be assigned to a specific conformation. Peak positions found in the liquid and for the gas-phase monomer and the corresponding mode assignments are summarized in Table 4.4.

Peaks centered at 2108 and 2231 cm^{-1} are assigned to the C-D bond stretching of the methyl group. The same peak is expected to appear at 2740 cm^{-1} in the protiated liquid (taking into account the reduced mass of the oscillator) compared to the experimental value of 3000 cm^{-1}. The difference is in part due to the inadequacy

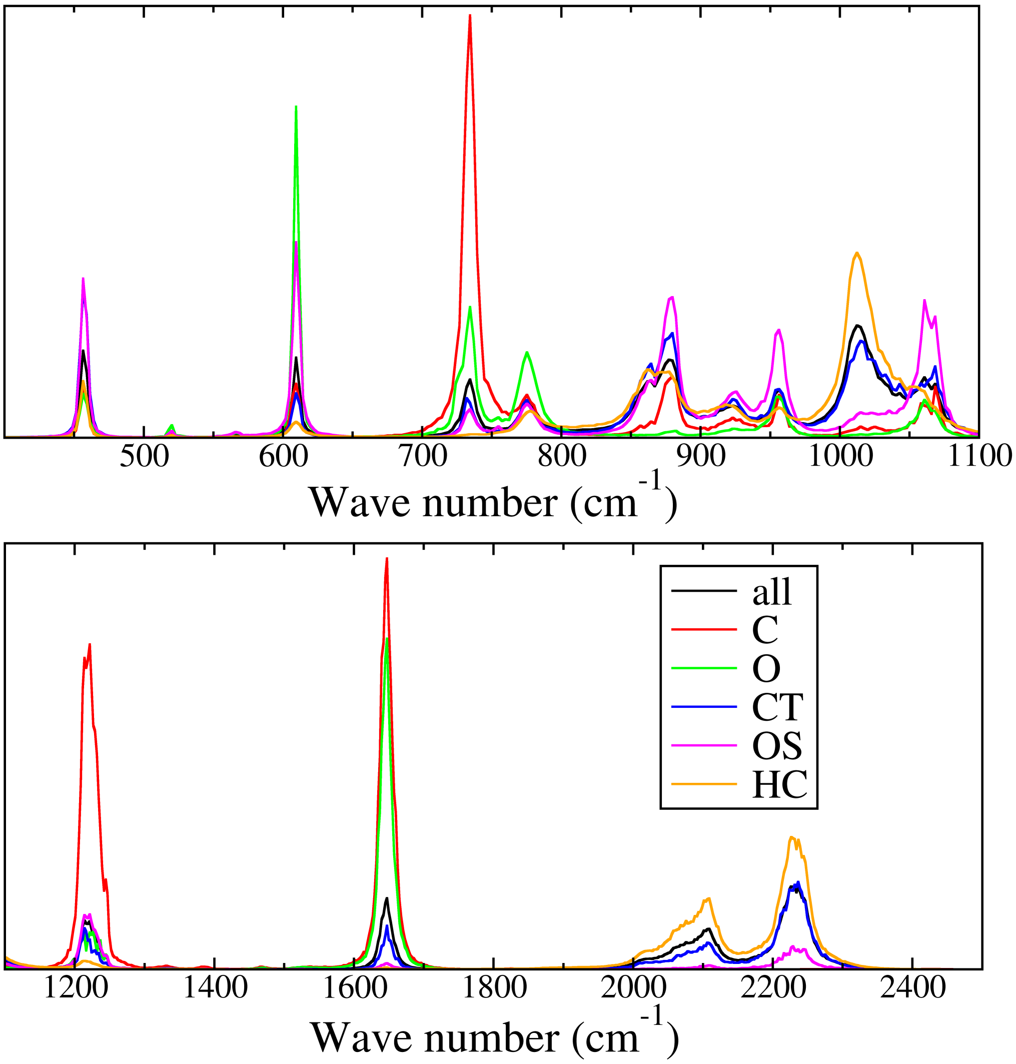

Figure 4.19: Power spectrum of deuterated liquid dimethyl carbonate in the range 400-1100 cm^{-1} (top) and 1100-2500 cm^{-1} (bottom) compared with its atomically decomposed vibrational density of states. Y-axis in bottom figure is scaled for clarity. Label scheme is same in both the panels.

of the exchange-correlation functional used that has been documented earlier. [35, 36] Another reason could be the artificial drag experienced by the electron in a CPMD simulation. [37, 38] The C=O stretch modes is at 1647 cm^{-1} in the liquid, whereas in the monomer, it appears at 1720 cm^{-1}. In the region 1500-1700 cm^{-1}, oxygen and carbon of the carbonyl group contribute to the total VDOS, while other atoms contribute much less, as seen from Figure 4.19. Asymmetric stretching of the OCO group shows peaks at 1213 and 1221 cm^{-1}, whereas symmetric stretching is observed at 1060 cm^{-1}. The experimental values of these modes show peaks at 1279 and 1120 cm^{-1}, respectively. Peak centered at 1012 cm^{-1} is due to bending of the CD_3 group. The VDOS of carbon and hydrogen atoms are clearly contributing more to the total VDOS in this region as seen from Figure 4.19. A peak at 879 cm^{-1} is assigned to the stretching of CD_3-O group. The rocking motion of CD_3 group is observed at 864 cm^{-1}. From Figure 4.19, we notice that this peak also has contribution from OS type oxygens. Bending of HCO group contributes to the peak at 775 cm^{-1}. The feature at 734 cm^{-1} can be assigned to out-of-plane motion of CO_3 group. Carbonyl oxygen and carbonyl carbon contribute more to this peak than other oxygen atoms as clearly seen in Figure 4.19. A peak centered at 609 cm^{-1} is assigned to the rocking motion of OCO_2 group. In this mode, all oxygens contribute more than any other atoms to the total VDOS. Significantly, the spectrum of the cis-trans monomer in the gas phase exhibits a feature at around 525 cm^{-1}, which could be assigned to the same mode. Thus, the exact location of the OCO_2 rocking mode can be used to distinguish between the two conformational states of DMC. The peak at 456 cm^{-1} is assigned to in-plane bending of the OCO group. Taking into account the substitution of deuterium for hydrogen, all calculated peak positions are more or less red-shifted compared to experimental values.

Table 4.4: Vibrational density of states of liquid and gas-phase monomer along with mode assignments. Frequencies are not scaled.

Sl. No.	Wave number (cm^{-1})		Assignment
	Monomer	Liquid	
1	2126-2289	1950-2300	νCD_3
2	1720	1647	ν(C=O)
3	1269	1213, 1221	ν_{as} OCO
4	1114	1060	ν_sOCO
5	1028-1067	1012	$\delta_{ip}CD_3$
6	989	-	δ_{ip}OCO & CD_2 rocking
7	936	-	$\delta_{ip}CO_3$ & δ_{ip}OCD
8	918	879	νCD_3-O
9	873-879	864	CD_3rocking
10	791	775	δ_{ip}DCO
11	758	734	$\delta_{oop}CO_3$
12	631	609	OCO_2 rocking
13	465	456	δOCO

4.4 Discussion and conclusions

Extensive MD simulations of an environmentally benign solvent and chemical reaction medium, dimethyl carbonate, based both on quantum Kohn-Sham density functional theory as well as on an empirical force field have been carried out. The liquid modelled with CPMD is predominantly constituted by molecules in the cis-cis conformation, whereas only about 2% (6% in force field based simulations) of molecules are present in the cis-trans conformation, under ambient conditions. The mean value of the molecular dipole moment calculated from our simulations agrees well with results from dielectric measurements. [6]

The DFT-based Car-Parrinello MD simulations were augmented with empirical van der Waals corrections. They predict slightly shorter intermolecular contacts than those from force field simulations, in particular for the carbonyl oxygen-methyl hydrogen distance. The dipole moment of molecules in the cis-trans conformation is around 4.5 D, while the value for those in the cis-cis conformation is around 1.0

D. This wide disparity in the dipole moment magnitudes can lead to heterogeneity in the liquid, although the concentration of molecules in the cis-trans conformation is dilute. Indeed, we have observed clustering of cis-trans molecules that arises from the higher binding energy (i.e., more stable) of dimers of like conformers than that of unlike conformers.

In the liquid, close neighbours of DMC lie with their molecular planes parallel to each other. However, the dipole vectors of neighbouring molecules do not show a preference for any specific orientation. Neighbors tend to form weak C-H$\cdots$O hydrogen bond with a central molecule and the tendency increases when the central molecule is a cis-trans conformer. Vibrational mode assignments obtained from our condensed phase CPMD simulations are in excellent agreement with experiments.

The current work has demonstrated the salient features of intermolecular structure and dynamics of this environmentally benign solvent. Simulations to discern the solvent's role in the conduct of specific chemical reactions can now be undertaken.

Bibliography

[1] Tundo, P.; Selva, M. *Acc. Chem. Res.* **2002**, *35*, 706–716.

[2] Righi, G.; Bovicelli, P.; Barontini, M.; Tirotta, I. *Green Chem.* **2012**, *14*, 495–502.

[3] Katon, J. E.; Cohen, M. D. *Can. J. Chem.* **1974**, *52*, 1994–1996.

[4] Katon, J. E.; Cohen, M. D. *Can. J. Chem.* **1975**, *53*, 1378–1386.

[5] Bohets, H.; van der Veken, B. J. *Phys. Chem. Chem. Phys.* **1999**, *1*, 1817–1826.

[6] Thiebaut, J.-M.; Rivail, J.-L.; Greffe, J.-L. *J. Chem. Soc., Faraday Trans. 2* **1976**, *72*, 2024–2034.

[7] Okada, O. *Mol. Phys.* **1998**, *93*, 153–158.

[8] Soetens, J. C.; Millot, C.; Maigret, B.; Bako, I. *J. Mol. Liq.* **2001**, *92*, 201–216.

[9] Jorgensen, W. L.; Maxwell, D. S.; TiradoRives, J. *J. Am. Chem. Soc.* **1996**, *118*, 11225–11236.

[10] Gontrani, L.; Russina, O.; Marincola, F. C.; Caminiti, R. *J. Chem. Phys.* **2009**, *131*.

[11] Frisch, M. J. et al. Gaussian 09 Revision A.1.

[12] Martyna, G. J.; Klein, M. L.; Tuckerman, M. *J. Chem. Phys.* **1992**, *97*, 2635–2643.

[13] Plimpton, S. *J. Comput. Phys.* **1995**, *117*, 1–19.

[14] Hutter, J.; Ballone, J. P.; Bernasconi, M.; Focher, P.; Fois, E.; Goedecker, S.; Marx, D.; Parrinello, M.; Tuckerman, M. E. CPMD, Version 3.13.2; Max Planck Institut fuer Festkoerperforschung: Stuttgart. 1990.

[15] Kuo, I. F. W.; Mundy, C. J.; McGrath, M. J.; Siepmann, J. I.; VandeVondele, J.; Sprik, M.; Hutter, J.; Chen, B.; Klein, M. L.; Mohamed, F.; Krack, M.; Parrinello, M. *J. Phys. Chem. B* **2004**, *108*, 12990–12998.

[16] Wendler, K.; Brehm, M.; Malberg, F.; Kirchner, B.; Delle Site, L. *J. Chem. Theory Comput.* **2012**, *8*, 1570–1579.

[17] Martyna, G. J.; Klein, M. L.; Tuckerman, M. *J. Chem. Phys.* **1992**, *97*, 2635–2643.

[18] Troullier, N.; Martins, J. L. *Phys. Rev. B* **1991**, *43*, 1993–2006.

[19] Perdew, J. P.; Burke, K.; Ernzerhof, M. *Phys. Rev. Lett.* **1996**, *77*, 3865–3868.

[20] Williams, R. W.; Malhotra, D. *Chem. Phys.* **2006**, *327*, 54–62.

[21] Balasubramanian, S.; Kohlmeyer, A.; Klein, M. L. *J. Chem. Phys.* **2009**, *131*.

[22] Silvestrelli, P. L.; Bernasconi, M.; Parrinello, M. *Chem. Phys. Lett.* **1997**, *277*, 478–482.

[23] Jmol: An open-source Java viewer for chemical structures in 3D; available at http://www.jmol.org/.

[24] McMahon, B.; Hanson, R. M. *J. Appl. Crystallogr.* **2008**, *41*, 811–814.

[25] Humphrey, W.; Dalke, A.; Schulten, K. *J. Mol. Graphics Modell.* **1996**, *14*, 33–38.

[26] Chia, L. H. L.; Kwan, K. J.; Huang, H. H. *Aust. J. Chem.* **197**, *34*, 349–355.

[27] Labrenz, D.; Schroer, W. *J. Mol. Struct.* **1991**, *249*, 327–341.

[28] Fumino, K.; Wulf, A.; Ludwig, R. *Angew. Chem. Int. Ed.* **2008**, *47*, 3830–3834.

[29] Samanta, A. K.; Pandey, P.; Bandyopadhyay, B.; Chakraborty, T. *J. Phys. Chem. A* **2010**, *114*, 1650–1656.

[30] Pandey, P.; Samanta, A. K.; Bandyopadhyay, B.; Chakraborty, T. *Vib. Spectrosc.* **2011**, *55*, 126–131.

[31] Wulf, A.; Fumino, K.; Ludwig, R. *Angew. Chem. Int. Ed.* **2010**, *49*, 449–453.

[32] Silvestrelli, P. L.; Marzari, N.; Vanderbilt, D.; Parrinello, M. *Solid State Commun.* **1998**, *107*, 7–11.

[33] Silvestrelli, P. L.; Parrinello, M. *J. Chem. Phys.* **1999**, *111*, 3572–3580.

[34] Silvestrelli, P. L.; Parrinello, M. *Phys. Rev. Lett.* **1999**, *82*, 3308–3311.

[35] Reddy, S. K.; Kulkarni, C. H.; Balasubramanian, S. *J. Chem. Phys.* **2011**, *134*, 124511.

[36] Handgraaf, J. W.; Meijer, E. J.; Gaigeot, M. P. *J. Chem. Phys.* **2004**, *121*, 10111–10119.

[37] Kirchner, B.; Hutter, J. *J. Chem. Phys.* **2004**, *121*, 5133–5142.

[38] Amira, S.; Spangberg, D.; Hermansson, K. *J. Chem. Phys.* **2006**, *124*, 104501.

Part II

Metal-Organic Frameworks

Chapter 5

Metal-Organic Frameworks for Gas Adsorption

Metal-organic frameworks are a new class of porous crystalline materials that are composed of ordered networks containing two constituents, metal ions and organic linkers. They are characterized by high surface areas, low densities, thermal stability, tunable pore size and functionality. [1–4] Due to their unique properties, they have found applications in catalysis, sensing and separation, gas storage, drug delivery, luminescence, magnetism, non-linear optics and molecular recognition. [5, 6] The organic linker or ligand coordinates with metals to form stable one-, two- or three-dimensional porous structures that extends infinitely in three directions. They can be easily prepared under mild conditions. The structure of MOFs containing metal ions and ligands can be determined using X-ray crystallography. [4] Instead of using organic cations, metal ions provide several advantages. Transition metal ions are often used and depending on their oxidation state and coordination number, many coordination environments can be obtained, some of which are linear, T or Y-shaped, tetrahedral, square-planar, square-pyramidal, trigonal-bipyramidal, octahedral, trigonal-prismatic, pentagonal-bipyramidal and their distorted forms. [4]

The strong interaction between the metal and the ligand offers high directionality compared to other weak interactions such as π-π interactions. [5]

Besides providing strong metal-ligand bonding, metals can also provide orthogonal angles for constructing extended structures. The coordination geometry of metal offers possible templating joints for bridging ligands. It is preferred over other materials such as activated carbons and zeolites due to their high crystalline nature that enables accurate determination of structure, and reproducibility among measured physical properties. [7] The crystal structure of MOFs can be obtained from single crystal X-ray crystallography.

In this Part of the thesis, we are focussed on computational studies of gas adsorption in a few MOF compounds, synthesized and characterized experimentally by the group of Professor Tapas Maji. The literature on MOFs is vast. Thus, in the following, we provide a brief summary of the existing knowledge on these interesting hybrid compounds to enable a better appreciation of the computational studies presented later.

MOFs are categorized into three classes, as follows. [2, 4, 8]

- **First generation** - These are microporous in nature that collapse irreversibly upon guest removal.
- **Second generation** - These are robust and rigid frameworks that maintain their crystalline nature even after the removal of guest molecules
- **Third generation** - These are flexible and dynamic frameworks, which respond to external stimuli such as temperature, pressure, guest molecules, etc. in a reversible manner.

Second generation MOFs: For storing and transporting a desired compound using MOFs, such as gases or liquids, it is important that the framework should be rigid and porous even in the absence of solvent molecules. So the second generation

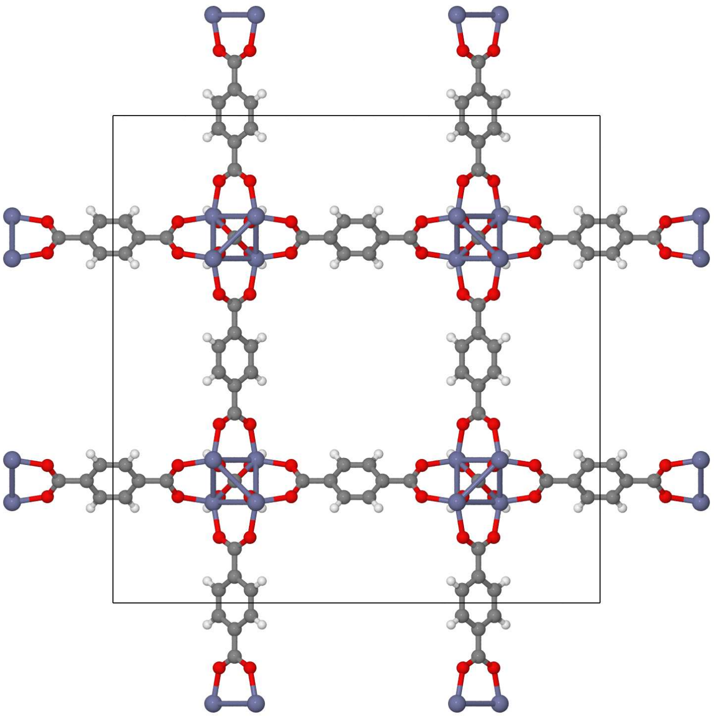

(a)

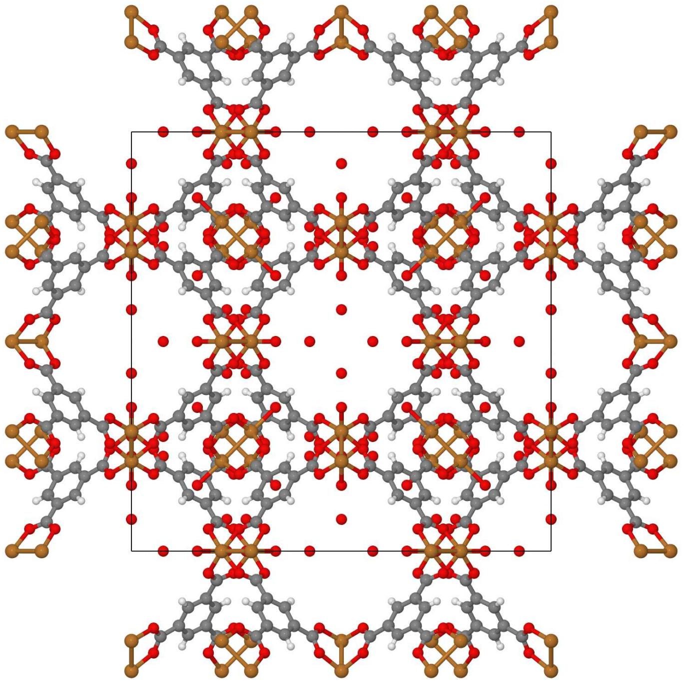

(b)

Figure 5.1: Crystal structures of a) MOF-5 b) HKUST-1 or Cu-BTC. Both are shown along the a-axis. [6, 9]

MOFs are useful in this context. MOF-5 and HKUST-1 or Cu-BTC are very well-known that come under this category (Figure 5.1). [6, 9, 10] They exhibit high surface areas (3,500 m^2g^{-1} for MOF-5, 1900 m^2g^{-1} for Cu-BTC). MOF-5 is made of Zn_4O cluster coordinated to 1,4-benzenedicarboxylate to form three-dimensional extended structure. The structure of Cu-BTC was first reported in 1999. It is composed of copper(II) paddle wheel unit and benzene-1,3,5-tricarboxylate. It possesses three cavities of different shape and size. [9] Both crystals show high thermal stability in the absence of solvent molecules. They are stable at temperatures higher than 200 °C also.

Third generation MOFs: These are also called as soft porous materials. They have highly ordered network, permanent porosity, long-range structural order and even in the absence of solvent molecules. [8] In addition, they also show structural transformability depending on external stimuli. In most of the cases, weak interactions are responsible for flexibility in these materials. These are, in general, interpenetrated structures - where several independent and identical networks are entangled. Two types of transformations are observed. These are named as crystal-to-crystal and crystal-to-amorphous transformations. In the latter, unlike other amorphous systems, the long-range order of the framework is reasonably preserved. [8] Depending on transformation type, such materials find applications in different disciplines. For instance, frameworks where the independent motifs slide or displace with respect to each other without any covalent bond breaking, have found applications in gas storage and separation. Such MOFs are characterized by a gate-type adsorption profile - there is no uptake of gas at low pressure and at a critical pressure, an abrupt increase in the adsorbed amount can be seen. Occasionally, the adsorption isotherms also show hysteresis, i.e., the adsorption and desorption curves may not coincide.

Instead of having rigid linkers, soft linkers can also be used during the synthesis

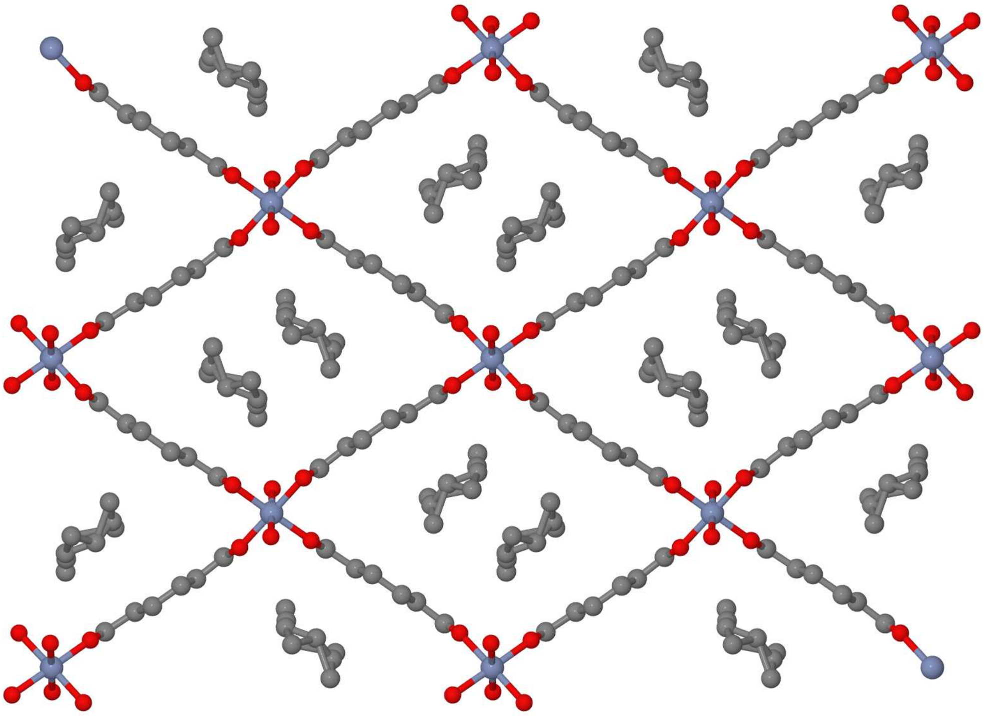

(a)

Figure 5.2: Crystal structure of MIL-53. [11] View along c-axis.

of MOF. Compared to the former, such frameworks have porosity even after the removal of solvent molecules. They possess both large and narrow pores in the presence and absence of guest molecules, respectively. These MOFs show breathing effect; on adsorption of guest molecules, the cell volume changes and the pore changes from narrow to large. [12] Such structural transformations may require only a few kJ/mol of energy. Since this value is in the range of hydrogen bonding, the change from small to large pore are mostly accompanied by these interactions. This property has been used in controlled delivery of anti-inflammatory drug, Ibuprofen, using flexible MIL-53 (Figure 5.2). [11, 13] The gas adsorption-desorption processes induce the structural transformation from porous to non-porous phase and vice versa. It has also been observed that even small interaction energies, (such as that involving the adsorption of H_2 molecule), was able to transform the framework from one structure to another. This phenomenon along with large hysteresis could be used to trap hydrogen gas via kinetic-based trapping mechanism. [8, 14] Electric and magnetic properties are also affected during the transformations. [15]

5.1 Ligands

As discussed before, organic molecules with specific functional groups are used as ligands. Figure 5.3 shows some of the common ligands used in the synthesis of MOF. Typically, these are multidentate bridging ligands with two or more linking sites or donor atoms, providing unique binding strength and topology. [3, 5] Physical properties can be tuned by changing the organic ligand. These properties are strongly dependent on the length of the ligand, and number of binding sites. [3] In general, ligands with carbon, oxygen or nitrogen are used in the synthesis of MOF. By carefully choosing the number of linking sites in the ligand, the metal coordination number can be controlled to be less than its full valence. In this manner, by carefully selecting the organic ligand, the dimensionality of MOF can be tuned to desired topologies and physical properties. Carboxylate ligands can form more stable framework structures due to strong electrostatic interaction and chelation effect. [3]

Two problems are associated with organic linkers. Firstly, the linkers which exhibit more than one conformation could lead to unpredictable structures. With such linkers, different crystal structures were formed simply by changing the concentration of reactants, type of anion, temperature, etc. [16] To overcome this problem, ligands with rigid backbones such as 4,4'-bipyridine, 2,4,6-tri-4-pyridyl-1,3,5-triazine, etc. have been introduced that restrict the orientational freedom of ligand lone pairs. [3] Second, large bridging ligands lead to networks with large cavities and these networks interpenetrate so that the resultant cavity size is decreased or vanished to zero. [3] A few strategies have been proposed to overcome this problem. They include using charged frameworks, bulky ligands, increase binding between guest molecules and framework, secondary building units, etc. [17–19]

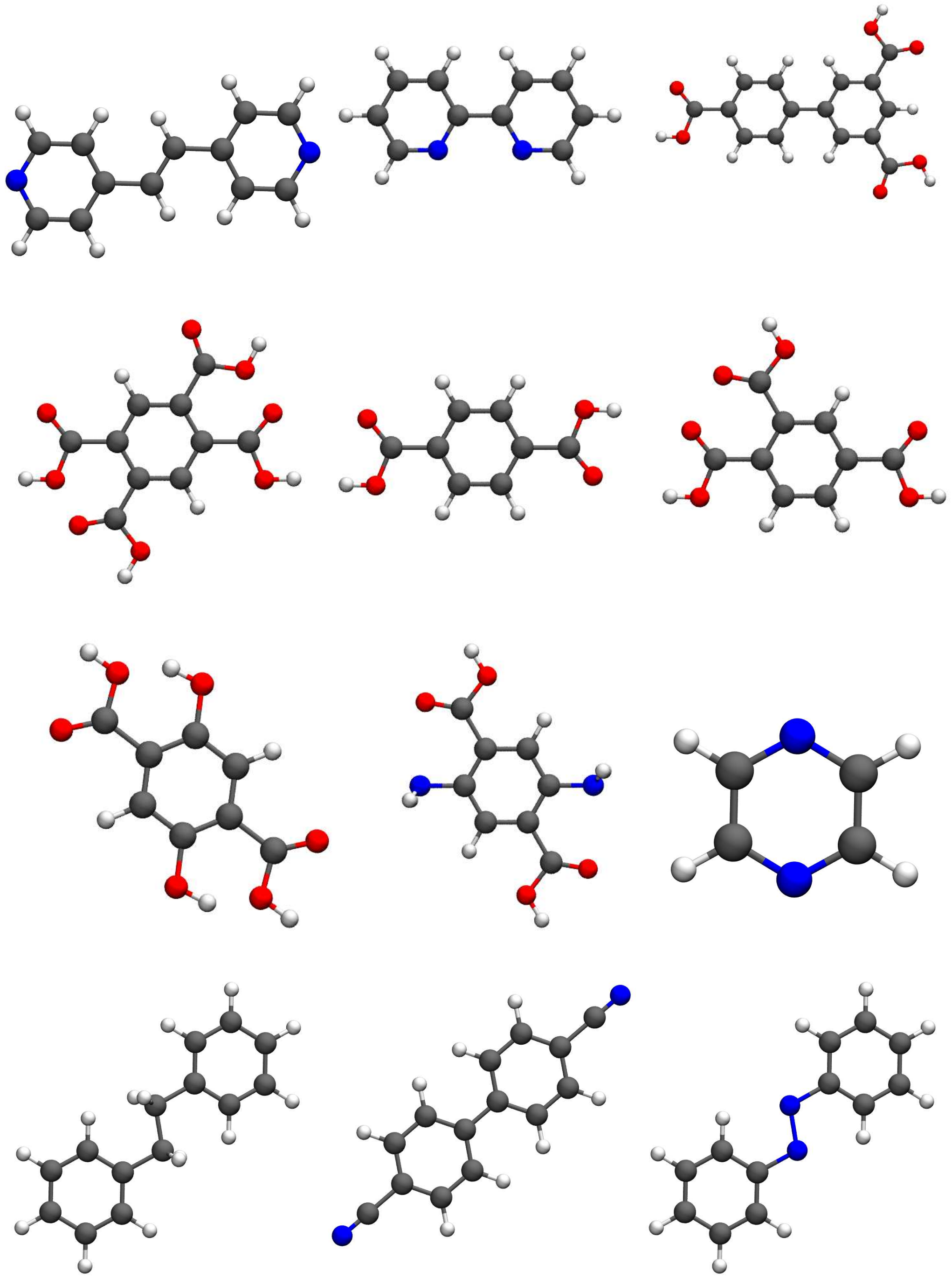

Figure 5.3: Examples of common ligands used. Colour code: C, grey; O, red; N, blue; H, white.

Since carboxylate groups can form stronger M-O-C bonds with metal atoms, these are used in the construction of new ligands called as secondary building units (SBU). [4, 20] These are defined as molecular complexes or polynuclear clusters constructed from two or more metal ions and multidentate carboxylate linkers. [4] One example of SBU is paddle wheel cluster where the two metal ions are locked into their positions by four carboxylate groups. Comparing this to single metal ion case, SBU offers more structural stability because of rigidity of the cluster. Since this cluster is neutral, a counterion need not be added to neutralize the framework.

5.2 Properties and applications

MOFs have found many applications in different areas. Some of them are discussed in the following.

Gas storage Due to the very high surface areas and pore volumes, they can be used to capture and store gases such as carbon dioxide, hydrogen, methane, nitrogen, etc. Among these, MOFs exhibit considerable promise for hydrogen and methane storage. [21] The gases can be released either by increasing temperature or decreasing pressure. The functionalization of pore surface allows one to increase adsorption capacity and heats of adsorption. These MOFs can be used to transport or store gases for clean energy applications. More details of H_2 and CO_2 adsorption are given in the next section.

Selective gas and liquid adsorption MOFs show gas or liquid selectivity due to molecular sieving effect and/or selective adsorption. The former is related to the size of the guest molecule and pore size and the latter depends on specific guest-host and guest-guest interactions. [21] Selectivity values depend on temperature and pressure.

Catalysis Since there are no limitations on pore size unlike zeolites, MOFs can be used in numerous catalytic applications. They provide homogeneous surface due to high crystallinity. Few strategies have been proposed for building MOFs specifically for catalytic applications, which are discussed in the following Refs. [22–24]

- Framework activity.
- Encapsulation of active species into the pores. MOF interacts with them through non-covalent interactions.
- Post-synthetic modification to introduce functional groups and metal complexes. These interact with MOF through covalent interactions.

The disadvantage of these materials for catalytic applications is the issue of stability under different environments and their cost.

5.3 Gas storage

Flue gases from coal plants (containing predominantly CO_2 and SO_2) need to be scrubbed off these gases before being released into the atmosphere. The gases could be stored permanently and/or converted to other forms. In addition, there is a growing interest across the world in using alternative technologies in place of conventional sources such as fossil fuels. For such purposes, large tanks containing H_2 or CH_4 are used for storage and transportation under hazardous conditions. Instead, MOFs can be used to store gases effectively at low pressures. This provides a safer and more economical method. An ideal adsorbent should have following criteria: [25]

- It should be a crystalline compound, stable under cycling, humidity and temperature.
- Tunable pores (size, functionality).
- Specific surface area

- Accessible adsorption sites
- Low cost, easy for large-scale production and shaping.
- It should be stable in the presence of water.

5.3.1 Hydrogen storage

Hydrocarbon sources are burnt to provide energy sources for human activities. Due to this, the concentration of CO_2 in the atmosphere is increasing leading to dreadful effects. It is also the primary cause for global warming. Thus, cleaner, renewable and economical alternative energy sources are required to be examined. H_2 gas is a good and clean energy carrier that also has three times the gravimetric heat of combustion of gasoline. [1] It can be produced from sources such as biomass, water, electricity, natural gas, etc. Hydrogen gas can also be used for transport in place of gasoline. During the combustion process, water is the only by-product, making it a clean energy reaction. In addition, it is also economical, safer than liquid fuels, reduces carbon and other hazardous gas emissions. [1]

Due to the low volumetric storage density of hydrogen, conventional methods for hydrogen storage are often disfavoured due to their cost. Current techniques use four processes for hydrogen storage: high pressure tanks, cryogenic tanks, chemisorption and physisorption. [1] The first two methods are associated with safety and economic issues while the third method has been disfavoured due to heat management, kinetics, and reversibility. Among several materials used for this purpose, MOFs are attractive due to their unique properties. [26–29] These were overcome in the physisorption method, in which the hydrogen gas interacts with MOF through van der Waals (vdW) interactions. Many have started researching on MOFs aiming for high adsorption capacities at room temperature. However, due to small interaction energies, it is difficult to use MOFs for practical applications. With respect to transport, hydrogen storage materials should be light, compact, economical and should have high gravimetric and volumetric densities. [1] U. S. Department of Energy has set a target binding energy in the range of -20 to -40 kJ/mol. Depending on interaction type, the hydrogen molecule exhibits a wide variety of binding energies. [30] H_2 gas interact with MOF through the following type of interactions: van der Waals, electrostatic and orbital interactions. [30]

Under physisorption conditions, to achieve high gas uptake, materials should possess a large surface area. MOF-5 and its isoreticular structures have been thoroughly examined for hydrogen storage. In this case, H_2 gas undergoes physisorption process. These structures showed heats of adsorption values in the range from 4-7 kJ/mol. Although the uptake amount is high at lower temperature, it decreases to lower values at 298 K. [31] Overall, under physisorption conditions, the values reported so far are in the range 4-10 kJ/mol. [23] These values decrease further as the gas loading increases.

Many strategies have been proposed to increase the binding energy. It has been shown that H_2 gas can interact strongly with small pores compared to larger ones because in the former case, H_2 molecule can gain additional stability through interaction with both sides of the pore wall. [32, 33] Based on computer simulations, a pore width of 6 Å was predicted to be ideal at low pressures for ensuring the strong interactions between H_2 gas and adsorbent. [34] Few approaches were reported in the literature to reduce the pore width. For a MOF whose structure is already established, one way to reduce the pore size is to introduce the bulky groups into the framework structure. The interaction energies obtained for such frameworks are comparable with those between hydrogen and unsaturated metal sites. Alternatively, interpenetrated MOFs can be used to reduce the pore width. Experiments and grand canonical Monte Carlo simulations have shown that interpenetrated MOF showed higher H_2 uptake compared to non-interpenetrated structures. [35, 36] However, the free volume decreases due to interpenetration and it may affect the adsorption capacities.

Solvent molecules which are coordinated to metal centers can be removed by heating under vacuum to generate unsaturated metal centers. H_2 gas shows strong affinity towards these sites and sometimes the binding energies are as high as -12-13 kJ/mol. [37, 38] For instance, in a neutron diffraction study of $Cu_3(BTC)_2$ framework, it was shown that hydrogen molecules prefer to interact with the unsaturated Cu site. [39] Further, the interaction energy due to electrostatic interactions is more than that of van der Waals interactions. Thus, the binding energy can be increased by decorating the pore surface with light-weight metal atoms or ions. These can interact electrostatically giving rise to higher interaction energies. The strength of this interaction depends on the type of metal ion used. In a computational study where Li^+ ions were decorated on the surface of MOF-5, the hydrogen binding energy was seen to increase to -24 kJ/mol from a value of -4.1 kJ/mol. [26, 33, 40] In addition to cations, anions and charged ligands can also be used to achieve high binding energies. [1, 23, 30, 41] In these studies, it is not clear whether H_2 molecule forms a covalent bond (chemisorption) with above metal ions or anions. Chemisorption though can lead to the following problems [30]

- Desorption process requires extreme, energy-intensive conditions due to strong gas-MOF binding
- Chemical nature of adsorbent might change during release of H_2. It might not show uptake during H_2 re-sorption.

5.3.2 CO_2 storage

CO_2 is a greenhouse gas that is emitted by two types of sources. One is anthropogenic sources that such as the burning of fossil fuels and the other are natural sources that include volcanic outgassing, wildfires, respiratory processes of living organisms. These processes increase the level of CO_2 concentrations in the atmosphere. [27, 42] This is in turn reflected in the increment of the average global temperature that has a huge impact on living organisms. Strategies to limit the amount of CO_2 released to the atmosphere are increasingly sought after. One of the possible ways is to capture the gas at existing emission sources and reuse or sequestrate it permanently. The most significant challenge is the cost associated with capturing and regenerating processes.

Three stages are involved in this process - capturing it at point sources, transportation and sequestration. Among these, the capturing process is challenging one. It demands the following material properties, as follows. [25]

- High selectivity for CO_2 gas
- High surface area and free volume
- Moderate heat of adsorption
- Stable against water vapour exposure
- Low cost
- Material should withstand many number of adsorption and desorption cycles
- High thermal stability and should posses long-term stability.
- High gravimetric and volumetric CO_2 adsorption
- Material should have scaffold-like structures allowing fast diffusion of CO_2 gas

Several technologies are available for capturing CO_2 gas. They include aqueous alkanolamine adsorbents, zeolites, activated carbons, covalent organic frameworks and amine-grafted silicas. [27, 43] In addition to the above, highly porous materials are of special interest due to their high surface area. In this category, MOFs are also be used for capturing CO_2 gas. The prime advantage of this over other materials is their low heat capacity. It is the amount of energy required for heating the adsorbent to release the adsorbate molecules. Their low values reduces the energy cost associated with desorption. In situ vibrational spectroscopy, computational methods and crystallographic methods are very helpful in understanding the locations of CO_2 molecules inside the framework. This also helps in identifying the portions of MOF that are responsible for material performance regarding gas storage and hence it is possible to enhance its performance by further modification of these components. In the following, features of MOFs pertaining to CO_2 adsorption are presented.

Adsorption capacity is a critical parameter in designing and selecting the MOF for CO_2 capture and storage. High volumetric and gravimetric amounts are a prerequisite for CO_2 adsorption. The chemical nature of the pore surface dictates the adsorption capacity of MOFs. One can expect high storage capacity from these MOFs depending on the nature of binding sites and their number within the pore. It has been shown that the pendant alkylamine functionalities incorporated into the pores is an effective way to achieve high uptake as well as high binding energy. [44, 45]

One more factor which plays a role in selecting MOF is the heat of adsorption. It tells the affinity of the pore surface towards CO_2 gas. It is also related to selectivity and energy cost associated with desorption process. If CO_2 molecule binds strongly with framework, then a large amount of energy should be supplied to release the gas. Where the heat of adsorption is low, it affects CO_2 selectivity and uptake. So, moderate values for heat of adsorptions of CO_2 are required for economical purposes and these can be obtained easily with functionalization of pore surface without changing the backbone structure. Since flue gas is a mixture of more than two gases, high selectivity for CO_2 gas is required for practical applications. Since MOFs which show high surface areas and pore volumes possess pore sizes larger than size of gas molecules, the CO_2 selectivity is defined by adsorption sites in the pore. [21, 27, 43] For example, CO_2 interacts strongly with amino group than N_2 does, so by incorporating amino groups in MOFs could lead to high selectivity.

However, many MOFs are not quite stable against water vapour due to high metal content. This observation hinders many reported MOFs from being used for CO_2 capture from flue gas. [46]

5.4 Role of computational studies

Computer simulations are important tools in understanding the atomistic details involved at the interface of gas and MOF. This knowledge can be used to design new MOFs, for specific applications. Importantly, the location of gas molecules inside the MOF is difficult to obtain experimentally. Often, the MOF turns into a polycrystalline powder upon desolvation – it is being a prerequisite for gas adsorption. It is nearly impossible to obtain coordinates of atoms from X-ray diffraction of the powder sample. Thus, one has to take recourse to local probes such as vibrational spectroscopy, NMR to identify their locations. On the other hand, simulations can easily identify gas molecules and their interactions sites within the framework. In this manner, the combination of both experiments and computer simulations allows one to design high-performance MOFs. Simulations require the modelling of both adsorbate and adsorbent. One can proceed in two ways to study the interactions - classical and quantum mechanical.

5.4.1 Classical force fields

Classical force fields allow one to study large systems in a relatively lesser time provided force field parameters are available. In general, the framework is considered to be rigid and this avoids the need to develop intramolecular parameters for adsorbent.

Lennard-Jones (LJ) parameters are taken from general all atom force fields such as UFF [47], OPLS-AA [48], DREIDING [49], etc. The charges for electrostatic interactions are derived from quantum mechanical calculations. Alternatively, LJ potential alone is used and the electrostatic contributions are assumed to be either negligible or are effectively subsumed into the LJ parameters. The adsorbates are typically modelled either as rigid coarse-grain bead/beads or rigid/flexible all-atoms. Adsorption isotherms of pure gas or mixture can be calculated using simulations carried out in the grand canonical Monte Carlo (GCMC) ensemble. It allows the fluctuation of the number of particles that exactly resembles the experimental conditions. Using GCMC simulations, CO_2 adsorption in MOF-5 was studied using the DREIDING force field. [49] The CO_2 isotherms exhibited a step which was attributed to structural changes within MOF. Later, it was recognized that attractive electrostatic interactions between CO_2 molecules was indeed responsible for the observed step in adsorption isotherms. [50] By replacing the hydrogen atoms of the linker with bromine atoms, GCMC simulations were carried out on MOF-5. It shows high heat of adsorption, but due to increased density, the adsorption amount is less than in pure MOF. [51] Snurr and coworkers also modelled new MOFs by replacing the organic linkers of MOF-5 with 1,4-tetrabromobenzenedicarboxylate and 9,10-anthracenedicarboxylate and these MOFs shows methane uptake increased by 23% and 36%, respectively. [51] Sometimes, the calculated adsorption characteristics of MOF do not match with experiments. Possible reasons for this include 1) inaccurate force field 2) errors in synthesis leading to defects etc. 3) improper activation of MOF leaving solvent molecule behind 4) MOF flexibility. [52–55] Monte Carlo method can also be used to calculate selectivities, surface areas and heats of adsorption. Experimentally, the former is calculated from N_2 adsorption measurements using BET theory.

Force field based simulations were also employed in crystal structure determination of MOFs. In isoreticular MOFs, when the linker is replaced with long organic ligands, it is difficult to obtain single crystals and thus, the crystal structure. In this case, their structures can be obtained from simulations with the help of original structure and powder pattern. Starting with the original framework, the ligand is replaced by a new one and then, the lattice energy minimizations are carried out to relax both the cell parameters and the ligand. The final structure is used as input for Rietveld refinements. [56–58] This ligand-replacement strategy and their isoreticular crystal structure determination using above methodology has been successfully employed in the case of MOF-5 and they show either high methane adsorption capacity or low densities than pure MOF-5. [59]

The crystal structure of flexible MOFs (third generation MOFs) is difficult to obtain in the absence of solvent molecules because of the polycrystalline nature of the sample or low quality powder patterns. [57] These MOFs are considered as efficient for gas separation. [60] The framework shows flexibility under pressure, temperature, guest adsorption, etc. However, their structures can in principle be modelled through computational methods. In contrast to MOFs discussed earlier, such crystalline systems cannot be treated as rigid during simulations. Additional parameters need to be included in the force field to treat such systems. In fact, in the case of MIL-53(Cr), it is shown that the bonded interactions terms and atomic charges are important for modelling flexible systems. [12] Using this force field, they could reproduce the large and narrow pore phase, CO_2 adsorbed phase successfully. By using experimental cell parameters as target values, the anisotropic pressure was applied on each cell parameter to derive the crystal structure of desolvated form of MIL-88. [56]

5.4.2 Quantum mechanical calculations

It includes electron-electron and electron-nucleus interactions explicitly in the simulations and thus, it is parameter-free (at least, in principle) and provides accurate interaction energies between the adsorbate and adsorbent. Due to its expensive nature, it is generally used to find locations of adsorbates inside the framework and their interaction energies. The calculations can be carried out by considering either the entire crystal (periodic calculations) or specific part of it (cluster or fragment calculations). In the former, Kohn-Sham density functional theory calculations augmented with van der Waals interaction terms are widely used while in the latter, other than DFT, wave function based methods such as second order Moeller-Plesset perturbation theory (MP2), coupled cluster techniques (CCSD), etc. have also been employed. Few examples are given for each case in the following discussion.

The role of dispersive interactions was examined by Poloni et al. who showed that the PBE functional without vdW corrections underestimates the binding energy of CO_2 in a MOF by about 50% compared to the experimental value. The addition of vdW terms made the calculated values to be in good agreement with the experimental one. [61, 62] To increase the binding energy, the pore surface of MOF-5 was decorated with Li atoms and it was tested for H_2 adsorption. This MOF showed good binding energy (-12 kJ/mol) and high uptake (2.0 wt% at 300 K) for H_2 gas. [63] When the metal ions were replaced by other ions having the same valency, it was found that the H_2 binding energy increases in the following order "$Zn^{2+} < Mn^{2+} < Mg^{2+} < Co^{2+} < Ni^{2+}$". [64] and the authors concluded that the ionic radii of metal ions can be used to predict the H_2 binding energies in the same metal coordination environment. Combined DFT and GCMC simulations were performed to study CO_2 adsorption in MIL-53(Al^{3+}) and their isoreticular structure where the linker was functionalized with four groups: $(CH_3)_2$, $(OH)_2$, NH_2 and COOH. A good agreement was found between both methodologies. The reasons for strong interaction between CO_2 and framework were attributed to a) local interactions of CO_2 with functional groups b) confinement effect. Further, it was shown that at low pressures, the functional groups play an important role in defining the interaction energies and adsorption capacities while at high pressures, their role was limited. At these pressures, the framework structural properties such as free volume, accessible surface area, etc. are responsible for adsorption characteristics. [65]

Cluster (or fragments in gas phase) calculations have also been performed on a specific part of the framework such as the linker to calculate the binding energy and compare them against experimental values of adsorption enthalpies. [30, 66–70] Due to the reduced number of electrons in this approach, accurate methods can be used for studying gas interactions with framework. Benzene molecule was taken as an example of linker and it was functionalized with several groups such as NO_2, NH_2, COOH, SO_3H and OH. These systems were studied for CO_2 affinity and its nature of interaction towards each functional group using DFT and MP2 methods. It was found that among these groups, the highest binding energy was obtained for SO_3H and COOH group with values -10 and -11 kJ/mol, respectively. [66] For H_2 adsorption, functional groups such as H, F, CH_3, NH_2 and OH were substituted the at the ortho position of benzenedicarboxylic acid. Calculations performed at MP2 level have shown that the ligands with F^- and ${SO_4}^{2-}$ interact strongly with H_2 yielding binding energy of -34 and -20 kJ/mol, respectively. [30] Additionally, since ${SO_4}^{2-}$ ion can provide multiple binding sites, MOFs which use such ligands may show more adsorption capacities. The interaction with unsaturated or open metal sites is also helpful to achieve high binding energies for H_2 gas. Head-Gordon group have shown that among alkali metal ions, Li^+ showed high affinity for H_2 molecule (-24 kJ/mol). But, when the number of H_2 molecules were increased, the binding energy decreased to -12 kJ/mol. [30]

In the subsequent chapters, we illustrate the use of such advanced computational methods in obtaining a microscopic understanding of gas adsorption in metal organic framework solids. In particular, Kohn-Sham density functional theory based ab initio MD simulations of small gas molecules in MOF solids yield a rich amount of information and are able to explain the observed gas uptake at different temperatures.

Bibliography

[1] Murray, L. J.; Dinca, M.; Long, J. R. *Chem. Soc. Rev.* **2009**, *38*, 1294–1314.

[2] Kitagawa, S.; Kondo, M. *Bull. Chem. Soc. Jpn.* **1998**, *71*, 1739–1753.

[3] James, S. L. *Chem. Soc. Rev.* **2003**, *32*, 276–288.

[4] Kitagawa, S.; Kitaura, R.; Noro, S.-i. *Angew. Chem. Int. Ed.* **2004**, *43*, 2334–2375.

[5] Janiak, C. *Dalton Trans.* **2003**, 2781–2804.

[6] Li, H.; Eddaoudi, M.; O'Keeffe, M.; Yaghi, O. M. *Nature* **1999**, *402*, 276–279.

[7] Kanoo, P.; Gurunatha, K. L.; Maji, T. K. *J. Mater. Chem.* **2010**, *20*, 1322–1331.

[8] Horike, S.; Shimomura, S.; Kitagawa, S. *Nat. Chem.* **2009**, *1*, 695–704.

[9] Chui, S. S.-Y.; Lo, S. M.-F.; Charmant, J. P. H.; Orpen, A. G.; Williams, I. D. *Science* **1999**, *283*, 1148–1150.

[10] Natarajan, S.; Mahata, P.; Sarma, D. *J. Chem. Sci.* **2012**, *124*, 339–353.

[11] Serre, C.; Millange, F.; Thouvenot, C.; Nogus, M.; Marsolier, G.; Lour, D.; Frey, G. *J. Am. Chem. Soc.* **2002**, *124*, 13519–13526.

[12] Salles, F.; Ghoufi, A.; Maurin, G.; Bell, R.; Mellot-Draznieks, C.; Frey, G. *Angew. Chem. Int. Ed.* **2008**, *47*, 8487–8491.

[13] Horcajada, P.; Serre, C.; Maurin, G.; Ramsahye, N. A.; Balas, F.; Vallet-Reg, M.; Sebban, M.; Taulelle, F.; Frey, G. *J. Am. Chem. Soc.* **2008**, *130*, 6774–6780.

[14] Coudert, F.-X.; Jeffroy, M.; Fuchs, A. H.; Boutin, A.; Mellot-Draznieks, C. *J. Am. Chem. Soc.* **2008**, *130*, 14294–14302.

[15] Halder, G. J.; Kepert, C. J.; Moubaraki, B.; Murray, K. S.; Cashion, J. D. *Science* **2002**, *298*, 1762–1765.

[16] Rowsell, J. L.; Yaghi, O. M. *Microporous Mesoporous Mater.* **2004**, *73*, 3–14.

[17] Hoskins, B. F.; Robson, R. *J. Am. Chem. Soc.* **1990**, *112*, 1546–1554.

[18] Yaghi, O. M.; Li, H.; Groy, T. L. *Inorg. Chem.* **1997**, *36*, 4292–4293.

[19] Reineke, T. M.; Eddaoudi, M.; Moler, D.; O'Keeffe, M.; Yaghi, O. M. *J. Am. Chem. Soc.* **2000**, *122*, 4843–4844.

[20] Eddaoudi, M.; Moler, D. B.; Li, H.; Chen, B.; Reineke, T. M.; O'Keeffe, M.; Yaghi, O. M. *Acc. Chem. Res.* **2001**, *34*, 319–330.

[21] Li, J.-R.; Kuppler, R. J.; Zhou, H.-C. *Chem. Soc. Rev.* **2009**, *38*, 1477–1504.

[22] Ranocchiari, M.; Bokhoven, J. A. v. *Phys. Chem. Chem. Phys.* **2011**, *13*, 6388–6396.

[23] Kuppler, R. J.; Timmons, D. J.; Fang, Q.-R.; Li, J.-R.; Makal, T. A.; Young, M. D.; Yuan, D.; Zhao, D.; Zhuang, W.; Zhou, H.-C. *Coord. Chem. Rev.* **2009**, *253*, 3042–3066.

[24] Farrusseng, D.; Aguado, S.; Pinel, C. *Angew. Chem. Int. Ed.* **2009**, *48*, 7502–7513.

[25] Ferey, G.; Serre, C.; Devic, T.; Maurin, G.; Jobic, H.; Llewellyn, P. L.; De Weireld, G.; Vimont, A.; Daturi, M.; Chang, J.-S. *Chem. Soc. Rev.* **2011**, *40*, 550–562.

[26] Srinivasu, K.; Ghosh, S. K. *J. Phys. Chem. C* **2011**, *115*, 16984–16991.

[27] D'Alessandro, D.; Smit, B.; Long, J. *Angew. Chem. Int. Ed.* **2010**, *49*, 6058–6082.

[28] Srinivasu, K.; Ghosh, S. K. *Int. J. Hydrogen Energy* **2011**, *36*, 15681–15688.

[29] Srinivasu, K.; Ghosh, S. K.; Das, R.; Giri, S.; Chattaraj, P. K. *RSC Adv.* **2012**, *2*, 2914–2922.

[30] Lochan, R. C.; Head-Gordon, M. *Phys. Chem. Chem. Phys.* **2006**, *8*, 1357–1370.

[31] Kaye, S. S.; Dailly, A.; Yaghi, O. M.; Long, J. R. *J. Am. Chem. Soc.* **2007**, *129*, 14176–14177.

[32] Latroche, M.; Surbl, S.; Serre, C.; Mellot-Draznieks, C.; Llewellyn, P. L.; Lee, J.-H.; Chang, J.-S.; Jhung, S. H.; Frey, G. *Angew. Chem. Int. Ed.* **2006**, *45*, 8227–8231.

[33] Zhao, D.; Yuan, D.; Zhou, H.-C. *Energy Environ. Sci.* **2008**, *1*, 222–235.

[34] Wang, Q.; Johnson, J. K. *J. Chem. Phys.* **1999**, *110*, 577–586.

[35] Rowsell, J. L. C.; Yaghi, O. M. *J. Am. Chem. Soc.* **2006**, *128*, 1304–1315.

[36] Jung, D. H.; Kim, D.; Lee, T. B.; Choi, S. B.; Yoon, J. H.; Kim, J.; Choi, K.; Choi, S.-H. *J. Phys. Chem. B* **2006**, *110*, 22987–22990.

[37] Chen, B.; Zhao, X.; Putkham, A.; Hong, K.; Lobkovsky, E. B.; Hurtado, E. J.; Fletcher, A. J.; Thomas, K. M. *J. Am. Chem. Soc.* **2008**, *130*, 6411–6423.

[38] Vitillo, J. G.; Regli, L.; Chavan, S.; Ricchiardi, G.; Spoto, G.; Dietzel, P. D. C.; Bordiga, S.; Zecchina, A. *J. Am. Chem. Soc.* **2008**, *130*, 8386–8396.

[39] Peterson, V. K.; Liu, Y.; Brown, C. M.; Kepert, C. J. *J. Am. Chem. Soc.* **2006**, *128*, 15578–15579.

[40] Wong-Foy, A. G.; Matzger, A. J.; Yaghi, O. M. *J. Am. Chem. Soc.* **2006**, *128*, 3494–3495.

[41] Trewin, A.; Darling, G. R.; Cooper, A. I. *New J. Chem.* **2008**, *32*, 17–20.

[42] Millero, F. J. *Chem. Rev.* **2007**, *107*, 308–341.

[43] Sumida, K.; Rogow, D. L.; Mason, J. A.; McDonald, T. M.; Bloch, E. D.; Herm, Z. R.; Bae, T.-H.; Long, J. R. *Chem. Rev.* **2012**, *112*, 724–781.

[44] Bae, Y.-S.; Farha, O. K.; Hupp, J. T.; Snurr, R. Q. *J. Mater. Chem.* **2009**, *19*, 2131–2134.

[45] Wang, Z.; Cohen, S. M. *Chem. Soc. Rev.* **2009**, *38*, 1315–1329.

[46] Simmons, J. M.; Wu, H.; Zhou, W.; Yildirim, T. *Energy Environ. Sci.* **2011**, *4*, 2177–2185.

[47] Rappe, A. K.; Casewit, C. J.; Colwell, K. S.; Goddard, W. A.; Skiff, W. M. *J. Am. Chem. Soc.* **1992**, *114*, 10024–10035.

[48] Jorgensen, W. L.; Maxwell, D. S.; Tirado-Rives, J. *J. Am. Chem. Soc.* **1996**, *118*, 11225–11236.

[49] Mayo, S. L.; Olafson, B. D.; Goddard, W. A. *J. Phys. Chem.* **1990**, *94*, 8897–8909.

[50] Walton, K. S.; Millward, A. R.; Dubbeldam, D.; Frost, H.; Low, J. J.; Yaghi, O. M.; Snurr, R. Q. *J. Am. Chem. Soc.* **2008**, *130*, 406–407.

[51] Dren, T.; Sarkisov, L.; Yaghi, O. M.; Snurr, R. Q. *Langmuir* **2004**, *20*, 2683–2689.

[52] Hafizovic, J.; Bjrgen, M.; Olsbye, U.; Dietzel, P. D. C.; Bordiga, S.; Prestipino, C.; Lamberti, C.; Lillerud, K. P. *J. Am. Chem. Soc.* **2007**, *129*, 3612–3620.

[53] Liu, J.; Culp, J. T.; Natesakhawat, S.; Bockrath, B. C.; Zande, B.; Sankar, S. G.; Garberoglio, G.; Johnson, J. K. *J. Phys. Chem. C* **2007**, *111*, 9305–9313.

[54] Yang, Q.; Zhong, C. *J. Phys. Chem. B* **2006**, *110*, 17776–17783.

[55] Duren, T.; Bae, Y.-S.; Snurr, R. Q. *Chem. Soc. Rev.* **2009**, *38*, 1237–1247.

[56] Mellot-Draznieks, C.; Serre, C.; Surbl, S.; Audebrand, N.; Frey, G. *J. Am. Chem. Soc.* **2005**, *127*, 16273–16278.

[57] Mellot-Draznieks, C. *J. Mater. Chem.* **2007**, *17*, 4348–4358.

[58] Surble, S.; Serre, C.; Mellot-Draznieks, C.; Millange, F.; Ferey, G. *Chem. Commun.* **2006**, *0*, 284–286.

[59] Eddaoudi, M.; Kim, J.; Rosi, N.; Vodak, D.; Wachter, J.; O'Keeffe, M.; Yaghi, O. M. *Science* **2002**, *295*, 469–472.

[60] Coudert, F.-X.; Mellot-Draznieks, C.; Fuchs, A. H.; Boutin, A. *J. Am. Chem. Soc.* **2009**, *131*, 11329–11331.

[61] Poloni, R.; Smit, B.; Neaton, J. B. *J. Phys. Chem. A* **2012**, *116*, 4957–4964.

[62] Poloni, R.; Smit, B.; Neaton, J. B. *J. Am. Chem. Soc.* **2012**, *134*, 6714–6719.

[63] Blomqvist, A.; Arajo, C. M.; Srepusharawoot, P.; Ahuja, R. *Proc. Natl. Acad. Sci. U. S. A.* **2007**, *104*, 20173–20176.

[64] Zhou, W.; Wu, H.; Yildirim, T. *J. Am. Chem. Soc.* **2008**, *130*, 15268–15269.

[65] Torrisi, A.; Bell, R. G.; Mellot-Draznieks, C. *Microporous Mesoporous Mater.* **2013**, *168*, 225–238.

[66] Torrisi, A.; Mellot-Draznieks, C.; Bell, R. G. *J. Chem. Phys.* **2010**, *132*, 044705.

[67] Tafipolsky, M.; Amirjalayer, S.; Schmid, R. *J. Phys. Chem. C* **2010**, *114*, 14402–14409.

[68] Fischer, M.; Kuchta, B.; Firlej, L.; Hoffmann, F.; Fróba, M. *J. Phys. Chem. C* **2010**, *114*, 19116–19126.

[69] Yazaydn, A. O.; Benin, A. I.; Faheem, S. A.; Jakubczak, P.; Low, J. J.; Willis, R. R.; Snurr, R. Q. *Chem. Mater.* **2009**, *21*, 1425–1430.

[70] Getman, R. B.; Miller, J. H.; Wang, K.; Snurr, R. Q. *J. Phys. Chem. C* **2011**, *115*, 2066–2075.

Chapter 6

Ab initio Studies of H_2 and CO_2 Adsorption in a Three-Dimensional Metal-Organic Framework with Highly Polar Pore Surface

6.1 Introduction

Metal organic frameworks (MOF) should have large surface area, pore volume and high heat of adsorptions (although not too high so as to make the desorption of gases energetically inexpensive) for practical applications. One of the method to

---

Major part of this chapter is reprinted with permission from "Three-dimensional metal-organic framework with highly polar pore surface: H_2 and CO_2 storage characteristics" *Inorg. Chem.* **2012**, *51*, 7103-7111. Copyright 2012, American Chemical Society. `http://pubs.acs.org/doi/abs/10.1021/ic202601y` obtain greater binding of the gas molecule is to introduce a heterogeneous surface structure with local dipoles that may enhance H_2 and CO_2 uptake capacity. The gas molecules can thus interact more strongly than what is possible through purely weak dispersion forces. Thus, the inclusion of heteroatoms or highly electronegative atoms like F, O, or N in the pore surface is an effective way to increase adsorption energies for H_2 and CO_2. [1–12] In addition, recent results suggest that modifying the pore surface by the incorporation of Lewis basic sites (-amino, -pyrimidine, -hydroxo) or organic cations enhances low pressure CO_2 uptake and isosteric heat of adsorption. [4–12] In this context, 4,5-imidazoledicarboxylicacid (H_3imdc) is a versatile linker having three pH dependent abstractable protons and may provide diverse binding mode based on two imidazole nitrogen and four carboxylate oxygen atoms. [13–18] Therefore, a MOF composed of H_3imdc and aromatic linkers can afford several adsorption sites for electrostatic interactions with H_2 or CO_2 and can increase adsorption enthalpy.

Single crystal of $[Cd(bipy)_{0.5}(Himdc)](DMF)]_n$ (**1**), (bipy = 4,4'-bipyridine and Himdc= 4,5-imidazoledicarboxylate) was synthesized and characterized experimentally by the research group of Prof. Tapas Maji whose structure was determined using X-ray diffraction. This compound crystallizes in the monoclinic $C2/c$ space group. It possesses high thermal stability and exhibits permanent porosity with moderate surface area. The structure shows a 3D pillared layer coordination framework of Cd(II) bridged by the Himdc and bipy linkers. Each Himdc chelates to two Cd(II) centers through N, O atoms and connects to another Cd(II) through oxo(μ_2-O) bridge and thus forming a two-dimensional (2D) $Cd(Himdc)_2$ corrugated layer in the crystallographic bc plane. The dimeric fragments $Cd_2(\mu_2\text{-}O)_2$ in the layer are connected in the axial coordination with bipy forming a 3D pillared-layer framework. The bipy pillars are aligned parallel along the crystallographic b-axis and they connect the Cd(Himdc)$_2$ corrugated layers diagonally, to form rectangular channels with dimensions of 3.84 x 1.06 Å^2. Along the c-axis, bipy pillars are in a criss-cross and canted fashion supported by π-π interactions which results in oval-shaped channels with dimensions of 4.68 x 3.84 Å^2 (Figure 6.1). In addition, the framework also shows rectangular channels of dimension of 3.2 x 2.1 Å^2 when viewed perpendicular to the b-axis. The 3D channels are occupied by the guest DMF molecules, and each pore is decorated by uncoordinated pendent oxygen atoms (O2, O3) from the Himdc and panels of bipy pillars, resulting in a highly polar pore surface (Figure 6.1). Calculation using PLATON [19] suggests that the 3D framework contains 42.2% void space to the total crystal volume, after removal of the guest DMF molecules. The Cd—Cd separation along the Himdc and bipy pillar are 8.894 and 11.596 Å, respectively.

The crystal was tested for adsorption capacities by loading the desolvated MOF (**1'**) with CO$_2$ and H$_2$ gases. Figure 6.2 shows the adsorption profiles measured for H$_2$ gas at 77 K and 87 K. At excess high pressure of H$_2$ gas, the storage capacity was found to be 1.23 wt% at 77 K which is about two H$_2$ molecules per formula unit. The steep uptake at low pressure regions (up to 3 bar) suggests strong interaction of H$_2$ with the pore surface of **1'**. The enthalpy of H$_2$ adsorption (ΔH_{ads}) was derived from the virial method which reduces to Henry's law at low pressure region and the enthalpy of adsorption is calculated to be -9.0 kJ/mol. The CO$_2$ gas sorption isotherms of **1** measured at 195 and 298 K are shown in Figure 6.2. The storage capacity of **1'** at ambient conditions is measured to be 9 wt% which is equivalent to one molecule of CO$_2$ per formula unit. The isosteric heat of adsorption (q_{st}), calculated using the Dubinin-Radushkevich (DR) equation, which is defined as [20]

$$W = W_0 \times \exp(-(RT\ln(P/P_0)/E)^2) \tag{6.1}$$

where W and W_0 are the adsorption amounts at a relative pressure (P/P_0) and

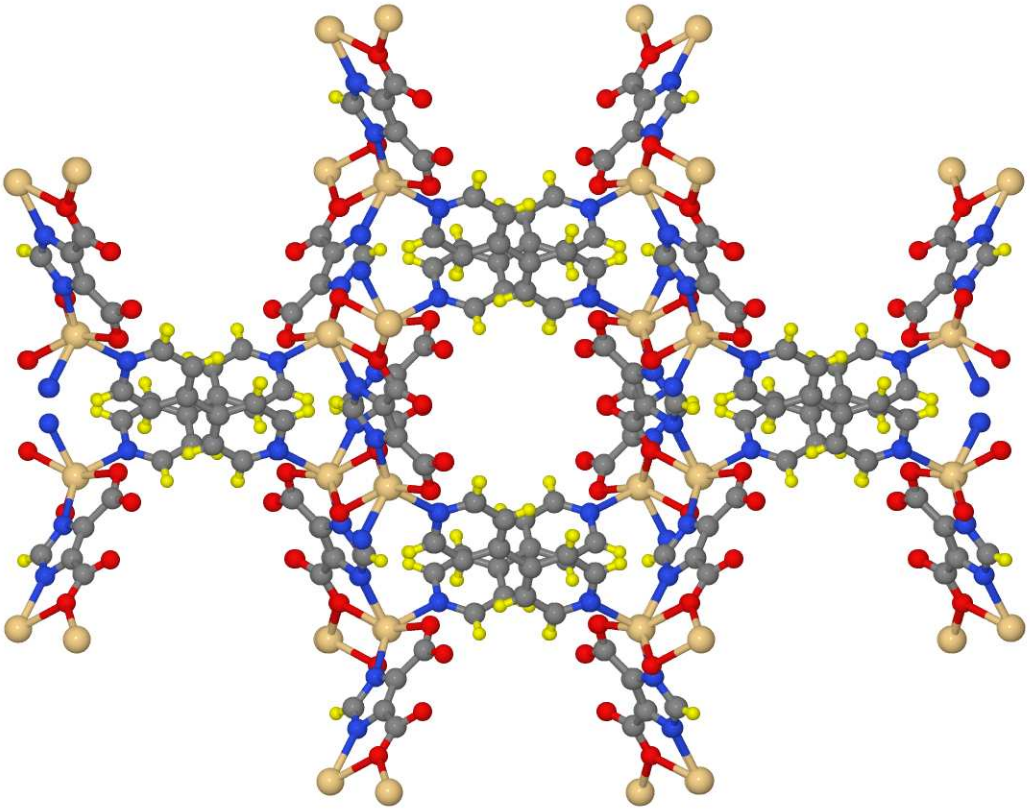

Figure 6.1: View of the 3D framework along the c-axis showing oval shaped channels decorated with pendent carboxylate oxygen atoms and pyridyl moieties. Colour Code: C, gray; H, yellow; N, blue; O, red; Cd, wheat.

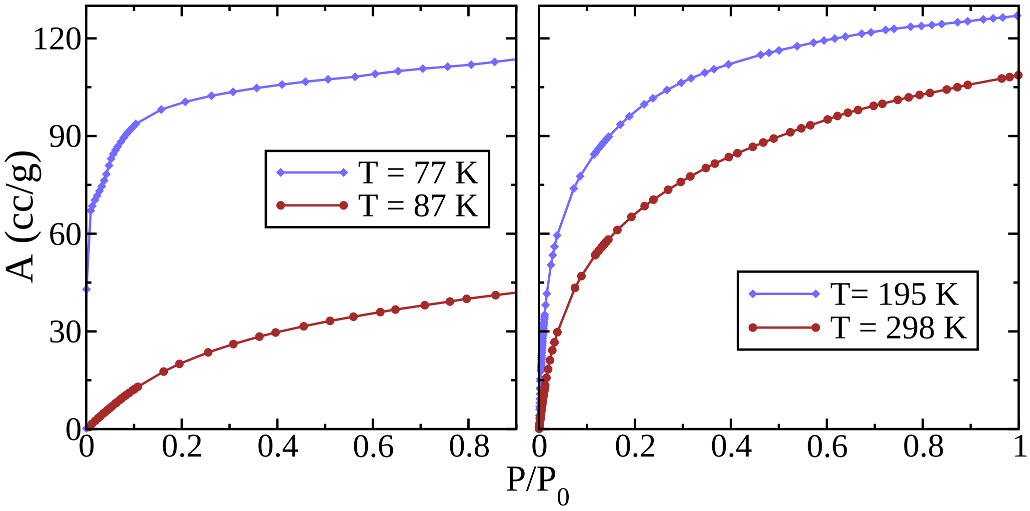

Figure 6.2: Experimentally determined H_2 and CO_2 sorption profiles for **1'**. Left panel shows H_2 isotherms at 77 and 87 K and the right panel shows CO_2 isotherms at 195 and 298 K.

saturation pressure (P_0), respectively. E_0 is the adsorption energy, the parameter β is the affinity coefficient which depends on adsorbate-adsorbent interaction. T and P are temperature and pressure, respectively. It gives a value of 35.4 kJ/mol for isosteric heat of adsorption.

The scope of the present investigation is to identify possible binding sites for the gas molecules with the framework using first principles calculations. Also, as discussed before, whether the hetero atoms play any role in the adsorption process or not needs to be explored.

6.2 Computational details

Bulk periodic Kohn-Sham density functional theory (DFT) calculations were carried out using the plane wave code CPMD. [21] The supercell consisted of one unit cell of the metal organic framework (MOF) and/or gas molecules (H_2 or CO_2). Solvent molecules were not included in modelling of these systems. Valence electrons were represented using a plane wave basis set with an energy cutoff of 80 Ry. The interaction of valence electrons with the core electrons and the nuclei were represented by a norm-conserving pseudopotential of Troullier and Martins type. [22] The cutoff radii of (s, p) orbitals used in pseudopotentials are (1.23, 1.23), (1.12, 1.12), (0.5, 0.38), (2.2, 2.6), (1.12, 1.12) (in a.u.) respectively for C, O, H, Cd and N elements. The gradient-corrected Becke, Lee, Yang, and Parr (BLYP) functional was employed [23, 24] to treat the exchange and correlation interactions. Initial calculations consisted of iterative optimization of the cell parameters and atomic positions until a minimum energy configuration was found. Cell volume was deviated to less than 0.5% compared to experimental value. Further, to identify the preferred locations of H_2 or CO_2 molecules in the MOF, molecular dynamics (MD) simulations using the Car-Parrinello method (CPMD) [25] were carried out at a temperature of 50 K. These were performed by constraining the MOF and allowing the gas molecules (H_2 or CO_2) to explore various regions within the framework as a function of time. Temperature was maintained through a Nóse-Hoover chain thermostat [26] using a coupling constant of 3250 cm^{-1}. In these runs, the hydrogen atoms were replaced by deuterium atoms so as to enable the use of a larger time step of 5 a.u. The trajectory was generated for 3 ps, and an animation demonstrated that the gas molecules explored all the regions of the pore(s). Locations of the gas molecules possessing low energies were identified from this trajectory. Direct optimization of the geometry (i.e., of the MOF and of the gas molecule) was initiated from such favored locations. Optimization of geometry was pursued until the maximum force on any atom was less than 10^{-4} a.u. Gas molecules are known to interact with MOF through van der Waals (vdW) forces in addition to other interactions. [27] While many methods to treat vdW interactions within the DFT formalism exist, an easier route is to add it as an empirical potential. In the present study, the vdW parameters of Grimme as derived for the BLYP functional is employed. [28] The binding energy of the gas

Table 6.1: Binding energies of H_2 and CO_2 molecules in the MOF calculated using BLYP/85 Ry level of theory with [28] and without empirical van der Waals corrections compared against experimental values of the heat of adsorption[a].

	H_2	CO_2
BLYP	-6.14	-6.44
BLYP + vdW	-8.0	-39.14
Experiment	-9.0[b] (-13.3)[c]	-35.4[d]

[a] The energies are in kJ/mol. [b] Adsorption enthalpy value based on virial method. [c] Based on Clausius-Clapeyron equation. [d] Adsorption enthalpy value based on Dubinin-Radushkevich (DR) equation.

molecule (H_2 or CO_2) with the MOF is calculated using the following formula,

$$\Delta E = E(MOF + gas) - E(MOF) - n \times E(gas) \tag{6.2}$$

where E(MOF + gas), E(MOF), and E(gas) represent the energies calculated for MOF with H_2 or CO_2, MOF and isolated gas molecule. Here, E(gas) was calculated in the same simulation box as that of the MOF and "n" gives the number of gas molecules present in the MOF. Thermal contributions to the binding energy were not considered. This contribution is expected to be less than 1 kJ/mol and would not change the results much. All the structures were visualized using Jmol [29, 30] and VMD. [31]

6.3 Results and discussion

Many researchers have explained successfully the adsorption of gas molecules in MOFs using computational methods. [32, 33] The optimal positions of the H_2 and CO_2 molecule in the MOF channel are shown in Figure 6.3.

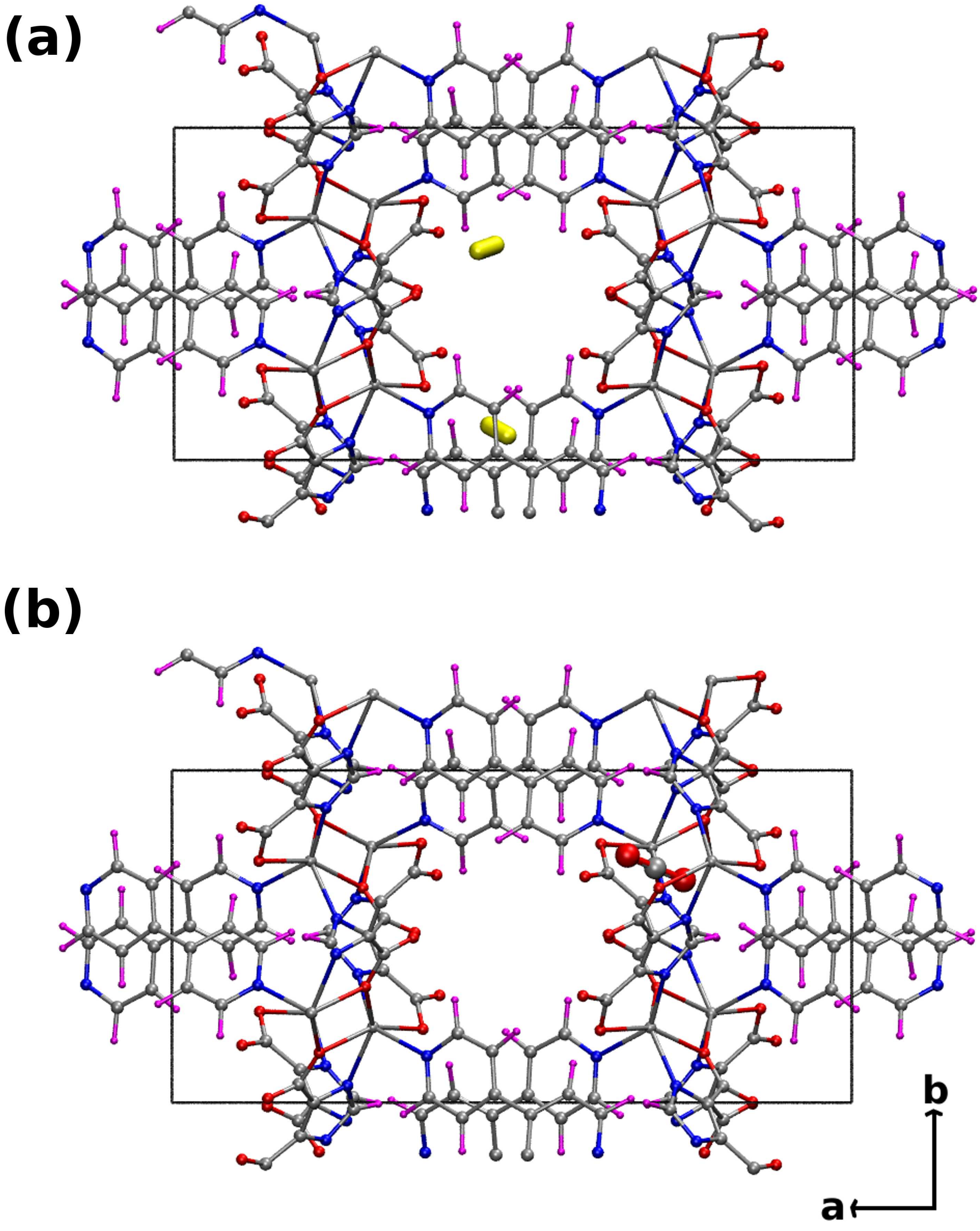

Figure 6.3: Locations of the (a) two H_2 molecules (shown as yellow dumbbells) (top panel) and (b) one CO_2 molecule (bottom panel) as determined using DFT calculations. The molecules are present in the oval shaped channels of the crystal viewed along the c-axis.

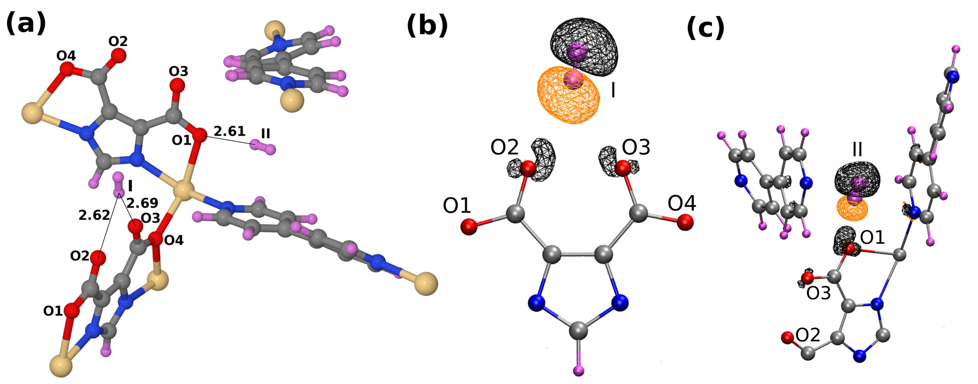

Figure 6.4: (a) Environment around the two adsorbed H_2 molecules at two different sites I and II as obtained from DFT calculations (distances are in Å). (b, c) Isosurface of the difference in the electron density of the system due to the adsorption of the H_2 molecules at I and II sites, respectively. Negative and positive values of electron density difference are shown in orange and black, respectively. Isosurface value is 0.0003 a.u. Colour code: C, gray; H, magenta; N, blue; O, red. Other atoms of MOF are not shown for clarity.

6.3.1 H_2 adsorption

For H_2, the experimental heat of adsorption (varying between 9.0 and 13.3 kJ/mol depending upon the method used) is reproduced when two H_2 molecules interact with the MOF and the calculated value is 8.0 kJ/mol obtained based on Boltzmann distribution. Figure 6.4a shows the positions of the two molecules, named as H_2-I and H_2-II, yielding this value. The contribution of the individual H_2 molecules to the total adsorption energy was also calculated, and the values are -5.74 and -8.00 kJ/mol for H_2-I and H_2-II molecules, respectively. Table 6.1 shows the binding energies of H_2 and CO_2 molecules with the MOF. van der Waals (vdW) corrections to the DFT energies are seen to be crucial to obtain a good comparison to experimental heats of adsorption, for both the gases. To identify the atoms of MOF interacting with the adsorbate and thus to understand the nature of interactions, the differences of electron densities are examined. Figures 6.4b and 6.4c show the difference plot of electron density. It is calculated as $\rho(MOF + H_2) - \rho(MOF) - \rho(H_2)$, where ρ is the electron density and the latter two terms are calculated for the pure MOF and for a H_2 molecule in the gas phase, respectively. A change in electron density of MOF atoms surrounding the H_2 molecules can be clearly seen. H_2-I molecule lies nearly in the plane of the imidazolium ring with one of its atoms slightly positively charged. The latter interacts electrostatically with the two free oxygens (O2 and O3) of the carboxylate groups of the Himdc linker (Figure 6.4a). The distances of this H_2 atom from these two free oxygen atoms are 2.62 and 2.69Å. The H_2-II molecule interacts in two ways: one is the electrostatic interaction between H_2 and the oxygen (O1) (which is bonded to the metal atom) atoms, and other is the interaction of the π-electron cloud over the pyridine ring with the H_2 molecule. This H_2 molecule is at a distance of 2.61Å from the oxygen atom (O1), and it lies between two pyridine rings at almost equal distance from both, with its molecular axis parallel to the plane of each ring (Figure 6.4a). The distances of this H_2 atom from these two free oxygen atoms are 2.62 and 2.69Å.

6.3.2 CO_2 adsorption

The binding energy for CO_2 adsorption is calculated to be -39.14 kJ/mol which is slightly larger than the experimental estimate of -35.4 kJ/mol. This overestimate could be possibly due to the vdW parameters employed here. These were originally developed to describe systems in the gas phase. It has been recently shown that these parameters could overestimate the vdW contribution to the total energy in the condensed state. [34] One needs a good qualitative description of these long-range interactions in periodic systems to be able to accurately reproduce the experimental heats of adsorption. The environment around the CO_2 molecule present within the MOF is shown in Figure 6.5a.

Three possible kinds of interaction between CO_2 and MOF are identified, based purely on its location. The primary contribution to the binding energy is likely to come from the interaction of the electron deficient carbon atom of CO_2 with the lone

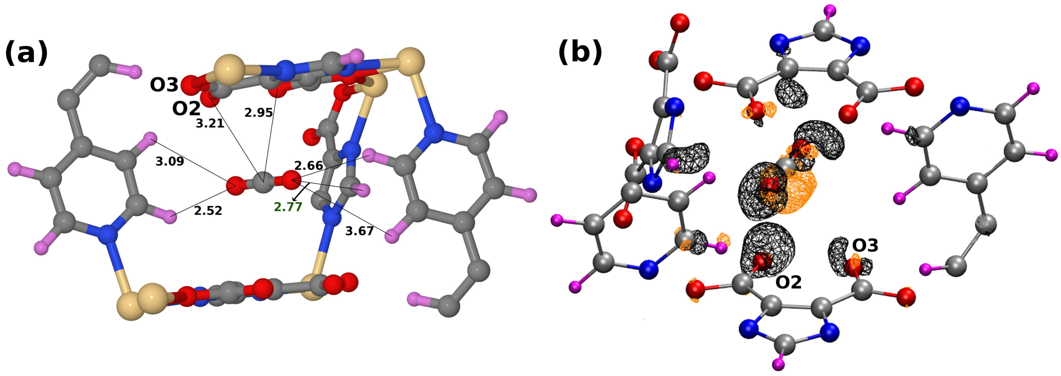

Figure 6.5: (a) View of the environment around the adsorbed CO_2 molecule obtained from DFT calculations (measured distances are in Å). Other atoms of the MOF are not shown for the sake of clarity. (b) Isosurface of the difference in the electron density of the system due to the adsorption of CO_2 molecule. Negative and positive electron density differences are shown in orange and black, respectively. The isosurface value is 0.0006 a.u. Colour code: C, gray; H, magenta; N, blue; O, red. Other atoms of MOF are not shown for clarity.

pairs of the two free oxygen atoms (O2 and O3) of carboxylate groups as shown in Figure 6.5a. This molecule is at a distance of 2.95 and 3.21Å from the two oxygens with its molecular axis parallel to the plane of imidazolium ring. A slight deviation of the backbone angle of CO_2 to a value of 178.1° is seen, with the carbon of the CO_2 bending toward the two free oxygen atoms. [35] The observed asymmetry in the measured distances from the carbon atom to the two carboxylate (free) oxygens is due to the existence of very weak hydrogen-bonding between one of the oxygen atoms of the CO_2 molecule and the acidic hydrogen of imidazolium ring as shown in Figure 6.5a. The hydrogen bond distance is 2.79Å and angle is 105.8°. This system is possibly further stabilized by a Coulombic interaction between the two oxygen atoms of CO_2 and the hydrogens of the pyridine ring. All these interactions are clearly captured in a plot of the difference in the electron density brought upon the system because of the adsorption of CO_2 as shown in Figure 6.5b.

6.4 Conclusions

In summary, the locations of gas molecules have been determined in a pillared-layer framework of Cd(II), $[\mathrm{Cd}\ (\mathrm{bipy})_{0.5}(\mathrm{Himdc})](\mathrm{DMF})]_n$ (**1**), (bipy = 4,4-bipyridine and Himdc = 4,5-imidazoledicarboxylate) using DFT calculations. The high adsorption energy for H_2 (estimated to be between 9.0 and 13.3 kJ/mol depending upon the method used) and of CO_2 (35.4 kJ/mol) in **1'** is realized by the interactions with pendant oxygen atoms and aromatic pyridyl moieties. DFT calculations quantitatively agree with the experimental values of heat of adsorption and are also able to uncover the nature of interactions between H_2 (or CO_2) with the atoms of the MOF. This has been made possible through detailed structural analyses augmented by an analysis of the electron density. The experimental and theoretical investigations unequivocally suggest that the high polarity of the pore surfaces decorated by the oxygen atoms and aromatic rings provide significant contribution for the high heat of adsorption values. Thus, by modulating the pore environment via immobilizing the hetero atoms (N, O, F) in the pore surface, the gas adsorption properties of the resulting MOF can be fine-tuned. This affords a methodology for the development of high capacity of H_2/CO_2 storage materials that may operate at ambient conditions which is significant in the context of global energy and environmental issues.

Bibliography

[1] Hulvey, Z.; Sava, D. A.; Eckert, J.; Cheetham, A. K. *Inorg. Chem.* **2011**, *50*, 403–405.

[2] Hazra, A.; Kanoo, P.; Maji, T. K. *Chem. Commun.* **2011**, *47*, 538–540.

[3] Uemura, K.; Maeda, A.; Maji, T. K.; Kanoo, P.; Kita, H. *Eur. J. Inorg. Chem.* **2009**, 2329–2337.

[4] Ferey, G.; Latroche, M.; Serre, C.; Millange, F.; Loiseau, T.; Percheron-Guegan, A. *Chem. Commun.* **2003**, 2976–2977.

[5] Rowsell, J. L. C.; Yaghi, O. M. *J. Am. Chem. Soc.* **2006**, *128*, 1304–1315.

[6] Dinca, M.; Dailly, A.; Tsay, C.; Long, J. R. *Inorg. Chem.* **2008**, *47*, 11–13.

[7] Vaidhyanathan, R.; Iremonger, S. S.; Shimizu, G. K. H.; Boyd, P. G.; Alavi, S.; Woo, T. K. *Science* **2010**, *330*, 650–653.

[8] Demessence, A.; D'Alessandro, D. M.; Foo, M. L.; Long, J. R. *J. Am. Chem. Soc.* **2009**, *131*, 8784–8786.

[9] Kanoo, P.; Ghosh, A. C.; Cyriac, S. T.; Maji, T. K. *Chem. Eur. J.* **2012**, *18*, 237–244.

[10] Chen, S. M.; Zhang, J.; Wu, T.; Feng, P. Y.; Bu, X. H. *J. Am. Chem. Soc.* **2009**, *131*, 16027–16029.

[11] Caskey, S. R.; Wong-Foy, A. G.; Matzger, A. J. *J. Am. Chem. Soc.* **2008**, *130*, 10870–10871.

[12] An, J.; Rosi, N. L. *J. Am. Chem. Soc.* **2010**, *132*, 5578–5579.

[13] Gurunatha, K. L.; Uemura, K.; Maji, T. K. *Inorg. Chem.* **2008**, *47*, 6578–6580.

[14] Maji, T. K.; Mostafa, G.; Chang, H. C.; Kitagawa, S. *Chem. Commun.* **2005**, 2436–2438.

[15] Gu, J.-Z.; Lu, W.-G.; Jiang, L.; Zhou, H. C.; Lu, T.-B. *Inorg. Chem.* **2007**, *46*, 5835–5837.

[16] Lu, W. G.; Su, C. Y.; Lu, T. B.; Jiang, L.; Chen, J. M. *J. Am. Chem. Soc.* **2006**, *128*, 34–35.

[17] Liu, Y. L.; Kravtsov, V. C.; Larsen, R.; Eddaoudi, M. *Chem. Commun.* **2006**, 1488–1490.

[18] Fang, R. Q.; Zhang, X. M. *Inorg. Chem.* **2006**, *45*, 4801–4810.

[19] Spek, A. L. *J. Appl. Crystallogr.* **2003**, *36*, 7–13.

[20] Matsuda, R.; Tsujino, T.; Sato, H.; Kubota, Y.; Morishige, K.; Takata, M.; Kitagawa, S. *Chem. Sci.* **2010**, *1*, 315–321.

[21] J., H.; P., B. J.; M., B.; P., F.; E., F.; S., G.; D., M.; M., P.; E., T. M. CPMD, Version 3.13.2; Max Planck Institut fuer Festkoerperforschung: Stuttgart. 1990.

[22] Troullier, N.; Martins, J. L. *Phys. Rev. B* **1991**, *43*, 1993–2006.

[23] Becke, A. D. *Phys. Rev. A* **1988**, *38*, 3098–3100.

[24] Lee, C. T.; Yang, W. T.; Parr, R. G. *Phys. Rev. B* **1988**, *37*, 785–789.

[25] Car, R.; Parrinello, M. *Phys. Rev. Lett.* **1985**, *55*, 2471.

[26] Martyna, G. J.; Klein, M. L.; Tuckerman, M. *J. Chem. Phys.* **1992**, *97*, 2635–2643.

[27] Sillar, K.; Hofmann, A.; Sauer, J. *J. Am. Chem. Soc.* **2009**, *131*, 4143–4150.

[28] Grimme, S. *J. Comput. Chem.* **2006**, *27*, 1787–1799.

[29] Jmol, An open-source Java viewer for chemical structures in 3D; http://www.jmol.org/.

[30] McMahon, B.; Hanson, R. M. *J. Appl. Crystallogr.* **2008**, *41*, 811–814.

[31] Humphrey, W.; Dalke, A.; Schulten, K. *J. Mol. Graphics* **1996**, *14*, 33–38.

[32] Kuc, A.; Heine, T.; Seifert, G.; Duarte, H. A. *Theor. Chem. Acc.* **2008**, *120*, 543–550.

[33] Arean, C. O.; Chavan, S.; Cabello, C. P.; Garrone, E.; Palomino, G. T. *ChemPhysChem* **2010**, *11*, 3237–3242.

[34] Bhargava, B. L.; Balasubramanian, S. *Chem. Phys. Lett.* **2007**, *444*, 242–246.

[35] Bucko, T.; Hafner, J.; Lebegue, S.; Angyan, J. G. *J. Phys. Chem. A* **2010**, *114*, 11814–11824.

Chapter 7

Unusual Room Temperature CO_2 Uptake in a Fluoro-Functionalized MOF: Insights from Theoretical Studies

7.1 Introduction

For real time applications, it is important to design a MOF that can capture CO_2 efficiently from flue gas at low pressures at room temperature. The large quadrupole moment of the CO_2 molecule and its predominant Lewis acidic character can favour

---

"Unusual room temperature CO_2 uptake in a fluoro-functionalized MOF: insight from Raman spectroscopy and theoretical studies" *Chem. Commun.* **2012**, *48*, 8487-8489 - Reproduced by permission of The Royal Society of Chemistry. `http://pubs.rsc.org/en/content/articlelanding/2012/CC/C2CC34276F` interactions with the large π-clouds and electronegative atoms which build a framework solid. In the recent past, fluoro-functionalized (e.g. -PF_6, -SiF_6) coordination polymers have proven to be highly promising for capturing CO_2 at low pressures. [1, 2] In this scenario, a metal organic framework, $[Zn(SiF_6)(pyz)_2].2MeOH_n$ (**1**), was prepared and its desolvated form (**1'**) was examined for gas storage capability by measuring adsorption isotherms. The channels along the c-direction in this compound are lined up with highly polar -$SiF_6{}^{2-}$ moieties ligated to Zn(II). It has a 3D framework structure with α-Po type topology where 2D $Zn(pyz)_{2n}$ layers are pillared by axially coordinating $SiF_6{}^{-2}$ ligands. The framework has 1D channels (4.5 x 4.5 $Å^2$) where non-coordinating pendant fluorine atoms are exposed to the pore surface (Figure 7.1a and b).

It is a well-known fact that gas uptake decreases with increasing temperature because of the higher kinetic energy of adsorbates and weaker adsorbate-adsorbent interaction at elevated temperatures. As the pore surface is decorated with strongly electronegative fluorine atoms, it is envisioned that compound **1** would exhibit high CO_2 uptake based on electrostatic interactions. Interestingly, the compound adsorbs higher amounts of CO_2 at elevated temperatures (273 and 298 K) than at 195 K. An in-depth understanding of the mechanism involved in such an unusual process cannot be readily obtained from the adsorption isotherms. Theoretical studies including molecular dynamics have been employed to obtain microscopic insight into the mechanistic aspects leading to this uncommon adsorption behaviour.

7.2 Computational details

Periodic Kohn-Sham density functional theory (DFT) calculations were performed using the CP2K package. [3] Geometry optimizations as well as molecular dynamics simulations were carried out using the QUICKSTEP module of CP2K. Simulations were carried out in a super cell of size 2 x 2 x 2 of the experimental unit cell. CP2K

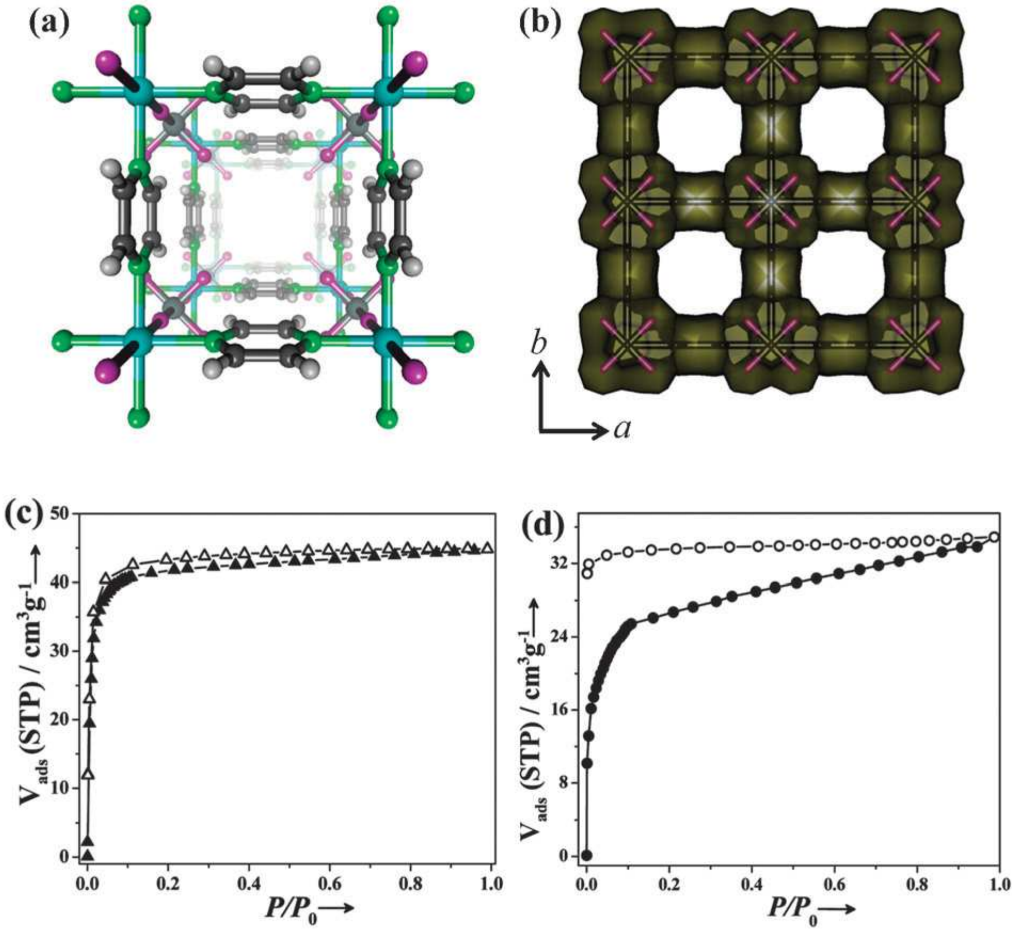

Figure 7.1: (a) View of the 1D pore showing that electronegative pendant fluorine atoms are aligned on the pore surface; (b) CPK diagram showing pores along the c-direction; (c) CO_2 adsorption-desorption isotherm measured at 298 K; (d) CO_2 adsorption-desorption isotherm measured at 195 K.

uses a mixed basis set in which the Kohn-Sham orbitals are expanded in an atom centered Gaussian basis set while the electronic charge density is described using an auxiliary plane wave basis set. Valence electrons were treated with the BLYP functional in the double-zeta single polarized basis set. [4–6] In addition, empirical van der Waals corrections prescribed by Grimme were employed. [7] Electron density was described with an energy cutoff of 280 Ry and the effect of core electrons and nuclei were represented using norm-conserving pseudopotentials of Goedecker-Teter-Hutter. [8] During the geometry optimization, component of forces on every atom were less than 10^{-4} a.u. To calculate the binding energy of CO_2 molecule with the MOF, first, geometry optimization of MOF and of one CO_2 adsorbed in the MOF (in the ratio of one CO_2 per formula unit of MOF) was carried out with CP2K package until the forces were converged. The energy of a geometry optimized, free CO_2 was also calculated. Binding energy was calculated using the following formula,

$$\Delta E = E(MOF + CO_2) - E(MOF) - E(CO_2) \tag{7.1}$$

where E(MOF+CO_2), E(MOF) and E(CO_2) represent the total energy of MOF with CO_2, MOF and CO_2 molecule, respectively.

Born-Oppenheimer molecular dynamics calculations were carried out using the hybrid Gaussian and plane wave basis as implemented in CP2K. Simulations were run at two temperatures, 195 and 300 K. Nóse-Hoover thermostat was used to maintain the temperature of the system at these values. [9] A time step of 0.5 fs was used to integrate the equations of motion. At each temperature, a 10 ps trajectory was generated of which the last 7 ps trajectory was used for analysis. Trajectory was visualized using VMD. [10]

7.3 Results and discussion

The microscopic nature of CO_2-MOF interactions as well as the interesting dynamics of the pyrazine rings were studied using Kohn-Sham density functional theory augmented by empirical van der Waals corrections. [11] Geometry optimization of **1'** results in a structure which has noteworthy differences from that of the experimental one determined for **1**. In this structure (shown in Figure 7.2), the pyrazine moieties along the c-axis are slanted. In **1**, the planes of two adjacent pyrazine rings are coplanar, whereas they are not so in the optimized geometry of **1'**. The plane formed by them makes a canting angle of 17.21 ° with the (200) plane containing Zn(II) and Si atoms. The optimized configuration of CO_2 in **1'** is when it is located at the center of the unit cell with its long axis along the c-direction. This binding is due to a strong electrostatic interaction between CO_2 and the pendant fluorine atoms exposed to the pore surface, as expected. The carbon of CO_2 has four fluorine neighbours at a distance of 3.39Å. The specific nature of charge transfer between the gas molecule and the MOF can be obtained by an examination of difference maps of electron density between the adsorbed system and that of the pure gas and the **1'**. The same is shown in Figure 7.2 in two different orientations. The fluorine atoms gain a partial electronic charge at the expense of the carbon atom of CO_2.

The π-system of the pyrazine too loses partial electronic charge upon adsorption of CO_2 (Figure 7.3). The charge transfer with the SiF_6 moieties is found to be larger in magnitude than with the π-system. The calculated enthalpy of adsorption is 48.03 kJ mol^{-1} which compares well with the experimental value of 46.7 kJ mol^{-1}. DFT calculations predict a maximum uptake of one CO_2 per formula unit of MOF; however, the experimental adsorption isotherm saturates at a value of 0.66. The difference can be explained to be due to the inaccessibility of pores whose openings are buried within the experimental sample and are thus unavailable for the gas. The problem is exacerbated due to the one dimensional nature of the pores. [12]

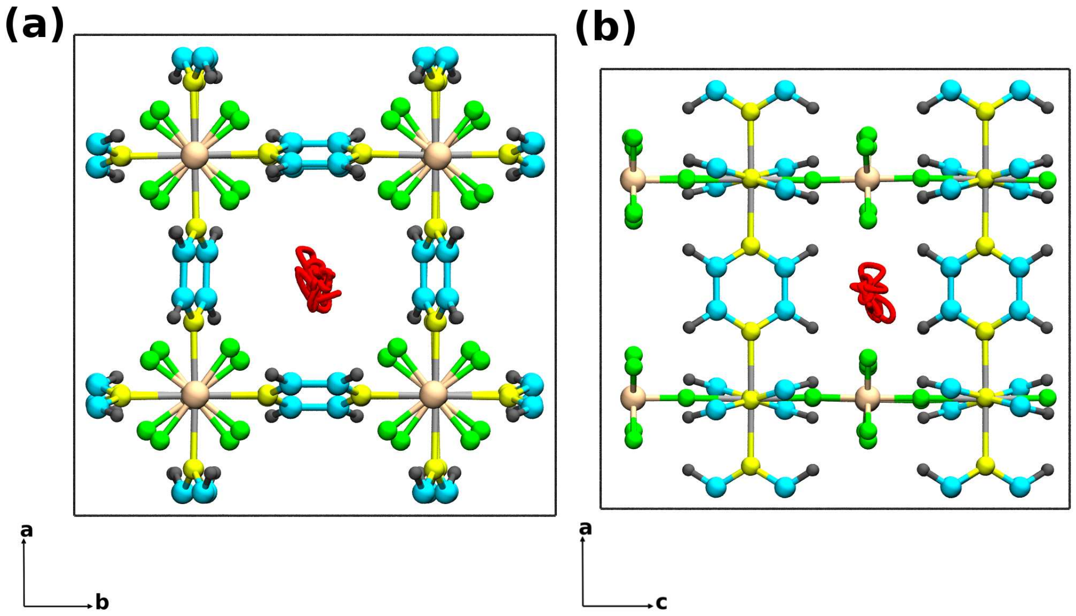

Figure 7.2: Trajectory of center of mass of CO_2 within MOF, shown in two crystallographic directions, obtained from Born-Oppenheimer molecular dynamics simulation at 195 K (shown in red). Panel (a) shows view along crystallographic c-axis. Adjacent pyrazine rings along the c-axis are not coplanar, (b) shows view along b-axis. Coordinates of the MOF shown here are those obtained from geometry optimization at zero Kelvin.

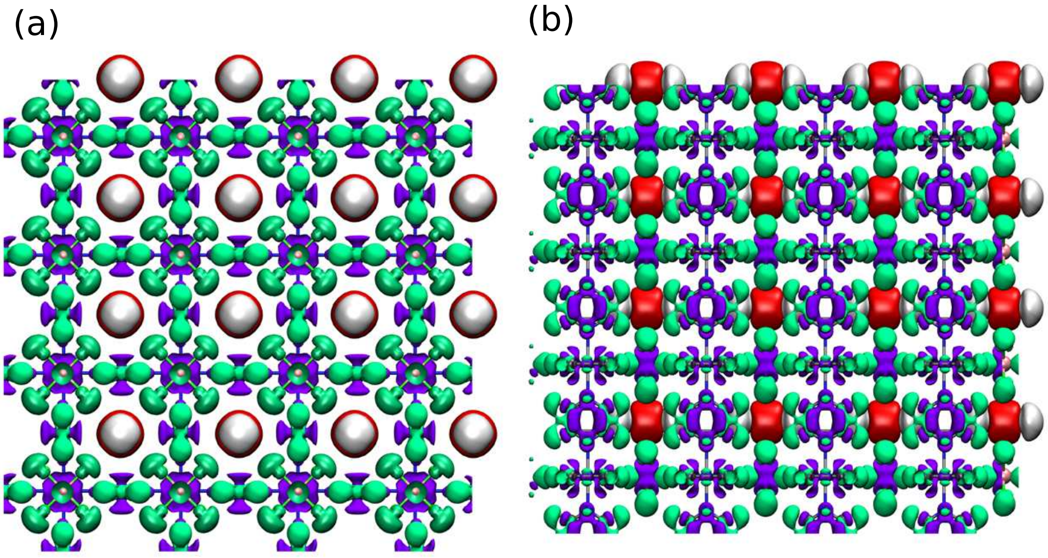

Figure 7.3: Electron density difference maps of **1'** plotted using an iso value of 0.00009 a.u. obtained from Kohn-Sham density functional theory. (a) View along c-axis and (b) view along a-axis. Regions in red and violet colour show electron loss and those in white and green show electron gain upon adsorption of CO_2. Loss of electrons from the π-cloud of pyrazines forms dumbbell-shaped iso surfaces (violet colour).

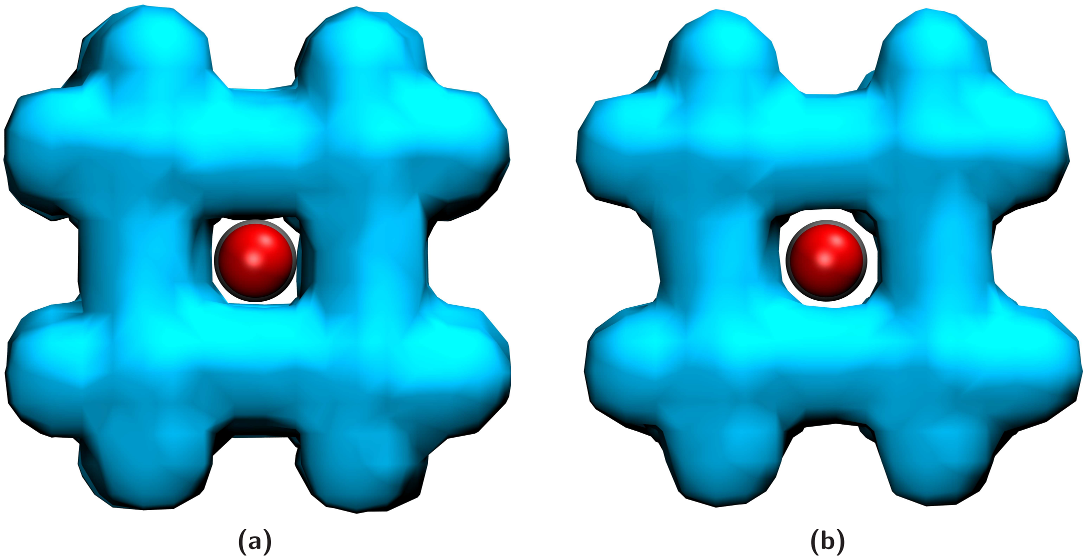
(a)

(b)

Figure 7.4: Time averaged structure of **1'** obtained from Born-Oppenheimer molecular dynamics simulations at temperatures (a) 195 and (b) 300 K. The blue surface denotes the position of any MOF atom with an isosurface value of 0.3 $Å^3$. The CO_2 molecule is shown inserted to easily identify the reduction in pore size at 195 K.

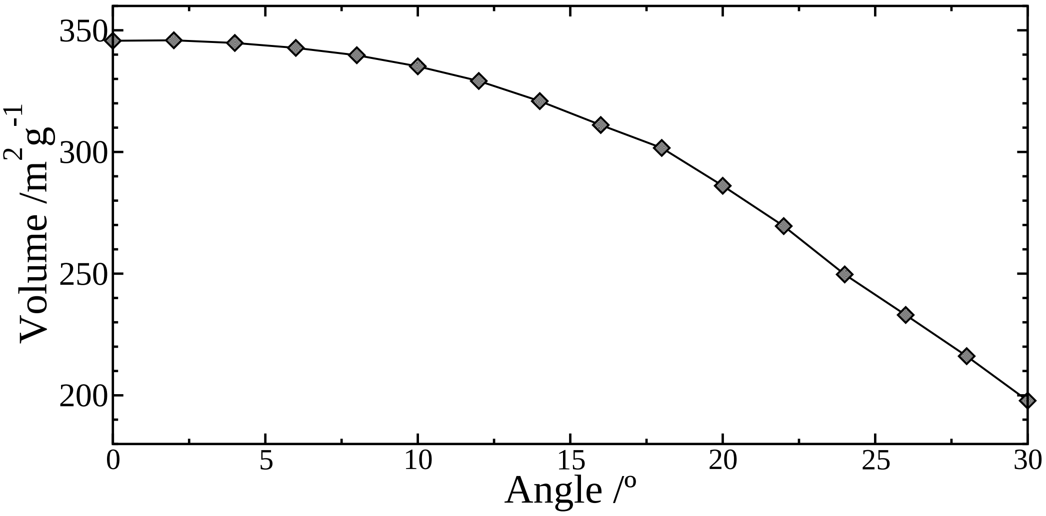

Figure 7.5: Calculated accessible surface area for CO_2 molecule as a function of the angle between planes of adjacent pyrazine rings and that formed by Si-Zn-Si atoms. [13]

The unusual temperature dependence of CO_2 uptake in this MOF system was also examined using DFT based Born-Oppenheimer molecular dynamics simulations. These were carried out for **1'** at temperatures of 195 and 300 K. The Born-Oppenheimer (BOMD) trajectory was generated for 10 ps, which is many times longer than the typical time taken for the flexing of the pyrazine rings. The time-averaged coordinates of each of the atoms in the MOF were obtained from this trajectory and these structures are shown in Figure 7.4. Such an analysis vividly brings out the vibrationally averaged pore surface. The pore volume is indeed smaller at 195 K than at 300 K, which can be ascribed clearly to the deviation (at low temperature) of adjacent pyrazine rings from coplanarity. The non-coplanarity of the pyrazine rings can also be identified through vibrational spectroscopy. Raman spectra of the pristine MOF show the lifting of the degeneracy of the C-H bond stretches due to the non-coplanarity. When the pyrazine groups are coplanar, one obtains a single band for the C-H stretch which splits into two peaks at low temperatures. [14] The impact of this reduction on the surface area accessible for carbon dioxide can be estimated. Using a UFF model for CO_2 in this MOF, we obtain the surface area for a MOF structure with coplanar pyrazine rings to be 345 m^2 g^{-1} which reduces to a value of 320 m^2 g^{-1} when the angle between the ring plane and that formed by Si, Zn(II) and Si atoms is 14°(Figure 7.5). [13, 15] Clearly, this reduction of 6% in the accessible surface area is the cause for the reduced uptake of CO_2 at 195 K.

7.4 Conclusions

In summary, in contrast to the anticipated temperature dependence, an unusual CO_2 adsorption phenomenon in a fluoro-functionalized 3D MOF (**1**) is observed. **1'** adsorbs higher amount of CO_2 gas at 298 K than it does at 195 K which has been explained to be due to the flexibility of the pyrazine rings. Raman spectroscopic studies on flexibility are consistent with these calculations. Simulations reveal that the slanted pyrazine rings in **1'** with an angle of 17.28° with respect to the (200) Zn(II)Si plane at low temperature, block the channel windows and thus reduce the uptake amount. This unprecedented observation would pave the way for designing new types of MOFs with room-temperature CO_2 uptake characteristics for potential applications in storage and separation.

Bibliography

[1] Burd, S. D.; Ma, S.; Perman, J. A.; Sikora, B. J.; Snurr, R. Q.; Thallapally, P. K.; Tian, J.; Wojtas, L.; Zaworotko, M. J. *J. Am. Chem. Soc.* **2012**, *134*, 3663–3666.

[2] Liu, J.; Thallapally, P. K.; McGrail, B. P.; Brown, D. R.; Liu, J. *Chem. Soc. Rev.* **2012**, *41*, 2308–2322.

[3] VandeVondele, J.; Krack, M.; Mohamed, F.; Parrinello, M.; Chassaing, T.; Hutter, J. *Comput. Phys. Commun.* **2005**, *167*, 103–128.

[4] VandeVondele, J.; Hutter, J. *J. Chem. Phys.* **2007**, *127*, 114105.

[5] Becke, A. D. *Phys. Rev. A* **1988**, *38*, 3098–3100.

[6] Lee, C.; Yang, W.; Parr, R. G. *Phys. Rev. B* **1988**, *37*, 785–789.

[7] Grimme, S. *J. Comput. Chem.* **2006**, *27*, 1787–1799.

[8] Hartwigsen, C.; Goedecker, S.; Hutter, J. *Phys. Rev. B* **1998**, *58*, 3641–3662.

[9] Martyna, G. J.; Klein, M. L.; Tuckerman, M. *J. Chem. Phys.* **1992**, *97*, 2635–2643.

[10] Humphrey, W.; Dalke, A.; Schulten, K. *Journal of Molecular Graphics* **1996**, *14*, 33 – 38.

[11] Poloni, R.; Smit, B.; Neaton, J. B. *J. Phys. Chem. A* **2012**, *116*, 4957–4964.

[12] Li, W.; Grimme, S.; Krieg, H.; Moellmann, J.; Zhang, J. *J. Phys. Chem. C* **2012**, *116*, 8865–8871.

[13] Duren, T.; Sarkisov, L.; Snurr, R. Q. Accessible surface area code, Copyright © 2007. http://www.see.ed.ac.uk/t̃duren/research/surface_area/ortho/.

[14] Kanoo, P.; Reddy, S. K.; Kumari, G.; Haldar, R.; Narayana, C.; Balasubramanian, S.; Maji, T. K. *Chem. Commun.* **2012**, *48*, 8487–8489.

[15] Rappe, A. K.; Casewit, C. J.; Colwell, K. S.; Goddard, W. A.; Skiff, W. M. *J. Am. Chem. Soc.* **1992**, *114*, 10024–10035.

Chapter 8

Breathing Effect and Gate-Opening in an Interpenetrated Metal-Organic Framework: A Computational Study

8.1 Introduction

Porous coordination polymers can be classified in many ways; among them, the ones based on the rigidity of the solid is the focus of the current chapter. MOFs can also be classified as either rigid or flexible; the latter are better recognised as soft porous crystals as they readily undergo structural deformation. [1–3] In most cases, the phase of the compound containing the guest molecule is dissimilar from the guest eliminated structure (activated). The polycrystalline nature of the latter is the biggest hurdle to get a better insight. Guest molecules (solvents) present in the pore stabilize the pore structure from collapsing. Once they are removed, the framework tries to gain stability by structural transformation either through rearrangement of (a) nets without any covalent bond breaking or (b) coordination environment by covalent bond breaking. [2] They also result in significant change in pore volume which is known as breathing effect. In many instances, a CO_2 gated-adsorption profile has been observed in these materials which is also gas-specific. [1]

A two-fold entangled compound, **1**, $\{[Zn_4(1,4\text{-ndc})_4(bpe)_2].2\text{-OMeEtOH.DMF.}2MeOH.H_2O\}_n$ (ndc = 1,4-napthalenedicarboxylate; bpe = 1,2-bis-4-pyridylethane; 2-OMeEtOH = 2-methoxyethanol; DMF = N, N-dimethylformamide) was synthesized by the research group of Prof. Tapas Maji at JNCASR. Its crystal structure was determined from single crystal X-ray diffraction. It consists of a paddle-wheel type secondary building unit, $Zn_2(COO)_4$ which is connected by the 1,4-ndc moiety along the ac-plane to create a 2D-sheet like arrangement. These square shaped 2D nets are pillared by *bpe* along the b axis to form a 3D framework structure (Figure 8.1). The space that a single net provides along the b-direction is adequate for the growth of another net leading to two-fold entanglement. Such phenomenon creates micropores along the b-axis which are occupied by solvent molecules. The void space available in this MOF is 478.1 Å^3 (7.8% of total cell volume). On heating this, it loses solvent molecules (desolvated MOF **1'**, $Zn_4(1,4\text{-ndc})_4(bpe)_2$) and the powder X-ray diffraction (PXRD) pattern of this structure is different from that of the as-synthesized MOF, **1**. This phenomenon is not unusual in framework materials and clearly indicates the flexibility associated with the structure. Due to the loss of single crystallinity, the crystal structure of the desolvated form (**1'**) could not be obtained from experiments. The lack of knowledge of the structure of the desolvated framework imposes a hurdle to the complete understanding of phenomena such as geometry change on gas adsorption, gate-opening, selective adsorption, etc.

The adsorption characteristics of the desolvated MOF **1'** at 195 K are shown in

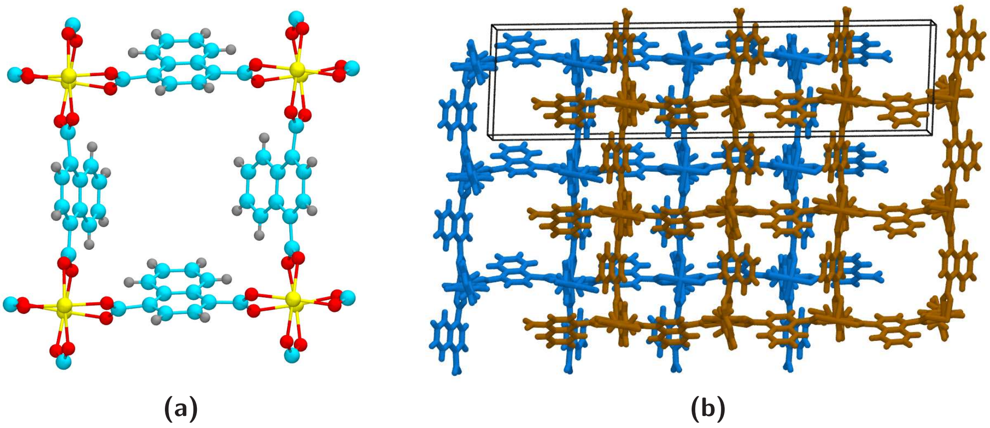
(a) (b)

Figure 8.1: a) Building unit of MOF **1** b) Its supercell of size 3x1x1 shown along b-direction. Solvent molecules are not shown.

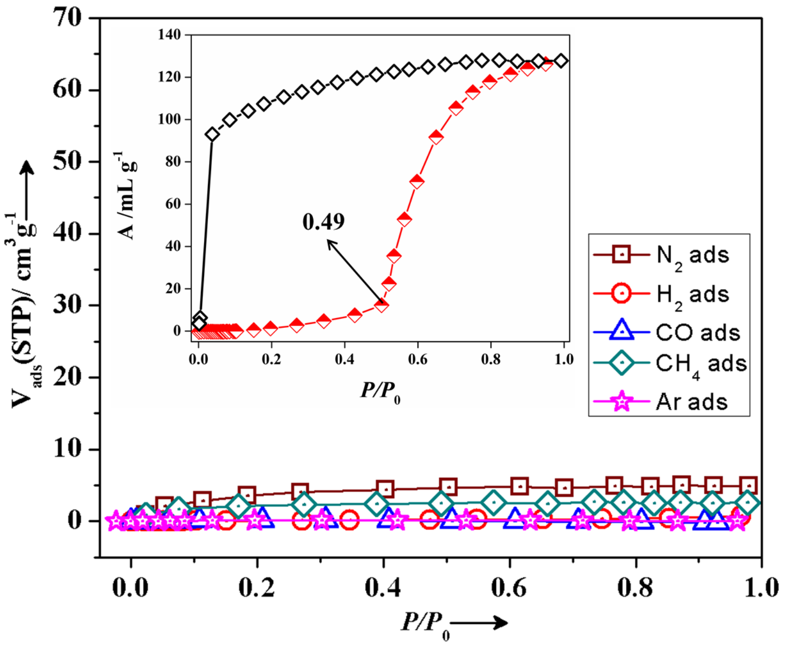

Figure 8.2: Experimentally determined CO_2, N_2, H_2, Ar adsorption isotherms of **1'** at 195 K.

Figure 8.2. This MOF does not show any uptake of CO_2 in the low pressure region. Beyond a threshold pressure (P_{th}) which is P/P_0 ~0.49, it shows a sudden rise in the uptake of CO_2 uptake. The maximum amount at the saturation level is 107 mL/g (~21 wt %). Until P/P_0 ~0.49, the channels are not accessible to CO_2 and beyond that, a sudden uptake indicates that pores become accessible to CO_2 – a process discussed above as gate-opening phenomenon. The large hysteresis signifies that the trapped CO_2 molecules interact significantly with the channel surface and only at very low pressure ($P/P_0 > 0.05$), those are released. Due to the lack of crystal structure data of **1'**, the changes which occurred after the removal of solvent molecules is not known. At 195 K, other gases like Ar, H_2, N_2, O_2 and CO are completely excluded making **1'** selective towards CO_2.

In situ technique reveals the pathway of structural rearrangement during adsorption process. Figure 8.3 shows the PXRD patterns during CO_2 adsorption at 195 K. Till point B, the PXRD pattern remains similar to desolvated phase (A) but after that at point C (saturated value) a distinct change occurs. Till point D in the desorption curve PXRD pattern remains same as that of D and at point E it again becomes similar to desolvated structure (point A). Most importantly, the PXRD pattern obtained at point C resembles to the PXRD patterns of as-synthesized **1**. Hence it can be perceived that after CO_2 diffusion into the pores the desolvated (heated) phase transforms to a phase which is very similar to as-synthesized. In other words, CO_2 compels the structural rearrangement.

Computational techniques have emerged as vital tools in exploring model crystal structures, provided the cell parameters of the desolvated MOF are known. These parameters can be used as target in a systematic approach towards finding the structure along with minimization techniques at either classical or ab initio level. Several researchers have employed UFF force field that reduces the computational cost tremendously compared to DFT calculations. [2, 4, 5] However, the accuracy of

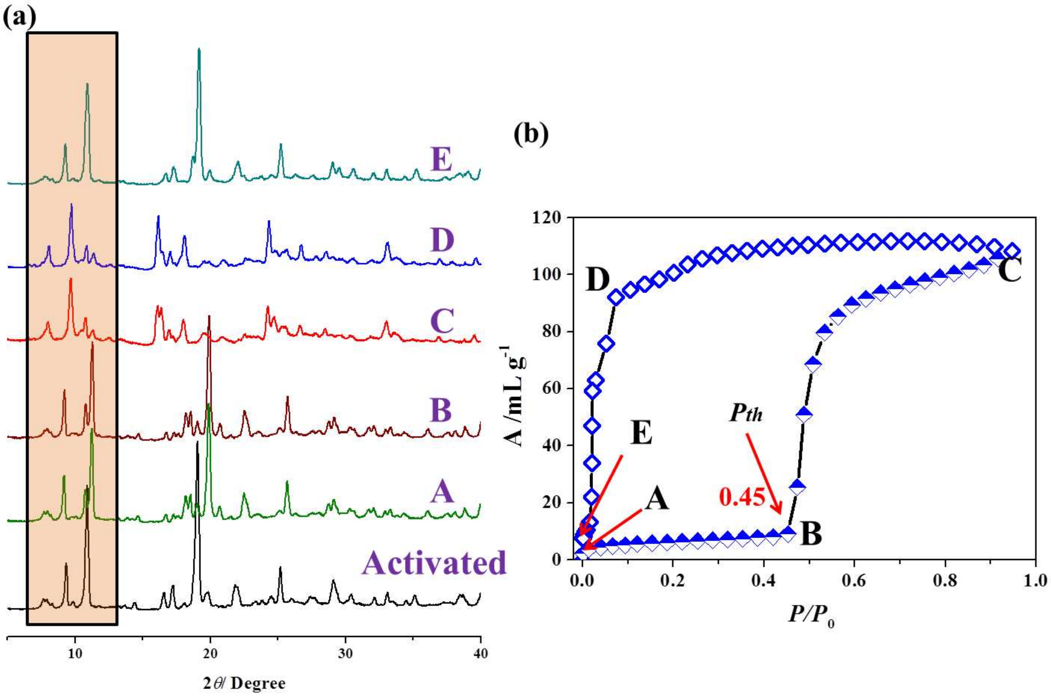

Figure 8.3: a) In situ powder X-ray diffraction (PXRD) patterns collected during CO_2 adsorption on **1**' at 195 K. b) Adsorption isotherm of CO_2 gas at 195 K.

such calculations entirely depends on force field parameters. Here, density functional theory is used to predict a model structure (called here as **1"**) for the desolvated MOF **1'**. The model structure is validated by a comparison with the powder XRD pattern of **1**. The mechanism of transformation from **1** to **1"** is then understood by a comparison of the crystal structures.

8.2 Computational details

Density functional theory (DFT) calculations presented here were carried out using CP2K software. [6, 7] All valence electrons were treated in a mixed basis set using molecularly optimized double-zeta single polarization (DZVP) short range basis with a density cutoff of 280 Ry. The effect of core electrons and nuclei was handled by using norm-conserving Goedecker-Teter-Hutter (GTH) pseudopotentials. [8] The

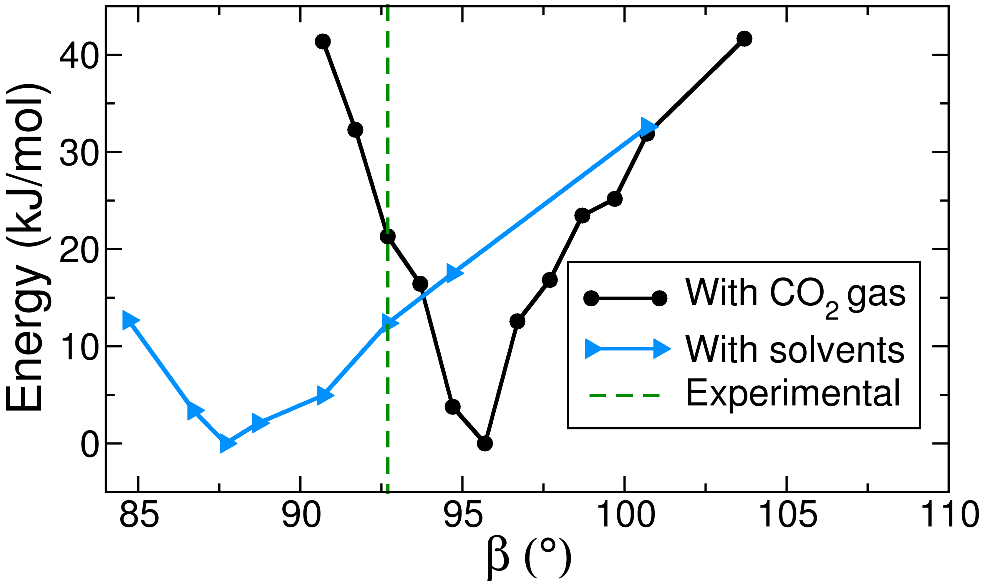

Figure 8.4: Relative energies (in kJ/mol) of **1** as a function of angle β obtained when MOF is fully loaded with either solvent molecules or CO_2 gas. Values are given with respect to the corresponding minima.

Becke, Lee, Yang and Parr (BLYP) functional was used to account for electron exchange and correlation interactions. [9] Empirical van der Waals (vdW) terms developed by Grimme were used to include dispersion interaction. [10] All atomic positions were optimized until each component of force was less than 10^{-4} a.u. The protocols employed to obtain the model structure **1"** for **1'** are given in next section. Binding energy is defined as

$$\Delta E = E(MOF + n(gas)) - E(MOF) - nE(gas) \tag{8.1}$$

where E(MOF + n(gas)) is the energy of the system that consists of 'n' number of gas molecules adsorbed in the MOF while E(MOF) and E(gas) denote energies of neat MOF and the isolated gas molecule, respectively. The energy of gas molecule is evaluated in a simulation cell whose dimensions correspond to the MOF. All molecules are visualized in VMD and Mercury. [11, 12]

Table 8.1: Calculated cell parameters and volume of **1** and **1'** along with their experimental values.

cell parameter	desolvated MOF (**1'**)			as-synthesized MOF (**1**)			fully CO_2 -loaded MOF
	calc.	exp.	deviation (%)	calc.	exp.	deviation (%)	
a (Å)	10.82	10.58	2.3	10.88	10.93	0.46	10.91
b (Å)	16.17	16.19	0.1	16.11	16.21	0.62	16.20
c (Å)	43.02	42.92	0.23	43.34	43.60	0.60	43.24
α ^{o}	90.0	90.0	0.0	90.0	90.0	0.0	90.0
β ^{o}	125.8	119.3	5.40	87.75	92.8	5.39	95.8
γ ^{o}	90.0	90.0	0.0	90.0	90.0	0.0	90.0
volume (Å^3)	6108.2	6409.2	4.7	7590.7	7716.9	1.64	7604.5

8.3 Results and discussions

8.3.1 Desolvated structure

First, the computational protocols were validated by studying the stability of **1**. Starting with the experimental crystal structure and including the solvent molecules, cell parameter and atom coordinate optimizations were performed in an iterative manner. The cell parameters for which an energy minimum was observed is tabulated in Table 8.1. Furthermore, since the β-parameter is a crucial one distinguishing **1** and **1'**, the stability of **1** with respect to β was examined. At each value of β, other cell parameters and atom coordinates were optimized until an energy minimum (for that value of β) was obtained. The total energy of the simulation cell plotted against β is shown in Figure 8.4, exhibits a minimum at 87.8°±1° (Figure 8.4) which is within 1.6% of the experimental value.

To understand the structural transformation from **1** to **1'** and also the underlying reason for the specificity of CO_2 in the gate-opening process, it's important to elucidate the structure of **1'**. The building of model structures from an arbitrary starting point and then refining them by using DFT calculations would be a tedious task. Hence, the atomic positions of **1** were employed as a starting point in arriving

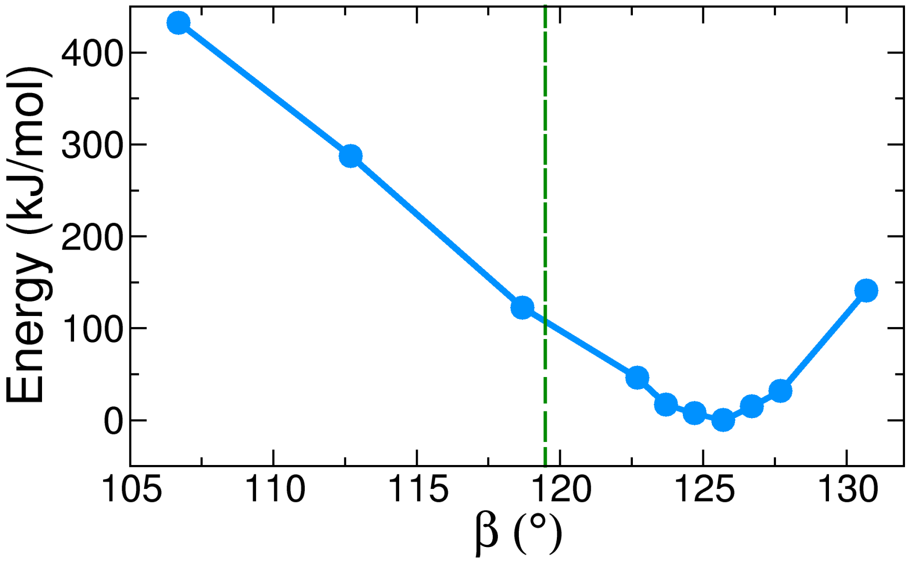

Figure 8.5: Relative energy (in kJ/mol) of **1'** as a function of β-value obtained from density functional theory calculations. Experimental β-value is shown as green dashed line. Error in cell volume between simulations and experiment is 4.7%.

at the structure of **1'**. The experimental cell parameters of both **1** and **1'** are known, so the differences between them can guide towards **1'**. An examination of their cell parameters reveals two differences in the β and c parameters. However, the c parameter of **1'** is related to that of **1** by an integral multiple while other parameters are similar in both the crystals structures.

Utilizing this data, DFT calculations of the desolvated **1** crystal were carried out by changing its cell parameters in a systematic way so as to arrive at the structure of **1'**. At each value of β, an iterative optimization of the other cell parameters and of the coordinates was performed until there was no further change in them. This procedure was repeated for different values of β. The total energy of the crystal as a function of β-angle is shown in Figure 8.5. Values are shown relative to that at the minimum. The energy is a minimum at a β value of 125.7°±1°, which differs from the experimental estimate of 119.3°. The error associated with density is calculated

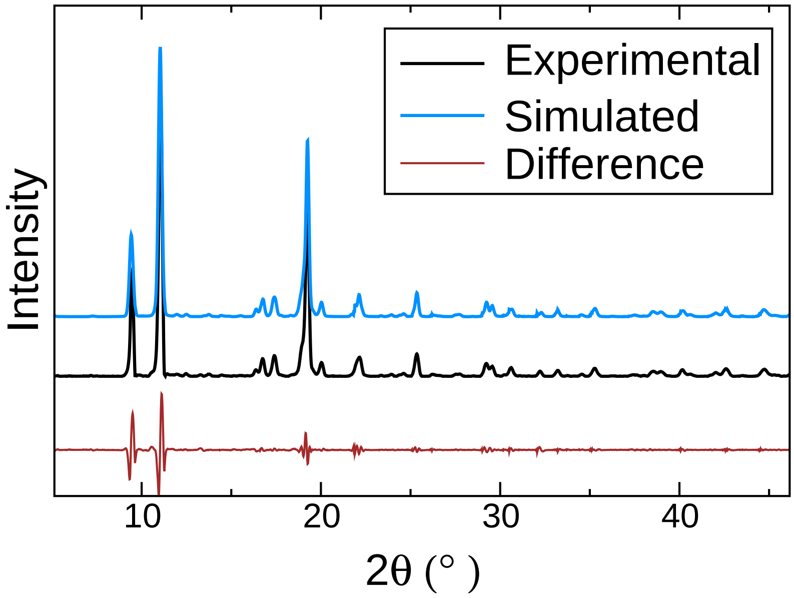

Figure 8.6: Powder XRD pattern of the calculated **1'** structure compared against experiment. The refinement was performed using GSAS software. [13]

to be 4.7%. Though the exact crystal structure of **1** is known experimentally, using computational methods the error in density value is calculated to be 1.6%. Given the approximations involved in DFT, the difference between the densities of **1'** and **1"** is acceptable. Further, the coordinates and cell parameters of **1"** are used as input for Rietveld refinements. Using GSAS program [13], the cell parameters are further refined without changing the atomic positions. The PXRD pattern of this structure is compared against experimental data (**1'**) in Figure 8.6. The PXRD pattern for the calculated structure shows a good match with experiment

As discussed before, **1'**, when exposed to CO_2, transforms back to a structure which is very similar to the as synthesized MOF (**1**). To verify this, another set of calculations were performed by loading CO_2 into MOF **1"**. Figure 8.4 shows the total energy of this system as a function of angle β. The minimum is now present at 95.7°± 1°, which is quite close to the experimental value for **1'** (92.7°). Thus, computation is able to closely reproduce the experimental cell parameters for the as-synthesized MOF, the desolvated MOF and the CO_2-loaded MOF.

8.3.2 Structural changes

On removal of solvent molecules by heating (desolvation process), the interaction energy of the MOF (in its structure **1**) with the solvent is lost. To compensate for this loss, structural rearrangements are likely. Since each net is interacting with the other through weak van der Waals interaction, it is easy for them to move relative to one another. Previous studies on such interpenetrated MOFs show that the rearrangement occurs by rotation around the carboxylate O-O axis without any apparent bond breaking [4], increased coordination around metal atom. [14]

The calculated structure has similar backbone interconnectivity as the as-synthesized framework. The change in b-parameter is marginal upon transformation which is expected to due to strong bond between nitrogen and metal. Two important changes are observed. First, two networks are displaced relative to each other such that a node formed by zinc atoms of one network is moved approximately towards the center of four nodes of another network. Secondly, the naphthalene rings, which exhibit rotational flexibility around the C-C axis (carboxylate carbon), rearranges in order to promote the relative network movements. These changes result in a change in the pore shape along the b-axis from square to parallelogram as shown in Figure 8.7. This conversion is also accompanied with reduction in pore volume as well as cell volume (Table 8.1) as is evident from pore surface parameters. The void space is reduced to 478.1 Å^3 (7.8% of total cell volume).

8.3.3 Effect of gas adsorption

Experimentally, it was observed that MOF **1’** also shows reversible transformation on exposure to CO_2 gas while other gases are not taken up much. To examine the specificity of CO_2 in opening the gate of the MOF, the binding energy of four molecules (CO_2, H_2, N_2 and Ar) with MOF **1’** was calculated. These values are reported in Table 8.2. Here, site-I refers to binding near the naphthalene ring and

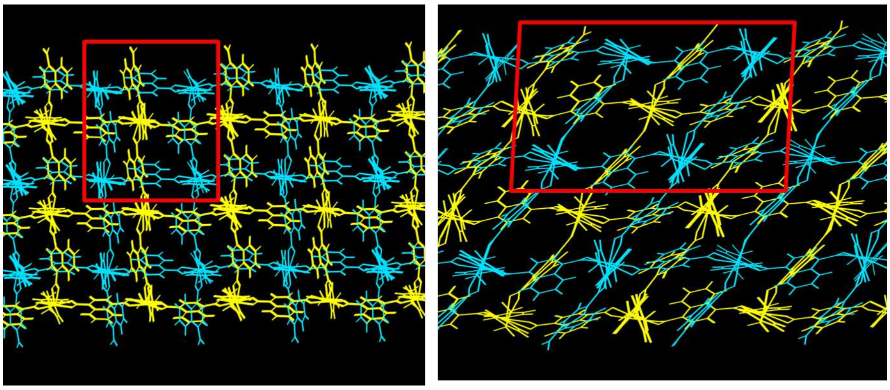

Figure 8.7: Comparison of experimental structure of **1** against the calculated one of **1**". The main difference, that causes the sliding of the nets, is the movement of the linker towards carboxylate group(s) for additional stability (enclosed in red boxes). View along b-axis. More details are given in text.

Table 8.2: Binding energies (kJ/mol) of four gas molecules (CO_2, H_2, N_2 and Ar) calculated for MOF **1**' using density functional theory. Here, site-I and site-II refer to adsorption near aromatic ring and carboxylate group or metal center, respectively.

	site-I		site-II	
	no BSSE	BSSE corrected	no BSSE	BSSE corrected
CO_2	-46.34	-41.70	-29.97	-25.56
H_2	-10.68	-7.39	-8.07	-1.33
N_2	-23.91	-20.42	-21.46	-16.09
Ar	-19.66	-17.96	-16.84	-14.94

site-II refer to that near the metal center. The values near site-I are consistently higher for all gas molecules compared to those in site-II. Among these, the highest binding energy is observed for CO_2 and this value is below -21 kJ/mol for other gases. This value could thus be assumed to be the threshold value for binding energy. Thus, gases whose binding energy is greater than this value can open the pore and get adsorbed into framework.

As discussed before, the nets slide relative to each other so as to gain stability by minimizing the strain developed on removal of solvents and to get an additional strength through the formation of H-bonds between CH_2-CH_2 group and carboxylate group. Due to the sliding, the pore is blocked and eventually does not allow any gas to enter the MOF. So, in order for the reverse transformation, the gas molecule should interact stronger than that of ethane linker and carboxylate group. When it occurs, the network moves towards one of the four nodes to provide enough space for gas molecule.

8.3.4 Role of linker in gate-opening

Another MOF was synthesized by replacing the -CH_2-CH_2 linker with -N=N- linker. Its crystal structure is similar to that of MOF **1** expect linker part. It also undergoes a two-fold entanglement and hence the void space reduces to 27.6% which is similar to that of **1**. Desolvated phase of this MOF (**2'**) is different from as-synthesized as the corresponding PXRD patterns are distinct from each other. At 195 K the desolvated phase shows gated adsorption behaviour for CO_2 and completely rejects other gases like Ar, N_2, O_2, H_2 and CO. The adsorption profile type is similar to that of **1'** but the gate-opening pressure is lowered to 0.17 (Figure 8.8). The change in linker functional group effects the gate-opening pressure as observed. The density functional theory calculations are used to understand the importance of linker in defining gate-opening pressure.

The gate-opening pressure is related to the binding energy of adsorbed gases. Thus, a gas with higher binding energy can open the pore at a lower pressure than one with a lower binding energy. As the calculations discussed here for **1'** demonstrate, an additional factor to consider is the interaction strength between the linker which is present in Net A and the carboxylate group which is located in Net B. This interaction substitutes for the solvent/gas when they are not present, leading to the structural transformation. Thus, a weaker interaction between these entities present in the two nets can result in lower gate-opening pressures. Since the crystal structure of **2'** is not known, the binding energy for CO_2 with it could not be calculated. Instead, the binding energies of the fully CO_2-loaded MOF **1'** and **2'** were

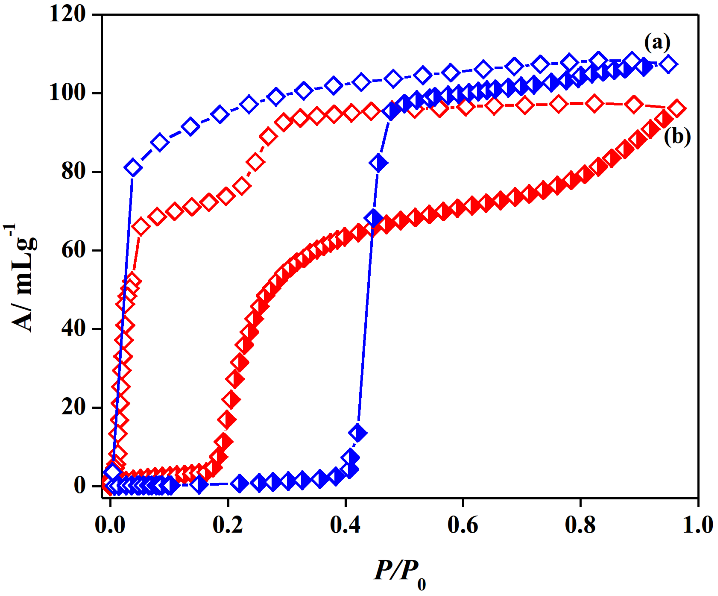

Figure 8.8: Comparison of experimentally determined CO_2 adsorption profiles at 195 K: (a) **1'** (b) **2'**.

calculated and these values are found to be -30.18 and -30.25 kJ/mol, respectively. Since CO_2 binding energies with these MOFs are found to be nearly equal, it can be concluded that the gate-opening pressure in these systems is determined purely by the interaction strength between the linker and carboxylate group. The azo MOF, exhibiting a lower gate-opening pressure must possess a weaker linker-carboxylate interaction than the MOF with the CH_2-CH_2 group. It translates to the fact that fewer CO_2 molecules are required to open **2'** than **1'**.

8.4 Conclusions

Using density functional theory, the possible crystal structure of **1'** has been predicted starting from its as-synthesized phase. The PXRD pattern of modelled structure is in agreement with experiment. Upon desolvation, the structure transforms from porous to non-porous form by sliding of two nets on each other in order to reduce the strain. The calculated gas binding energies with **1'** suggest that they should be in the range from -21 to -30 kJ/mol or higher in order to open the gate. The linker plays an important role in stabilizing the MOF upon guest removal. The strength of interaction between linker and carboxylate groups is found to be proportional to gate-opening pressure. So, one can easily tune the gate-opening pressure simply by changing linker part.

Bibliography

[1] Horike, S.; Shimomura, S.; Kitagawa, S. *Nat. Chem.* **2009**, *1*, 695–704.

[2] Ferey, G.; Serre, C. *Chem. Soc. Rev.* **2009**, *38*, 1380–1399.

[3] Kitagawa, S.; Kitaura, R.; Noro, S.-i. *Angew. Chem. Int. Ed.* **2004**, *43*, 2334–2375.

[4] Serre, C.; Mellot-Draznieks, C.; Surbl, S.; Audebrand, N.; Filinchuk, Y.; Frey, G. *Science* **2007**, *315*, 1828–1831.

[5] Salles, F.; Ghoufi, A.; Maurin, G.; Bell, R.; Mellot-Draznieks, C.; Frey, G. *Angew. Chem. Int. Ed.* **2008**, *47*, 8487–8491.

[6] VandeVondele, J.; Hutter, J. *J. Chem. Phys.* **2007**, *127*, 114105.

[7] VandeVondele, J.; Krack, M.; Mohamed, F.; Parrinello, M.; Chassaing, T.; Hutter, J. *Comput. Phys. Commun.* **2005**, *167*, 103–128.

[8] Hartwigsen, C.; Goedecker, S.; Hutter, J. *Phys. Rev. B* **1998**, *58*, 3641–3662.

[9] Becke, A. D. *Phys. Rev. A* **1988**, *38*, 3098–3100.

[10] Grimme, S. *J. Comput. Chem.* **2006**, *27*, 1787–1799.

[11] Macrae, C. F.; Bruno, I. J.; Chisholm, J. A.; Edgington, P. R.; McCabe, P.; Pidcock, E.; Rodriguez-Monge, L.; Taylor, R.; van de Streek, J.; Wood, P. A. *J. Appl. Crystallogr.* **2008**, *41*, 466–470.

[12] Humphrey, W.; Dalke, A.; Schulten, K. *J. Mol. Graphics Modell.* **1996**, *14*, 33–38.

[13] Larson, A. C.; Von Dreele, R. B. General Structure Analysis System (GSAS), Los Alamos National Laboratory Report LAUR 86-748 (2000).

[14] Henke, S.; Schmid, R.; Grunwaldt, J.-D.; Fischer, R. A. *Chem. Eur. J.* **2010**, *16*, 14296–14306.

Appendix A

Theoretical Methods

In this section, some of the theoretical methods used in this thesis are described in brief for the sake of completeness. Complete details of these techniques are documented in several textbooks as well as reviews. [1–10]

A.1 Molecular dynamics

Molecular dynamics (MD) is a method used to generate the trajectory of an interacting system of atoms in phase space. It can be naturally extended to ensembles other than just microcanonical. Thus, control of temperature, pressure and any other external variable is possible in MD. In principle, since every thermodynamic variable can be expressed as a function of position and momentum, it is possible to calculate all the physical properties (i.e., static structure as well as transport) using MD simulations. The Lagrangian (L), which gives information about dynamics of the system, is a function of kinetic and potential energies and these are related by,

$$L(\mathbf{r}_N, \dot{\mathbf{r}}_N) = \sum_{i=1}^{N} \frac{1}{2} m_i \dot{\mathbf{r}}_i^2 - U(\mathbf{r}_i) \tag{A.1}$$

The corresponding equations of motion can be obtained from the Euler-Lagrange equation,

$$\frac{d}{dt}\left(\frac{\partial L}{\partial \dot{\mathbf{r}}_i}\right) - \frac{\partial L}{\partial \mathbf{r}_i} = 0 \tag{A.2}$$

Taking the derivative of eq. A.1 with respect to $\dot{\mathbf{r}}_i$ and $\mathbf{r}_i$ results in,

$$\frac{\partial L}{\partial \dot{\mathbf{r}}_i} = m_i \dot{\mathbf{r}}_i$$
$$\frac{\partial L}{\partial \mathbf{r}_i} = -\frac{\partial U}{\partial \mathbf{r}_i} = \mathbf{F}_i$$

Substituting these in eq. A.2 gives the familiar Newton's equations of motion.

The kernel in any MD simulation is the calculation of force on the atoms which is the negative gradient of the potential energy with respect to the atom coordinate. In a system consisting of N particles, assuming that the potential energy depends only on positions of the atoms $\mathbf{r}_1$,$\mathbf{r}_2$, $\mathbf{r}_3$, $\cdots$, $\mathbf{r}_N$, one can write,

$$\mathbf{F}_i = -\nabla_i U(\mathbf{r}_1, \mathbf{r}_2, \mathbf{r}_3, \cdots, \mathbf{r}_N) \tag{A.3}$$

In empirical potential MD (also called "classical MD"), the interaction potential is a function only of the atomic coordinates. However, in ab initio MD (by which we refer to the one based on Kohn-Sham density functional theory), the potential energy is dependent on both electronic and nuclear degrees of freedom.

A.2 Classical molecular dynamics simulations

In this method, the potential energy is calculated from functional forms which depend on the atom coordinates. Parameters in the potential energy expression are determined either on an empirical basis or through quantum chemical calculations.

The total potential energy can be written as a sum of two terms, as follows.

$$U = U_b + U_{nb} \tag{A.4}$$

where U$_b$ and U$_{nb}$ are potential energies due to bonded and non-bonded interactions respectively. Frequently, the former is written as a sum of four terms, as follows.

$$U_b = U_{bond} + U_{angle} + U_{dihedral} + U_{improper} \tag{A.5}$$

where U$_{bond}$, U$_{angle}$, U$_{dihedral}$, U$_{improper}$ are energies due to bonds, angles, dihedrals and improper torsions present in a molecule respectively. The non-bonded interactions are calculated using interatomic potentials. It can be written as a sum of two-body (also called as pair-potential), three-body, $\cdots$, N-body interactions, as follows.

$$U_{nb} = U_{2body} + U_{3body} + U_{4body} + \cdots + U_{Nbody} \tag{A.6}$$

In many cases, the three-body and higher order body terms are ignored as they are relatively expensive to calculate. Furthermore, a pairwise potential is often an effective potential which subsumes the many-body effects. This term can be written as a function of distance between two particles, as follows.

$$U_{nb} = \sum_{i=1}^{N} \sum_{j<i}^{N} U_{ij}(\mathbf{r}_i - \mathbf{r}_j) \tag{A.7}$$

The most widely used pair-potential is the Lennard-Jones potential of 12-6 form which captures the dispersion interaction between atoms and is defined as,

$$U_{LJ} = 4\epsilon \left[\left(\frac{\sigma}{r}\right)^{12} - \left(\frac{\sigma}{r}\right)^{6} \right] \tag{A.8}$$

where ϵ and σ are the well-depth and the distance at which the energy goes to zero respectively. Charge-charge interactions are modelled using the Coulomb potential which is defined as

$$U_{es} = \sum_{i=1}^{N}\sum_{j=1}^{N} \frac{q_i q_j}{4\pi\epsilon_0 r_{ij}} \tag{A.9}$$

where 'q_i' and 'q_j' are quantities of charge on particles i and j respectively.

A.2.1 Force calculation and integrators

This part is the most time-consuming in any MD simulation. Without using any approximations or algorithmic improvements, the time required to compute the forces on the particles scales as N^2. In order to reduce the computational time, these are calculated for those particles which are separated by certain value 'r_c'. Furthermore, the choice of the cutoff (being less than half the box length) ensures that no interaction is counted twice. In any event, most potentials die off within the cutoff value and hence interactions beyond it can be neglected without much loss of accuracy. Periodic boundary conditions are employed to remove surface effects and to simulate the bulk behaviour of a liquid or a solid. The force components between two particles 'i' and 'j' are calculated using the following equation,

$$F_{ij}^{k} = -\frac{k}{r}\frac{\partial U(r)}{\partial r} \tag{A.10}$$

where k = x, y or z. Coulomb interaction is long ranged, i.e., it dies off much slower than r^{-3}. Further, the Coulomb sum is conditionally convergent, i.e., the Coulomb energy depends on the order in which the pairs are considered. Hence, it is important that it is handled carefully. One way to treat it accurately is the Ewald summation method which modifies the charge-charge interaction in real space so as to make it negligible within the cutoff and takes care of the long range contribution in reciprocal space. [11] The particle-particle particle-mesh (PPPM) method employs a mesh and Fast Fourier Transform methods to calculate the reciprocal sum faster. [12, 13]

Integrators are required to integrate the equations of motion and thus to advance the positions and velocities to the next timestep, starting from an initial configuration. For this purpose, many numerical algorithms are available: Verlet algorithm, leap-frog algorithm, velocity Verlet algorithm, Beeman algorithm, Gear predictor-corrector algorithm etc. [2, 3] The most widely used algorithm is the velocity Verlet whose equations can be written as,

$$\boldsymbol{p}_i(t + \frac{1}{2}\delta t) = \boldsymbol{p}_i(t) + \frac{1}{2}\delta t \boldsymbol{f}_i(t) \tag{A.11}$$

$$\boldsymbol{r}_i(t + \delta t) = \boldsymbol{r}_i(t) + \delta t \boldsymbol{p}_i(t + \frac{1}{2}\delta t)/m_i \tag{A.12}$$

$$\boldsymbol{p}_i(t + \delta t) = \boldsymbol{p}_i(t + \frac{1}{2}\delta t) + \frac{1}{2}\delta t \boldsymbol{f}_i(t + \delta t) \tag{A.13}$$

A.3 Ab initio molecular dynamics simulations

This approach is similar to classical molecular dynamics; however the potential or forces acting on the atoms are calculated in an alternative manner instead of from a pre-defined potential. The electronic degrees of freedom are considered explicitly in these simulations. In Born-Oppenheimer molecular dynamics (BOMD) simulations, the electronic structure problem is solved at each time step, for a given nuclear configuration. The electronic ground state is determined and the force on each nuclei not only comes from nuclei-nuclei interactions, but it also comes from the electronic ground state, through the Hellmann-Feynman theorem. In these calculations, the electronic structure for the ground state has to be solved quite accurately; else, it can lead to an error in the calculation of forces on the nuclei which can further lead to drifts in the total energy of the system. In an alternative to BOMD, Car-Parrinello

MD (CPMD) can also be employed. Herein, the coefficients of the electronic wave function are treated as variables of an extended system and are propagated as a function of time. The dynamics of the electrons is fictitious. The electron is provided a fictitious mass which is light. Typical mass values range between 400-800 a.u. In this approach, once the system is started in the electronic ground state, it continues to be resident there, due to (i) the lightness of the electron fictitious mass and (ii) the lack of momentum transfer between the electronic and nuclear degrees of freedom. The latter can be verified by comparing the phonon and electronic density of states of the system. Adiabaticity is guaranteed, if these two do not overlap.

Naturally, in CPMD, one has to employ a small time step – typically around 5 a.u. or so (1 a.u. $\approx$ 0.024 fs), whereas in BOMD, one can use a time step of 30 a.u. or more. BOMD can be expensive as the electronic ground state has to be determined accurately through successive iterations. However, recent algorithmic and methodological developments have enhanced its efficiency and thus appeal [14].

A.3.1 Born-Oppenheimer molecular dynamics

In this approach, the forces are calculated from the electronic structure calculations by solving the time-independent Schrödinger equation. This method involves propagating the nuclei using Newtonian equation of motion and at each timestep, the electronic wave function is restricted to be ground state ($\boldsymbol{\psi}_0$) for fixed nuclear coordinations during the trajectory. For given nuclear positions, the electronic ground state is solved. Effectively, the Born-Oppenheimer molecular dynamics method can be written as,

$$M_I \ddot{\mathbf{R}}_I(t) = -\nabla_I \min_{\boldsymbol{\psi}_0} < \boldsymbol{\psi}_0 | H_e(\mathbf{r}_i, \mathbf{R}_I) | \boldsymbol{\psi}_0 > \tag{A.14}$$

where

$$H_e(\mathbf{r}_i,\mathbf{R}_I) = -\sum_i \frac{\hbar^2}{2m_e}\nabla_i^2 + \frac{1}{4\pi\epsilon_0}\sum_{i<j}\frac{e^2}{|\mathbf{r}_i-\mathbf{r}_j|} - \frac{1}{4\pi\epsilon_0}\sum_{i,I}\frac{e^2 Z_I}{|\mathbf{R}_I-\mathbf{r}_i|} + \frac{1}{4\pi\epsilon_0}\sum_{I<J}\frac{e^2 Z_I Z_J}{|\mathbf{R}_I-\mathbf{R}_J|}$$

The electronic ground state and hence the ground state energy can be calculated from Kohn-Sham formulation of density functional theory. [15, 16]

A.3.2 Car-Parrinello molecular dynamics

The BOMD method can be expensive since it involves the calculation of electronic ground state at each timestep. To reduce the computational cost, Car and Parrinello proposed a different approach where they assigned a fictitious mass to the electrons and modified the Lagrangian to include the electron dynamics. [17] In this manner, the electrons (rather the coefficients of the wave function expressed in the chosen basis set) are treated as dynamical variables and propagated along with the nuclei during the generation of the trajectory. The modified Lagrangian leads to coupled electron-ion dynamics. The modified Lagrangian can be written as,

$$L_{CP}[\mathbf{R}^N, \dot{\mathbf{R}}^N, \dot{\boldsymbol{\psi}}_i, \boldsymbol{\psi}_i] = \sum_{I=1}^{N}\frac{1}{2}M_I\dot{\mathbf{R}}_I^2 + \sum_i \mu < \dot{\boldsymbol{\psi}}_i|\dot{\boldsymbol{\psi}}_i > -\varepsilon^{el}[\{\boldsymbol{\psi}_i\};\mathbf{R}_I] + \mathit{constraints} \tag{A.15}$$

where ε is the Kohn-Sham energy functional dependent on both $\boldsymbol{\psi}_i$ and $\mathbf{R}^N$. The constraints impose the orthonormality condition for the electronic wave function. Once the electronic ground state is found at first timestep, the fictitious dynamics of electrons keep them on the BO surface corresponding to nuclear positions during trajectory. This avoids the electronic minimization step and thus, reduces the computational cost. The modified Euler-Lagrange equations for this method are,

$$\frac{d}{dt}\frac{\partial L_{CP}}{\partial \dot{\mathbf{R}}_I} = \frac{\partial L_{CP}}{\partial \mathbf{R}_I} \tag{A.16}$$

$$\frac{d}{dt}\frac{\partial L_{CP}}{\partial \langle \dot{\boldsymbol{\psi}}|_i} = \frac{\partial L_{CP}}{\partial \langle \boldsymbol{\psi}_i|} \tag{A.17}$$

Following above equations, the Car-Parrinello equations of motion are derived.

$$M_I \ddot{\mathbf{R}}_I = -\frac{\partial E^{el}}{\partial \mathbf{R}_I} + \sum_{ij} \Lambda_{ij} \frac{\partial}{\partial \mathbf{R}_I} < \boldsymbol{\psi}_i | \boldsymbol{\psi}_j > \tag{A.18}$$

$$\mu |\ddot{\boldsymbol{\psi}}\rangle_i = -\frac{\partial E^{el}}{\partial |\boldsymbol{\psi}\rangle_{\boldsymbol{i}}} + \sum_j \Lambda_{ij} |\boldsymbol{\psi}_j\rangle \tag{A.19}$$

where μ and Λ_{ij} are fictitious mass of the electron and Lagrange multipliers. The units of the former are energy times a squared time. As seen in eq. A.15, the constraints introduce "constraint forces" in the equation of motion and they depend on both Kohn-Sham orbitals and nuclear positions. For obtaining stable dynamics, they must be included in the equation of motion to maintain energy conservation. The constant of energy is given as,

$$E_{cons} = \sum_I \frac{1}{2} M_I \dot{\mathbf{R}}_I^2 + \sum_i \mu < \dot{\boldsymbol{\psi}}_i | \dot{\boldsymbol{\psi}}_i > + E^{KS}[\{\boldsymbol{\psi}_i\}, \mathbf{R}^N] \tag{A.20}$$

This quantity can be used to check for stable dynamics during the trajectory. The nuclei and electrons propagate at instantaneous temperatures $\propto \sum_I M_I \dot{\mathbf{R}}_I^2$ and $\propto \sum_i \mu < \dot{\boldsymbol{\psi}}_i | \dot{\boldsymbol{\psi}}_i >$ respectively. During molecular dynamics, the ground state wave function obtained for the initial configuration continues to be resident on the BO surface provided they are kept at a sufficiently low temperature (either through a thermostat or naturally, if there is no momentum transfer between the electronic and nuclear degrees of freedom). The fictitious mass value should be chosen carefully so that there should be adiabatic energy-scale separation between ions and electrons. This means that the highest phonon frequency of ions should be much smaller than its lowest electronic frequencies. Further, there should be no transfer of energy between them.

A.3.3 Hohenberg-Kohn theorem and Kohn-Sham functional

Two theorems were proposed based on the idea that the energy of the system can be written in terms of the electronic density. [15, 16] These two theorems state that "the external potential is univocally determined by the electronic density, besides a trivial additive constant" and "electronic density also determines the ground state wave function $\boldsymbol{\psi}$ which should be obtained by solving the full many-body Schrödinger equation". [1, 15, 16] The variational energy E$_v$ is written as,

$$E_v[\rho] = F[\rho] + \int \rho(\mathbf{r}) V_{ext}(\mathbf{r}) d\mathbf{r} \tag{A.21}$$

$$\text{where} \qquad F[\rho] = < \boldsymbol{\psi}[\rho] | T + U_{ee} | \boldsymbol{\psi}[\rho] > \tag{A.22}$$

Using the variational principle and imposing the constraint that the number of electrons is conserved and is equal to 'N', it leads to

$$\delta \left\{ E_v[\rho] - \mu \int (\rho(\mathbf{r}) d\mathbf{r} - N) \right\} = 0 \tag{A.23}$$

$$\mu = \frac{\delta E_v[\rho]}{\delta \rho} = V_{ext}(\mathbf{r}) + \frac{\delta F[\rho]}{\delta \rho} \tag{A.24}$$

where μ is the Lagrange multiplier. F[ρ] is a universal functional for N electrons which depends on density alone. Since the exact form of this functional is not known, approximations are made to replace the effect of this functional. The final Kohn-Sham functional is written as (it is obtained from A.21)

$$E_{KS}[\rho] = T_R[\rho] + \int \rho(\mathbf{r}) V_{ext}(\mathbf{r}) d\mathbf{r} + \frac{1}{2} \int \int \frac{\rho(\mathbf{r})\rho(\mathbf{r}')}{|\mathbf{r} - \mathbf{r}'|} dr dr' + E_{XC}[\rho] \tag{A.25}$$

A.3.4 Forces in BOMD and CPMD

In both CPMD and BOMD, the forces and thus the total ground state energy acting on the ions are calculated from the Kohn-Sham functional. In BOMD, the forces can be calculated from the extended energy functional,

$$\varepsilon_{KS} = E^{KS} + \sum_{ij} \Lambda_{ij} \left(< \boldsymbol{\psi}_i | \boldsymbol{\psi}_j > -\delta_{ij}\right) \tag{A.26}$$

The derivative of this equation with respect to nuclear positions gives the forces acting on the ions. The resultant equation is,

$$F^{KS}(\mathbf{R}_I) = -\frac{\partial E^{KS}}{\partial \mathbf{R}_I} + \sum_{ij} \Lambda_{ij} \frac{\partial}{\partial \mathbf{R}_I} < \boldsymbol{\psi}_i | \boldsymbol{\psi}_j > \tag{A.27}$$

From this equation, it is clear that the accuracy of force calculation on ions depends linearly on the accuracy of minimization of Kohn-Sham energy.

In case of CPMD, the forces on the ions are calculated in the same way as for BOMD using eq. A.27 For electrons, the forces are given by

$$f_i = -\frac{\delta E^{el}}{\delta \langle \boldsymbol{\psi}_i |} + \sum_j \Lambda_{ij} | \boldsymbol{\psi}_{ij} \rangle \tag{A.28}$$

A.4 Pseudopotentials

In a plane wave basis, a large energy cut-off is required to represent a wave function because of rapid oscillations of the wave function near the nucleus and also due to the orthogonality condition. Further, explicit consideration of all the electrons would increase the computational cost enormously. Fortunately, the role of core electrons for understanding the chemistry between atoms is limited. So, the effect of the core electrons and of the nuclei on the valence electrons can be considered using effective potentials or pseudopotentials. The true wave function is also replaced by a nodeless pseudo wave function the description of which requires only a few number of plane waves.

Electronic states are categorized into three: core, valence, and semi-core. During the pseudopotential development, it is assumed that there is no significant overlap of core states with valence states. So, in general, the valence states alone are considered for the construction of pseudopotentials. The pseudopotential and pseudo wave function are constructed such that beyond a given radius 'r_c', they should match the original potential and true wave function respectively. Pseudopotentials with large r_c value are called softer because they require less number of plane waves. They are also less transferable i.e., the same pseudopotential of an atom may not be appropriate in different chemical environments. Pseudopotentials are divided into two: norm-conserving and non norm-conserving or ultrafast pseudopotentials. The former imposes the condition that outside r_c, the norm of the pseudo wave function or charge density should be same as that of true wave function. For eg: Troullier-Martins pseudopotentials. [18] In these, the pseudo wave function ($\boldsymbol{\psi}_l$) is approximated to an analytical function form which is written as,

$$\boldsymbol{\psi}_l(r) = r^{l+1} \exp(p(r)) \qquad r < r_c \tag{A.29}$$

$$\text{where} \quad p(r) = c_0 + c_2 r^2 + c_4 r^4 + c_6 r^6 + c_8 r^8 + c_{10} r^{10} + c_{12} r^{12}$$

Here, the coefficients c_n are determined from norm conservation, continuity of the pseudo wave function and its first four order derivatives and the zero curvature of pseudopotential at the origin. In ultrafast pseudopotentials, the normalization constraint is relaxed which allows further reduction in the number of plane waves.

Bibliography

[1] Kohanoff, J. *Electronic Structure Calculations for Solids and Molecules*; Cambridge University Press, 2006.

[2] Frenkel, D.; Smit, B. *Understanding Molecular Simulation: From Algorithms to Applications*; Computational science; Elsevier Science, 2001.

[3] Allen, M.; Tildesley, D. *Computer Simulation of Liquids*; Oxford Science Publications; Clarendon Press, 1989.

[4] Marx, D.; Hutter, J. In *Modern Methods and Algorithms of Quantum Chemistry*; Grotendorst, J., Ed.; NIC; Forschungszentrum Jlich, 2000; Chapter 13, pp 301–449.

[5] Marx, D.; Hutter, J. *Ab Initio Molecular Dynamics: Basic Theory and Advanced Methods*; Ab Initio Molecular Dynamics: Basic Theory and Advanced Methods; Cambridge University Press, 2009.

[6] Martin, R. *Electronic Structure: Basic Theory and Practical Methods*; Cambridge University Press, 2008.

[7] Remler, D. K.; Madden, P. A. *Mol. Phys.* **1990**, *70*, 921–966.

[8] Tuckerman, M. E. *J. Phys.: Condens. Matter* **2002**, *14*, R1297.

[9] Kühne, T. D. *ArXiv e-prints* **2012**,

[10] Tuckerman, M. E.; Martyna, G. J. *J. Phys. Chem. B* **2000**, *104*, 159–178.

[11] Hansen, J.-P. In *Molecular Dynamics Simulation of Statistical Mechanical Systems*; Ciccotti, G., Hoover, W. G., Eds.; 1986.

[12] Hockney, R.; Eastwood, J. *Computer Simulation Using Particles*; Taylor & Francis, 2010.

[13] Pollock, E.; Glosli, J. *Computer Physics Communications* **1996**, *95*, 93 – 110.

[14] VandeVondele, J.; Krack, M.; Mohamed, F.; Parrinello, M.; Chassaing, T.; Hutter, J. *Comput. Phys. Commun.* **2005**, *167*, 103–128.

[15] Hohenberg, P.; Kohn, W. *Phys. Rev.* **1964**, *136*, B864–B871.

[16] Kohn, W.; Sham, L. J. *Phys. Rev.* **1965**, *140*, A1133–A1138.

[17] Car, R.; Parrinello, M. *Phys. Rev. Lett.* **1985**, *55*, 2471–2474.

[18] Troullier, N.; Martins, J. L. *Phys. Rev. B* **1991**, *43*, 1993–2006.

List of Publications

- Theoretical Investigations of Candidate Crystal Structures for β-Carbonic Acid
  Reddy, S. K.; Kulkarni, C. H; Balasubramanian, S.
  J. Chem. Phys. **2011**, *134* , 124511.

- Vibrational Spectra of Linear Oligomers of Carbonic Acid: A Quantum Chemical Study.
  Reddy, S. K.; Kulkarni, C. H; Balasubramanian, S.
  J. Phys. Chem. A **2012**, *116* , 1638-1647.

- Liquid Dimethyl Carbonate: A Quantum Chemical and Molecular Dynamics Study.
  Reddy, S. K.; Balasubramanian, S.
  J. Phys. Chem. B **2012**, *116* , 14892-14902.

- Three-Dimensional Metal-Organic Framework with Highly Polar Pore Surface: H_2 and CO_2 Storage Characteristics.
  Jayaramulu, K; Reddy, S. K.; Hazra, A.; Balasubramanian, S.; Maji, T. K.
  Inorg. Chem. **2012**, *51* , 7103-7111.

- Unusual Room Temperature CO_2 Uptake in a Fluoro-Functionalized MOF: Insight from Raman Spectroscopy and Theoretical Studies.

Kanoo, P; Reddy, S. K.; Kumari, G; Haldar, R; Narayana, C.; Balasubramanian, S.; Maji, T. K.
Chem. Commun. **2012**, *48* , 8487-8489.

- Low-Frequency Vibrational Modes of Room Temperature Ionic Liquids.
  Sarangi, S. S.; Reddy, S. K.; Balasubramanian, S.
  J. Phys. Chem. B **2011**, *115* , 1874-1880.

- Cooperativity in the Stacking of Benzene-1,3,5-tricarboxamide: The role of dispersion.
  Kulkarni, C. H.; Reddy, S. K.; George, S. J.; Balasubramanian, S.
  Chem. Phys. Lett. **2011**, *515* , 226-230.

- Carbonic Acid: Molecule, Crystal and Aqueous Solution.
  Reddy, S. K.; Balasubramanian, S. (To be submitted)

- Breathing Effect and Gate-Opening in an Interpenetrated Metal-Organic Framework: A Computational Study
  Kanoo, P.; Haldar, R.; Reddy, S. K.; Hazra, A.; Bonakala, S.; Matsuda, R.; Kitagawa, S.; Balasubramanian, S.; Maji, T. K. (Manuscript in preparation).